8-23-2016 12:00 AM

Reactor Performances and Hydrodynamics of Various Gas-Solids Fluidized Beds

Jiangshan Liu
The University of Western Ontario

Supervisor
Dr. Jesse Zhu
The University of Western Ontario

Graduate Program in Chemical and Biochemical Engineering
A thesis submitted in partial fulfillment of the requirements for the degree in Doctor of Philosophy

ABSTRACT

The reactor performances and hydrodynamics were systematically studied in a multifunctional fluidized-bed system which included a bubbling fluidized bed (BFB), a turbulent fluidized bed (TFB) as well as a newly identified circulating turbulent fluidized bed (CTFB) using the same batch of activated FCC particles. Catalytic ozone decomposition was employed as the model reaction to experimentally investigate the reactor performances of BFB, TFB and CTFB. The complete mappings of ozone concentration were obtained in these fluidized beds, showing close relationship with the solids holdup distributions. In the BFBs and TFBs, the study of scale-up effect revealed that the static bed height had almost no influence on the ozone concentration distributions, whereas the bed diameter affected the concentration distributions, especially in the bubbling regime. This work, for the first time, examined the reactor performance of a CTFB: the ozone concentration decreased along the axial direction with a large portion of reaction happening in the entrance section, while the "centre-high" and "wall-low" radial profile of ozone concentration was presented.

Comprehensive evaluations on reactor performance were then conducted across the full spectrum of the commonly used fluidized-bed reactors, including BFB, TFB, CTFB, riser and downer, in order to illustrate the superior and inferior features for each. The clear correlations between ozone concentrations and solids holdups confirmed that the reactor performances were essentially controlled by the flow structures including gas/solids behaviour and distributions. Furthermore, the CTFB and downer showed a comparable reactor performance that was very close to that of a plug-flow reactor, resulting from the uniform flow structures with little backmixing. While the TFB demonstrated favourable reactor performance, the CTFB is still superior in reactor efficiency. The further deviation of the BFB and riser from a plug-flow reactor was due to the significant gas bypassing and backmixing. The performances of the various fluidized beds were then quantitatively characterized by gas-solids contact efficiencies.

The hydrodynamics of the BFB, TFB and CTFB were also studied in order to help understand their reactor performances. An optical fibre probe was used to obtain the spatial distribution (i.e., axial and radial profiles of time-average data) and the temporal variation (i.e., time-serial data) of solid holdup. By analysing the instantaneous signals of solids holdup, the BFB was found to be

dominated by a dense (solid) phase with a discrete dilute (bubble) phase, while the TFB exhibited a dynamic flow structure with the comparable dense (cluster) and dilute (void) phases. The CTFB experienced even more transient behaviour over the TFB, causing more interfacial activities. In addition, the CTFB successfully achieved a gas/solids upflow with solids circulation rates as high as 300 kg/m^{2}s while maintaining a dense bed with solids holdup ranging from 0.25 to 0.35. The CTFB possesses many hydrodynamic advantages, such as uniform axial flow structure, homogeneously inter-diffused dilute/dense phases and no net solids downflow, leading to very favourable mass transfer and highly efficient gas-solids contact.

Keywords: bubbling fluidized bed, turbulent fluidized bed, circulating turbulent fluidized bed, circulating fluidized bed, gas/solids flow, hydrodynamics, solids holdup, reactor performance, conversion distribution, contact efficiency

CO-AUTHORSHIP

Chapter 4: Hydrodynamics of low-velocity gas-solids fluidized beds

Authors: Jiangshan Liu and Jesse Zhu

Jiangshan Liu carried out all the experimental work and data analysis under the guidance of Dr. Jesse Zhu. The draft of this manuscript was written by Jiangshan Liu. Revisions were carried out under the close supervision of Dr. Jesse Zhu. The final version is ready for submission.

Chapter 5: Hydrodynamics of a circulating turbulent fluidized bed

Authors: Jiangshan Liu and Jesse Zhu

Jiangshan Liu carried out all the experimental work and data analysis under the guidance of Dr. Jesse Zhu. The draft of this manuscript was written by Jiangshan Liu. Revisions were carried out under the close supervision of Dr. Jesse Zhu. The final version is ready for submission.

Chapter 6: Reactor performances of low-velocity gas-solids fluidized beds

Authors: Jiangshan Liu and Jesse Zhu

Jiangshan Liu carried out all the experimental work and data analysis under the guidance of Dr. Jesse Zhu. The draft of this manuscript was written by Jiangshan Liu. Revisions were carried out under the close supervision of Dr. Jesse Zhu. The final version is ready for submission.

Chapter 7: Reactor performance of a circulating turbulent fluidized bed

Authors: Jiangshan Liu and Jesse Zhu

Jiangshan Liu carried out all the experimental work and data analysis under the guidance of Dr. Jesse Zhu. The draft of this manuscript was written by Jiangshan Liu. Revisions were carried out under the close supervision of Dr. Jesse Zhu. The final version is ready for submission.

Chapter 8: Comparative study on reactor performances of various fluidized beds

Authors: Jiangshan Liu, Chengxiu Wang and Jesse Zhu

Jiangshan Liu carried out the experimental work of the bubbling fluidized bed, turbulent fluidized bed and circulating turbulent fluidized bed. Dr. Chengxiu Wang carried out the experimental work of the circulating fluidized bed riser and downer. The data analysis was performed by Jiangshan Liu under the guidance of Dr. Jesse Zhu. The draft of this manuscript was written by Jiangshan Liu. Revisions were carried out under the close supervision of Dr. Jesse Zhu. The final version is ready for submission.

ACKNOWLEDGEMENT

I would like to express my sincere appreciation to my supervisor, Dr. Jesse Zhu, for his constant guidance, motivation and support, without which this work would not have been possible. He also has been acting as a mentor sharing his valuable professional and personal experiences.

I am grateful to Mr. Jianzhang Wen for helping me setup and maintain the experimental apparatus. Much gratitude is extended to Dr. Chengxiu Wang for the constructive discussion and suggestions. Many thanks to Shanyun Liu, Zhuoran Jiang and Sizhe Wu who were Master or undergraduate students temporarily involving in this project.

My most heartfelt appreciation is given to my parents and girlfriend, Yunhan Zhang. During these years, they have always been with me, shared my happiness and sadness, and encouraged me to make every progress.

I also would like to thank my colleagues and friends in my research group for all the fun and help throughout the years.

TABLE OF CONTENTS

LIST OF TABLES

LIST OF FIGURES

Chapter 1 Introduction

1.1. Background

Particulate solids play an important role in chemical, mineral, pharmaceutical, energy-related processes, etc. (Grace, Knowlton et al. 1997). Among particle processing units, fluidized beds exhibit many favourable features, such as good heat/mass transfer, uniform temperature distribution, easy handling of large quantity of particles and so forth (Lim, Zhu et al. 1995). The particles are characterized as "fluidized" because the fluid/solids suspension possesses many physical properties of a fluid (Davidson and Harrison 1963). Based on the different fluid media, it can be categorized as gas-solid fluidization, liquid-solid fluidization and gas-liquid-solid fluidization. In this thesis, all have been written about gas-solid fluidization if not otherwise specified.

The existence of different types of fluidized beds under different operating conditions is well-known and extensive research has been done in establishing the regime demarcation and transition velocities (Zenz 1949, Yerushalmi and Cankurt 1979, Bi and Grace 1995, Smolders and Baeyens 2001). The most general classification is particulate fluidized bed, bubbling fluidized bed (BFB), turbulent fluidized bed (TFB), fast/circulating fluidized bed (CFB) and pneumatic transport, with increasing fluidizing gas velocity. In addition, newly identified fluidized beds, such as high density/flux circulating fluidized bed (HDCFB or HFCFB) (Zhu and Bi 1995, Grace, Issangya et al. 1999) and circulating turbulent fluidized bed (CTFB) (Qi, Zhu et al. 2009), have been proposed and situated on the typical regime map based on the distinctive hydrodynamic characteristics and unique operating processes. In contrast with the conventional CFB risers where both gas and solids flow upwards, a new type of reactor, CFB downer, where both gas and solids flow downwards in the same direction of the gravity, has drawn great interest as well (Zhu, Yu et al. 1995).

Since different fluidized-bed reactors can have different applications based on the various flow structures, the in-depth understanding on the reactor performance of all types of fluidized beds is of crucial importance. Experimental studies with chemical reactions (so-called "hot-model" studies) can provide more direct and reliable information for reactor performance investigations

than other methods. For instance, the axial and radial profiles of reactant conversion obtained in the "hot-model" studies are essential to understand mass transfer characteristics, to optimize reactor designs, and to develop and verify reactor models (Grace and Bi 1997).

A literature review on earlier experimental studies of fluidized-bed reactor performance is written in Chapter 2, revealing the following issues all of which are addressed in this study: most previous reactor performance studies have been done for BFBs and low density CFB risers, while TFBs, HDCFBs and downers have received very limited attention. Moreover, almost all of them were conducted only in each individual type of fluidized bed with different reactor dimensions and catalyst particles. As a consequence, the superior and inferior features of the various fluidized beds are difficult to be identified. Therefore, a systematic study covering the complete spectrum of commonly used fluidized beds under industrial operating conditions is very necessary. For the first time, herewith, our group has investigated the reactor performances of a BFB, a TFB, a CTFB, a CFB riser and a dower in a multifunctional fluidized-bed system using the same catalyst particles, the same reaction and the same reactor diameter for the sake of reliability and convenience of comparisons. By doing so, the distinctive characteristics of each bed can be identified, providing solid scientific basis for selecting suitable fluidized-bed reactors in industries. The BFB, TFB and CTFB are studied in this work, while the work of the CFB riser and downer has been done by Wang (Wang 2013) including high density/flux flow conditions. On the other hand, more efforts in research of reactor performance are required. For BFBs, although the reactor performance has received extensive studies since sixty years ago (Frye, Lake et al. 1958), the reports of complete spatial reactant conversion distributions, especially radial distributions, are insufficient (the references are listed in Table 2.2). For TFBs, only a few experimental studies of the reactor performance have been done, and no conversion mapping is available, even though they have much more commercial applications than BFBs. Furthermore, as a newly invented fluidized bed, the reactor performance study of CTFBs has not yet been reported.

A variety of reactions have been employed to investigate gas-solids fluidized-bed reactor performances (the references are listed in Chapter 2). Among the ever-reported reactions, catalytic decomposition of ozone was the most popular model reaction in various fluidized beds due to its advantages in the lab-scale research. Firstly, ozone can decompose to oxygen in the

ambient conditions by the catalytic effect of some inexpensive metallic oxides, like ferric oxide. Secondly, since the ozone decomposition is a simple first-order reaction, the yield can be easily evaluated by the conversions which are independent of the initial reactant concentrations. Additionally, the reaction has negligible heat effect, as well as being non-toxic to the catalysts. Thus, catalytic decomposition of ozone has been employed in this work.

The hydrodynamics of fluidized beds, including solids holdup, particle velocity/flux, their distributions and fluctuations, and gas/solids behaviour, have been found to significantly affect the reactor performance, such as the extent of reaction, gas/solids mixing and contacting, mass/heat transfer and so on, through numerous practical experiences and experimental results. For instance, it is well-known that BFBs have a dense phase flow structure with dispersed bubbles, resulting in high mass transfer resistance between the bubble phase and the dense phase. Besides, there are much less particles inside the bubbles than the surrounding dense phase, leading to less conversions in the bubbles (Chavarie and Grace 1975). In contrast, TFBs have a dilute phase vigorously competing with a comparable dense phase, so that the heat and mass transfers tend to reach the maximum (Bi, Ellis et al. 2000). For CTFBs, many hydrodynamic advantages, such as high density upflow without net downflow, homogeneously mixed gas and solids, and uniform flow structure, can lead to highly efficient gas/solids contacting and narrow residence time distribution (Zhu 2010). Therefore, in order to help understand the reactor performances of the various fluidized beds, hydrodynamic study is indispensable. Furthermore, it can provide more data to further understand the underlying phenomena and develop numerical simulations.

1.2. Research objectives

Based on a literature review of the previous studies on both fluidized-bed reactor performances and hydrodynamics, the objectives of this study are:

- To comprehensively study the reactor performances of various types of fluidized beds using the same reactor system, the same reaction (catalytic ozone decomposition) and the same batch of catalyst particles;

- To obtain the axial and radial profiles of ozone conversion in a BFB and a TFB, to evaluate their reactor performances, and also to study the scale-up effects;
- To obtain the axial and radial profiles of ozone conversion in a CTFB, and to evaluate its reactor performance;
- To compare the reactor performances of the BFB, TFB, CTFB, CFB riser and downer, and to identify the superior and inferior features of each fluidized-bed reactors;
- To obtain the axial and radial profiles of solids holdup and its fluctuation, and to investigate the local transient gas/solids behaviour in the BFB, TFB and CTFB.

1.3. Thesis structure

Chapter 1 gives a general introduction of this study.

Chapter 2 presents a detailed literature review on the hydrodynamic studies and the reactor performance studies using ozone decomposition of various types of fluidized beds.

Chapter 3 describes the experimental setup, measurement techniques and experiment procedures.

Chapter 4 investigates the hydrodynamics of the BFB and the TFB in terms of differential pressure profiles, local solids holdup distributions, local flow fluctuations and their changes with operating conditions. Additionally, the effect of static bed height and the effect of bed diameter on the hydrodynamics are investigated.

Chapter 5 investigates the hydrodynamics of the CTFB regarding the axial and radial profiles of solids holdup, the local flow fluctuations, and the effects of operating conditions and gas distributor.

Chapter 6 reports the experimental results of axial and radial profiles of ozone concentration in the BFB and the TFB. The ozone conversions are correlated with the solids holdups. The reactor performances are evaluated by gas-solids contact efficiency. In addition, the effects of static bed height and bed diameter on reactor performance are investigated.

Chapter 7 reports the experimental results of axial and radial profiles of ozone concentration in the CTFB under various operating conditions. The ozone conversions are correlated with the solids holdups. The reactor performances are evaluated by gas-solids contact efficiency.

Chapter 8 compares the reactor performances of the BFB, TFB, CTFB, CFB riser and downer in terms of axial/radial profiles of ozone concentration, correlations between conversion and solids holdup and gas-solids contact efficiency. The characteristics of each type of fluidized bed are discussed and the mechanisms are analysed.

Chapter 9 gives general conclusions of this study.

References

Bi, H., N. Ellis, I. Abba and J. Grace (2000). A state-of-the-art review of gas–solid turbulent fluidization. *Chemical Engineering Science* **55**(21): 4789-4825.

Bi, H. and J. Grace (1995). Flow regime diagrams for gas-solid fluidization and upward transport. *International Journal of Multiphase Flow* **21**(6): 1229-1236.

Chavarie, C. and J. R. Grace (1975). Performance analysis of a fluidized bed reactor. II. Observed reactor behavior compared with simple two-phase models. *Industrial & Engineering Chemistry Fundamentals* **14**(2): 79-86.

Davidson, J., D. Harrison (1963). *Fluidized Particles*. Cambridge, England.

Frye, C., W. Lake and H. Eckstrom (1958). Gas‐solid contacting with ozone decomposition reaction. *AIChE Journal* **4**(4): 403-408.

Grace, J. R. and H. Bi (1997). Introduction to circulating fluidized beds. *Circulating Fluidized Beds*, Springer**:** 1-20.

Grace, J. R., A. S. Issangya, D. Bai, H. Bi and J. Zhu (1999). Situating the high‐density circulating fluidized bed. *AIChE Journal* **45**(10): 2108-2116.

Grace, J. R., T. Knowlton and A. Avidan (1997). *Circulating fluidized beds*. London, Blackie Academic and Professional.

Lim, K., J. Zhu and J. Grace (1995). Hydrodynamics of gas-solid fluidization. *International Journal of Multiphase Flow* **21**: 141-193.

Qi, X., H. Zhu and J. Zhu (2009). Demarcation of a new circulating turbulent fluidization regime. *AIChE Journal* **55**(3): 594-611.

Smolders, K. and J. Baeyens (2001). Gas fluidized beds operating at high velocities: a critical review of occurring regimes. *Powder Technology* **119**(2): 269-291.

Wang, C. (2013). *High density gas-solids circulating fluidized bed riser and downer reactors*, The University of Western Ontario.

Yerushalmi, J. and N. Cankurt (1979). Further studies of the regimes of fluidization. *Powder Technology* **24**(2): 187-205.

Zenz, F. A. (1949). Two-phase fluid-solid flow. *Industrial & Engineering Chemistry* **41**(12): 2801-2806.

Zhu, J. (2010). Circulating turbulent fluidization—a new fluidization regime or just a transitional phenomenon. *Particuology* **8**(6): 640-644.

Zhu, J. X. and H. T. Bi (1995). Distinctions between low density and high density circulating fluidized beds. *The Canadian Journal of Chemical Engineering* **73**(5): 644-649.

Zhu, J. X., Z. Q. Yu, Y. Jin, J. Grace and A. Issangya (1995). Cocurrent downflow circulating fluidized bed (downer) reactors—a state of the art review. *The Canadian Journal of Chemical Engineering* **73**(5): 662-677.

Chapter 2 Literature Review

Particles normally can be suspended in a vessel by introducing gas from the bottom. By doing so, the interstitial space among particles can be greatly enlarged and the inter-particle forces can be significantly reduced. Thereby these particles can flow freely and possess fluid-like properties (Gelperin and Einstein 1971). The unit operation using such physical principle is broadly defined as "fluidization" with advantages of high gas-solids contact efficiency, favourable heat/mass transfer, uniform temperature distribution, capability of continuous feeding and removal of particles, etc. A fluidized bed consists of gas/solids mixture that behaves as a fluid. It presents different flow structures with varying gas velocity. With increasing fluidizing gas velocity, the fluidization regimes typically can be classified as particulate, bubbling/slugging, turbulent, fast (circulating) and pneumatic transport fluidization in sequence. General introductions of fluidization can be referred to Lim, Zhu et al. (1995), Grace and Bi (1997) and Bi, Ellis et al. (2000). The review of industrial applications of fluidization can be found in Zhu and Cheng (2006).

2.1. Hydrodynamics of bubbling fluidized beds

The bubbling fluidization is the first regime that has received extensive research since 1960s in the aspects of experimental study and numerical simulation (Davidson and Harrison 1963). Bubbling fluidized beds have visible bubbles with relatively clear boundary to the surrounding continuous particulate phase, which is the most distinctive characteristic to the other types of fluidized beds. The bubble behaviour are closely related with reaction conversion, heat and mass transfer, gas and solids mixing and so forth. Therefore, hydrodynamics of bubbling fluidized beds are of great interest, which includes bubble size, shape, distribution, rising velocity, flow pattern, etc. Besides, it is also necessary to understand solids behaviour, such as solids mixing, segregation, particle motion, entrainment/elutriation and so on, because the most common applications of bubbling fluidization are for solid chemical reactions and physical processes where particles are the reactants or raw materials. However, bubbling fluidized beds are not favourable for gas-phase catalytic reactions, due to poor mass transfer between bubble phase and solid phase and insufficient gas/solids contacting inside bubbles.

2.1.1. Bubble behaviour in bubbling fluidized beds

It is well identified that bubble behaviour are normally affected by operating conditions, such as superficial gas velocity, vessel pressure, particle characteristics and static bed height, as well as reactor designs, such as column size, gas distributors and internal parts. Despite the complex relationship, the typical examples shown here are able to demonstrate the general trends. Hatano, Khattab et al. (1986) conducted spatial-temporal measurements of bubble properties in a 3-dimensional free-bubbling fluidized bed by using a reflective optical fibre probe with double-line arrays. The probe has two horizontally paralleled lines with 13 probes in each. The radial distributions of bubble diameter, frequency and holdup were obtained at different bed elevations. It was observed that the bubbles did not rise in a constant shape and at a steady velocity. As shown in Figure 2.1, the bubble size gradually increases from the bottom, but reaches a constant at a certain height, and the central region generally has more and larger bubbles compared with the wall region. Moreover, the relationship between bubble rising velocity and bubble size was found as well, showing that bubble velocity increased with bubble size.

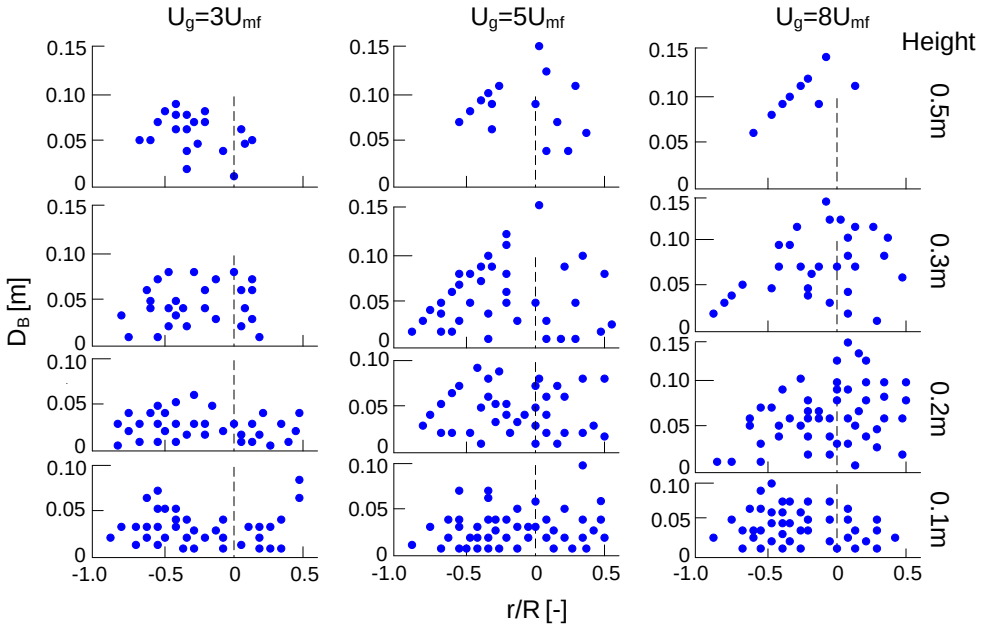

Figure 2.1 Spatial distribution of bubble diameter at different superficial gas velocity and bed elevations (Hatano, Khattab et al. 1986)

There are several techniques can measure bubble rising velocity, such as optical fibre probes, photography (applied in 2-D beds), X-ray tomography and so on, among which optical fibre probes are well developed and widely used. The accurate bubble rising velocity should be

obtained by using at least two vertically aligned optical fibre probes. It is then calculated from the time delays between two channel signals through a cross-correlation method. In practice, however, usually the signal valleys do not have rectangular shapes (indicating a passing bubble) and/or show no matched patterns in two channels. These problems result from bubbles passing the lower probe but not the upper one, splitting/coalescence of bubbles after passing the lower probe, and elongation or acceleration of bubbles when passing the probes (Geldart and Xie 1992).

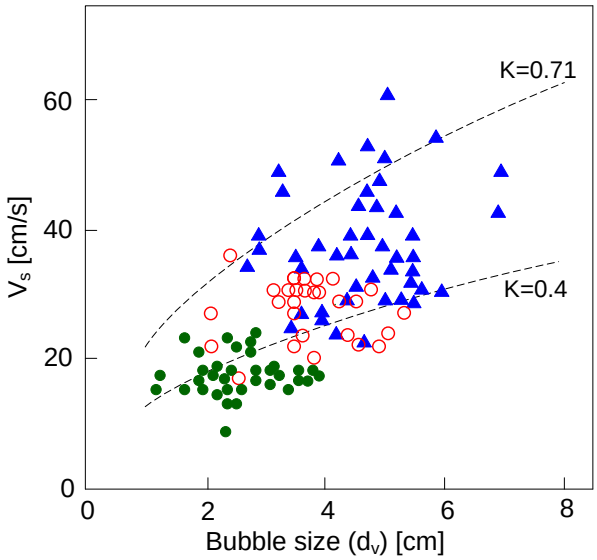

Figure 2.2 Bubble velocity V_s and size d_v for different bubble shapes (Lim and Agarwal 1992)

In spite of the difficulty in measuring bubble behaviour by using the intrusive probe technique (e.g. optical fibre probes), several improved methods have been developed in order to accurately measure bubble rising velocities. Lim and Agarwal (1992) reported that the bubble's rising motion angle must be considered when analysing the signals, especially for double-channel probes. It was also demonstrated that the elimination of non-vertical rising bubbles' signals did not affect the results of bubbling characteristics. Additionally, multi-probe sets were suggested rather than double-channel probes. The relationship between bubble rising velocity and size is shown in Figure 2.2, where different symbols represent different bubble shapes and K is bubble rising velocity coefficient ($V_{bubble} = K(gd_{bubble})^{1/2}$). Generally, the bubble velocity increased with the bubble size. The correlations were different for bubble swarms (triangular symbols) and single bubbles (circular symbols), and the bubble swarms showed a more scattered velocity distribution than the single bubbles due to the interactions. Since intrusive probes (e.g., optical fibre probes) just measure so-called pierced lengths of bubble (not the actual bubble sizes), a

forward transform method (Clark and Turton 1988) and a backward transform method (Turton and Clark 1989, Clark, Liu et al. 1996) have been proposed to estimate real bubble sizes, in which the latter one is more practical. In addition, Lim and Agarwal (1992) used an imaginary probe to explore the relationship between pierced length and bubble size in a 2-D bed.

The mass transfer of gas between the bubble phase and the particulate phase in a bubbling fluidized bed can cause the gas throughflow. The gas throughflow is defined as the gas flow in a bubble, relative to the bubble, across a plane perpendicular to the vertical axis of the bubble (Leung and Sandford 1969). A good understanding of the magnitude of throughflow velocity is very necessary, since it is related to mass transfer between the dilute-phase and dense-phase, stability of bubbles and division of gas between the dilute and dense phases (Lim, Zhu et al. 1995). A number of investigations about gas throughflow have been conducted (Hilligardt and Werther 1986, Hailu, Plaka et al. 1993, Gautam, Jurewicz et al. 1994), even though the measurements are very challenging.

2.1.2. Particle behaviour in bubbling fluidized beds

The studies of particle behaviour, including solids mixing, segregation, particle motion and gas mixing (Bellgardt, Schoessler et al. 1987), are of importance to the designs of physical and chemical processes, such as combustion and gasification. For instance, each bubble has a wake containing a large amount of solids at its bottom and carries the wake. It has been observed that the bubble drift and wake transport give rise to the gross circulation of solids, and the bubble wakes conduct local-mixing simultaneously. Therefore, bubbling fluidized beds have favourable axial solids mixing (Kunii and Levenspiel 1991). However, lateral solids mixing is much less prominent (Fan, Chen et al. 1990).

Tracer particles are usually used for experimentally investigating the solids mixing in bubbling fluidized beds (Yates and Simons 1994). Axial solids dispersion coefficient can be used to characterize the extent of axial solids mixing. The coefficient is calculated from the counter-current flow model which worked well in bubbling fluidized beds. Avidan and Yerushalmi (1985) reported that the axial solids dispersion coefficients increased with superficial gas velocity and with the square root of bed diameter which can greatly affect solids mixing in scaling-up. This conclusion was further proven by Du, Fan et al. (2002) who used electrical capacitance

tomography with no interruption to the flow behaviour. Lim, Gururajan et al. (1993) found that the solids mixing became increasingly significant with increasing particle size by using an imaging technique in a 2-D fluidized bed. Moreover, the wake exchange coefficient was affected by the gas velocity and particle size.

2.2. Hydrodynamics of turbulent fluidized beds

Turbulent fluidized beds have a large number of commercial applications, e.g., FCC regenerators, acrylonitrile, maleic and phthalic anhydride, ethylene dichloride, zinc sulfide roasting, as well as some physical processes like drying. The wide applications of turbulent fluidized beds should be attributed to the high solids holdup, vigorous gas-solids contacting, favourable bed-to-surface heat transfer and limited gas axial mixing (Bi, Ellis et al. 2000). Nevertheless, the design and scale-up of turbulent fluidized-bed reactors still have difficulties due to less understanding of the underlying phenomena and mechanism, which is one of the cases where fundamental research falls behind practical applications (Grace 2000).

2.2.1. Transition velocities in turbulent fluidized beds

Turbulent fluidization has been gradually accepted as an individual flow regime between bubbling fluidization and fast fluidization, due to its distinctive hydrodynamics and the popularity in industries (Bi and Fan 1992). In a bubbling fluidized bed, the volumetric fraction of bubbles increases with superficial gas velocity. Eventually, the bubbles cannot keep their steady forms and start to break up into smaller and chaotic voids. These voids split and coalesce extensively and frequently in this stage. It is found that the voids just have 0.1-0.5s existing time and move upwards with random routes. Besides, unlike bubbling fluidized beds, turbulent fluidized beds have no clear continuous and discrete phases. Instead, a dense (solid) phase vigorously interacts with a comparable dilute (void) phase (Zenz 1949, Kehoe and Davidson 1971, Horio, Ishii et al. 1992).

The experimental studies have given two general transition modes which are classified as whether it transforms from bubbling or slugging fluidization. If a bed transits from bubbling fluidization, it typically can be seen a sharp hydrodynamics change (Yerushalmi and Cankurt 1979, Tsukada, Nakanishi et al. 1993, Bi, Grace et al. 1995). It usually occurs in the bed using Geldart A particles which has small bubble size and slugging-free systems. Therefore, the onset

of this transition mode is related to particle size, size distribution and ratio of maximum bubble diameter to reactor diameter. On the other hand, a gradual change is presented with intermittency of small slugging and fast fluidization structures, when the transition proceeds from slugging fluidization (Rowe and MacGillivray 1980, Brereton and Grace 1992, M'chirgui 1999). This mode probably occurs in Geldart B/D particles systems or large ratio of maximum bubble diameter to reactor diameter. However, the individual identity of such mode is still controversial.

The boundaries of turbulence regime are commonly denoted by transition velocities, including bubbling to turbulent fluidization and turbulent to fast fluidization. However, the determination of transition velocities is still controversial. Local voidage fluctuations can be employed to determine the transition velocity from bubbling to turbulent fluidization. Some studies (Abed 1984, Chehbouni, Chaouki et al. 1994) reported that the standard deviation of voidage increased with the superficial gas velocity until reaching a maximum value afterwards it decreased instantly. Moreover, the experimental results of Zhu and Zhu (2008a) revealed that the local voidage increased with superficial gas velocity, but levelled off in a period, finally then kept increasing. The constant level also can be found on the curve of standard deviation of voidage against superficial gas velocity. It was suggested that the beginning and end points of the plateau should be considered as the transition points in order to adequately reflect the transformation of dense phase. Additionally, the transition velocities based on local measurements varied in different locations in the work of Zhu and Zhu (2008a).

The transition velocities also can be determined by pressure fluctuations, which was developed by Yerushalmi and Cankurt (1979). As schematically shown in Figure 2.3, the transition velocities U_c and U_k in turbulent fluidization can be determined by standard deviation of pressure fluctuation. The onset of turbulent fluidization U_c is located at the maximum standard deviation, whereas the onset of fast fluidization U_k is located at the point where the standard deviation levels off. The pressure fluctuations were obtained as absolute values or differential (pressure drop) values in different studies. Meanwhile, different interpretation methods were conducted on the pressure fluctuations results as well, since U_c could differ by different methods (Lee and Kim 1988, Brereton and Grace 1992, Bi, Grace et al. 1995). Overall, standard deviation of pressure fluctuation is the most widely applied method to determine the onset of turbulent fluidization from bubbling fluidization.

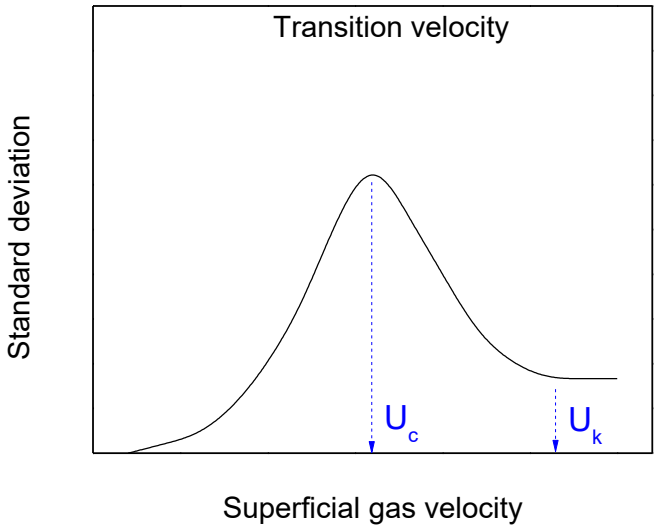

Figure 2.3 The transition velocities U_c and U_k in turbulent fluidization according to standard deviation of pressure (Yerushalmi and Cankurt 1979)

Many factors are able to influence the transition velocity U_c. Since the transition is related to changes of bubble behaviour, those affecting bubble properties apparently influence U_c as well, such as particle size (Cai 1989), particle size distribution (Sun and Grace 1992), system pressure (Tsukada, Nakanishi et al. 1993) and system temperature (Peeler, Lim et al. 1999).

A fluidized bed is characterized as transition from turbulent to fast fluidization when solids entrainment largely increases and bed surface becomes blurred. The transition velocity between turbulent and fast fluidization can be determined in several methods. A transport velocity U_{tr} from phase diagram was proposed by Yerushalmi and Cankurt (1979), Li and Kwauk (1980) and Bi (1994). A critical velocity U_{se} from solids entrainments were studied by Yerushalmi (1979) and Bi (1995), etc. A transition velocity U_k from pressure fluctuations were reported by Schnitzlein (1988) and Bi (1992), etc.

2.2.2. Flow characteristics of turbulent fluidized beds

It is commonly accepted that turbulent fluidized beds are comprised of a dilute phase (voids) and a dense phase. Thus, the volumetric fraction of the dilute phase and the voidage of the dense phase have received a great of interests.

Although the dense phase voidage is difficult to be measured by the bed collapse method, Wang, Wang et al. (1997) achieved it by using a column in which the bed and the freeboard can be physically segregated, so that the entrainments could not affect the bed height. The results

showed that the dense phase voidage stayed constant in the gas velocity's range of 0.1 m/s to 0.5 m/s (i.e. bubbling regime). In contrast, the dilute phase volumetric fraction as well as the dense phase voidage increased with superficial gas velocity in the turbulent fluidization regime (Yamazaki, Asai et al. 1991, Werther and Wein 1994). It was also found that the dense phase voidage did not vary with radial positions.

The average solids holdup in the axial direction can be simply obtained by differential pressure measurements. The bed average solids holdup (~0.25-0.35) reduces as gas velocity increases, while the solids holdup in freeboard gradually increases, as shown in Figure 2.4. For the local two-phase behaviour, the signals obtained by optical fibre probes are of great help. Regarding the radial flow structure, the particles generally flow downwards close to the wall, whereas the voids tend to flow upwards through the central region. The profiles of voids fraction presented that the radial non-uniformity became more severe with increasing gas velocity and bed height (Nakajima, Harada et al. 1991, Farag, Grislingås et al. 1997, Zhang, Qian et al. 1997). The experimental results (Avidan and Yerushalmi 1982, Abed 1984, Nakajima, Harada et al. 1991) revealed that static bed heights can influence flow patterns and higher static bed height led to more uniform void distribution in the radial direction. The beds with larger diameter resulted to better radial uniformity of voids distribution due to the reduced wall effect, reported by Farag, Grislingås et al. (1997) and Ege (1995).

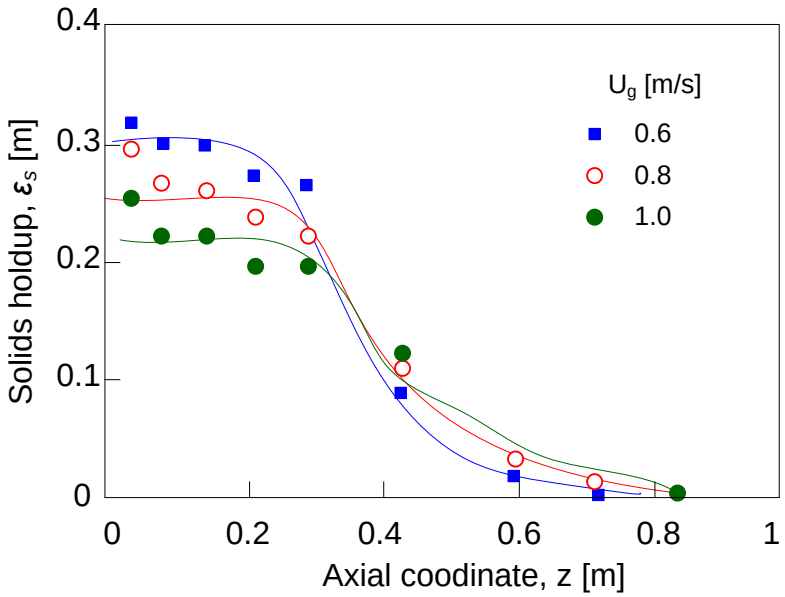

Figure 2.4 Axial solids holdup profiles at various superficial gas velocities in a turbulent fluidized bed (Venderbosch 1998)

2.2.3. Gas and solids mixing of turbulent fluidized beds

A good understanding of gas and solids mixing in turbulent fluidized beds is of key significance to study the reactor performance. The gas axial dispersion coefficient has been extensively studied and adopted, whereas the gas radial dispersion was proven much weaker than the axial dispersion in turbulent fluidized beds (Lee and Kim 1990). Most investigations of gas axial dispersion employed tracer techniques. Li and Wu (1991) calculated the axial dispersion coefficient by fitting the tracer residence time distribution to a one-dimensional pseudo-homogeneous diffusion model, and found that the axial dispersion coefficient decreased with solids holdup reducing but gas velocity increasing. This finding coincided with that of Foka, Chaouki et al. (1996), Krambeck, Avidan et al. (1987) and Wei, Lin et al. (1993) who reported that larger reactor diameter resulted to increased axial dispersion coefficient. Guo (1987) reported that the axial dispersion coefficient increased with static bed height.

The back-mixing coefficient is also vital to gas/solids mixing studies. All experimental results showed higher tracer concentration close to the wall (Cankurt and Yerushalmi 1978, Lee and Kim 1989, Li and Wu 1991, Zhang, Lu et al. 2009). The back-mixing coefficient increases gradually in the bubbling regime, but decreases in the turbulent regime (Cankurt and Yerushalmi 1978, Venderbosch 1998).

Compared to the gas mixing, the solids mixing has received much less investigations in turbulent fluidization. However, the importance of it cannot be ignored as it affects gas-solids contact, heat transfer and gas mixing. It was found that the solids axial dispersion coefficient had a positive function of bed diameter (Wei, Lin et al. 1993). Lee and Kim (1990) reported that the solids axial dispersion coefficient increased with gas velocity.

2.3. Hydrodynamics of circulating fluidized beds

Solids entrainments would significantly increase and quickly empty a particulate bed if no particle were to be fed, when gas velocity is beyond a critical value. The critical gas velocity U_{sc} can denote the transition from turbulent fluidization to fast fluidization (Bi and Grace 1995). As bubbling and turbulent fluidized beds are operated at a low gas velocity range (~0.1-2.0 m/s), the flow regime beyond turbulent fluidization has been named fast fluidization because of the high gas velocity (>5.0 m/s). Continuous operation can be achieved by separating solids and

circulating them back to the bottom of bed. Therefore, the reactors operated in fast fluidization regime are named as circulating fluidized beds (CFBs) or fast fluidized beds (Grace 1990). CFBs have many advantages, such as high production capacity, reduced axial gas back-mixing, continuous operation, independent control of gas and solids residence time, and enhanced heat/mass transfer rate.

The most common CFBs are riser reactors where both gas and solids flow upwards. A novel CFB, so-called downer reactor in which gas and solids flow downwards, has been studied and applied (Zhu and Wei 1996). In this session, both riser and downer reactors are introduced.

2.3.1. Hydrodynamics of CFB riser reactors

As the hydrodynamics of CFBs affect the mass/heat transfer, gas/solids mixing and reactor performance (Grace 1990), the hydrodynamic studies are very necessary. The hydrodynamics of CFBs are commonly characterized by solids holdup, solids flux, particle velocity, their distributions, etc., which significantly vary with operating conditions.

In the early literature of fast fluidization, almost all studies' operation conditions (e.g., solids circulation rate $G_s < 200$ kg/m^{2}s, superficial gas velocity $U_g < 10$ m/s and solids holdup $\varepsilon_s < 0.1$) were largely below those in industries ($G_s \approx 400$~1200 kg/m^{2}s, $U_g \approx 5$~28 m/s). Thus, academic research provided limited guidance for industrial process developments (Grace 2000). The dense suspension upflow (DSU) representing the flow conditions of industrial circulating fluidized beds has received increasing attention in the past 20 years. In order to distinguish the fluidization operations, Zhu and Bi (1995) defined those at high solids flux and/or high solids holdup as high density/flux circulating fluidized beds (HDCFB or HFCFB). The HDCFB has difficulties to be achieved in laboratories as requiring strong air blower capacity and high solids inventory height. Some experimental results have been reported (Wei, Lin et al. 1998, Issangya, Bai et al. 1999, Pärssinen and Zhu 2001, Kim, Kirbas et al. 2004, Wang, Zhu et al. 2014a).

The understanding of HDCFBs is still far from perfect. A few literature has been published to present the spatial distributions of solids holdup, particle velocity and particle flux, while the micro-scale phenomena (e.g., cluster behaviour and local solids backmixing) are uncertain. More experimental work is required to study the underlying phenomena. In addition, there is few modelling work has been done for HDCFBs, and whether the current models fit to HDCFBs is

unknown as well. The hydrodynamics of HDCFBs are mainly introduced in this session due to its prominent role.

Axial profiles of solids holdup and particle velocity

CFB risers normally present S-shape profiles of solids holdup which has a dense bottom region, a dilute upper region and a transition in between. Figure 2.5 shows a schematic diagram of axial profiles of solids holdup in CFB risers. The "C"-shape profile occurs when there is a restricted exit, therefore particles accumulate in the top part. The exponential shape profiles usually appear at low solids circulation rate, i.e. low solids holdup. Particle velocity becomes constant rapidly resulting to a short particle acceleration region close to the distributor.

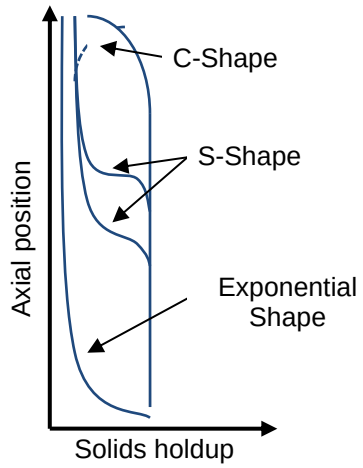

Figure 2.5 Typical axial profiles of solids holdup in a CFB (Zhu 2005)

The solids holdup axial profile is mainly affected by solids circulation rate (G_s), superficial gas velocity (U_g), solids inventory, gas distributor and exit configuration. The experimental study of Wang, Zhu et al. (2014a) were conducted in a 10m-high and 7.6cm i.d. riser using FCC particles under industrial operating conditions. It was found that solids holdup increased to very high values (~0.2-0.35) with solids circulation rate increasing, but decreased with increasing gas velocity, as shown in Figure 2.6. The length of bottom dense region grew with increasing solids circulation rate. Such high solids holdup and uniform axial distribution in the HDCFB are favourable to gas-solids contacting and bed-wall heat transfer.

Axial profiles of particle velocity were also reported by Wang, Zhu et al. (2014b). The results revealed that the particle velocity axial profiles at high G_s (> 700 kg/m^{2}s) presented more

uniform distribution than those at low G_s. The authors suggested that the particle velocity might be unable to be fully accelerated due to strong inter-particle interaction in such dense flow.

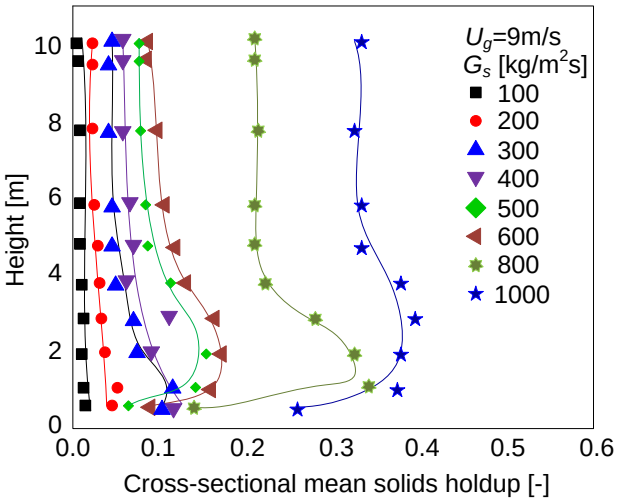

Figure 2.6 Solids holdup axial profiles at various circulation rate in a HDCFB (Wang, Zhu et al. 2014a)

Radial profiles of solids holdup and particle velocity

CFB risers normally show a core-annulus flow structure in the radial direction, i.e., a core region with low solids concentration, high gas/solids velocity surrounded by an annular region with high solids concentration, low upward or even downward solids velocity (Bai, Shibuya et al. 1996). Such non-uniform radial distribution could result in significant gas bypassing through the core region, solids back-mixing in the annulus region, low gas/solids contact efficiency and poor selectivity of reactions (Grace and Bi 1997).

Wang et al. (2014b) reported the radial profiles of solids holdup, particle velocity and particle flux with G_s as high as 1000 kg/m^{2}s (shown in Figure 2.7). The solids holdup radial distributions showed a clear core-annulus structure under all conditions, and the dense annular region expanded towards the centre with G_s, resulting in even higher non-uniformity. The radial distributions of particle velocity became increasingly steeper with G_s. The experimental results revealed that all net solids fluxes were positive, i.e., no solids back-mixing taking place, when G_s is relatively high (>200 kg/m^{2}s). Same results can be found in the work of Issangya, Grace et al. (2000). The reason for this advantage might be high gross solids circulation rate and upward momentum of particles in the wall region.

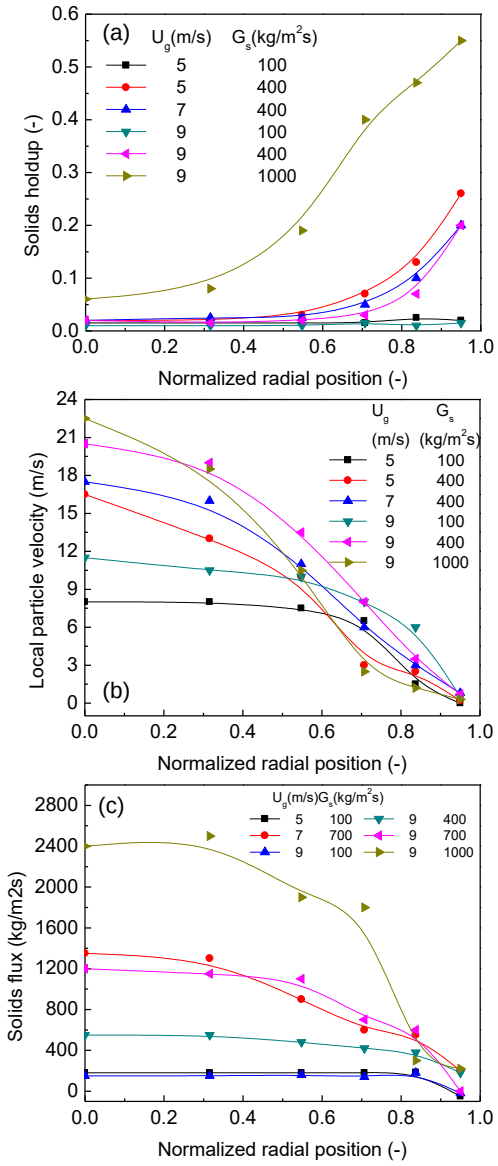

Figure 2.7 Radial profiles of (a) solids holdup, (b) particle velocity and (c) particle flux in a HDCFB (Wang, Zhu et al. 2014)

2.3.2. Hydrodynamics of CFB downer reactors

A co-current gas-solids downflow circulating fluidized bed, or so-called downer reactor, has been developed and studied in recent years (Gross and Ramage 1983, Zhu, Yu et al. 1995, Zhu and Wei 1996, Herbert, Gauthier et al. 1998, Li 2010, Wang, Barghi et al. 2014). System configurations of downer reactors are similar to that of CFB risers, but oppositely the reactions occur in the column where particles flow downwards. Downer reactors have drawn increasingly more research interests due to the advantages over riser reactors, such as uniform axial/radial

solids distribution, no gas/solids back-mixing and similarity to plug flow (Bai, Shibuya et al. 1995, Zhu, Yu et al. 1995).

Axial profiles of flow structure

Wang studied the hydrodynamics of a downer reactor with G_s as high as 300 kg/m^{2}s (Wang, Barghi et al. 2014, Wang, Li et al. 2015a, Wang, Li et al. 2015b). The solids holdup axial distributions are shown in Figure 2.8. It was notable that the downers showed uniform axial distributions but relatively low solids holdups compared with riser reactors, which was consistent with previous literature (Wei, Wang et al. 1994, Zhang, Zhu et al. 1999, Qi, Zhang et al. 2008). The solids holdup was higher near the distributor and then became almost constant, according to the different particle acceleration sections. Moreover, the solids holdup increased with G_s.

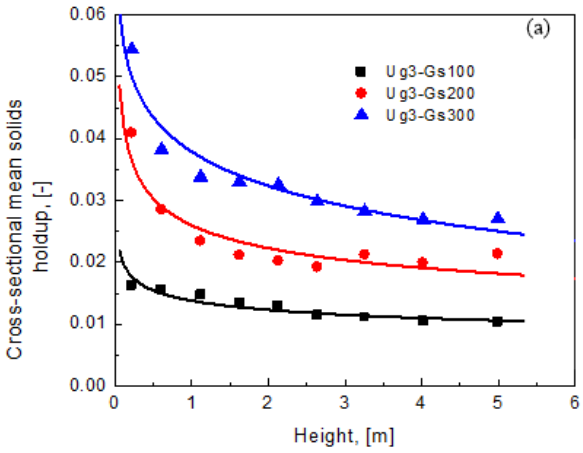

Figure 2.8 Solids holdup axial profile in a downer reactor (Wang, Li et al. 2015a)

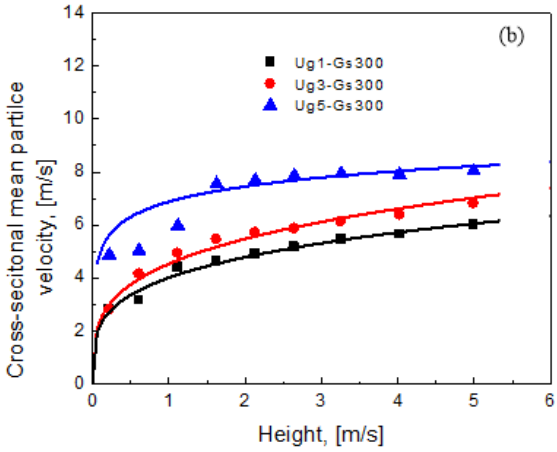

Figure 2.9 Particle velocity axial profiles in a downer reactor (Wang, Li et al. 2015a)

As both gravity and gas/solids flow direction are downward in downers, three particle flow sections are normally presented, including (1) first acceleration section where both the gravity and drag force are downward, (2) second acceleration section where the particle velocity is larger than the gas velocity and the drag force turns upward, (3) constant velocity section where the gravity equals to the drag force. Such flow structure can be reflected by the axial profiles of particle velocity in Figure 2.9.

Radial profiles of flow structure

Compared with riser reactors, downer reactors generally have more uniform radial gas/solids flow structures, due to the same direction of the gravity and gas/solids flow (Zhu, Yu et al. 1995) (shown in Figure 2.10). It is established that high local solids concentration or cluster formation leads to reduction in drag force coefficient (Zhang, Huang et al. 2001). In riser reactors, the drag force is the driving force making particles flow upwards. The aggregation of particles results in reduction of drag coefficient and further decrease of particle velocity, further increase of particle aggregation tendency. Consequently, such mutual effect makes the radial non-uniformity of flow structure in riser reactors. On the contrary, in downer reactors, particle aggregation leads to higher velocity which prompts aggregation breaking up due to higher shear force. Therefore, downer reactors present more uniform radial flow structure, which is of key importance to mass transfer and gas-solids contacting.

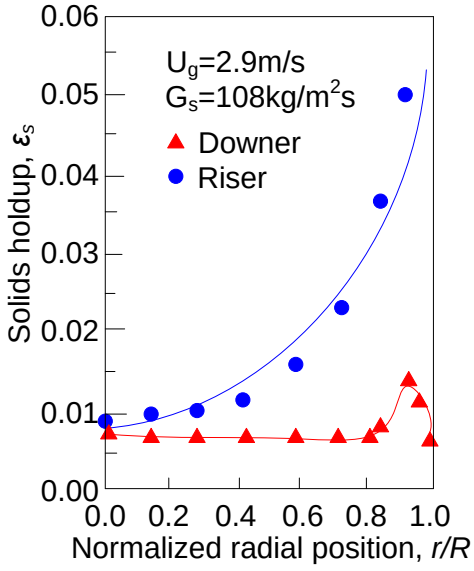

Figure 2.10 Solids holdup radial profiles in a downer and a riser
(Zhang, Zhu et al. 1999)

2.4. Hydrodynamics of circulating turbulent fluidized beds

Most commercial fluidized bed reactors are operated as turbulent fluidized beds (TFBs) or circulating fluidized bed (CFB) risers (Grace 2000). The typical advantages and drawbacks of TFBs and CFBs are summarized in Table 2.1 (Grace and Bi 1997, Bi, Ellis et al. 2000).

Table 2.1 Typical advantages and drawbacks of TFBs and CFBs

	Advantages	Drawbacks
TFB	High solids holdup Uniform lateral flow structure Vigorous gas-solids contacting	Serious gas/solids back-mixing Low throughput
CFB	Reduced gas/solids back-mixing Solids circulating operation High throughput	Low solids holdup Lateral gas/solids segregation

A novel fluidized bed reactor was developed by Zhu and Zhu (2008b) in order to explore improved reactor performance with better gas/solids contacting efficiency and higher conversion per unit volume. The fluidized bed was named as circulating turbulent fluidized bed (CTFB), because a solids circulating operation with turbulent gas-solids flow characteristics was achieved (Zhu 2010). The experimental results demonstrated that the CTFB successfully integrated the advantages of TFBs and CFBs (e.g., high solids holdup, uniform flow structure, high solids circulation rate and reduced solids back-mixing), meanwhile overcoming several disadvantages of them (Zhu and Zhu 2008b). These characteristics are of great favour to high gas-solids contacting efficiency, uniform gas/solids residence time, reactions requiring catalyst regeneration, etc.

2.4.1. Apparatus setup of circulating turbulent fluidized beds

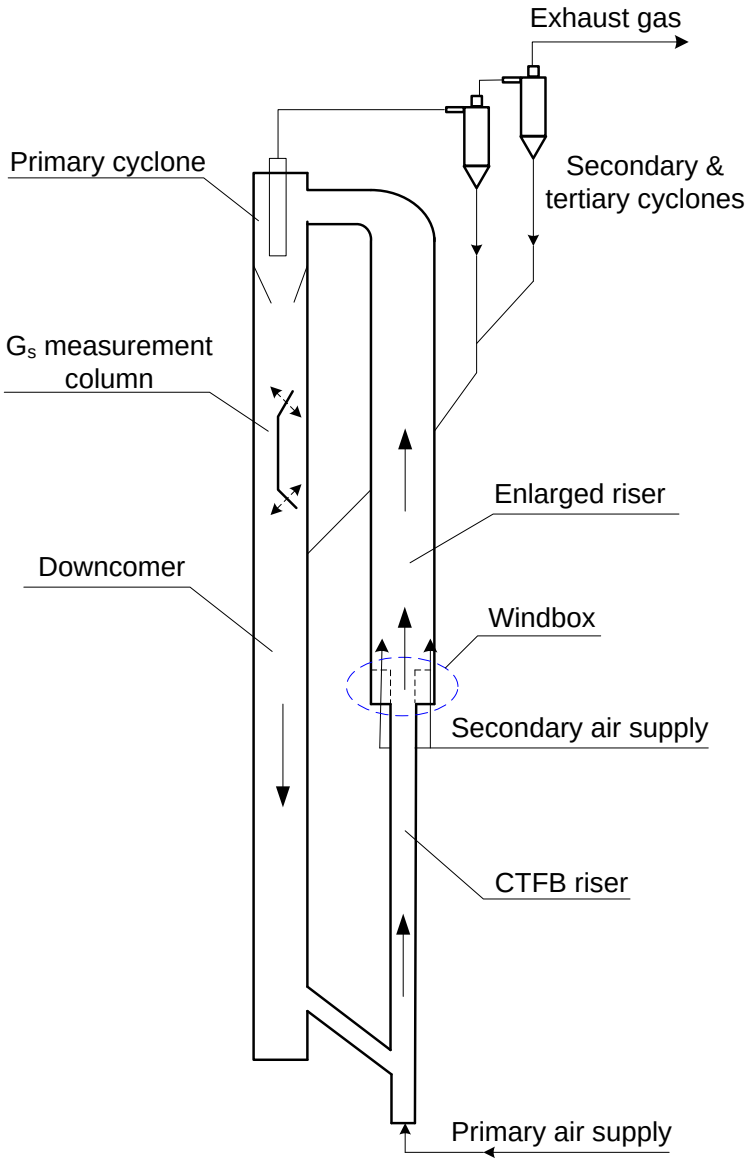

Figure 2.11 Schematic drawing of a circulating turbulent fluidized bed (Zhu and Zhu 2008b)

The apparatus setup is shown in Figure 2.11. The riser consists of a thinner column at the bottom and an enlarged column above. A downcomer serves for returning particles beside the riser. Particles are released from the downcomer to the bottom of 102mm i.d. riser, and are blown upwards by the primary gas (~1.0 m/s-3.0 m/s). The enlarged section (204mm i.d.) with a secondary gas supply injecting through an annular gas distributor is the most unique configuration of a CTFB. After particles enter the enlarged section, the solids concentration of the flow would be significantly diluted due to space expansion and velocity acceleration. The cyclones are used to capture solids and recycle them to the downcomer.

Bi and Zhu (1993) reported a pressure drop analysis in a circulating fluidized bed. Under steady operating conditions, the equation below can be obtained in a CTFB as well:

$$P_{blower}+P_{downcomer} = \Delta P_{bottom\ riser}+ \Delta P_{upper\ riser} + \Delta P_{friction}$$

where P_{blower} is the pressure head of blower,

$P_{\text{downcomer}}$ is the pressure head of downcomer (static pressure head of the inventory),

$\Delta P_{bottom\ riser}$ is the pressure drop along the bottom section of riser,

$\Delta P_{upper\ riser}$ is the pressure drop along the upper enlarged riser,

$\Delta P_{friction}$ is a collective item including pressure drops of wall friction, joint frication, valve friction, cyclones, etc.

P_{blower}, $P_{downcomer}$, and $\Delta P_{\text{friction}}$ are constant for a given system. A much more dilute region is created in the enlarged section by the way mentioned above, leading to lower $\Delta P_{upper\ riser}$. To keep the equation balanced, the pressure drop of the bottom section $\Delta P_{bottom\ riser}$ should be greatly increased, thereby the solids holdup being enhanced as well. Thus, the turbulent dense upflow occurs in the bottom section.

2.4.2. Hydrodynamics of circulating turbulent fluidized beds

The hydrodynamics of circulating turbulent fluidized beds are normally characterized by differential pressure, solids holdup, particle velocity and solids flux and their distributions.

Axial flow structure

Differential pressure profiles were used to characterize the global hydrodynamic behaviour in the CTFB by Zhu and Zhu (2008b), as displayed in Figure 2.12(a). The differential pressure profiles exhibited highly uniform distributions along the CTFB. Consistent with the differential pressure profiles, the standard deviation values also increased with increasing G_s or decreasing U_g, reflecting the increasingly vigorous flow fluctuations caused by particle-particle interactions.

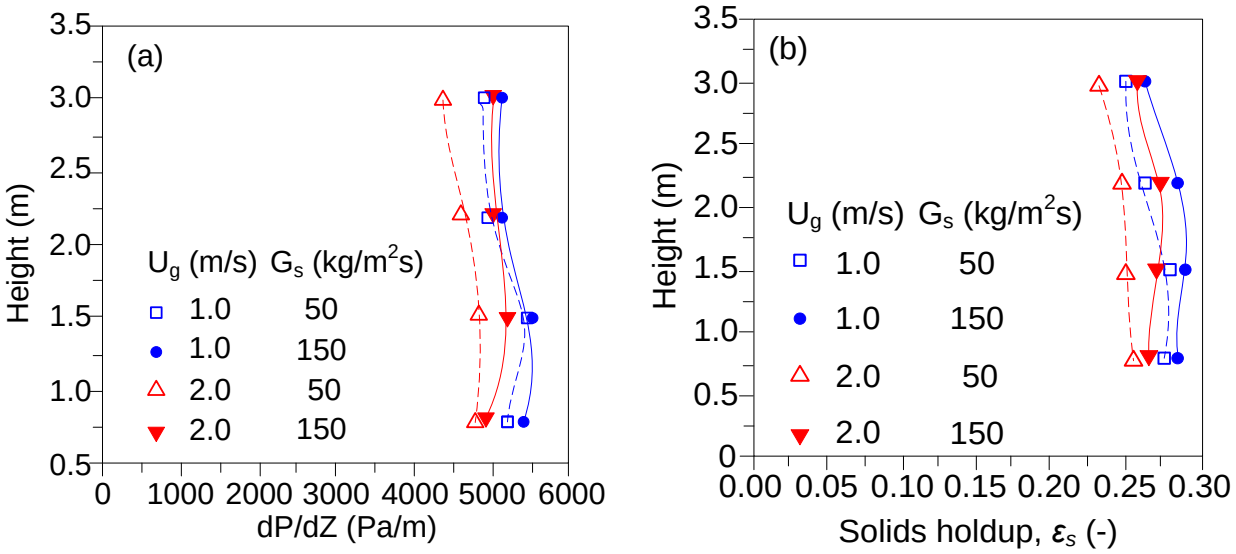

Figure 2.12 axial profiles of (a) pressure drop and (b) solids holdup in a CTFB (Zhu and Zhu 2008b)

The profiles of cross-sectional average solids holdups also demonstrated a uniform and dense gas-solids suspension with solids concentration of 0.25-0.30, as shown in Figure 2.12(b). The high solids concentration and uniform axial flow structure in the CTFB are advantageous over CFBs.

Radial flow structure

The radial profiles of solids holdup in a CTFB (Zhu and Zhu 2008b) are shown in Figure 2.13(a). Radial non-uniformity of solids holdup is presented under all operating conditions in the CTFB, which is similar to the radial structure of CFB risers. Furthermore, it was identified that the solids holdup radial profiles were slightly influenced by operating conditions, since the gas/solids flow likely reached a saturation state. On the other hand, the particles have faster velocity in the core region than those in the annular region, as shown in Figure 2.13(b). The product of solid density ρ_p, local solids holdup ε_s and local particle velocity V_p gives the value of local solids flux. Qi, Zhu et al. (2012) reported that the local solids fluxes distributed uniformly in the core region, but decreased dramatically near the wall. More importantly, solids back-mixing was negligible in most operating conditions, possibly leading to narrow gas/solids residence time distribution, as shown in Figure 2.14.

Zhu, Qi et al. (2013) proposed a moment consistency data processing method (MCDPM) based on the signals of optical fibre probes, in order to obtain hydrodynamic information of the dense phase and the dilute phase separately. It is worth noting that the voids in the CTFB contained large quantity of particles (ε_s=0.1~0.3), potentially leading to high gas-solids contact efficiency.

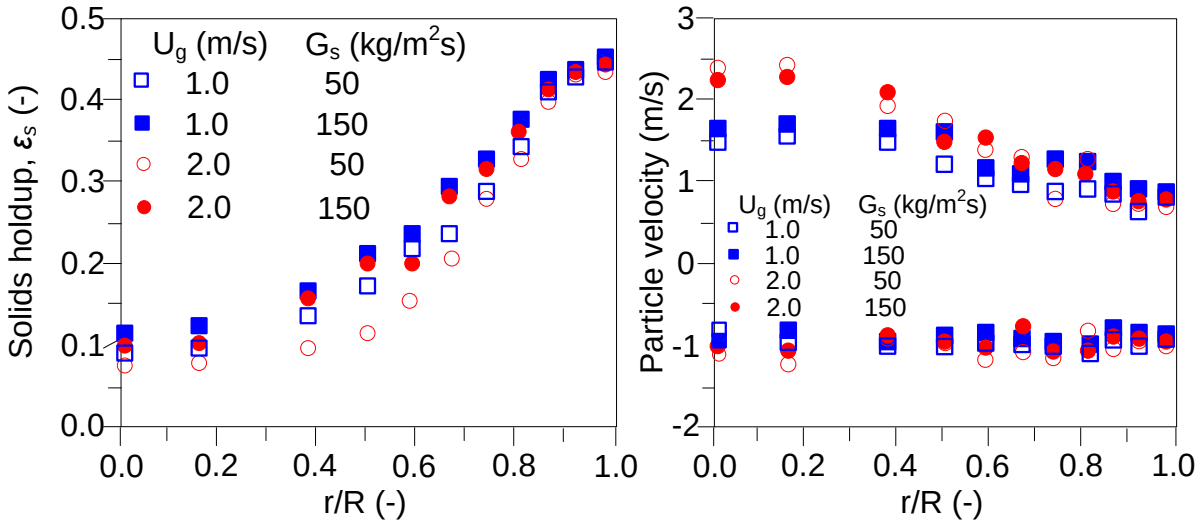

Figure 2.13 Radial profiles of (a) solids holdup and (b) particle velocity in a CTFB (Zhu and Zhu 2008)

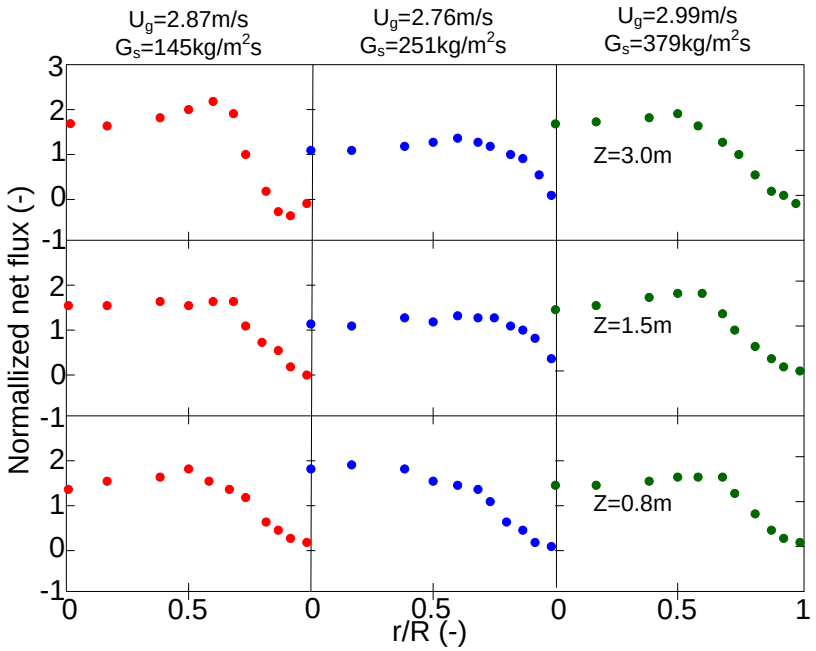

Figure 2.14 Radial profiles of solids flux in a CTFB (Qi, Barghi et al. 2012)

2.4.3. Demarcation of circulating turbulent fluidized beds

After the results of CTFB were published, it has caused interest to compare CTFB with other types of fluidized beds and locate it in the fluidization regime. Comparative investigations were conducted by Zhu and Zhu (2008c) and Qi, Zhu et al. (2009) in terms of macroscopic and microscopic analysis. The macroscopic flow structure usually refers to axial and radial distributions of solids holdup and particle velocity, whereas the microscopic flow structure refers to local behaviour of the dense phase and the dilute phase. Qi, Zhu et al. (2009) concluded that the circulating turbulent fluidization can be an independent flow regime due to several distinctions to the other existed fluidization regimes. The solids flows in CTFB and TFB are dominated by inter-particle interactions due to high solids density, which are totally different from those in CFB risers and downers where the particle motion is mainly controlled gas-solids interactions. Furthermore, the upward net solids flux with reduced solids back-mixing in CTFB is an advantage over TFB. Comparison of transient solids holdup signals showed that CTFB has higher turbulence intensity and frequency than TFB. These findings were confirmed by Qi, Barghi et al. (2012) who calculated the solids holdups of the dense phase and the dilute phase separately.

2.5. Reactor performances of various fluidized beds

A good understanding of fluidized-bed reactor performance is of key importance to process design, modification and scale-up. However, compared with the extensive studies of hydrodynamics, only a few experimental studies of reactor performance have been done so far, which provides insufficient information. Conducting chemical reactions and measuring reaction conversions in fluidized beds can provide the most direct data for the reactor performance studies. This literature review introduces the studies of gas-solids fluidized-bed reactor performance using gas-phase catalytic reactions.

Various reactions have been employed to investigate gas-solids fluidized-bed reactor performance, such as catalytic decomposition of nitrous oxide in a bubbling fluidized bed (Shen and Johnstone 1955), hydrogenation of ethylene in a bubbling fluidized bed with excess of ethylene (Lewis, Gilliland et al. 1959), catalytic oxidation of ammonia in a bubbling fluidized bed (Massimilla and Johnstone 1961), propylene-based acrylonitrile process in

bubbling/turbulent flow regimes (Pell and Jordan 1987), conversion of methane using Pd/Al_2O_3 catalyst in a turbulent fluidized bed (Foka, Chaouki et al. 1994), maleic anhydride process in turbulent fluidized beds (Ihara, Kayou et al. 1996), partial oxidation of methane in a circulating fluidized bed (Pugsley and Malcus 1997, Yin, Wang et al. 2007), oxidation of CO on Pt catalyst in bubbling/turbulent flow regimes (Venderbosch, Prins et al. 1998), cumene hydroperoxide decomposition (Huang, Han et al. 2002), catalytic propane dehydrogenation (Gascon, Tellez et al. 2005). However, difficulties are likely encountered in correlating the reactions with the hydrodynamics due to the complex reaction kinetics and/or catalyst deactivation problems.

Frye, Lake et al. (1958) used catalytic ozone decomposition as a model reaction to study the reactor performance of a bubbling fluidized bed, aiming to develop empirical correlations based on reaction kinetic data for commercial reactors designs. Catalytic ozone decomposition has many advantages in lab-scale research, such as first-order reaction, inexpensive catalysts, conducting in ambient pressure and temperature, non-toxic to catalysts and convenient measurement of concentration. The most commonly-used catalyst is FCC particles impregnated with ferric oxide. Ozone can be continuously produced by a corona ozone generator, and its concentration can be measured on-site by a UV-absorption instrument.

A number of investigations using ozone decomposition have been reported, which are summarized in Table 2.2 and Table 2.3. Most previous reactor performance studies were conducted in bubbling fluidized beds and low density/flux risers, while turbulent fluidized beds, high density/flux risers and downers have received very limited attentions.

Table 2.2 Studies of fluidized-bed reactor performance using ozone decomposition in bubbling & turbulent fluidized beds

	Reactor diameter (cm)	Bed height (cm)	U_g (m/s)	Regime	Type of FCC	Particle size (μm)	Particle density (kg/m^3)	Reaction rate (1/s)
Frye, Lake et al. (1958) Frye and Potter (1976)	22.9	12.0-80.0	0.024-0.017	bubbling	quartz sand+ ferric oxide	117	2650	0.05 – 7.75
Chavarie and Grace (1975)	2-D 245*56*1.0	130	0.13-0.23	bubbling	glass bead+ alumina+ ferric nitrate	215	2400	0.06 – 0.40
Lin, Arastoopour et al. (1986)	7.8	40.0	0.05-0.13	bubbling	alumina	76		~0.002
Van Lare, Piepers et al. (1990)	10.0	40.0	0.046, 0.071, 0.125	bubbling	quartz sand+ iron oxide	67	2590	0.0001-0.01 $m^3/(kg.s)$
Sun and Grace (1990)	10.0	~100	0.06-1.80	bubbling, slugging, turbulent, fast fluidization	FCC+ ferric nitrate	60 with different size distributions	1384 - 1591	1.0 – 9.0

Table 2.3 Studies of fluidized-bed reactor performance using ozone decomposition in CFB riser and down reactors

	Reactor diameter (mm)	Reactor height (m)	U_g (m/s)	Reactor	G_s (kg/m^{2}s)	Type of FCC	Particle size (μm)	Particle density (kg/m^3)	Reaction rate (1/s)
Jiang, Bi et al. (1991)	102	6.32	1.5 - 2.5	riser+ baffle ring	5.1-28.9	FCC+ferric nitrate	89	1500	2.81-5.1
Pagliolico, Tiprigan et al. (1992)	50	4.5	3.8 - 8.8	riser	20.4-102	γ-alumina+ ferric oxide	82	2970	44.71
Ouyang, Li et al. (1995)	254	10.85	2.0 - 7.5	riser	10-206	FCC+ ferric oxide	65	1380	3.9-57.2
Schoenfelder, Kruse et al. (1996)	400	15.6	2.4 - 4.5	riser	9-45	aluminium hydro silicate +10% silica + iron oxide	50	1420	0.001-0.003 m^3/(kg.s)
Bolland and Nicolai (2001)	411	8.5	5.6-7.2	riser	31-53	angular cast steel	117	3320	26-62
Fan, Zhang et al. (2008)	90	8.5	2.2 - 3.7	downer	8.4-28.8	FCC+ferric nitrate	72	1400	0.098
Li, Ray et al. (2013)	76	10	2.0 - 5.0	riser	50-150	FCC+ ferric nitrate	67	1370	4.0
Li, Zhu et al. (2011)	76	5	2.0 - 5.0	downer	50-150	FCC+ ferric nitrate	67	1370	4.0
Wang, Wang et al. (2014)	76	10	5.0 - 9.0	riser	100-800	FCC+ ferric nitrate	78	1780	40-50
Wang, Barghi et al. (2014)	76	5	3.0 - 7.0	downer	100-300	FCC+ ferric nitrate	78	1780	40-50

2.5.1. Reactor performances of bubbling & turbulent fluidized beds

Frye, Lake et al. (1958) presented ozone conversion profiles in a bubbling fluidized bed. In the axial profile, there existed a minimum concentration within the bed as shown in Figure 2.15(a), which was likely caused by the gas back-mixing. Compared with the axial profile, the author reported that the conversion radial profile did not show significant variations. Besides, the reaction conversions were related with the operating conditions. High bed height and low gas velocity resulted in lower concentrations (higher conversions) due to longer gas residence time, as shown in Figure 2.15(b).

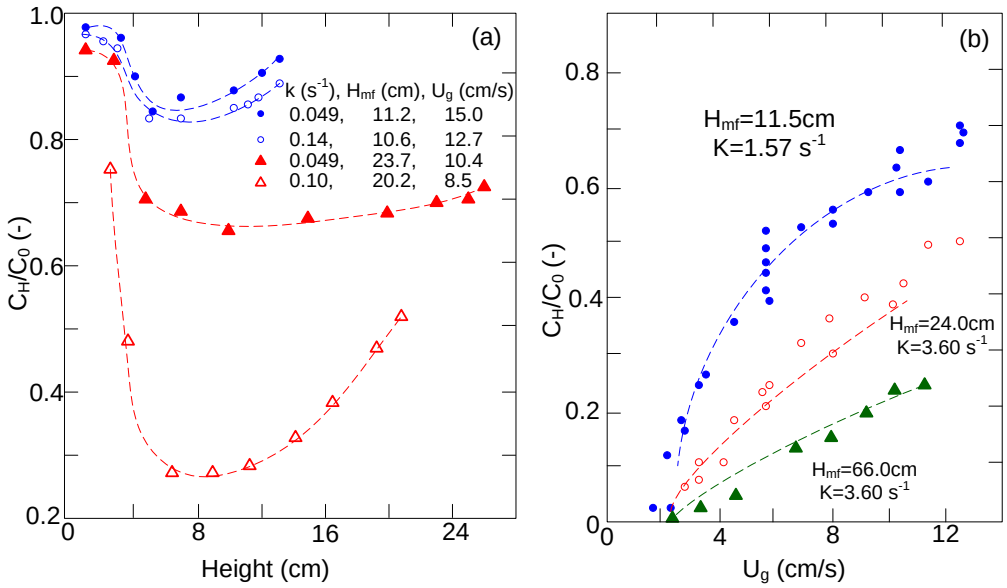

Figure 2.15 (a) outlet ozone concentrations varying with gas velocity at different bed heights, (b) cross-sectional average ozone concentration axial profiles under different operating conditions in a bubbling fluidized bed (Frye and Potter 1976)

Chavarie and Grace (1975) measured the ozone concentrations in the bubble phase and the dense phase separately in a bubbling fluidized bed. The bubble phase's ozone concentrations were measured by UV beams and reference beams. The ozone in the dense phase was withdrawn through a porous disk. The experimental results showed that the bubble phase had higher ozone concentrations than the dense phase, due to the poor gas/solids contacting within the bubbles, see Figure 2.16. The concentrations in both phases sharply dropped near the gas distributor and decreased gradually upwards. It is worth noting that the experiments of Chavarie were conducted in a 2-D bed, while expending the results to 3-D beds would be controversial. In addition, poor

fittings were found between the experimental results and the ideal models of the dense phase perfectly mixed (DPPM) model and the dense phase plug flow (DPPF) model (Figure 2.16).

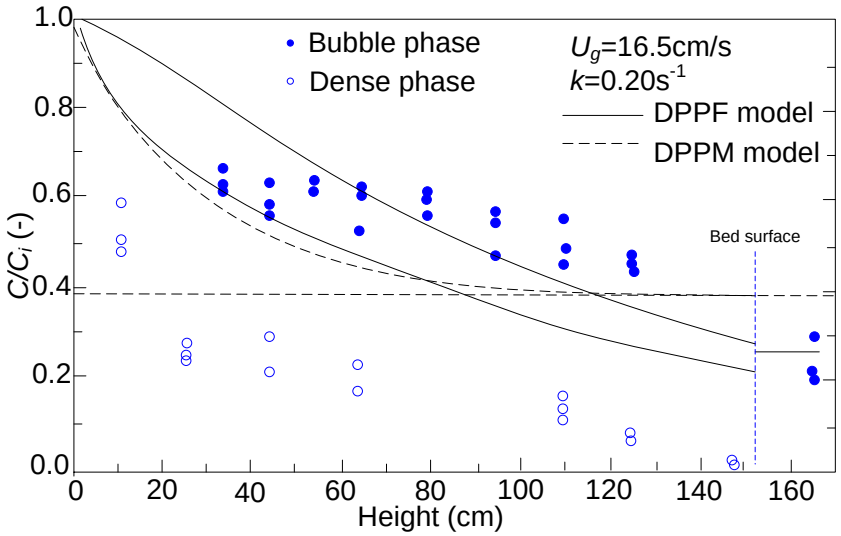

Figure 2.16 Ozone concentration axial profiles of bubble and dilute phases in a bubbling fluidized bed (Chavarie and Grace 1975)

Lin, Arastoopour et al. (1986) examined the baffle effect to bubbling fluidized-bed reactor performance using catalytic decomposition of ozone. The ozone concentrations reduced significantly at baffles, resulting from bubble breakage, reformation to smaller ones and enhanced gas exchange (Figure 2.17). This result likely indicated the poor mass transfer of gas within bubbles.

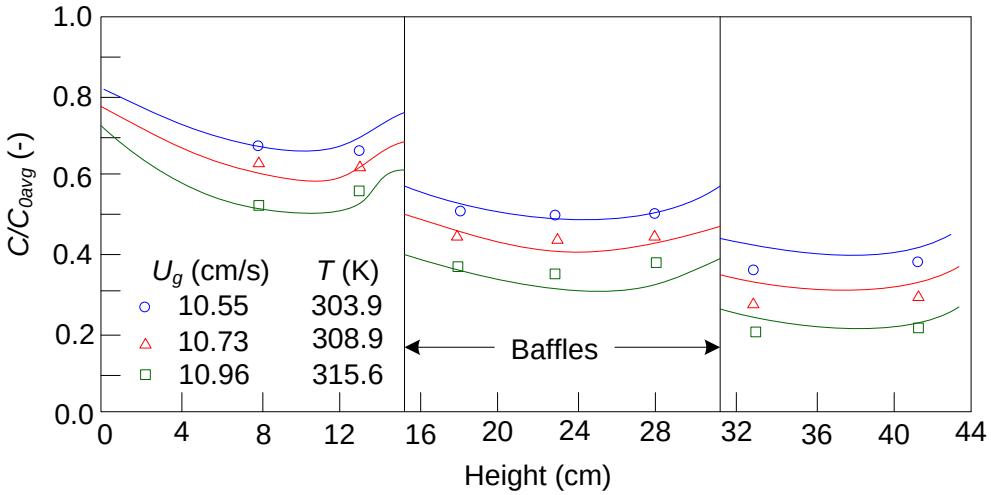

Figure 2.17 Cross-sectional average ozone concentration axial profiles in a bubbling fluidized bed with two baffles (Lin, Arastoopour et al. 1986)

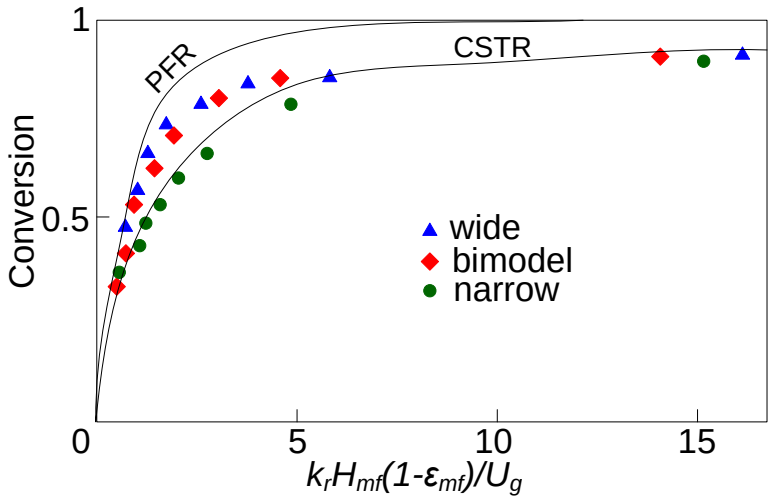

Figure 2.18 Effect of particle size distributions on ozone conversion in fluidized beds at low gas velocities (Sun and Grace 1990)

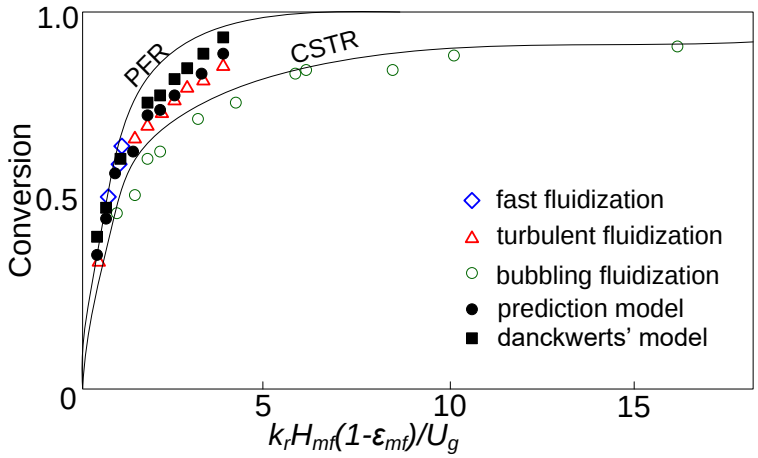

Figure 2.19 Ozone conversion comparison of different fluidized beds (Sun and Grace 1990)

Sun and Grace (1990) evaluated the effects of particle size distribution to the reactor performances of various fluidized beds from bubbling to fast fluidization. The particle size distributions had three types: wide, narrow and bimodal (two peaks on size distribution curve). The conversion results were compared based on a normalized number $k_rH_{mf}(1-\varepsilon_{mf})/U_g$ with the plug flow and perfect mixing ideal reactor models (shown in Figure 2.18). ε_{mf} and H_{mf} are voidage and bed height respectively at the minimum fluidization. k_r and U_g are reaction rate constant and superficial gas velocity respectively. It was demonstrated that the wide particle size distribution led to higher conversions, followed with the bimodal and narrow distribution particles. The particles with narrow size distribution resulted in even poorer reactor performance than CSTR. This finding re-confirmed the relationship between the hydrodynamics and the reaction in fluidized beds. To be specific, the wide size distribution led to smaller bubble/void

size and higher solids holdup inside, which were favourable to mass transfer of reactant gas (Sun and Grace 1992). This phenomenon was more prominent in turbulent and fast fluidization than bubbling fluidization. Additionally, the reactor performances of different fluidized beds were compared by Sun and Grace (1990) as well. Figure 2.19 showed that the turbulent and fast fluidized beds generally had higher conversions than the bubbling fluidized beds under the same normalized operating conditions.

2.5.2. Reactor performances of CFB riser and downer reactors

Reactor performance of CFB risers

The literature of the reactor performance of CFB risers and downers were published in recent years. Li, Ray et al. (2013) reported the axial and radial distributions of ozone concentration in a CFB riser reactor. The results demonstrated that the ozone concentration decreased rapidly in the bottom region, and the decreasing rate gradually slowed down with increasing elevation. This trend corresponded to the axial profiles of solids holdup, showing strong correlation between the conversions and the solids holdups, as shown in Figure 2.20. However, the experiments were performed at low solids circulation rates (smaller than 100 kg/m^{2}s), like other earlier literature.

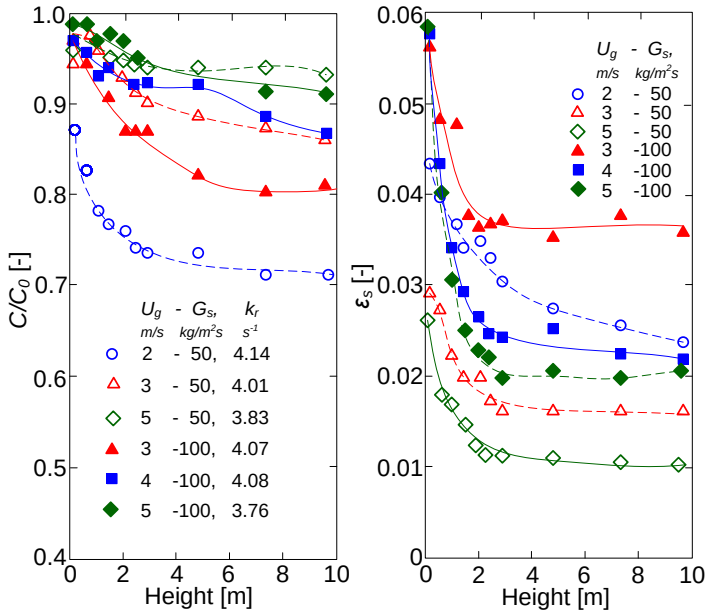

Figure 2.20 ozone concentration (a) and solids holdup (b) axial profiles in a CFB riser reactor (Li, Ray et al. 2013)

Wang, Wang et al. (2014) investigated the reactor performance of a CFB riser with solids circulation rate G_s as high as 1000 kg/m^{2}s. The correlation between the axial profiles of ozone concentration and solids holdup was consistent with the work of Li, Ray et al. (2013). As shown in Figure 2.21(a), the radial non-uniformity of ozone concentration were presented for various G_s, because the higher solids holdup near the wall likely resulted in higher reaction rate Jiang, Bi et al. (1991). But the radial non-uniformity could be mitigated under higher G_s, reported by Schoenfelder, Kruse et al. (1996). It was also noticed that the ozone concentration decreased with solids circulation rate and the associated increase of solids holdup. In Figure 2.21(b), the ozone concentration in the central region dramatically decreases with elevation, whereas that in the wall region remains almost constant, due to the severe lateral gas/solids segregation.

Additionally, the effect of baffles on the reactor performance in a riser reactor was investigated by Jiang, Bi et al. (1991). It was identified that baffles can improve conversions by means of disturbing the core-annular flow structure.

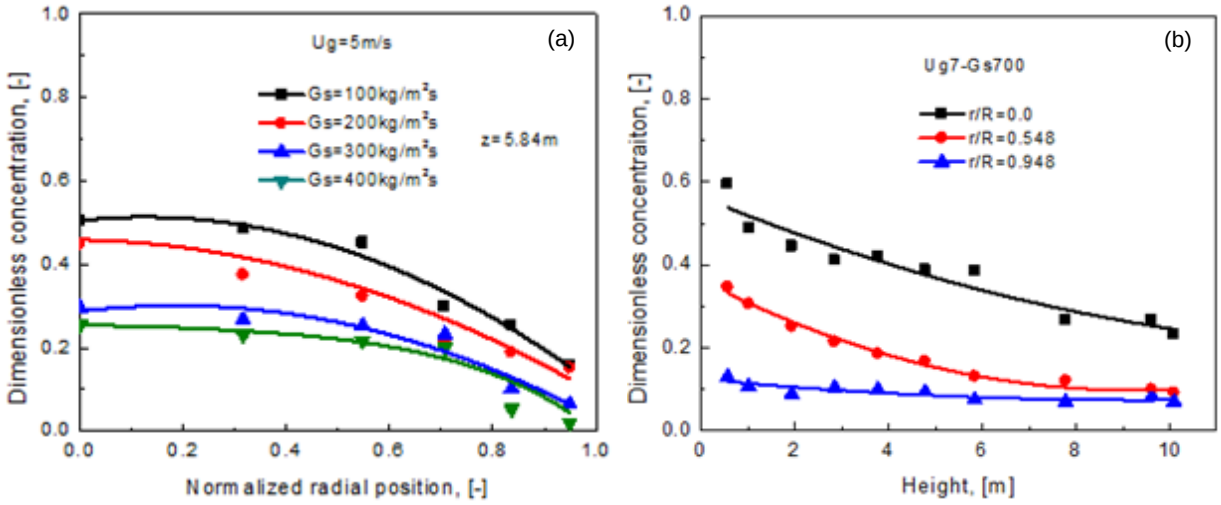

Figure 2.21 ozone concentration radial profiles under various G_s (a) and ozone concentration axial profiles (b) at different radius in a CFB riser (Wang, Wang et al. 2014)

Reactor performance of CFB downers

As a newly invented fluidized-bed reactor, there have been many interests in studying downer reactor performance. The axial ozone concentration profiles were presented by Fan, Zhang et al. (2008) in Figure 2.22. There are three flow development regions in the axial direction as mentioned before. The ozone concentration reduced drastically in the acceleration region near the distributor due to the higher solids holdup, while it decreased slightly in the fully developed

region. Besides, the ozone conversion increased with solids circulation rate and solids holdup, which was similar to the trend in riser reactors.

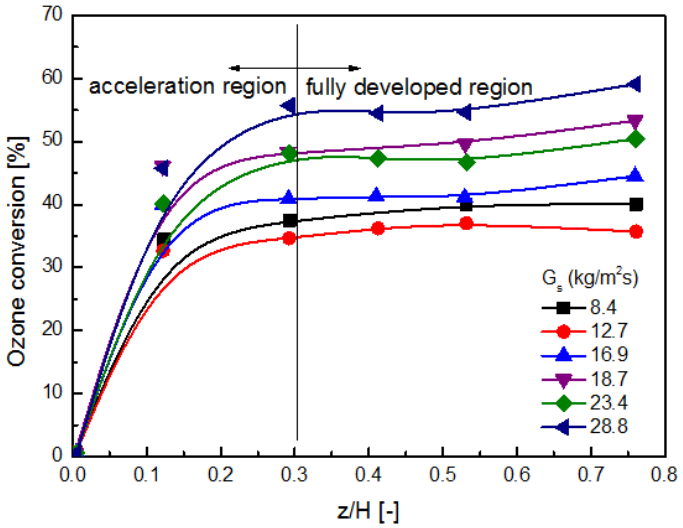

Figure 2.22 Ozone concentration axial profiles under various solids circulation rate in a CFB downer reactor (Fan, Zhang et al. 2008)

Wang, Barghi et al. (2014) conducted ozone decomposition experiments in a downer reactor with G_s up to 300 kg/m^{2}s. The radial profiles of ozone concentration and axial profiles at different radius were presented in Figure 2.23. The ozone concentration distribution was relatively uniform radially, consistent with the radial solids holdup distribution. Besides, the axial profiles at three different radial locations exhibited similar reaction rates. These phenomena were considered to be determined by the uniform gas/solids flow in the downer reactor.

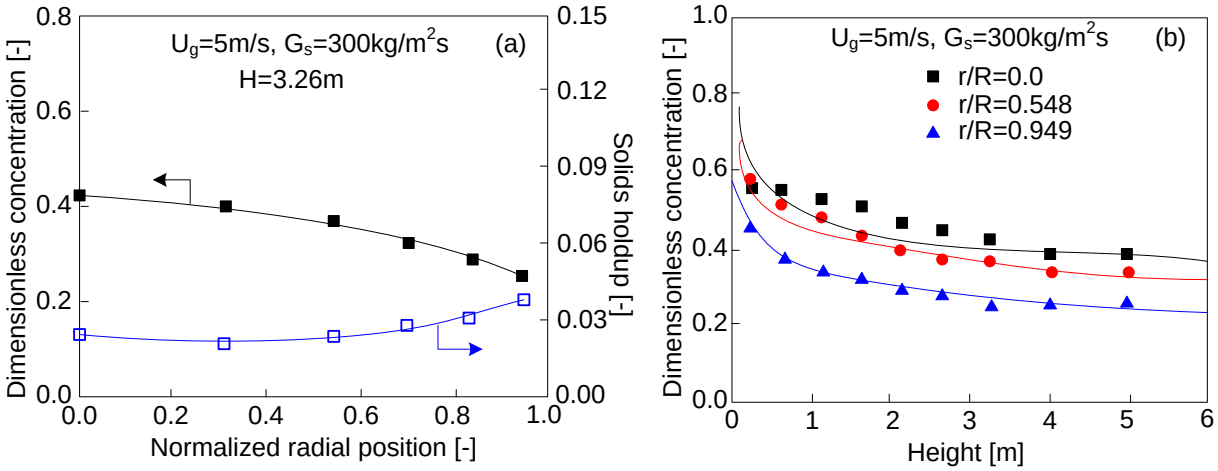

Figure 2.23 ozone concentration & solids holdup radial profiles (a), ozone concentration axial profiles (b) at different radius in a downer reactor (Wang, Barghi et al. 2014)

Gas-solids contact efficiency

Ozone decomposes very slowly at ambient temperature and pressure if without catalysts or ultraviolet. The reactant-gas residence time in fluidized-bed reactors is in the magnitude of several seconds. Therefore, catalytic ozone decomposition can be assumed that the reaction only occurs if the reactant-gas contacts with the catalyst-solids. In gas-solids fluidized beds, the interstitial space is largely expanded by the fluidizing gas, leading to reduced possibility of gas contacting with solids. In other words, the gas-solids mixing and contacting deviate from those of a plug flow reactor. Therefore, gas-solids contact efficiency can characterize fluidized-bed reactor performances. However, only a few publications discussed the contact efficiency in fluidized beds (Sun and Grace 1990, Jiang, Bi et al. 1991, Ouyang, Li et al. 1995, Li, Zhu et al. 2011, Li, Ray et al. 2013, Wang, Zhu et al. 2015).

Sun and Grace (1990) proposed a definition of contact efficiency. It was defined as the ratio of the catalyst volume ($V_{c,p}$) of the plug flow reactor to the catalyst volume ($V_{c,f}$) of the actual fluidized bed for achieving the same conversion with the same flow rate. $V_{c,p}$ can be calculated by the ideal plug flow reactor model, and $V_{c,f}$ comes from experimental results.

Jiang, Bi et al. (1991) defined contact efficiency as the fraction of the external surface area of catalysts available for the gas-phase reactant. Based on the pseudo-homogeneous plug-flow model, the contact efficiency, α, was defined as:

$$1-X=\exp\left[-\alpha k_r \bar{\varepsilon}_s H/U_g\right] \text{ or } 1-X=\exp\left[-\alpha k_r^{'}\right]$$

where $k_r^{'}=k_r\bar{\varepsilon}_s H/U_g$ is Damköhler number, k_r (s^{-1}) is reaction rate coefficient, ε_s (-) is average solids holdup, H (m) is bed height, U_g (m/s) is superficial gas velocity, and X (-) was conversion.

Sun and Grace (1990) concluded that the contact efficiency of turbulent and fast fluidized beds were better than bubbling/slugging fluidized beds, as shown in Figure 2.19. It was explained by the low efficient gas-solids contact within bubbles and the high mass transfer resistance across bubble boundary.

Wang, Zhu et al. (2015) compared the contact efficiency of a riser and a downer with the same bed diameter, as shown in Figure 2.24. The downer showed higher contact efficiency than the riser, as the downer's uniform gas/solids flow structure was more similar to a plug flow reactor. The results also indicated that the contact efficiency of both riser and downer decreased with increasing solids holdup.

Based on the literature review, almost all previous reactor performance studies were conducted only in each individual fluidization regime with different reactor dimensions and catalyst particles. As a consequence, the advantages and drawbacks of the various fluidized beds are difficult to be identified. Sun and Grace (1990) carried out comparative investigations in a BFB, a TFB and a CFB riser, but only outlet conversions were provided under low operation conditions (e.g., U_g<1.8 m/s). Wang, Zhu et al. (2015) just compared the reactor performances of a CFB riser and a CFB downer. Therefore, it is highly necessary for a comprehensive study covering the full spectrum of the commonly used fluidized beds under industrial operating conditions.

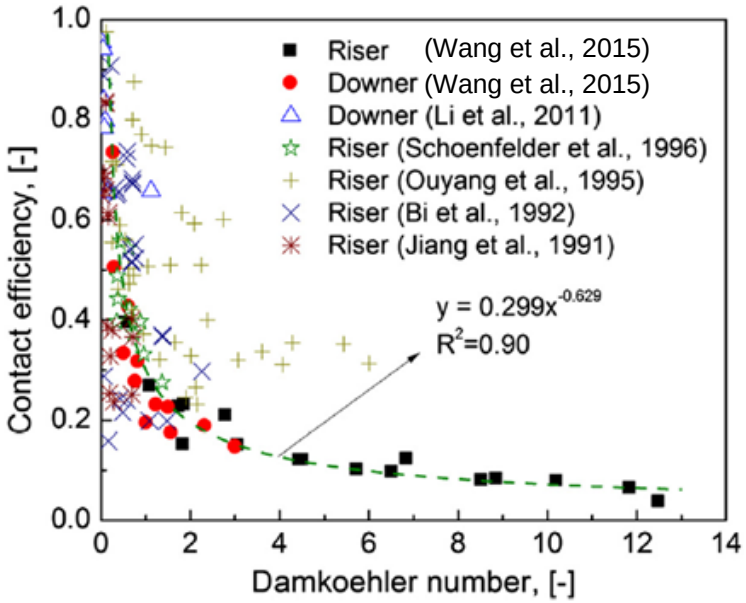

Figure 2.24 Comparison of contact efficiencies of riser and downer reactors (Wang, Zhu et al. 2015)

Nomenclature

C	ozone (reactant) concentration [ppm]
C_0	initial ozone (reactant) concentration [ppm]
d_p	particle diameter [m]
G_s	solids circulation rate [kg/(m^2·s)]
H	height of the bed [m]
H_{mf}	height of the bed at minimum fluidization [m]
h	axial coordinate [m]
k_r	reaction rate constant [s^{-1}]
k_r'	Damköhler number, $k_r\bar{\varepsilon}_s H/U_g$ [-]
R	column radius [m]
r/R	dimensionless position [-]
U_g	superficial gas velocity [m/s]
V_p	particle velocity [m/s]
$V_{c,f}$	catalyst volume in fluidized bed [m^3]
$V_{c,p}$	catalyst volume in fixed bed [m^3]
X	conversion [-]
z	axial coordinate [m]

Greek letters

α	gas-solid contact efficiency [-]
ε	voidage [-]
ε_s	solids holdup, 1- ε [-]
ε_{mf}	voidage at minimum fluidization, 1-$\varepsilon_{s,mf}$ [-]
$\bar{\varepsilon}_s$	cross-sectional average solids holdup [-]

Subscripts

g	gas
p	particle
r	reaction
s	solid

References

Abed, R. (1984). The characterization of turbulent fluid bed hydrodynamics. *Fluidization IV*. D. K. R. Toei. New York, Engineering Foundation**:** 137-144.

Avidan, A. and J. Yerushalmi (1982). Bed expansion in high velocity fluidization. *Powder Technology* **32**(2): 223-232.

Avidan, A. and J. Yerushalmi (1985). Solids mixing in an expanded top fluid bed. *AIChE Journal* **31**(5): 835-841.

Bai, D., E. Shibuya, Y. Masuda, N. Nakagawa and K. Kato (1996). Flow structure in a fast fluidized bed. *Chemical Engineering Science* **51**(6): 957-966.

Bai, D., E. Shibuya, Y. Masuda, K. Nishio, N. Nakagawa and K. Kato (1995). Distinction between upward and downward flows in circulating fluidized beds. *Powder Technology* **84**(1): 75-81.

Bellgardt, D., M. Schoessler and J. Werther (1987). Lateral non-uniformities of solids and gas concentrations in fluidized bed reactors. *Powder Technology* **53**(3): 205-216.

Bi, H. (1994). *Flow regime transitions in gas-solid fluidization and transport*. Ph.D., University of British Columbia.

Bi, H., N. Ellis, I. Abba and J. Grace (2000). A state-of-the-art review of gas–solid turbulent fluidization. *Chemical Engineering Science* **55**(21): 4789-4825.

Bi, H. and L. S. Fan (1992). Existence of turbulent regime in gas‐solid fluidization. *AIChE Journal* **38**(2): 297-301.

Bi, H. and J. Grace (1995). Flow regime diagrams for gas-solid fluidization and upward transport. *International Journal of Multiphase Flow* **21**(6): 1229-1236.

Bi, H., J. Grace and K. Lim (1995). Transition from bubbling to turbulent fluidization. *Industrial & Engineering Chemistry research* **34**(11): 4003-4008.

Bi, H. and J. Zhu (1993). Static instability analysis of circulating fluidized beds and concept of high‐density risers. *AIChE Journal* **39**(8): 1272-1280.

Bolland, O. and R. Nicolai (2001). Describing mass transfer in circulating fluidized beds by ozone decomposition. *Chemical Engineering Communications* **187**(1): 1-21.

Brereton, C. and J. Grace (1992). The transition to turbulent fluidization: chemical reaction engineering. *Chemical Engineering Research & Design* **70**(A3): 246-251.

Cai, P. (1989). *The transition of flow regime in dense phase gas-solid fluidized bed*. Ph.D., Tsinghua University.

Cankurt, N. and J. Yerushalmi (1978). *Gas backmixing in high velocity fluidized beds*. Fluidization: Proceedings of the Second Engineering Foundation Conference, Trinity College, Cambridge, England 2-6 April 1978, CUP Archive.

Chavarie, C. and J. R. Grace (1975). Performance analysis of a fluidized bed reactor. II. Observed reactor behavior compared with simple two-phase models. *Industrial & Engineering Chemistry Fundamentals* **14**(2): 79-86.

Chehbouni, A., J. Chaouki, C. Guy and D. Klvana (1994). Characterization of the flow transition between bubbling and turbulent fluidization. *Industrial & Engineering Chemistry Research* **33**(8): 1889-1896.

Clark, N. N., W. Liu and R. Turton (1996). Data interpretation techniques for inferring bubble size distribution from probe signals in fluidized systems. *Powder Technology* **88**(2): 179-188.

Clark, N. N. and R. Turton (1988). Chord length distributions related to bubble size distributions in multiphase flows. *International Journal of Multiphase Flow* **14**(4): 413-424.

Davidson, J., D. Harrison (1963). *Fluidized Particles*. Cambridge, England.

Du, B., L. S. Fan, F. Wei and W. Warsito (2002). Gas and solids mixing in a turbulent fluidized bed. *AIChE Journal* **48**(9): 1896-1909.

Ege, P. E. (1995). *Investigation of the flow structure in turbulent fluidized beds*.

Fan, C., Y. Zhang, X. Bi, W. Song, W. Lin and L. a. Luo (2008). Evaluation of downer reactor performance by catalytic ozone decomposition. *Chemical Engineering Journal* **140**(1): 539-554.

Fan, L., Y.-M. Chen and F. Lai (1990). Recent developments in solids mixing. *Powder Technology* **61**(3): 255-287.

Farag, H., A. Grislingås, P. Ege and H. De Lasa (1997). Flow patterns in a pilot plant ‐ scale turbulent fluidized bed reactor: Concurrent application of tracers and fiber optic sensors. *The Canadian Journal of Chemical Engineering* **75**(5): 851-860.

Foka, M., J. Chaouki, C. Guy and D. Klvana (1994). Natural gas combustion in a catalytic turbulent fluidized bed. *Chemical Engineering Science* **49**(24): 4269-4276.

Foka, M., J. Chaouki, C. Guy and D. Klvana (1996). Gas phase hydrodynamics of a gas-solid turbulent fluidized bed reactor. *Chemical Engineering Science* **51**(5): 713-723.

Frye, C., W. Lake and H. Eckstrom (1958). Gas ‐ solid contacting with ozone decomposition reaction. *AIChE Journal* **4**(4): 403-408.

Frye, C. and O. E. Potter (1976). Experimental investigation of models for fluidized bed catalytic reactors. *AIChE Journal* **22**(1): 38-47.

Gascon, J., C. Tellez, J. Herguido and M. Menendez (2005). A two-zone fluidized bed reactor for catalytic propane dehydrogenation. *Chemical Engineering Journal* **106**(2): 91-96.

Gautam, M., J. Jurewicz and S. Kale (1994). An experimental investigation of throughflow velocities in two-dimensional fluidized bed bubbles: laser Doppler anemometer measurements. *Journal of Fluids Engineering* **116**(3): 605-612.

Geldart, D. and H. Xie (1992). *Use of Pressure Probes in Fluidized Beds of Group A Powders*. Proceedings of the 7th Engineering Foundation Conference on Fluidization, Brisbane, Australia.

Gelperin, N. and V. Einstein (1971). Fluidization. *edited by JF Davidson and D. Harrison*: 541-568.

Grace, J. (1990). High-velocity fluidized bed reactors. *Chemical Engineering Science* **45**(8): 1953-1966.

Grace, J. R. (2000). Reflections on turbulent fluidization and dense suspension upflow. *Powder Technology* **113**(3): 242-248.

Grace, J. R. and H. Bi (1997). Introduction to circulating fluidized beds. *Circulating Fluidized Beds*, Springer**:** 1-20.

Gross, B. and M. P. Ramage (1983). FCC reactor with a downflow reactor riser, Google Patents.

Guo, F. (1987). Gas flow and mixing behavior in fine‐powder fluidized bed. *AIChE Journal* **33**(11): 1895-1898.

Hailu, L., F. Plaka, R. Clift and J. Davidson (1993). Measurement of gas flow through a two-dimensional bubble in a fluidised bed: particle processing. *Chemical Engineering Research & Design* **71**(4): 382-389.

Hatano, H., I. A. H. Khattab, K. NAKAMURA and M. ISHIDA (1986). Spatiotemporal measurement of bubble properties in free-bubbling fluidized beds. *Journal of Chemical Engineering of Japan* **19**(5): 425-430.

Herbert, P., T. Gauthier, C. Briens and M. Bergougnou (1998). Flow study of a 0.05 m diameter downflow circulating fluidized bed. *Powder technology* **96**(3): 255-261.

Hilligardt, K. and J. Werther (1986). *Gas flow in and around bubbles in gas fluidized beds—local measurements and modelling considerations*. Proceedings of World Congress III of Chemical Engineering.

Horio, M., H. Ishii and M. Nishimuro (1992). On the nature of turbulent and fast fluidized beds. *Powder Technology* **70**(3): 229-236.

Huang, D., M. Han, J. Wang and Y. Jin (2002). Catalytic decomposition process of cumene hydroperoxide using sulfonic resins as catalyst. *Chemical Engineering Journal* **88**(1): 215-223.

Ihara, T., A. Kayou and Y. Natori (1996). *Scaleup Study of the Turbulent Fluidized Bed Reactor*. AIChE Symposium Series, American institute of chemical engineers.

Issangya, A., D. Bai, H. Bi, K. Lim, J. Zhu and J. Grace (1999). Suspension densities in a high-density circulating fluidized bed riser. *Chemical Engineering Science* **54**(22): 5451-5460.

Issangya, A. S., J. R. Grace, D. Bai and J. Zhu (2000). Further measurements of flow dynamics in a high-density circulating fluidized bed riser. *Powder Technology* **111**(1): 104-113.

Jiang, P., H. Bi, R. H. Jean and L. S. Fan (1991). Baffle effects on performance of catalytic circulating fluidized bed reactor. *AIChE Journal* **37**(9): 1392-1400.

Kehoe, P. K. and J. Davidson (1971). *Continuously slugging fluidised beds*. British Chemical Engineering.

Kim, S. W., G. Kirbas, H. Bi, C. J. Lim and J. R. Grace (2004). Flow behavior and regime transition in a high-density circulating fluidized bed riser. *Chemical Engineering Science* **59**(18): 3955-3963.

Krambeck, F., A. Avidan, C. Lee and M. Lo (1987). Predicting fluid‐bed reactor efficiency using adsorbing gas tracers. *AIChE Journal* **33**(10): 1727-1734.

Kunii, D. and O. Levenspiel (1991). Solid Movement: Mixing, Segregation, and Staging. *Fluidization Engineering*: 211-235.

Lee, G. S. and S. D. KIM (1988). Pressure fluctuations in turbulent fluidized beds. *Journal of Chemical Engineering of Japan* **21**(5): 515-521.

Lee, G. S. and S. D. Kim (1989). Gas mixing in slugging and turbulent fluidized beds. *Chemical Engineering Communications* **86**(1): 91-111.

Lee, G. S. and S. D. Kim (1990). Axial mixing of solids in turbulent fluidized beds. *The Chemical Engineering Journal* **44**(1): 1-9.

Leung, L. and I. Sandford (1969). On the percolation of fluid through bubbles in fluidised beds. *Chemical Engineering Science* **24**(8): 1391-1395.

Lewis, W., E. Gilliland and W. Glass (1959). Solid‐catalyzed reaction in a fluidized bed. *AIChE Journal* **5**(4): 419-426.

Li, D. (2010). *Investigation of circulating fluidized bed riser and downer reactor performance for catalytic ozone decomposition*.

Li, D., A. K. Ray, M. B. Ray and J. Zhu (2013). Catalytic reaction in a circulating fluidized bed riser: Ozone decomposition. *Powder Technology* **242**: 65-73.

Li, D., J. Zhu, M. B. Ray and A. K. Ray (2011). Catalytic reaction in a circulating fluidized bed downer: ozone decomposition. *Chemical Engineering Science* **66**(20): 4615-4623.

Li, Y. and M. Kwauk (1980). The dynamics of fast fluidization. *Fluidization*, Springer**:** 537-544.

Li, Y. and P. Wu (1991). A study on axial gas mixing in a fast fluidized bed. *Circulating Fluidized Bed Technology III*: 581-586.

Lim, K. and P. K. Agarwal (1992). Bubble velocity in fluidized beds: the effect of non-vertical bubble rise on its measurement using submersible probes and its relationship with bubble size. *Powder Technology* **69**(3): 239-248.

Lim, K., J. Zhu and J. Grace (1995). Hydrodynamics of gas-solid fluidization. *International Journal of Multiphase Flow* **21**: 141-193.

Lim, K. S., V. S. Gururajan and P. K. Agarwal (1993). Mixing of homogeneous solids in bubbling fluidized beds: theoretical modelling and experimental investigation using digital image analysis. *Chemical Engineering Science* **48**(12): 2251-2265.

Lin, S.-C., H. Arastoopour and H. Kono (1986). Experimental and theoretical study of a multistage fluidized-bed reactor. *Powder Technology* **48**(2): 125-140.

M'chirgui, A., L. Tadrist and S. Radev (1999). Analysis of the hydrodynamics instabilities in a gas fluidzied bed. *Circulating Fluidized Bed Technology VI*. J. Werther. Frankfurt: Dechema**:** 137-142.

Massimilla, L. and H. Johnstone (1961). Reaction kinetics in fluidized beds. *Chemical Engineering Science* **16**(1): 105-112.

Nakajima, M., M. Harada, M. Asai, R. Yamazaki and G. Jimbo (1991). Bubble fraction and voidage in an emulsion phase in the transition to a turbulent fluidized bed. *Circulating Fluidized Bed III*: 79-84.

Ouyang, S., X. G. Li and O. Potter (1995). Circulating fluidized bed as a catalytic reactor: experimental study. *AIChE Journal* **41**(6): 1534-1542.

Pagliolico, S., M. Tiprigan, G. Rovero and A. Gianetto (1992). Pseudo-homogeneous approach to CFB reactor design. *Chemical Engineering Science* **47**(9): 2269-2274.

Pärssinen, J. and J. X. Zhu (2001). Axial and radial solids distribution in a long and high - flux CFB riser. *AIChE Journal* **47**(10): 2197-2205.

Peeler, P., K. Lim and R. Close (1999). Effect of temperature on the turbulent fluidization regime transition. *Circulating Fluidized Bed Technology VI, Dechema, Frankfurt*: 125-130.

Pell, M. and S. Jordan (1987). Effects of fines and velocity on fluid bed reactor performance, American Institute of Chemical Engineers, New York, NY.

Pugsley, T. and S. Malcus (1997). Partial oxidation of methane in a circulating fluidized-bed catalytic reactor. *Industrial & Engineering Chemistry Research* **36**(11): 4567-4571.

Qi, M., S. Barghi and J. Zhu (2012). Detailed hydrodynamics of high flux gas–solid flow in a circulating turbulent fluidized bed. *Chemical Engineering Journal* **209**: 633-644.

Qi, M., J. Zhu and S. Barghi (2012). Particle velocity and flux distribution in a high solids concentration circulating turbulent fluidized bed. *Chemical Engineering Science* **84**: 437-448.

Qi, X., H. Zhu and J. Zhu (2009). Demarcation of a new circulating turbulent fluidization regime. *AIChE Journal* **55**(3): 594-611.

Qi, X.-B., H. Zhang and J. Zhu (2008). Solids concentration in the fully developed region of circulating fluidized bed downers. *Powder Technology* **183**(3): 417-425.

Rowe, P. and H. MacGillivray (1980). The Structure of a 15 cm Diameter Gas Fluidised Bed Operated at up to 1 m/s and Seen by X-rays. *Fluidization*, Springer**:** 545-553.

Schnitzlein, M. G. and H. Weinstein (1988). Flow characterization in high-velocity fluidized beds using pressure fluctuations. *Chemical Engineering Science* **43**(10): 2605-2614.

Schoenfelder, H., M. Kruse and J. Werther (1996). Two‐dimensional model for circulating fluidized‐bed reactors. *AIChE Journal* **42**(7): 1875-1888.

Shen, C. and H. Johnstone (1955). Gas‐solid contact in fluidized beds. *AIChE Journal* **1**(3): 349-354.

Sun, G. and J. R. Grace (1990). The effect of particle size distribution on the performance of a catalytic fluidized bed reactor. *Chemical Engineering Science* **45**(8): 2187-2194.

Sun, G. and J. R. Grace (1992). Effect of particle size distribution in different fluidization regimes. *AIChE Journal* **38**(5): 716-722.

Tsukada, M., D. Nakanishi and M. Horio (1993). The effect of pressure on the phase transition from bubbling to turbulent fluidization. *International Journal of Multiphase Flow* **19**(1): 27-34.

Turton, R. and N. Clark (1989). Interpreting probe signals from fluidized beds. *Powder Technology* **59**(2): 117-123.

Van Lare, C., H. Piepers and D. Thoenes (1990). Scaling and particle size optimization of mass transfer in gas fluidized beds. *Chemical Engineering Science* **45**(8): 2211-2217.

Venderbosch, R., W. Prins and W. Van Swaaij (1998). Platinum catalyzed oxidation of carbon monoxide as a model reaction in mass transfer measurements. *Chemical Engineering Science* **53**(19): 3355-3366.

Venderbosch, R. H. (1998). *The role of clusters in gas-solids reactors. An experimental study*, Universiteit Twente.

Wang, C., S. Barghi and J. Zhu (2014). Hydrodynamics and reactor performance evaluation of a high flux gas‐solids circulating fluidized bed downer: Experimental study. *AIChE Journal* **60**(10): 3412-3423.

Wang, C., C. Li and J. Zhu (2015a). Axial solids flow structure in a high density gas–solids circulating fluidized bed downer. *Powder Technology* **272**: 153-164.

Wang, C., C. Li, J. Zhu and S. Barghi (2015b). A comparison of flow development in high density gas‐solids circulating fluidized bed downer and riser reactors. *AIChE Journal* **61**(4): 1172-1183.

Wang, C., G. Wang, C. Li, S. Barghi and J. Zhu (2014). Catalytic ozone decomposition in a high density circulating fluidized bed riser. *Industrial & Engineering Chemistry Research* **53**(16): 6613-6623.

Wang, C., Y. Wang, Y. Jin (1997). Effect of particle mean size on the performance of fluidized beds with FCC particles. *Symposium of the first annual conference of Chinese Society of Particle Technology*. Beijing, China**:** 333-337.

Wang, C., J. Zhu and S. Barghi (2015). Performance evaluation of high density riser and downer: Experimental study using ozone decomposition. *Chemical Engineering Journal* **262**: 478-489.

Wang, C., J. Zhu, S. Barghi and C. Li (2014a). Axial and radial development of solids holdup in a high flux/density gas–solids circulating fluidized bed. *Chemical Engineering Science* **108**: 233-243.

Wang, C., J. Zhu, C. Li and S. Barghi (2014b). Detailed measurements of particle velocity and solids flux in a high density circulating fluidized bed riser. *Chemical Engineering Science* **114**: 9-20.

Wei, F., H. Lin, Y. Cheng, Z. Wang and Y. Jin (1998). Profiles of particle velocity and solids fraction in a high-density riser. *Powder Technology* **100**(2): 183-189.

Wei, F., S. Lin and G. Yang (1993). Gas and solids mixing in a commercial FCC regenerator. *Chemical Engineering & Technology* **16**(2): 109-113.

Wei, F., Z. Wang, Y. Jin, Z. Yu and W. Chen (1994). Dispersion of lateral and axial solids in a cocurrent downflow circulating fluidized bed. *Powder Technology* **81**(1): 25-30.

Werther, J. and J. Wein (1994). *Expansion behavior of gas fluidized beds in the turbulent regime*. AIChE Symposium Series, New York, NY: American Institute of Chemical Engineers, 1971-c2002.

Yamazaki, R., M. Asai, M. Nakajima and G. Jimbo (1991). *Characteristics of transition regime in a turbulent fluidized bed*. Proceedings of the Fourth China-Japan Fluidization Conference", Science Press, Beijing.

Yates, J. and S. Simons (1994). Experimental methods in fluidization research. *International Journal of Multiphase Flow* **20**: 297-330.

Yerushalmi, J. and N. Cankurt (1979). Further studies of the regimes of fluidization. *Powder Technology* **24**(2): 187-205.

Yin, L., S. Wang, H. Lu, J. Ding, R. Mostofi and Z. Hao (2007). Simulation of effect of catalyst particle cluster on dry methane reforming in circulating fluidized beds. *Chemical Engineering Journal* **131**(1): 123-134.

Zenz, F. A. (1949). Two-phase fluid-solid flow. *Industrial & Engineering Chemistry* **41**(12): 2801-2806.

Zhang, H., W. X. Huang and J. X. Zhu (2001). Gas‐solids flow behavior: CFB riser vs. downer. *AIChE Journal* **47**(9): 2000-2011.

Zhang, H., J. Zhu and M. Bergougnou (1999a). Hydrodynamics in downflow fluidized beds (1): solids concentration profiles and pressure gradient distributions. *Chemical Engineering Science* **54**(22): 5461-5470.

Zhang, H., J. X. Zhu and M. A. Bergougnou (1999b). Flow development in a gas‐solids downer fluidized bed. *The Canadian Journal of Chemical Engineering* **77**(2): 194-198.

Zhang, X., Y. Qian, S. Guo and Y. Zhang (1997). Application of the optical fiber probe to the measurement of the bubble characteristics in a turbulent fluidized bed with FCC particles. *Journal of South China University of Technology* **25**(8): 20-24.

Zhang, Y., C. Lu and M. Shi (2009). Evaluating solids dispersion in fluidized beds of fine particles by gas backmixing experiments. *Chemical Engineering Research and Design* **87**(10): 1400-1408.

Zhu, H. and J. Zhu (2008a). New investigation in regime transition from bubbling to turbulent fluidization. *The Canadian Journal of Chemical Engineering* **86**(3): 553-562.

Zhu, H. and J. Zhu (2008a). Comparative study of flow structures in a circulating-turbulent fluidized bed. *Chemical Engineering Science* **63**(11): 2920-2927.

Zhu, H. and J. Zhu (2008c). Gas‐solids flow structures in a novel circulating‐turbulent fluidized bed. *AIChE Journal* **54**(5): 1213-1223.

Zhu, J. (2010). Circulating turbulent fluidization—a new fluidization regime or just a transitional phenomenon. *Particuology* **8**(6): 640-644.

Zhu, J. and Y. Cheng (2006). Fluidized-bed reactors and applications. *CRC Press, Boca Raton*.

Zhu, J., M. Qi and S. Barghi (2013). Identification of the flow structures and regime transition in gas‐solid fluidized beds through moment analysis. *AIChE Journal* **59**(5): 1479-1490.

Zhu, J. and F. Wei (1996). Recent developments of downer reactors and other types of short contact reactors. *Fluidization VIII, Engineering Foundation, New York*: 501-510.

Zhu, J. a. Y. C. (2005). Fluidized bed reactors and applications. *Multiphase flow handbook*. C. Crowe. New York, CRC Press**:** 5.55-55.93.

Zhu, J. X. and H. T. Bi (1995). Distinctions between low density and high density circulating fluidized beds. *The Canadian Journal of Chemical Engineering* **73**(5): 644-649.

Zhu, J. X., Z. Q. Yu, Y. Jin, J. Grace and A. Issangya (1995). Cocurrent downflow circulating fluidized bed (downer) reactors—a state of the art review. *The Canadian Journal of Chemical Engineering* **73**(5): 662-677.

Chapter 3
Experimental Setup and Measurement Techniques

3.1 Experimental setup

A multifunctional fluidized-bed system was used in this work, which is schematically shown in Figure 3.1. In this system, bubbling fluidized bed (BFB), turbulent fluidized bed (TFB), circulating fluidized bed (CFB) riser and downer reactors, and circulating turbulent fluidized bed (CTFB) can be operated. A riser column is on the left-hand side, which contains a 10m-high, 76mm i.d. column and a 3.3m-high, 152mm i.d. switchable column for the middle section. Two downer columns with different diameters (76mm i.d. and 50mm i.d. respectively) are located on the right-hand side. Between the riser and downer, there is a downcomer with 203mm i.d. for returning high flux solids flow.

The CFB riser can be operated by using the 76mm i.d. straight column. A gas distributor made of double-layer perforated plates with 2mm×176 holes and 12% opening area is mounted at the bottom of the riser column. The particles slid down to the distributor and were conveyed upwards along the riser column by the air passing through the distributor. The gas supply was at 172.4kPa and room temperature (20℃). A mechanical valve was used to control the solids circulation rate in the inclined feeding pipe. At the top of the riser, gas and particles were separated by three cyclones in series. Most particles can be captured within the cyclones and returned to the downcomer, but those escaping fine particles can be collected by the bagfilter before exhausting. The amount of collected fine particles was very little, so they were recycled periodically. At the bottom of the downcomer, there is a solids storage tank with 457mm i.d. These two parts both can store solids. There are several gas injections around the storage tank in order to keep the stored solids aerated or loosely packed. The total FCC particles inventory in the storage tank and downcomer was kept 6.0m high approximately, equivalent to 450 kg in weight. Such high solids inventory can provide sufficient back pressure head for achieving high solids circulation rates.

The CFB downers can be operated by switching the top diverter valves to the downer side. Particles were firstly conveyed to the top of the riser, separated by the primary cyclone, and then

fed to the downers. There is a gas-solids distributor at the top of each downer column, where particles can be uniformly distributed and flow downwards with air co-currently. The downer columns' bottoms are connected with the storage tank. The fluidizing air coming down was released through an exhaust pipe. Most particles can settle down in the storage tank, but the escaping particles can be recycled by two cyclones in series at the top of the exhaust pipeline.

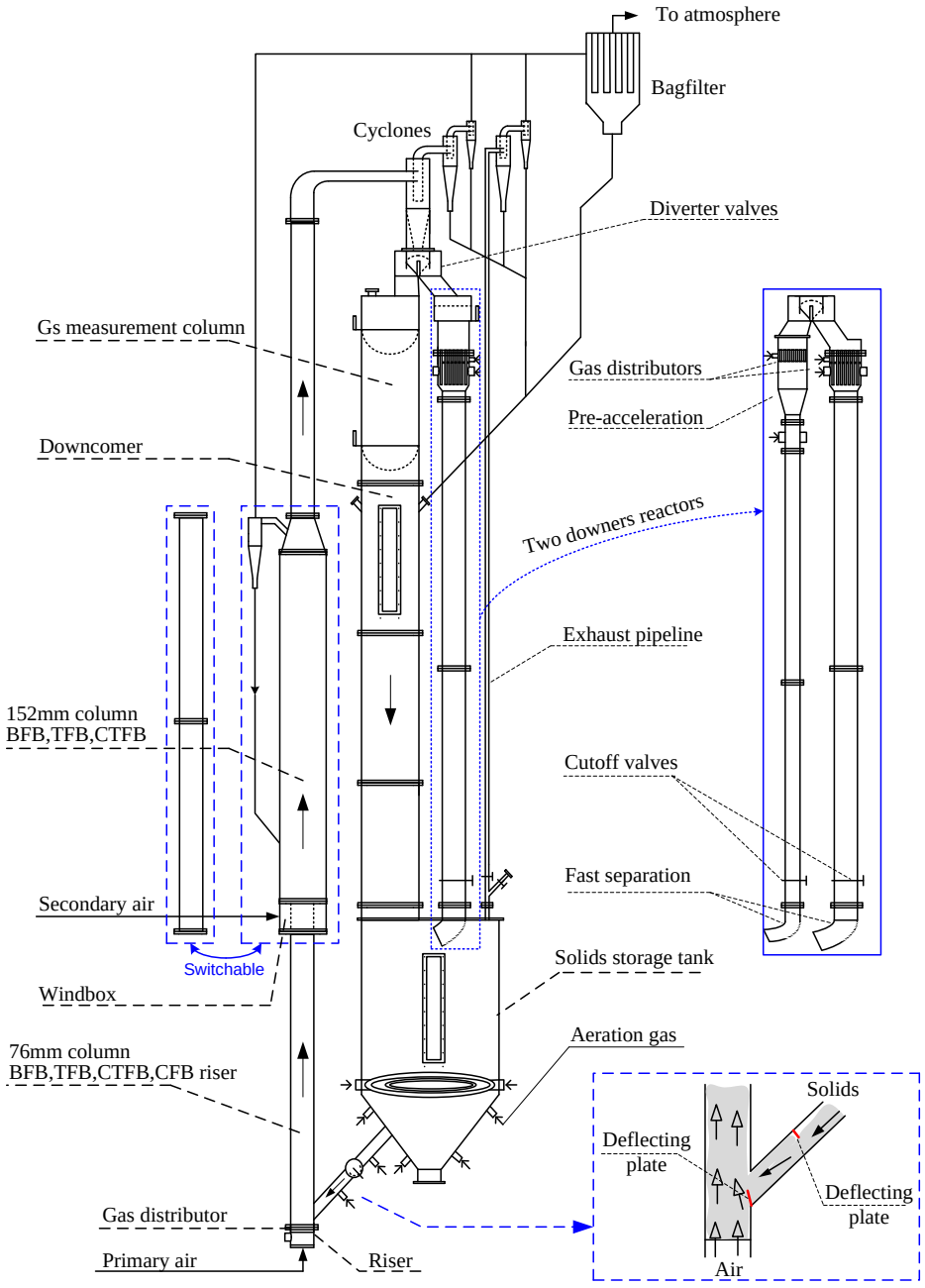

Figure 3.1 Schematic diagram of the multifunctional fluidized-bed system

The CTFB can be operated by switching the middle section of the CFB riser to the 152mm i.d. enlarged column, as shown in Figure 3.1. Particles were lifted by the primary gas from the riser bottom to the enlarged column, and were further accelerated by the secondary gas with a much higher gas velocity. The secondary gas supply was injected through an annular shape perforated distributor (5mm i.d. hole × 44, 10% opening area).The recycling of particles was the same as for CFB riser operation.

The BFB and TFB can be operated by loading certain amounts of particles into the 76mm i.d. riser and operating at low gas velocities. The feeding valve in the inclined feeding pipe should be shut down during the operations. The 152mm i.d. enlarged column is able to greatly reduce particle velocity, so the solid entrainments can be returned due to loss of velocity. The BFB and TFB also can be operated in the 152mm i.d. enlarged column by mounting another perforated gas distributor (5mm i.d. hole × 89, 10% opening area) at its bottom and loading particles into it. The connection between the enlarged column and the upper 76mm i.d. column should be cut off. Additionally, two cyclones were employed in parallel to recycle solid entrainments. The fluidizing gas was released through the bagfilter to atmosphere.

The multifunctional fluidized-bed system is mainly made of aluminium for conducting ozone decomposition experiments. In order to prevent electrostatic charges accumulation and to avoid the effect, the entire system is grounded. A measurement section is installed at the top of the downcomer for measuring solids circulation rates. When operating the CTFB and the high flux CFB, some fluidizing gas possibly flew into the solids storage tank and the downcomer, which could lower the cyclones' separating efficiency. In order to overcome this problem, two deflecting plates were installed in the inclined solids feeding pipe. One was at the entering of riser and vertically covers the lower part of the cross-sectional area by 30%. The other one was at the half-way of the feeding pipe and covers the upper part of the cross-sectional area by 30%. The second solution was installing another exhaust pipe on the top of the downcomer to discharge the backflowing fluidizing gas. It was found that these designs did significantly reduce the backflow of fluidizing gas and facilitate particle feeding.

3.2 Measurements of superficial gas velocities and solids circulation rates

3.2.1 Measurement of superficial gas velocities U_g

Superficial gas velocities were measured by rotameters. The rotameters had been calibrated by the manufacturer using air under the standard calibration condition (P_c = 101325Pa, T_c = 293.15K). Actual gas flowrates in experiments were calculated by the equation below:

$$Q_{actual} = Q_{reading}\sqrt{\frac{P_c T_a}{P_a T_c}} \qquad \text{Eq. 3.1}$$

where P_a is the actual upstream pressure of the rotameter (Pa), T_a is the actual air temperature (K). Superficial gas velocities are the results of actual flowrates divided by cross-sectional area of reactor.

3.2.2 Measurement of solids circulation rates G_s

Solids circulation rates were determined in a measurement column located at the top of the downcomer. The column is divided into two halves by a vertical plate with two flapper valves installed at the plate's top and bottom. Initially, two flapper valves stay on the same side, and particles fall to the downcomer through the other half column. When a measurement starts, the whole column is cut off by flipping the bottom valve by 180°, thereby particles accumulating in the half column. After a certain period of time Δt, the half column with accumulated particles is sealed by flipping the top valve from one side to the other. The height of accumulated particles is read and the particles volume ΔV can be calculated. Finally, the solids circulation rate can be determined by the following equation:

$$G_s = \frac{\Delta V \cdot \rho_b}{A \cdot \Delta t} \qquad \text{Eq. 3.2}$$

where ΔV is the volume of the particles accumulated in the half column, ρ_b is the particle bulk density, A is the cross-sectional area of the column, and Δt is the measurement time of particle accumulation. The measurement was repeated several times to check whether the system reached a steady state and to ensure data accuracy.

3.3 Measurements of solids holdups and particle velocities

Optical fibre probes (Model: PV6D) were used to measure solids holdups ε_s in this work. The probes were manufactured by the Institute of Processing Engineering, Chinese Academy of Science, Beijing, China. By illuminating a small area and measuring the intensity of light reflected by particles, the optical fibre probe can correlate volumetric solids holdup data with voltage signals converted from the light intensity. Optical fibre probes cause only minor disturbance to the gas/solids flow, and are subjected to negligible interference by electrostatics, temperature and humidity. (Zhang, Johnston et al. 1998). Thus, the reflective optical fibre probe is one of the most reliable and widely-applied instruments so far in hydrodynamic studies.

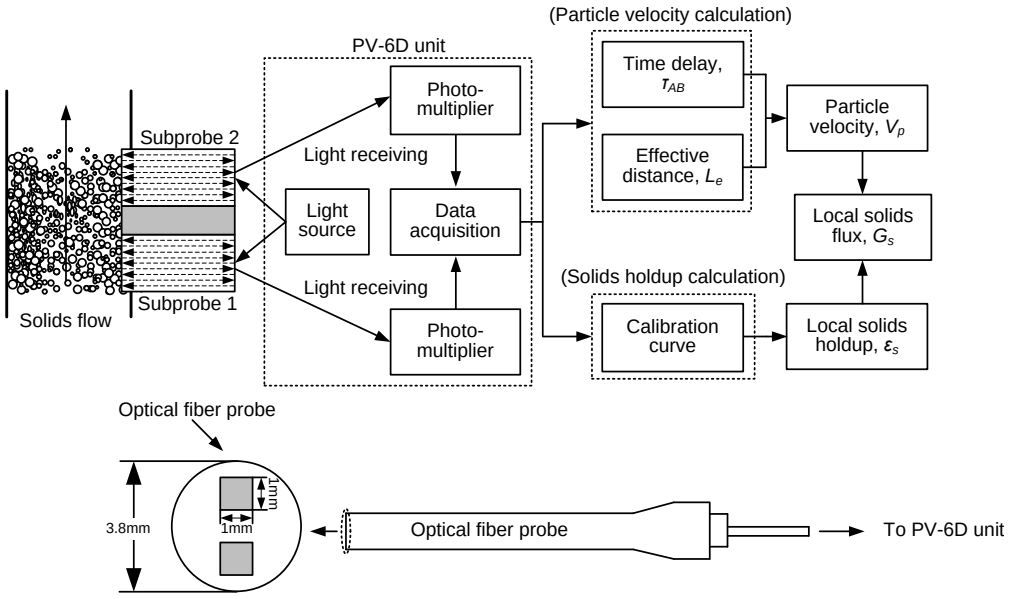

Figure 3.2 PV6D optical fibre probe's internal structure and working block diagram

The probe's internal structure and working block diagram are schematically shown in Figure 3.2. The diameter of the probe is 3.8mm with 2 vertically aligned sub-probes in a square shape of $1\times1mm^2$. The effective (Oki, Walawender et al. 1977) distance between the two sub-probes is 2.08mm, noting it is not the actual distance between the axes of two sub-probes (Liu, Grace et al. 2003). Each sub-probe has a bundle of 8000 quartz fibres, each with diameter of $15\mu m$. Half of the quartz fibres are emitting fibres and the others are receiving fibres. They are arranged alternatively. A Plexiglas pad of 0.2mm thickness is covered the probe tip in order to prevent particles from occupying the blind zone (Liu, Grace et al. 2003).

The light coming from the emitting fibres illuminates a small area. Those receiving fibres can capture the light reflected by particles in the detected area and send it to the photo-multipliers where the light intensity signals are converted to voltage signals. More particles can reflect more light, i.e., higher light intensity, resulting in higher voltage. So the voltage signals are correlated to the volumetric fraction of particles of the detected area or so-called the local solids holdup. But the correlation equation should be determined by calibrations.

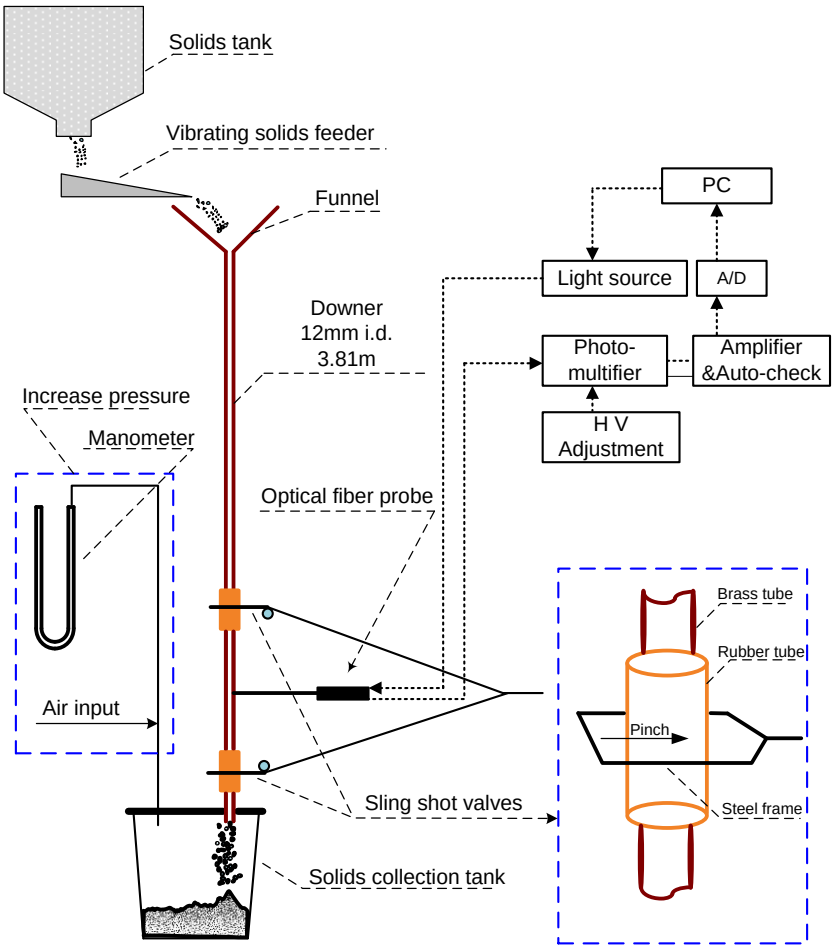

Figure 3.3 Schematic diagram of the optical fibre probe calibration system

A calibration method of optical fibre probes has been developed by Zhang, Johnston et al. (1998). The calibration in this work was conducted in a downer system as shown in Figure 3.3. Particles were fed into a vertically standing brass pipe with 12mm i.d. and 3.81m height from the top. The small pipe diameter was selected to avoid the radial deviation of solids holdup. A valve at the exit of solids tank was used to control the feeding rate. A vibrating solids feeder ensured

continuous and steady feeding. The optical fibre probe was inserted into the brass pipe but not blocking the solids flow. The probe insertion location was close to the pipe bottom, where the solids flow was considered to reach the steady state with uniform distribution and constant velocity. There each had one sling shot valve above and below the optical fibre probe and they can be cut off simultaneously. Falling particles can be trapped by the sling shot valves. The solids holdup can be calculated from the weight of trapped particles, the particle apparent density and the volume of the trap section. By doing so, the voltage produced by the probe can be correlated to the corresponding solids holdup. By measuring under various solids circulation rates, a calibration curve of the solids holdup and the voltage output was obtained, as shown in Figure 3.4. The dense solids flow corresponding to the high voltage was achieved by increasing the pressure in the sealed solids collection tank. The enhanced back pressure can slow particle falling velocity down and increase measured solids holdup.

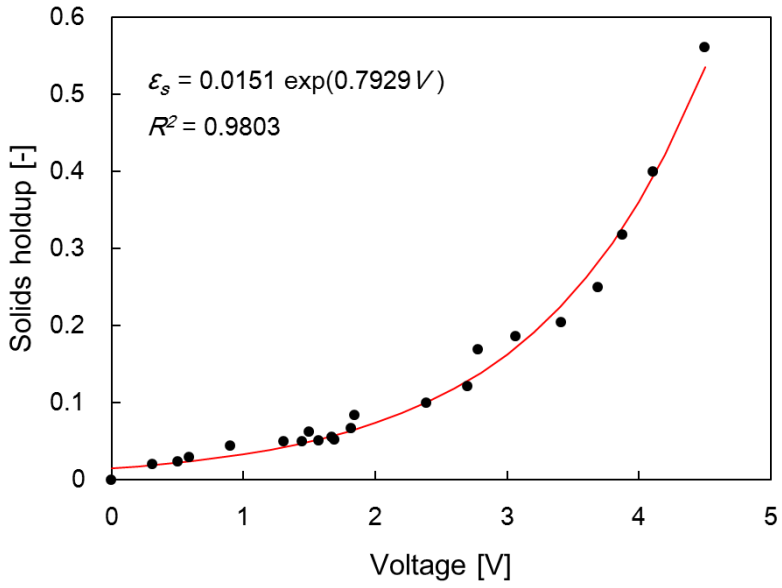

Figure 3.4 Solids holdup calibration curve of the optical fibre probe for the FCC particles

Instantaneous local solids holdup $\varepsilon_s(t)$ can be obtained by the calibration equation with voltage data $V(t)$:

$$\varepsilon_s(t) = f\left[V(t)\right] \qquad \text{Eq. 3.3}$$

where f is the calibration function.

Time-mean solids holdup ε_s can be calculated by integrating $\varepsilon_s(t)$ over a time span T:

$$\varepsilon_s = \frac{1}{T}\int_0^T \varepsilon_s(t)dt \qquad \text{Eq. 3.4}$$

Cross-sectional average solids holdup $\bar{\varepsilon}_s$ can be calculated by integrating ε_s over the cross-sectional area of reactor:

$$\bar{\varepsilon}_s = \frac{1}{\pi R^2}\int_0^R 2\pi r\varepsilon_s \mathrm{d}r = \frac{2}{R^2}\int_0^R \varepsilon_s r\mathrm{d}r \qquad \text{Eq. 3.5}$$

Particle velocities can be obtained by using signals of both sub-probes. The sub-probes could give two identical signals with a time delay τ, when a particle passes them successively. The time delay τ can be calculated by cross-correlation method. Therefore, particle velocities are determined by:

$$V_p = \frac{L_e}{\tau} \qquad \text{Eq. 3.6}$$

where V_p is instantaneous local particle velocity, L_e is the effective distance of the two sub-probes and τ is the time delay of two identical signals.

In practice, some particles might not pass vertically over the two sub-probes giving two similar signals, i.e. particles only passed over one sub-probe. This could result in low or indeterminate cross-correlation coefficients (Liu, Grace et al. 2003). Therefore, only the results with acceptable cross-correlation coefficients can reflect the real particle velocity. In this work, the results with cross-correlation coefficients higher than 0.6 were saved, which was consistent with the work of Werther (1999) and Zhu, Li et al. (2001).

Cross-sectional average particle velocities can be calculated by:

$$\overline{V_p} = \frac{2}{R^2\bar{\varepsilon}_s}\int_0^R V_p\varepsilon_s r dr \qquad \text{Eq. 3.7}$$

At each measuring point, 20 groups of data were collected by the optical fibre probe in order to ensure accuracy. Each group had 32,768 data points detected at the frequency of 50kHz.

3.4 Measurement of ozone concentrations

3.4.1 Ozone generation

An electronic corona discharge ozone generator (Model AE15M, manufactured by Absolute Ozone Inc.) was used to provide ozone in this work. Using bottled oxygen as the gas supply, the ozone generator produced up to 30g/h of ozone depending on the oxygen flowrate and the electrical current settings. It can work at the pressure of 34-340kPa with oxygen flowrate of 0.1-10 standard litre per minute (SLPM).

The generator's performance test was carried out at 20°C after the generator warming-up for more than 30min. Different oxygen flow rates and potentiometer settings were tested, as presented in Table 3.1. Higher oxygen flowrate and electrical current throughput led to higher ozone production. But after oxygen flowrate reached 5LPM, the increase of ozone production was not very significant. Besides, the output ozone concentration (4-12wt%) decreases as oxygen flowrate increases.

Table 3.1 Ozone generator performance test

Oxygen flow	Gas pressure	Current potentiometer	Ozone production	Ozone concentration
[SLPM]	[psig]	[%]	[g/h]	[% wt]
0.5	20	40	4.79	11.99
1	20	50	8.27	10.35
2	20	60	14.77	9.24
3	20	70	19.86	8.29
4	20	80	24.09	7.54
5	20	100	26.99	6.76
6	20	100	28.70	5.99
7	20	100	30.09	5.38
8	20	100	31.02	4.85
9	20	100	31.29	4.35

The O_2-O_3 mixture gas exiting from the ozone generator was mixed into the primary fluidizing air before entering the fluidized beds. By passing a fairly long flow path and several L-bends in the primary air feeding pipeline, ozone was considered to be mixed thoroughly. To ensure that the O_2-O_3 mixture gas could be smoothly injected into the primary air stream, an output pressure of 240kPa was set by the regulator on the oxygen gas cylinder, since the pressure of the primary air stream was up to 172kPa. In all experiments, the ozone generator's potentiometer setting was fixed and the primary air flowrate was constant under each operating condition. Thus the initial ozone concentrations of fluidizing air were adjusted effectively by a rotameter in the oxygen supply stream.

It is essential to maintain a stable inlet ozone concentration during all experimental runs. A test for the stability of the initial ozone concentration was conducted. First, the ozone generator and ozone analyser were warmed-up for 1hr before the test. The stability test was ran in a turbulent fluidized bed by pre-loading some particles into the 76mm i.d. column at the superficial gas velocity of 1.0 m/s, lasting for 3 hours. The inlet air sample was withdrawn from the windbox under the gas distributor. The results are presented in Figure 3.5. After reaching the steady state, the ozone concentration fluctuations were within the range of ±1.5% around the mean value. It was concluded that the stable ozone concentration can last at least 3 hours, long enough for each experimental run which typically took less than 2 hours.

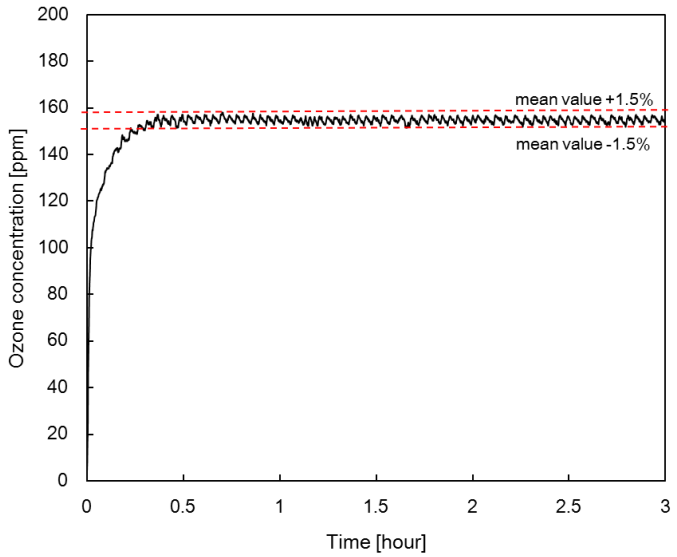

Figure 3.5 Stability test for the inlet ozone concentration

3.4.2 Ozone sampling

In order to prevent ozone decomposing in the sampling process, ozone-inert materials were adopted, e.g. aluminium, brass, stainless steel and Teflon. Although aluminium and brass would be oxidized by ozone, an inert oxide layer could form quickly. The schematic diagram of the ozone sampling system is shown in Figure 3.6. Brass tubes (6mm o.d., 0.36mm wall thickness and 15.0cm length) were inserted horizontally into the column as the sampling probes. The tip of the sampling probe was covered with stainless wire mesh to prevent particles leaking to the ozone analyser. There was a vacuum pump inside the ozone analyser for withdrawing sample gas continuously. The sampling gas velocity was up to 1.5LPM, low enough to assure minimal disturbance to the gas-solids flow in the fluidized beds. High pressure purging air of 100psi was used to clean the particle cakes possibly formed on the probe tips.

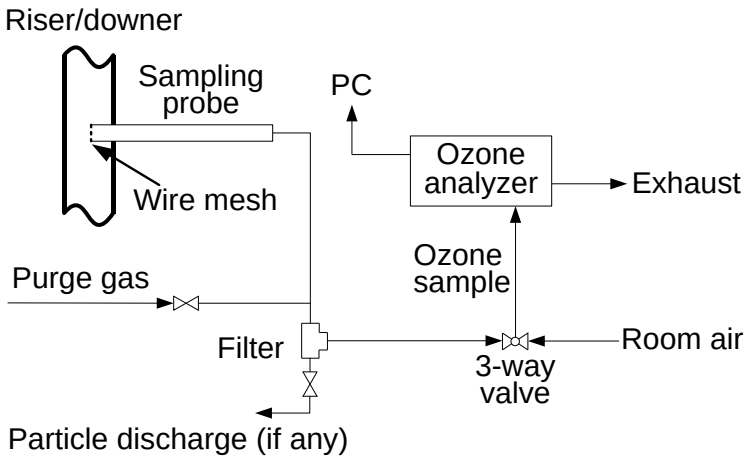

Figure 3.6 Schematic diagram of the ozone sampling system

3.4.3 Ozone detecting

Ozone concentration can be determined by many methods (Seinfeld and Pandis 2006). Ultraviolet absorption method is one of the major techniques due to its simplicity and reliability. The measurement of ozone based on UV absorbance is an absolute method requiring no external calibration, as the ozone absorption in the UV wavelength range has been accurately measured (Sen, Sheldon et al. 1996, Li, Lee et al. 2006). Moreover, this method can be applied on-site and measure continuously.

In this study, an ozone analyser (Model 49i, Thermo Electron Inc.) employing the UV photometric method of measurement was used to measure the ozone concentration in the sample gas. The UV light source used in ozone photometers is 253.7nm from a low-pressure Hg discharge lamp. At this wavelength, the absorptivity of ozone is very close to unity and with little interference from other gases (Seinfeld and Pandis 2006). The analyser is a dual-cell photometer, having both sample and reference air flowing at the same time. Each cell has a length of 37.84cm and an inner diameter of 0.91cm, with the internal surfaces coated with polyvinylidine fluoride (PVDF) to ensure that ozone undergoes no decomposition during testing. The light intensities in the sample air and the sample-free air are used to calculate ozone concentration according to the Beer-Lambert law:

$$C = \left(10^6 \times \frac{P_0 T}{P T_0}\right) \frac{1}{\sigma l} \ln\left(\frac{I_0}{I}\right) \qquad \text{Eq. 3.8}$$

I_0 intensity of the light beam with no ozone present [cd]

I intensity of the light beam after passing through the sample [cd]

l length of the light path through the sample [cm]

C molar fraction of ozone in the sample [ppm]

σ specific absorption coefficient of ozone at wavelength 253.7 nm, 308 cm^{-1}

P pressure [mmHg]

P_0 standard pressure, 760 mmHg

T temperature [K]

T_0 standard temperature, 273.15 K

The schematic diagram of the TEI 49i ozone analyser's configuration is shown in Figure 3.7. The sample gas is sucked through the analyser by a vacuum pump at the exit of the analyser. Ozone concentration is measured in the cells using UV radiation. The solenoid valves operating under computer control allow sample gas to pass through Cell A, and reference gas (with ozone depleted in an ozone scrubber) through Cell B, or *vice versa*, depending upon which cycle the instrument is performing. In addition, the analyser monitors the temperature (accuracy ± 0.2°C), pressure (accuracy ± 0.3 mmHg) and flowrates of the sample gas.

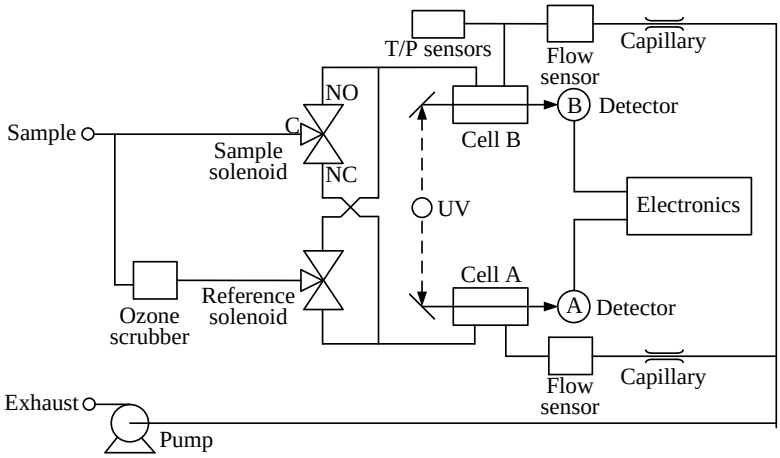

Figure 3.7 Schematic diagram of TEI 49i ozone analyser's configuration

3.5 Sampling locations

The hydrodynamic parameters and ozone concentrations were measured in the axial and radial directions. There were many openings at different elevations along the columns. These openings were shared by the optical fibre probe and the ozone sampling probes, i.e. the hydrodynamic parameters and the ozone concentrations have corresponding measuring points in this work. At each elevation, the data were measured along only one radius to reflect the cross-sectional situation.

The elevations of sampling ports on the 76mm i.d. column (at the bottom) and the 152mm i.d. column (in the middle), and the radial measuring locations are listed in Table 3.2.

Table 3.2 Axial and radial sampling locations of the fluidized beds

	Distance from gas distributor [m]	
Port No.	76mm i.d. column	152mm i.d. column
1	0.25	0.22
2	0.56	0.53
3	1.02	0.79
4	1.47	1.04
5	1.93	1.30
6	2.39	1.55
7		1.80
8		2.34

Radial sampling locations, r/R [-]					
0	0.316	0.548	0.707	0.837	0.950

3.6 Measurement of pressure drops

To obtain pressure drops along the three beds, 14 differential pressure transducers from Omega Engineering were installed along the columns. The excitation voltage required for these pressure transducers is 8VDC (at 20 mA each), giving a voltage output of 1 to 5VDC over their respective pressure ranges.

A manometer was employed to calibrate the pressure transducers as shown in Figure 3.8. Each pressure transducer has two pins for detecting the pressure difference between two points. An air source was connected to one end of the manometer and the high-pressure pin of the differential pressure transducer. The other end of the manometer and the other pin of the pressure transducer were open to surrounding air. Every pressure transducers were calibrated with different amounts of gas being pushed into the manometer. Linear calibration equations fit the data very well. One example of the calibration curves is shown in Figure 3.8.

Differential pressure data were acquired by an on-line personal computer via a 16-bits A/D converter. The transducer output signals were linearly proportional to the pressure drop in the range of 0 to 10kPa. The sampling frequency was 1000Hz and one sampling period was 40s, hence 40,000 data were produced within one sampling group. The locations of pressure taps on the 76mm i.d. column (at the bottom) and the 152mm i.d. column (in the middle) are listed in Table 3.3.

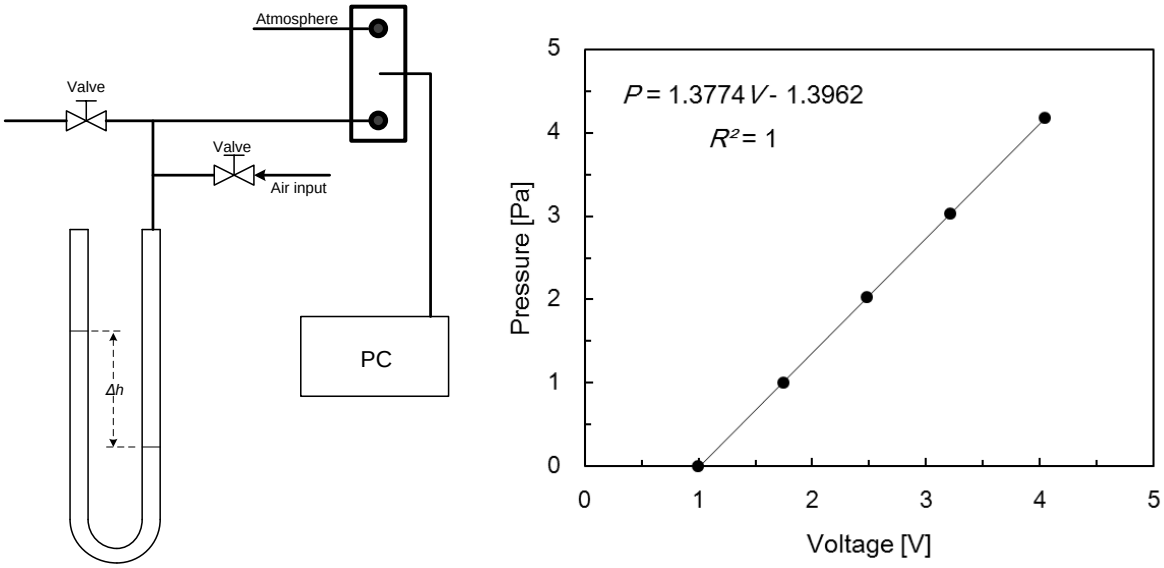

Figure 3.8 Schematic diagram of the pressure transducer calibration

Table 3.3 Locations of pressure taps on the fluidized beds

76mm i.d. column		152mm i.d. column	
Transducer No.	Distance from gas distributor [m]	Transducer No.	Distance from gas distributor [m]
1	0.11-0.56	1	0.22-0.53
2	0.56-1.02	2	0.53-0.79
3	1.02-1.47	3	0.79-1.04
4	1.47-1.93	4	1.04-1.30
5	1.93-2.39	5	1.30-1.55
6	2.39-2.85	6	1.55-1.80
		7	1.80-2.09
		8	2.09-2.34

3.7 Preparation of particles

Ozone decomposition is a thermodynamically favoured process:

$$O_3 \rightarrow 1.5\ O_2$$

$$\Delta H^0_{298} = -138\text{kJ/mol and } \Delta G^0_{298} = -162\text{kJ/mol}$$

Ozone decomposes very slowly at the room temperature (20℃) in the absence of catalysts or ultraviolet (Wojtowicz 2005) and the gas residence time is just up to 10s in this study, so catalysts are necessary for the experiments. It can be assumed that ozone decomposes only when contacting with catalysts. The heat effect and change in volume of the reaction can be neglected under dilute reactant concentration conditions. Therefore, the inlet ozone concentration was set at around 150ppm in the reaction experiments.

Ferric oxide was the catalytic component and was loaded onto fluid catalytic cracking (FCC) particles in this work. FCC particles have been proven to be stable in the ozone decomposition reaction (Sun 1991). The catalyst activation was achieved by the impregnation method, as shown in Figure 3.9. FCC particles were firstly impregnated in a 40wt% $Fe(NO_3)_3$ solution for 12 h, and then the wet particles were dried at 120°C for 6 h in an oven followed by calcination at 450°C for 4 h. After calcination, ferric nitrate was decomposed to ferric oxide loaded on the particles. A

ball mill was used to break up the agglomerates formed during calcination. The particles processed by the ball mill were sifted using a sieve with pore opening of 250μm. Scanning electron microscopy (SEM) photos of the FCC particles illustrate that the particle size and size distribution keep consistent before and after activation, see Figure 3.10.

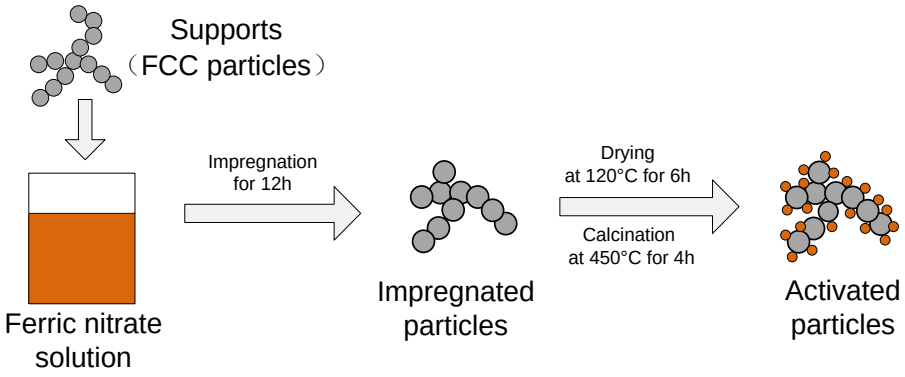

Figure 3.9 Particle activation process

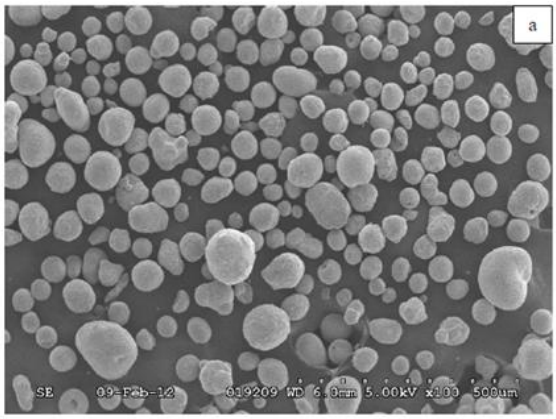

Figure 3.10 SEM photos of the FCC particles before and after activation at ×100 magnification

As the impregnated particles were over active, they were blended with the original (non-activated) FCC particles in order to reduce the overall catalytic activity. The blending was accomplished in the circulating fluidized bed running for long time (approx. 12 h). The particle size d_p and size distribution were measured by BT-9300s laser particle size analyser. The Sauter mean diameter $d[3,2]$, defined as $1/\sum(x_i/d_{p,i})$, was used. The particle apparent density ρ_p and bulk density ρ_b are normally required in fluidization studies. The apparent density ρ_p was obtained by the "wet cake" method (Abrahamsen and Geldart 1980). The bulk density ρ_b was determined by the ratio of the weight of a certain amount of particles to the volume of these particles loosely packed in a graduate cylinder. The particle information is listed in Table 3.4. The size distributions of blended FCC particles are similar before and after all the hydrodynamic and reaction experiments (shown in Figure 3.11), because the very fine particles were elutriated in the long blending process.

Table 3.4 Particle information

Apparent density [kg/m^3]	1780	Bulk density [kg/m^3]	890
d[4,3], [μm]	106.3	d[3,2], [μm]	78.6
Particle size distribution (Vol.%)			
Diameter [μm]	Vol.%	Diameter [μm]	Vol.%
11.11 - 17.05	0.81	105.24 - 117.13	8.78
17.05 - 23.51	1.32	117.13 - 130.37	8.82
23.51 - 32.41	2.64	130.37 - 145.10	8.34
32.41 - 44.69	5.2	145.10 - 161.5	7.27
44.69 - 55.36	5.88	161.5 - 179.75	5.75
55.36 - 68.58	8.75	179.75 - 200.06	4.02
68.58 - 84.96	12.32	200.06 - 222.66	2.43
84.96 - 94.56	7.53	222.66 - 247.83	1.22
94.56 - 105.24	8.29	247.83 - 307.00	0.63

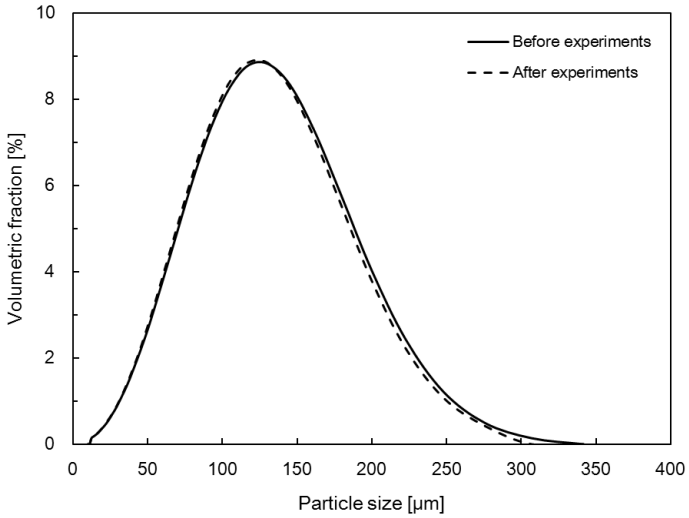

Figure 3.11 Size distribution of the blended FCC particles

3.8 Measurement of reaction rate constants

The catalytic ozone decomposition is a first-order reaction and the reaction rate is expressed as:

$$r_{O_3} = -\frac{dC_{O_3}}{dt} = k_r C_{O_3} \Rightarrow \ln\frac{C_{in}}{C_{out}} = k_r t \qquad \text{Eq. 3.9}$$

where

r_{O3}	reaction rate [mol/m^3.s]
C_{O3}	ozone concentration [mol/m^3]
k_r	apparent reaction rate constant [s^{-1}]
t	reaction time [s]
C_{in}/C_{out}	ratio of inlet to outlet ozone concentration [-]

The ozone conversion is independent with the initial ozone concentration, which is one of reasons to choose ozone decomposition as the model reaction for this project. Frye, Lake et al. (1958) reported that the apparent reaction rate constant k_r for a first order reaction can be determined in a small integral reactor (or a fixed-bed reactor) by the following equation, if it runs as a plug-flow reactor isothermally with minimal transport gradients.

$$k_r = \frac{F_g \rho_b}{m_c} \ln\frac{C_{in}}{C_{out}} \qquad \text{Eq. 3.10}$$

where F_g is the volumetric gas flowrate (m^3/s), ρ_b is the bulk density (kg/m^3), and m_c is the mass of catalyst (kg).

A small fixed-bed reactor (16mm i.d.) made of brass pipe was used to measure the reaction rate constant k_r of ozone decomposition over ferric oxide. The fixed-bed reactor was standing vertically and its bottom was covered by a stainless mesh. 4g of the blended FCC particles was placed in the reactor. The air containing ozone flew through the reactor from top to bottom. The inlet and outlet ozone concentrations, and the volumetric gas flowrate were measured by the ozone analyser. It took some time for the outlet ozone concentration to stabilize, due to reaching the absorption equilibrium and eliminating the dead zones. Three tests were carried out to measure the reaction rate constant at room temperature (20℃), showing the average reaction rate constant of the catalyst in this work was 4.15 s^{-1} (shown in Table 3.5). It is demonstrated that k_r measured at different ozone concentrations are almost constant, further confirming that ozone decomposition is a first-order reaction.

Table 3.5 Measurement of the reaction rate constant of the blended FCC particles

C_{in} [ppm]	C_{out} [ppm]	$F_g\rho_b/ m_c$ [s^{-1}]	k_r [s^{-1}]
115.1	50.7	5.03	4.12
88.7	38.3	5.04	4.23
52.2	22.9	5.00	4.11

Additionally, the axial dispersion effects, interphase and interparticle gradients, and isothermicity of the fixed-bed reactor were all satisfied for the assumptions of Eq. 3.10, checked by Sun (1991) who used a similar fixed bed and similar FCC particles.

Previous work (Frye, Lake et al. 1958) reported that the activity of ozone decomposition varied with temperature and the reciprocal third order of water vapour concentration. In this work, a humidity meter and a thermometer were used to monitor the humidity and temperature of the air supply in the upstream. The relative humidity of air supply was constantly at a level of 19%, while the temperature remained at 20 ℃. Therefore, the moisture and temperature would not influence the reaction rate in the experiments. In addition, the reaction rate constant was tested after every experimental run, showing no obvious variance.

Nomenclature

A	cross-sectional area of the column [m^2]
C_{O3}	ozone concentration [mol/m^3]
C_{in}	inlet (initial) ozone concentration [ppm]
C_{out}	outlet ozone concentration [ppm]
d_p	particle size [μm]
F_g	volumetric gas flowrate (m^3/s)
G_s	solids circulation rate [$kg/(m^2 \cdot s)$]
m_c	mass of catalyst [kg]
I	intensity of the light beam after passing through the sample [cd]
I_0	intensity of the light beam with no ozone present [cd]
k_r	apparent reaction rate constant [s^{-1}]
L_e	Effective distance between two sub-probes
l	length of the light path through the sample [cm]
P	pressure [Pa]
P_c	standard pressure [Pa]
P_a	actual upstream pressure of the rotameter [Pa]
Q_a	actual volumetric flowrate of the air [m^3/s]
Q_{read}	volumetric flowrate of the air reading from the rotameter [m^3/s]
R	radius of the column [m]
r	radial location [m]
r_{O3}	reaction rate [$mol/m^3.s$]

t time [s]

Δt measurement time period [s]

T temperature [K], or time interval [s]

T_c standard temperature, 273.15K

T_a actual air temperature [K]

U_g superficial gas velocity [m/s]

V_p particle velocity [m/s]

V voltage [volt]

Greek letters

ε_s solids holdup [-]

$\overline{\varepsilon}_s$ cross-sectional average solids holdup [-]

ρ_b particle bulk density [kg/m^3]

ρ_p particle apparent density [kg/m^3]

σ specific absorption coefficient of ozone at 253.7 nm, 308 cm^{-1}

τ time delay between two identical signals caused by one particle [s]

ΔV volume of the particles accumulated in the measurement column

Subscripts

g gas

p particle

r reaction

s solid

References

Abrahamsen, A. R. and D. Geldart (1980). Behaviour of gas-fluidized beds of fine powders part I. Homogeneous expansion. *Powder Technology* **26**(1): 35-46.

Frye, C., W. Lake and H. Eckstrom (1958). Gas‐solid contacting with ozone decomposition reaction. *AIChE Journal* **4**(4): 403-408.

Li, Y., S.-R. Lee and C.-Y. Wu (2006). UV-absorption-based measurements of ozone and mercury: an investigation on their mutual interferences. *Aerosol and Air Quality Research* **6**(4): 418-429.

Liu, J., J. R. Grace and X. Bi (2003). Novel multifunctional optical‐fiber probe: I. Development and validation. *AIChE Journal* **49**(6): 1405-1420.

Oki, K., W. Walawender and L. Fan (1977). The measurement of local velocity of solid particles. *Powder Technology* **18**(2): 171-178.

Seinfeld, J. and S. Pandis (2006). Atmospheric Chemistry and Physics, A Wiley-Inter Science Publication, John Wiley & Sons Inc, New York.

Sen, B., W. Sheldon and J. Benbrook (1996). Ultraviolet-absorption photometer for measurement of ozone on a rocket-boosted payload. *Applied Optics* **35**(30): 6010-6014.

Sun, G. (1991). *Influence of particle size distribution on the performance of fluidized bed reactors*. Ph.D., University of British Columbia.

Werther, J. (1999). Measurement techniques in fluidized beds. *Powder Technology* **102**(1): 15-36.

Wojtowicz, J. A. (2005). Ozone. *Encyclopedia of Chemical Technology*. Kirk-Othmer, John Wiley & Sons.

Zhang, H., P. Johnston, J.-X. Zhu, H. De Lasa and M. Bergougnou (1998). A novel calibration procedure for a fiber optic solids concentration probe. *Powder Technology* **100**(2): 260-272.

Zhu, J.-X., G.-Z. Li, S.-Z. Qin, F.-Y. Li, H. Zhang and Y.-L. Yang (2001). Direct measurements of particle velocities in gas–solids suspension flow using a novel five-fiber optical probe. *Powder Technology* **115**(2): 184-192.

Chapter 4
Hydrodynamics of low-velocity gas-solids fluidized beds

4.1. Introduction

Gas-solid fluidized beds have widespread industrial applications at present, such as catalytic cracking, combustion, gasification, calcination and partial oxidation (Kunii and Levenspiel 1991, Bi, Grace et al. 1997). As the fluidizing gas velocity increases, a gas-solids fluidized bed can experience particulate fluidization, bubbling (slugging) fluidization, turbulent fluidization, fast fluidization and pneumatic transport (Chehbouni, Chaouki et al. 1994). In addition, new fluidization regimes, e.g., dense suspension upflow (DSU) (Grace 2000) and circulating turbulent fluidization (Qi, Zhu et al. 2009), have been proposed and situated in the typical fluidization map, based on the identical hydrodynamic characteristics and the unique operating processes. Although controversies still exist in the regime demarcation, it is widely accepted that bubbling fluidized beds(BFBs) and turbulent fluidized beds(TFBs) are classified as low-velocity fluidized beds due to the low fluidizing gas velocity (approx. < 2.0 m/s) and high solids holdup (approx. > 0.25).

BFBs have the longest history of investigation, dating back to the 1960s. Bubbling behaviour are the most distinctive features in BFBs over other types of fluidized beds. The majority of fluidizing gas flows through the particulate bed in the form of bubbles. These bubbles have a low concentration of solids inside and a relatively clear boundary with the surrounding continuous particulate phase (Davidson and Harrison 1963). Therefore, bubble behaviour (e.g., bubble size, shapes, distribution, rising velocity and flow patterns) are of great importance in understanding the reaction conversion, gas and solids mixing, heat and mass transfer, etc., in BFBs (Hatano, Khattab et al. 1986, Lim and Agarwal 1992, Hailu, Plaka et al. 1993, Halow, Fasching et al. 1993). The motion of bubbles is favourable for solids mixing, which has positive effects for some non-catalytic reactions and physical processes. However, BFBs are normally considered not to fit gas-phase catalytic reactions due to the high mass transfer resistance across bubble boundary and the insufficient gas-solids contact inside bubbles.

Turbulent fluidization has been widely accepted as an individual flow regime between bubbling and fast (circulating) fluidization (Bi and Fan 1992). By further increasing the fluidizing gas velocity in BFBs, the volumetric fraction of bubbles increases. But the bubbles eventually cannot keep their steady forms and tend to split into smaller and chaotic voids that have more solids and a less distinguishable boundary with the particle phase. In this regime, these voids split and coalesce extensively and move upwards in random routes (Bi, Grace et al. 1995a). There are no clear continuous and discrete phases, i.e., the dense (particle) phase and dilute (gas) phase are considered to be inter-dispersed (Matsen 1997). Such flow dynamic characteristics lead to vigorous gas-solids contacting and mixing, reduced gas bypassing and intense heat and mass transfer, which are appealing for chemical reaction processes (Bi, Ellis et al. 2000).

Extensive studies have been conducted to understand the turbulent phenomena, as well as flow structure formation and evolution mechanism (Bi, Ellis et al. 2000). The global flow behaviour, such as regime transition velocities, bed pressure drops, bed expansions and axial voidage profiles, were investigated in the early years (Yerushalmi and Cankurt 1979, Lee and Kim 1988, Bi and Fan 1992, Werther and Wein 1994, Foka, Chaouki et al. 1996, Cui, Mostoufi et al. 2000). More recently, increasing attention has been concentrated in the local hydrodynamic behaviour, e.g. local solids holdups and fluctuations, particle motion, and local dense/dilute phase behaviour (Dry, Christensen et al. 1987, Bi and Zhu 1993, Bai and Kato 1995, Cui, Mostoufi et al. 2000, Zhu and Zhu 2008a, Zhu, Qi et al. 2013). However, some aspects of turbulent fluidization, such as particle velocity, gas-solids mixing and scale-up effect, still have controversies due to the complex flow dynamics.

In-depth understanding of the hydrodynamics of low-velocity gas-solid fluidized beds is necessary to study the reaction conversion, heat and mass transfer, gas/solids mixing and so on. For gas-phase catalytic reactions in fluidized beds, the reactor performance is closely related to the hydrodynamics (Wang, Zhu et al. 2015), so detailed hydrodynamic information is of importance. The hydrodynamic results are used to understand the reactor performances of BFB and TFB in Chapter 6. In addition, comprehensive experimental measurements can provide more data resources for developing numerical simulations. The objective of this study is to carry out comprehensive experimental investigations for BFBs and TFBs in terms of bed pressure drops, local solids holdup distributions, flow fluctuations and their changes with operating conditions.

Additionally, the effects of static bed height and bed diameter on the hydrodynamics of BFBs and TFBs are investigated.

4.2. Experimental setup

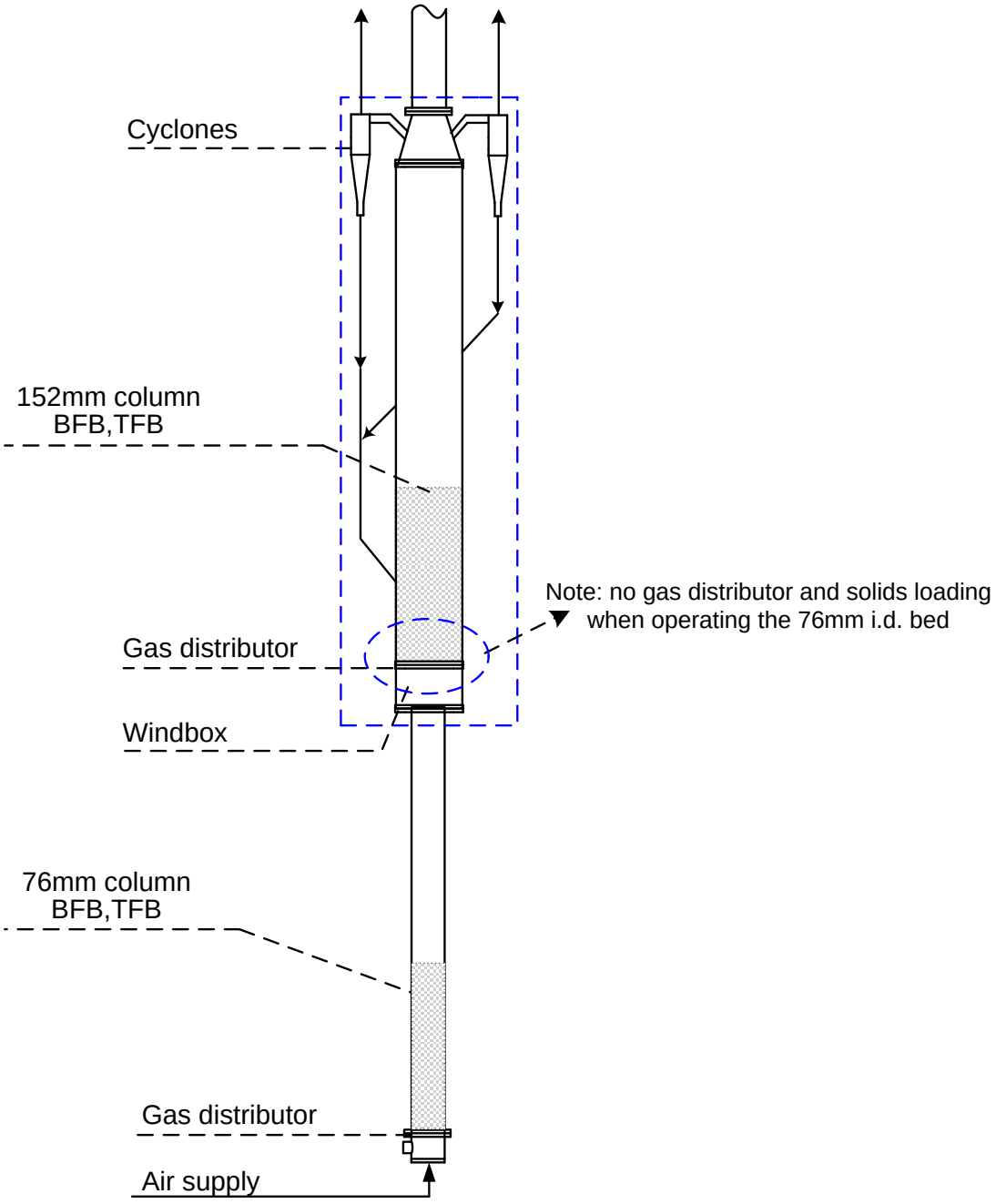

Figure 4.1 Schematic diagram of BFBs and TFBs

Each of the BFB and TFB was operated in either the 76mm i.d. column or the 152mm i.d. column of the multifunctional fluidized-bed system introduced in Chapter 3. As shown in Figure 4.1, the bottom column is 76mm i.d. and 3.0m in length, with a gas distributor made of perforated plates (2mm i.d. hole × 176, 12% opening area) installed at its bottom. The upper enlarged column is able to greatly reduce particle velocity, so that the entrained solids can be returned due to loss of velocity. The experiments were performed by loading certain amounts (1.0m and 1.9m static bed height) of particles into the column and introducing fluidizing gas at the superficial velocities of 0.3 m/s - 1.2 m/s from the bottom.

The upper column is 152mm i.d. and 3.0m in length. Another perforated-plate gas distributor (5mm i.d. hole × 89, 10% opening area) was installed at the upper column's bottom after finishing experiments in the 76mm i.d. column. The connection between the enlarged column and the top 76mm i.d. column was blocked. Additionally, two cyclones were employed in parallel to recycle entrained solids. The fluidizing gas was introduced from the bottom column as well in the range of 0.1 m/s to 1.0 m/s and at static bed heights of 0.79m and 1.0m.

The multifunctional fluidized-bed system is mainly made of aluminium with some portions made of Acrylic for visual observation. In order to prevent electrostatic charges accumulation, the entire system is grounded.

Local solids holdups were measured by optical fibre probes (Model: PV6D) that was manufactured by the Institute of Processing Engineering, Chinese Academy of Science, Beijing, China. The configuration, work mechanism, calibration process and calculations are introduced in Section 3.3. In order to obtain the complete mapping of solids holdup, several sampling ports were opened at different elevations and 6 radial measuring positions were selected on each axial level, which are listed in Table 4.1. At each measuring point, 20 groups of data were collected by the optical fibre probe in order to ensure accuracy and repeatability. Each group had 32,768 data points detected at the frequency of 50kHz.

Table 4.1 Axial and radial sampling locations of the fluidized beds

	Distance from gas distributor [m]	
Port No.	76mm i.d. column	152mm i.d. column
1	0.25	0.22
2	0.56	0.53
3	1.02	0.79
4	1.47	1.04
5	1.93	1.30
6	2.39	1.55
7		1.80
8		2.34

Radial sampling locations, r/R [-]					
0	0.316	0.548	0.707	0.837	0.950

Bed pressure drops were measured by 14 differential pressure transducers (Omega Engineering Inc.) installed along the columns. The work mechanism and calibration process are introduced in Section 3.6. The middle point of each measuring length was used as the representative height for the corresponding bed pressure drop. On the 76mm i.d. column, H=0.33, 0.79, 1.25, 1.70, 2.16, 2.62m above its gas distributor. On the 152mm i.d. column, H=0.38, 0.66, 0.92, 1.17, 1.43, 1.68, 1.95, 2.22m above its gas distributor. To acquire valid results, the measurements lasted at least 4 minutes with sampling frequency of 1000Hz.

FCC particles impregnated with ferric oxide were used in this study, as well as in the experiments of catalytic ozone decomposition. The particle information is listed in Table 4.2. The particle size distributions before and after the experiments were similar, because the very fine particles were elutriated in the long blending process, see Section 3.7.

Table 4.2 Particle information

Apparent density [kg/m^3]	1780	Bulk density [kg/m^3]	890
d[4,3], [*μm*]	106.3	*d*[3,2], [*μm*]	78.6
Particle size distribution (Vol.%)			
Diameter [*μm*]	Vol.%	Diameter [*μm*]	Vol.%
11.11 - 17.05	0.81	105.24 - 117.13	8.78
17.05 - 23.51	1.32	117.13 - 130.37	8.82
23.51 - 32.41	2.64	130.37 - 145.10	8.34
32.41 - 44.69	5.2	145.10 - 161.5	7.27
44.69 - 55.36	5.88	161.5 - 179.75	5.75
55.36 - 68.58	8.75	179.75 - 200.06	4.02
68.58 - 84.96	12.32	200.06 - 222.66	2.43
84.96 - 94.56	7.53	222.66 - 247.83	1.22
94.56 - 105.24	8.29	247.83 - 307.00	0.63

4.3. Results and discussion

4.3.1 Bed differential pressure profiles and regime transition velocity

The bed pressure drop of each measurement section is normalized as differential pressure ($\Delta P/H$) to provide more localized information (Bi, Grace et al. 1995b). The profiles of differential pressure as a function of superficial gas velocity (U_g) in the two columns with different static bed heights (H_0) are shown in Figure 4.2(a)(b) and Figure 4.3(a)(b). In all cases, the differential pressure sharply decreases with increasing U_g at the start, but turns to decrease slowly or even level off after U_g exceeds 0.5–0.8 m/s. Moreover, the differential pressure decreases as the elevation (H) increases, and the axial gradient keeps enlarging until the profiles become relatively flat. This phenomenon suggests the axial uniformity of the bed density reduces with increasing U_g in the low-velocity fluidized beds.

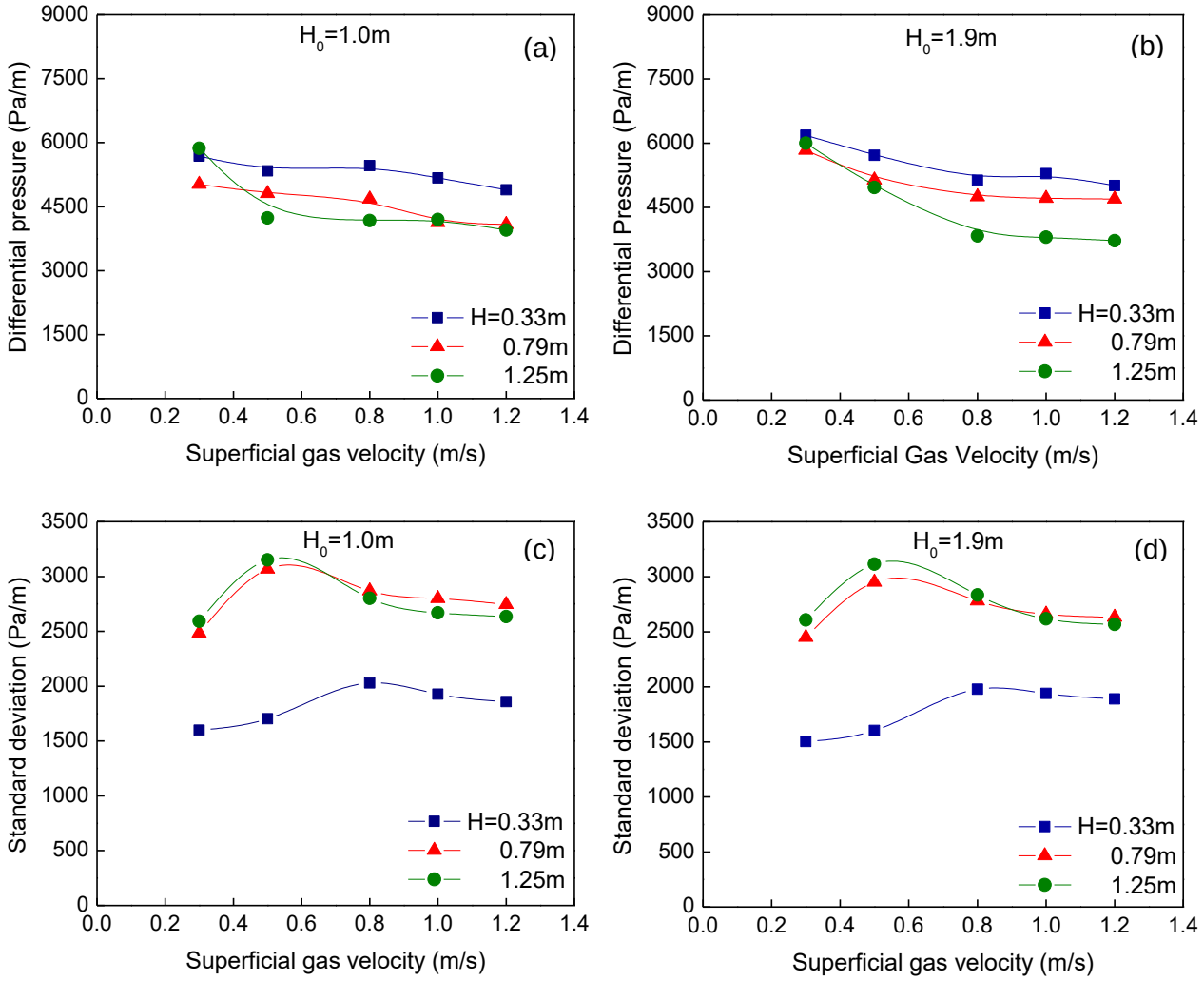

Figure 4.2 Differential pressure and standard deviation profiles in the 76mm i.d. column with different static bed height (H_0)

Pressure fluctuations represented by standard deviations of differential pressure can be used to identify the transition from a BFB to a TFB, which is one of the widely used methods (Yerushalmi and Cankurt 1979, Bi, Grace et al. 1995a). The superficial gas velocity at which the pressure standard deviation reaches its maximum is referred as the transition velocity from bubbling fluidization to turbulent fluidization. As presented in Figure 4.2(c)(d) and Figure 4.3(c)(d), the standard deviations at H=0.79, 1.25m and 0.66, 0.92m show the highest values at U_g=0.5 m/s and gradually level off with further increasing U_g, whereas those at H=0.33m and 0.38m show peaks at U_g=0.8 m/s. As the change of standard deviation at the bottom (H=0.33m or 0.38m) is not significant, the fluidized beds operated below U_g=0.5 m/s are considered as BFBs, whereas those operated above U_g=0.5 m/s are identified as TFBs in this study.

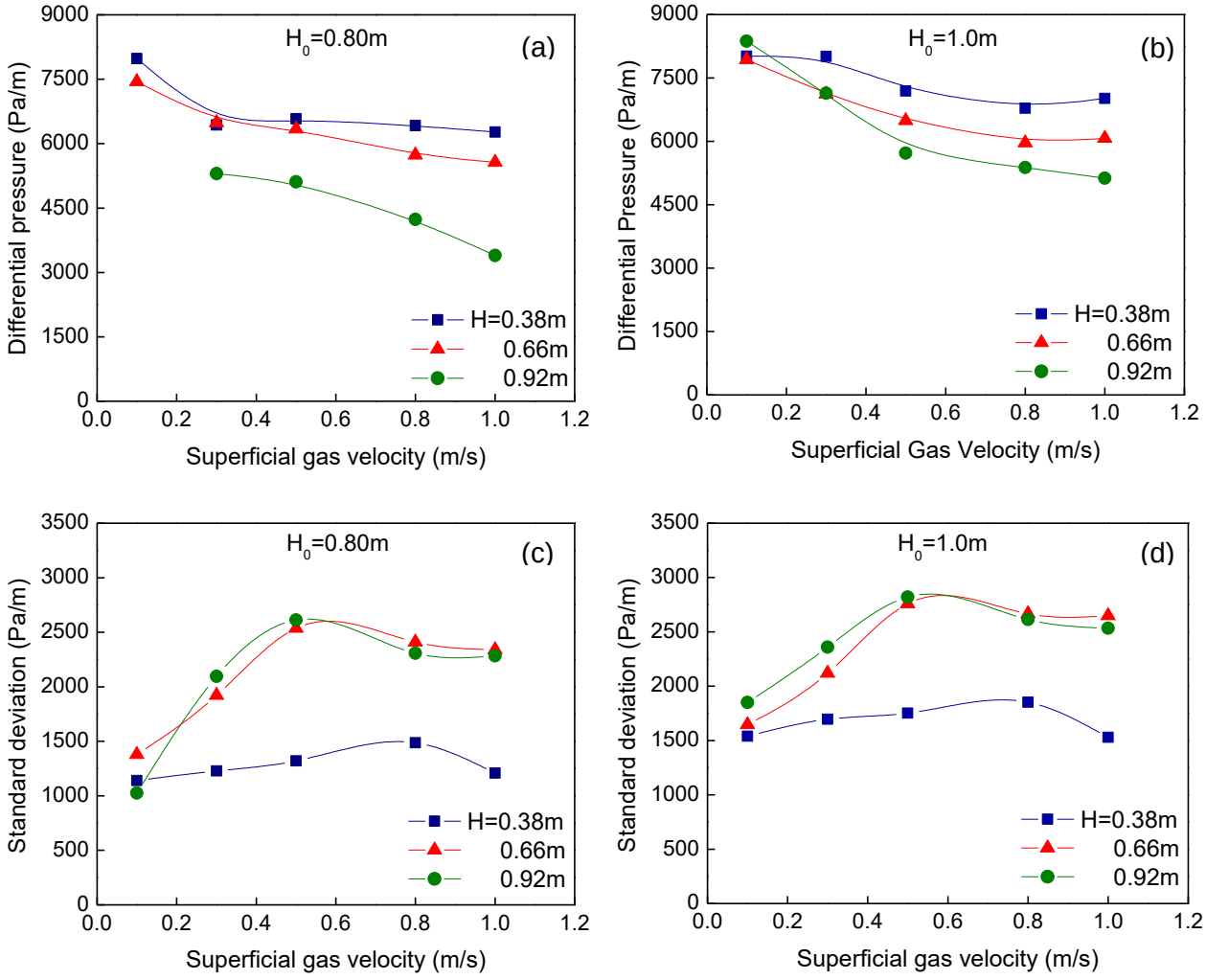

Figure 4.3 Differential pressure and standard deviation profiles in the 152mm i.d. column with different static bed height (H_0)

In addition, the standard deviations at the bottom are obviously smaller than those at the upper elevations when U_g>0.1 m/s. This result can be attributed to the fact that most bubbles/voids are generated at the bed bottom with small sizes and grow to maximum beyond a certain height. Upon entering the turbulent regime, the bubbles with large sizes hardly keep the forms and tend to split to smaller voids, so that the upper bed enters the turbulent regime first (Zhu and Zhu 2008b). The splitting and passing of bubbles/voids are reflected by the higher standard deviations of pressure.

4.3.2 Axial profiles of solids holdup

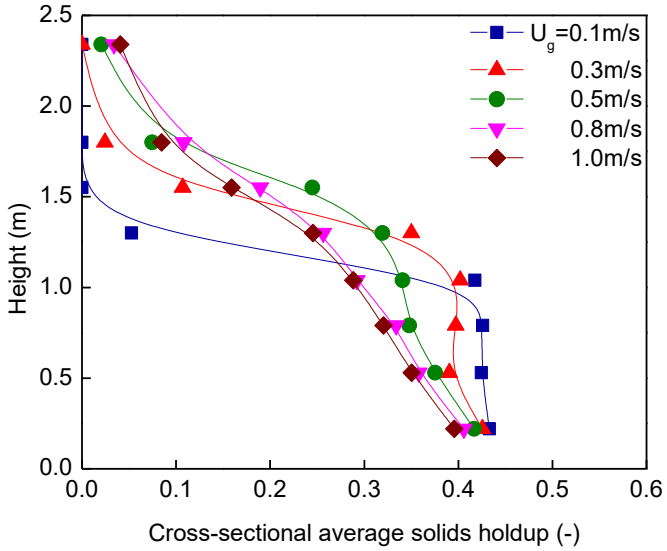

Figure 4.4 Axial profiles of average solids holdup at various U_g (H_0=1.0m, D_T=152mm)

The axial profiles of cross-sectional average solids holdup at various U_g in the 152mm i.d. column with the static bed height of 1.0m are plotted in Figure 4.4. The cross-sectional average solids holdups were obtained by integrating the local solids holdups at different radial positions based on cross-sectional area. It is found that the BFB (U_g≤0.5 m/s) shows a very uniform axial distribution in the dense particulate bed. Despite having slight solid entrainments, a clear bed surface can be seen in the BFB. For the TFB (U_g≥0.8 m/s), the average solids holdup reduces continuously and smoothly with increasing elevation along the entire bed, indicating the disappearance of a detectable bed surface and the large entrainment. This is also a typical feature of TFBs, which can qualitatively denote the transition to TFBs (Bi, Ellis et al. 2000). The non-uniformity of the solids holdup axial distribution in the TFB coincides with the phenomenon reflected by the differential pressure profiles.

The local solids holdups (ε_s) in different radial regions (r/R=0, 0.707 and 0.95) are plotted against U_g at several measuring elevations, as shown in Figure 4.5. The solids holdups reduce with increasing U_g in the central region (r/R=0) and the middle central (r/R=0.707), whereas they stay almost constant (ε_s>0.4) in the wall region (r/R=0.95) due to the boundary-layer effect. It is also shown that the most significant change of solids holdup occurs in the central region with increasing U_g, and the magnitude of solids holdup's reduction increases with elevation, leading to the non-uniform axial distribution in TFBs.

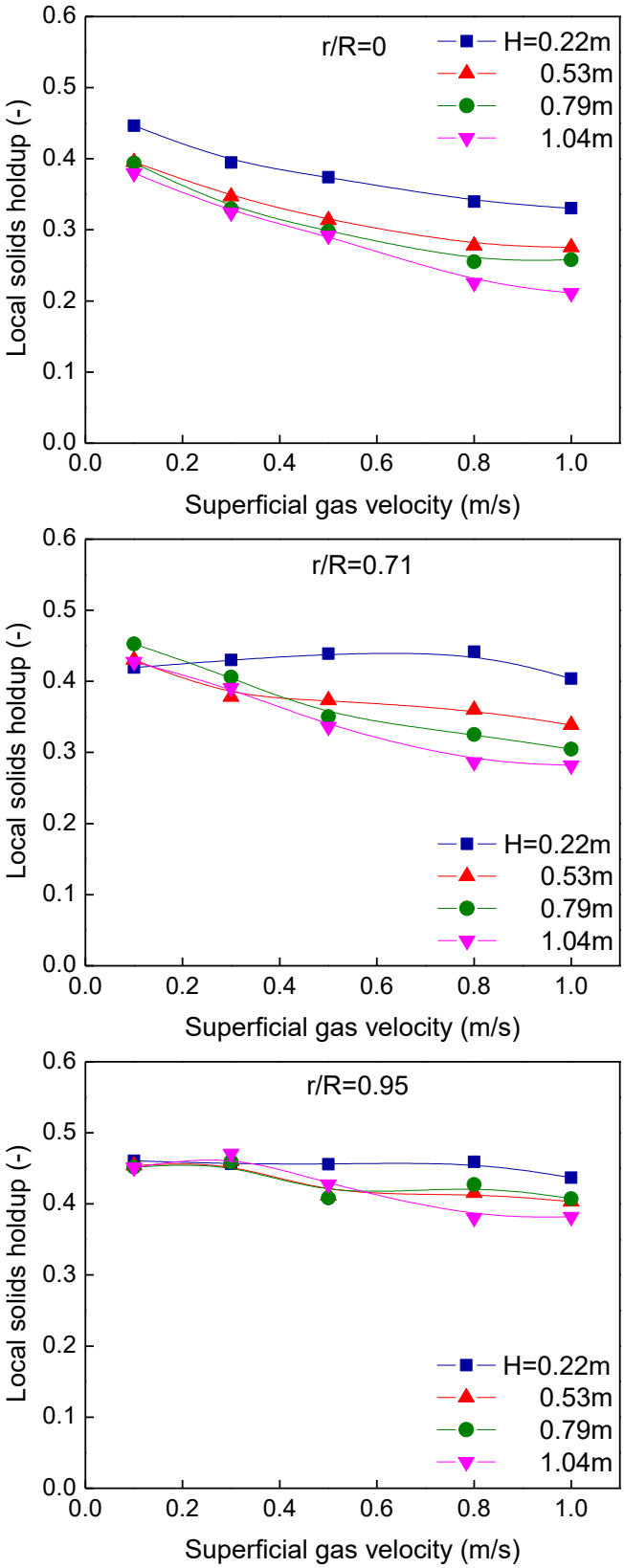

Figure 4.5 Solids holdup profiles as a function of U_g at various heights (H_0=1.0m, D_T=152mm)

4.3.3 Radial profiles of solids holdup

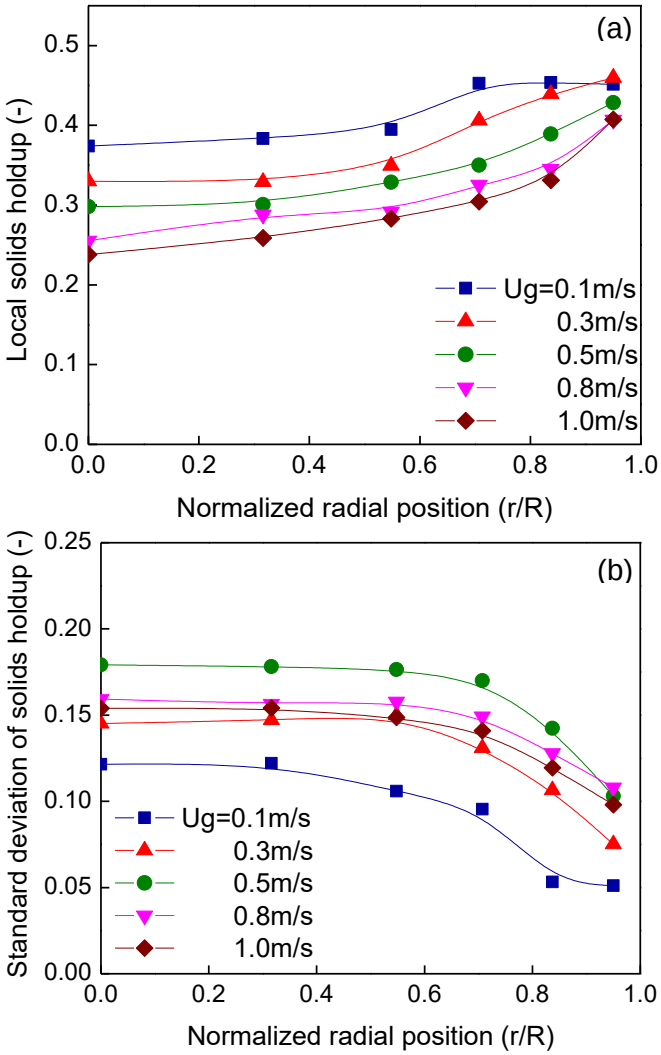

Figure 4.6 Radial profiles of (a) solids holdup and (b) standard deviation at various U_g and height of 0.79m (H_0=1.0m, D_T=152mm)

Radial profiles of solids holdup (ε_s) at various U_g are displayed in Figure 4.6(a). The results were obtained from the 152mm i.d. column with the static bed height of 1.0m. The local solids holdups increase from the center to the wall at all U_g, presenting non-uniform radial distributions. The non-uniformity becomes more serious with increasing U_g, i.e., the solids holdup radial distribution of TFB is less uniform than that of BFB. For the profiles in the BFB, there exist a lower and flat section from r/R=0 to 0.548 and a higher section with ε_s close to that in the minimum fluidization (ε_s=0.49). It is indicated that bubbles are prone to rise in the central region (Hatano, Khattab et al. 1986). For the TFB, the solids holdup is as low as 0.22 in the centre but reaches 0.4 near the wall, showing the transition tendency to the fast fluidized bed with the core-

annular radial structure. In detail, the radial profile appears to be a concave parabolic shape when beyond U_g=0.5 m/s, suggesting a much thinner wall region. This is likely attributed to the smaller void size and the widespread dynamic flow in TFBs (Du, Warsito et al. 2003).

To further understand the local flow behaviour, it is necessary to examine the flow fluctuations that are quantified by standard deviations here. The radial profiles of standard deviation of solids holdup at the height of 0.79m are displayed in Figure 4.6(b). The profiles are flat and higher from r/R=0 to 0.707, but drop drastically towards the wall. The result indicates that the interaction between bubbles/voids and solids mainly happens in the central and middle regions, while the wall region is less active.

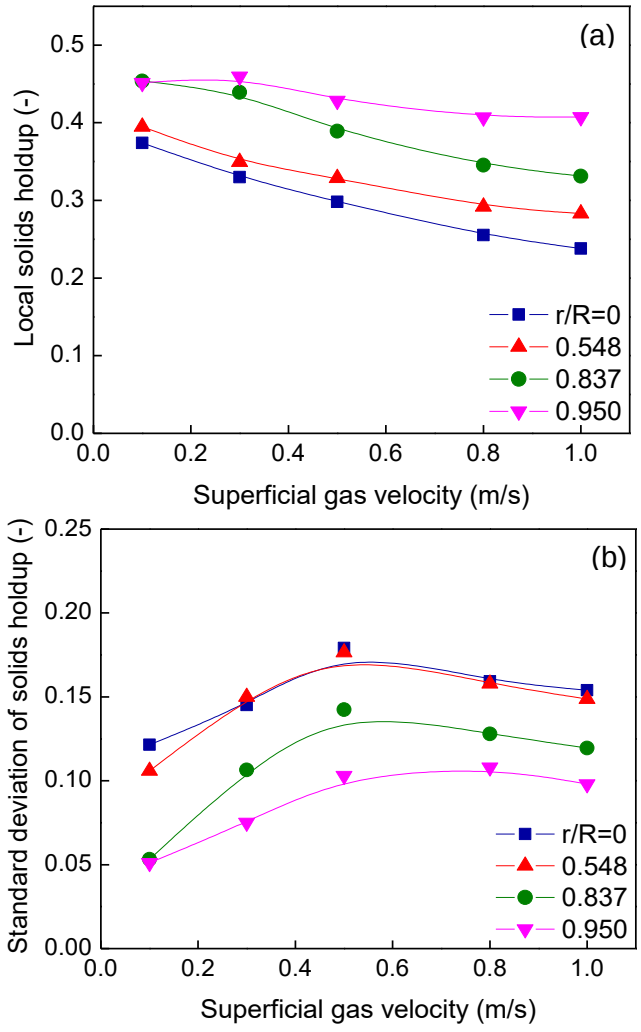

Figure 4.7 Solids holdup(a) and its standard deviation(b) profiles as a function of U_g at different radial positions and height of 0.79m (H_0=1.0m, D_T=152mm)

The solids holdup profiles as a function of U_g at four different radial positions (r/R=0, 0.548, 0.837 and 0.95) are shown in Figure 4.7(a). The results were obtained from the height of 0.79m in the 152mm i.d. column with the static bed height of 1.0m. The solids holdups decrease as U_g increases in all radial positions, while the central region shows the most significant decrease. Moreover, the solids holdup at r/R=0.837 starts to decrease when beyond U_g=0.5 m/s (i.e., transforming to TFB), indicating the shrinkage of the dense wall region and more solids involving to gas-solids mixing.

The corresponding standard deviation profiles are shown in Figure 4.7(b). It is shown that the standard deviations increase with U_g until reaching the maximum at U_g=0.5 m/s, excluding the profile of r/R=0.95. This trend is owing to the growing number of bubbles with increasing U_g. After entering the turbulent regime, the standard deviations slightly reduce with further increasing U_g. The turnover trend results from the smaller void size and their transient characteristics which can cause moderate fluctuations in TFBs (Rowe and MacGillivray 1980, Du, Warsito et al. 2003).

4.3.4 Instantaneous solids holdups

Study of instantaneous solids holdups and their fluctuations can obtain more information about the transient behaviour of gas and solid phases in the microscopic scale, which is able to reflect the performance of gas-solids mixing, contacting and mass transfer (Cui, Mostoufi et al. 2000). The instantaneous solids holdups are plotted against time at U_g=0.1, 0.5 and 1.0 m/s including BFB and TFB (shown in Figure 4.8). The solids holdup signals were acquired at three radial positions (r/R=0, 0.707 and 0.95) and the elevation of 0.79m with a time length of 5s.

For the BFB (U_g=0.1 m/s), the majority of transient signals stay on high levels (ε_s≈0.45) with appearances of sharp drops denoting the passing of bubbles. By close examination, the solids holdup inside the bubbles is as low as 0.02-0.05. Moving from the centre to the wall, although the level of the plateau remains constant, the frequency of bubbles reduces, as well as the width of the signal valleys which indicates bubble size. The signals evidently demonstrate a two-phase structure with a discrete dilute (bubble) phase and a continuous dense (particulate) phase, and a flow pattern with more bubbles of large sizes in the centre and less bubbles of small sizes near the wall.

Furthermore, the signals break down to many peaks with various heights and widths when transforming to the TFB (U_g=1.0 m/s). In other words, the stable dense phase diminishes in the TFB, accompanied with the disappearance of the aforementioned two-phase structure (Lim, Zhu et al. 1995). Instead, the turbulent dense phase with various densities and dimensions is termed as the cluster phase. Additionally, the signal fluctuations in the wall region become more intense in the TFB than those in the BFB, indicating more gas enters the wall region and more solids get involved in the turbulent flow.

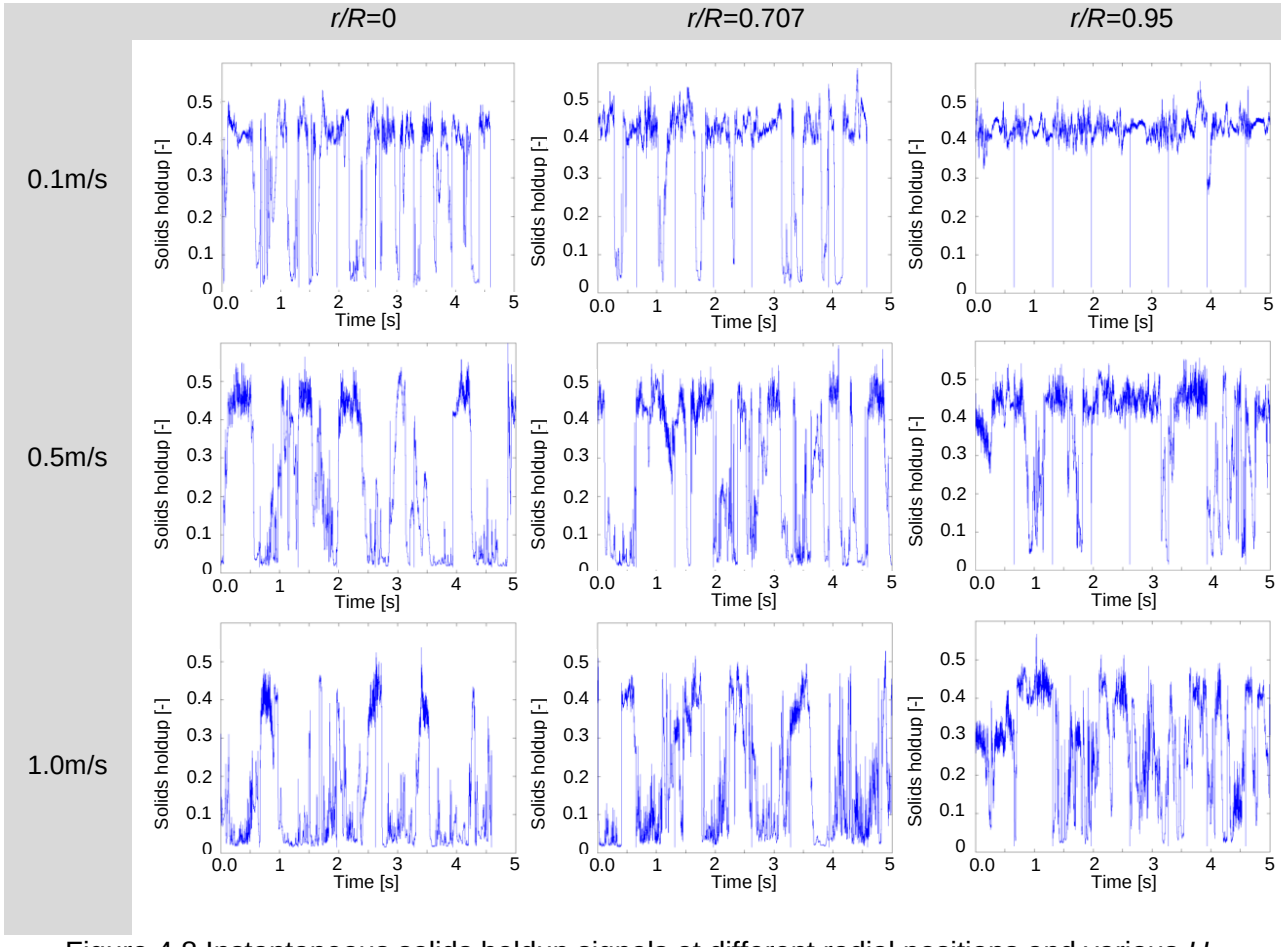

Figure 4.8 Instantaneous solids holdup signals at different radial positions and various U_g (H=0.79m, H_0=1.0m, D_T=152mm)

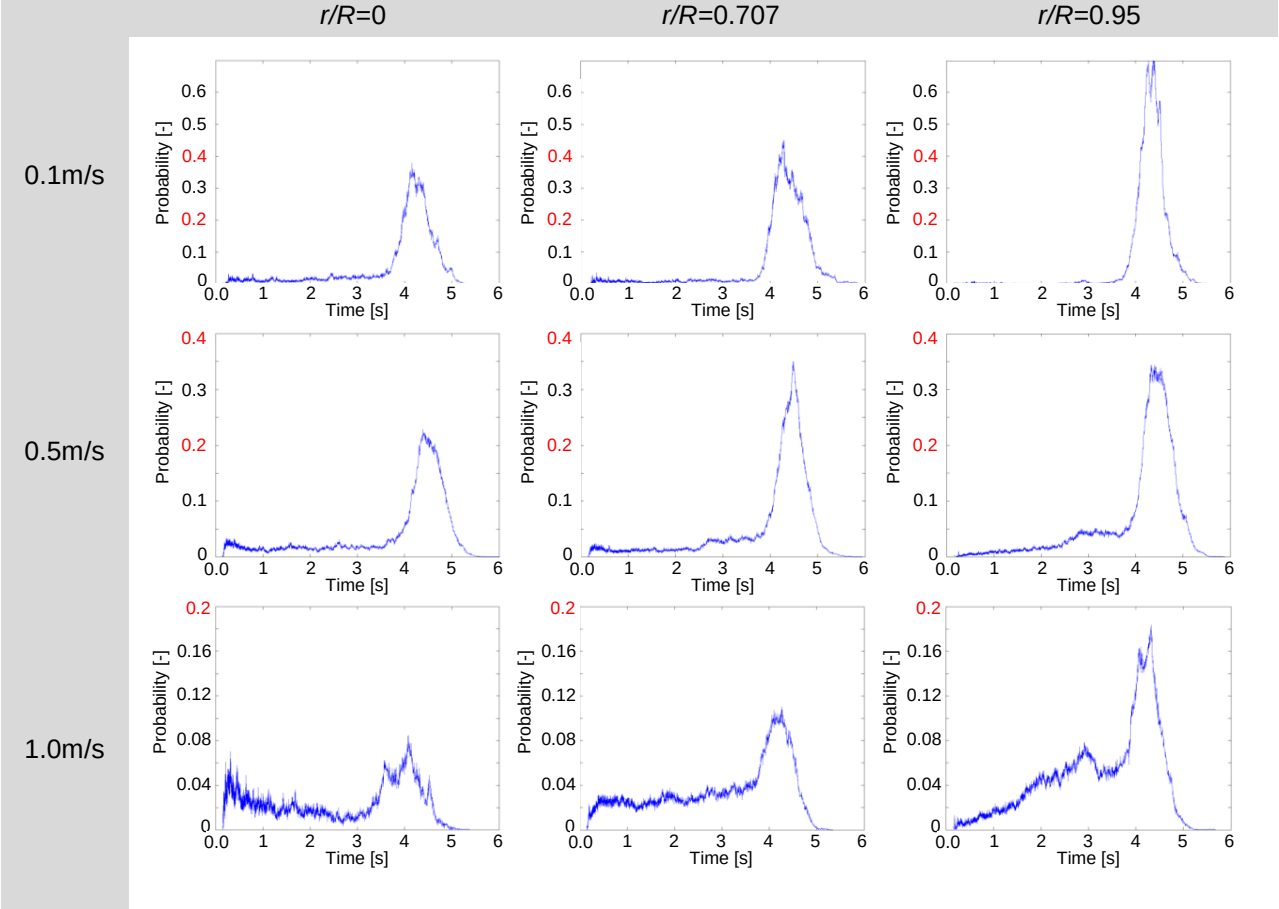

Figure 4.9 Probability density distribution of local solids holdups at different radial positions and various U_g (H=0.79m, H_0=1.0m, D_T=152mm)

The probability density distribution (PDD) of instantaneous solids holdup can help improve understanding of the local flow structures. Figure 4.9 displays the PDDs corresponding to the solids holdup signals in Figure 4.8. Generally, the peaks at ε_s=0.4-0.5 indicate the existence of the dense phase, whereas the peaks at ε_s=0-0.1 indicate the appearance of the dilute phase. At U_g=0.1 m/s, only a single peak with high magnitude exists in every radial position, illustrating the dense phase is dominant in the BFB. It is found that the peak of the dense phase becomes shorter and broader towards the centre, which re-confirms bubbles prefer to rise in the central track. At the transition velocity U_g=0.5 m/s, although the PDD curve still presents a single peak with a tail on the left, the probability of high solids holdups decreases while the probability of low solids holdups somewhat increasing. When entering the turbulent regime, the PDD curve displays a two-peak shape in the central region, which was also reported by previous studies (Bai, Issangya et al. 1999, Cui, Mostoufi et al. 2000, Zhu, Zhu et al. 2008a). Besides, the curves in all

radial positions become even broader and flatter. The broad and continuous distributions suggest an inter-diffused state of the gas and solids phases, with more gas entering the dense phase while more solids are dispersed into the dilute phase. This result is a favourable flow structure for the gas-phase catalytic reactions in fluidized beds, owing to the excellent mixing and contacting characteristics. Therefore, it also explain that TFBs are more widely applied in industries compared with BFBs.

4.3.5 Effect of static bed height

The effect of static bed height (H_0) on hydrodynamics is investigated from the bubbling regime to the turbulent regime in this study. The solids holdup (ε_s) axial distributions obtained from different H_0 (0.8m and 1.0m) at U_g=0.3 m/s (BFB) and 1.0 m/s (TFB) are displayed in Figure 4.10(a) and (b). It is shown that higher H_0 leads to denser solids holdups on all elevations in both BFB and TFB, which agrees with Zhu, Zhu et al. (2008a). In the BFB, two profiles have a similar trend, but the overall solids holdup ε_s of the bed with higher H_0 is 0.4, whereas ε_s is 0.35 at the lower H_0, as shown in Figure 4.10(a). In the TFB, the solids holdup at the lower H_0 reduces faster with increasing elevation than that at the higher H_0 in the particulate bed, but the trend reverses in the freeboard, as shown in Figure 4.10(b). Such denser ε_s in the bed with higher H_0 may be attributed to the larger solids loading and the lower bed expansion ratio.

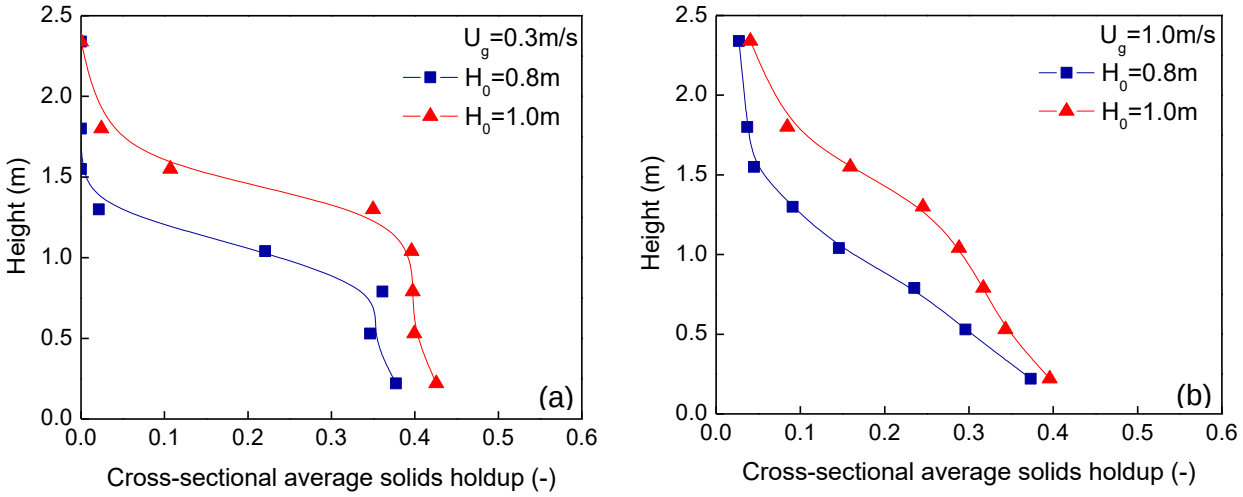

Figure 4.10 Effect of static bed height on solids holdup axial profiles in the BFB and TFB (D_T=152mm)

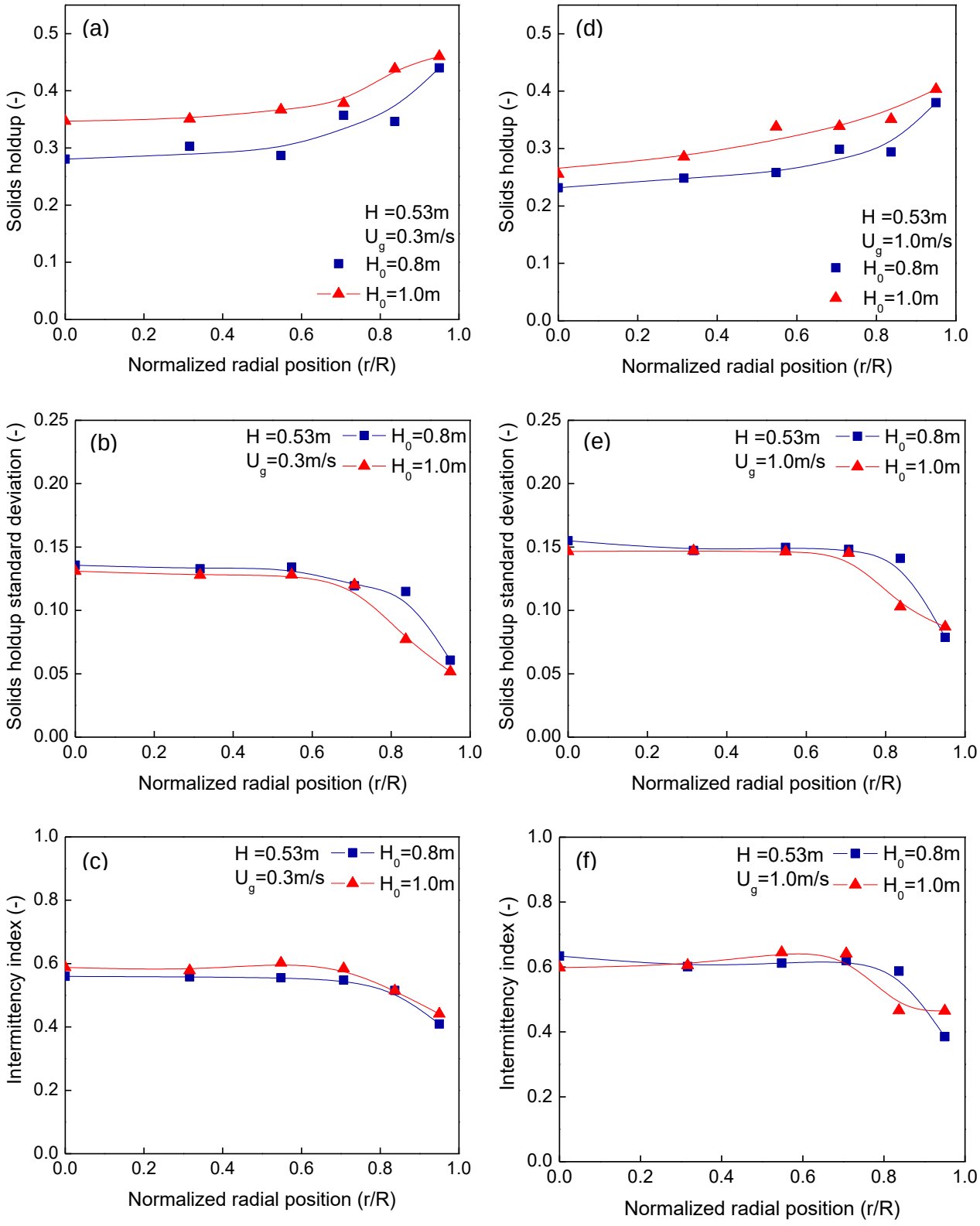

Figure 4.11 Effect of static bed height on radial profiles of solids holdup, standard deviation of solids holdup and intermittency index in the BFB and TFB (D_T=152mm)

The effect of static bed height (H_0) on local flow behaviour including solids holdup, standard deviation and intermittency index, is studied as well, as presented by the categories of BFB and TFB in Figure 4.11. The results were acquired at the height of 0.53m. Similar to the findings from the axial profiles, higher H_0 leads to higher solids holdups in all radial positions for both BFB and TFB. However, it is worth noting that the difference of solids holdup becomes much less noticeable in the wall region.

The standard deviations of solids holdup do not vary significantly with the change of H_0, except those at r/R=0.837 where the bed with low H_0 has higher standard deviations, as displayed in Figure 4.11(b) and (e). Furthermore, flow fluctuations also can be quantified by intermittency indexes of solids holdup, which was proposed by Brereton and Grace (1993) originally for circulating fluidized beds. Higher intermittency index means more intense fluctuation. Besides, the level of segregation of gas and solids can be evaluated by intermittency indexes as well. The value of the intermittency index equal to one suggests “perfect mixing”, while the value is zero if there is a “complete segregation”, e.g., a bubble without any solids inside surrounded by a dense solids phase. As shown in Figure 4.11(c) and (f), the different H_0 leads to close magnitude of intermittency index at every radial position, which indicates a similar degree of interaction and mixing between the gas and solid phases. Overall, the static bed height has no appreciable effect on the flow fluctuations in low-velocity fluidized beds.

4.3.6 Effect of bed diameter

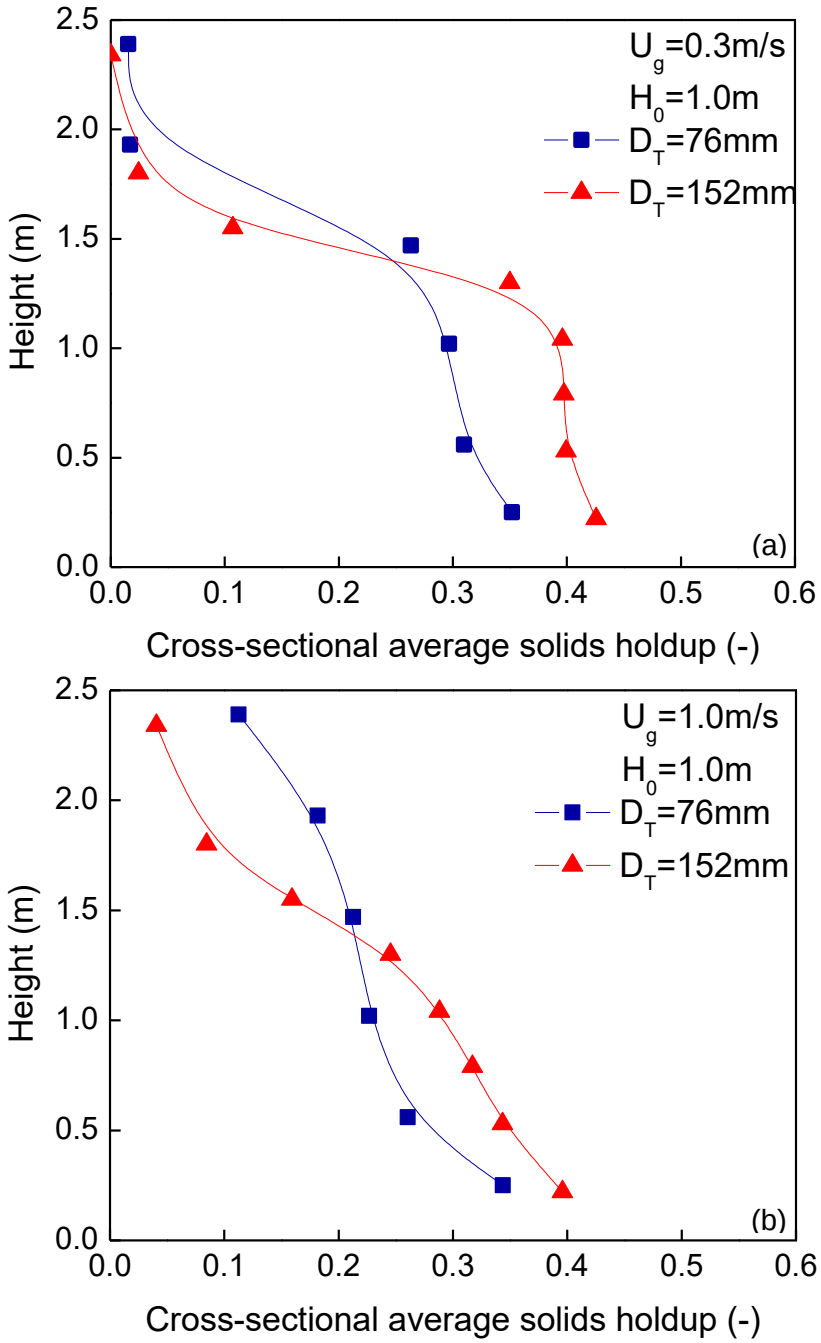

Figure 4.12 Effect of bed diameter (D_T) on solids holdup axial profiles in the BFB (U_g=0.3 m/s) and TFB (U_g=1.0 m/s) at the same static bed height (H_0=1.0m)

The scale-up of fluidized-bed reactors is widely known to be more challenging than for other types of reactors, because the enlargement of reactor size (especially bed diameter D_T) essentially affects the hydrodynamics (Matsen 1997). Although some work has studied the bed diameter scale-up modelling (Kunii and Levenspiel 1991, Werther 1992), such efforts have led to limited success due to the complicated situations involving diverse particle properties, various operating conditions and so on (Knowlton, Karri et al. 2005). Therefore, more experimental studies are necessary to understand the change of flow structures with scaling-up bed diameter D_T and to improve the modelling accuracy.

This study compares the hydrodynamics in the 76mm i.d. and 152mm i.d. beds for a static bed height of 1.0m. The solids holdup (ε_s) axial profiles at U_g=0.3 m/s and 1.0 m/s representing BFB and TFB respectively are displayed in Figure 4.12. In both BFB and TFB, the bed of larger D_T leads to higher solids holdups than the bed of smaller D_T in the particulate bed, but inversely, it shows lower solids holdups in the freeboard. The same result was also observed by Werther (Werther 1992). Moreover, the difference of solids holdup between the bed diameters becomes less significant within the particulate bed when entering the turbulent regime, as shown in Figure 4.12(b). However, the solids holdup in the freeboard of the smaller bed increases more rapidly than that of the larger bed in the TFB. As a result, the bed of smaller D_T possesses lower overall bed solids holdup (ε_s=0.25) with a relatively uniform axial distribution and taller bed height.

The radial profiles of solids holdup, standard deviation and intermittency index by the effect of bed diameter are shown in Figure 4.13, aiming to compare the local flow dynamics. For solids holdup, the large D_T results in a higher magnitude than the smaller D_T, meanwhile the two profiles showing the parallel trends. For the profiles of standard deviation as shown in Figure 4.13(c) and (d), it is observed that the profiles have a similar trend that has a flat and higher stage in the core region but a sharp decrease near the wall. Besides, the bed of smaller D_T exhibits higher standard deviations than the bed of larger D_T in the whole cross section, indicating more intense flow fluctuations and gas-solids interactions in the smaller column. The same phenomenon also can be reflected in the intermittency index profiles in Figure 4.13(e) and (f). It is further suggested that improved gas-solids contacting occurs in the bed of smaller D_T, which is a preferred feature in reactor performance.

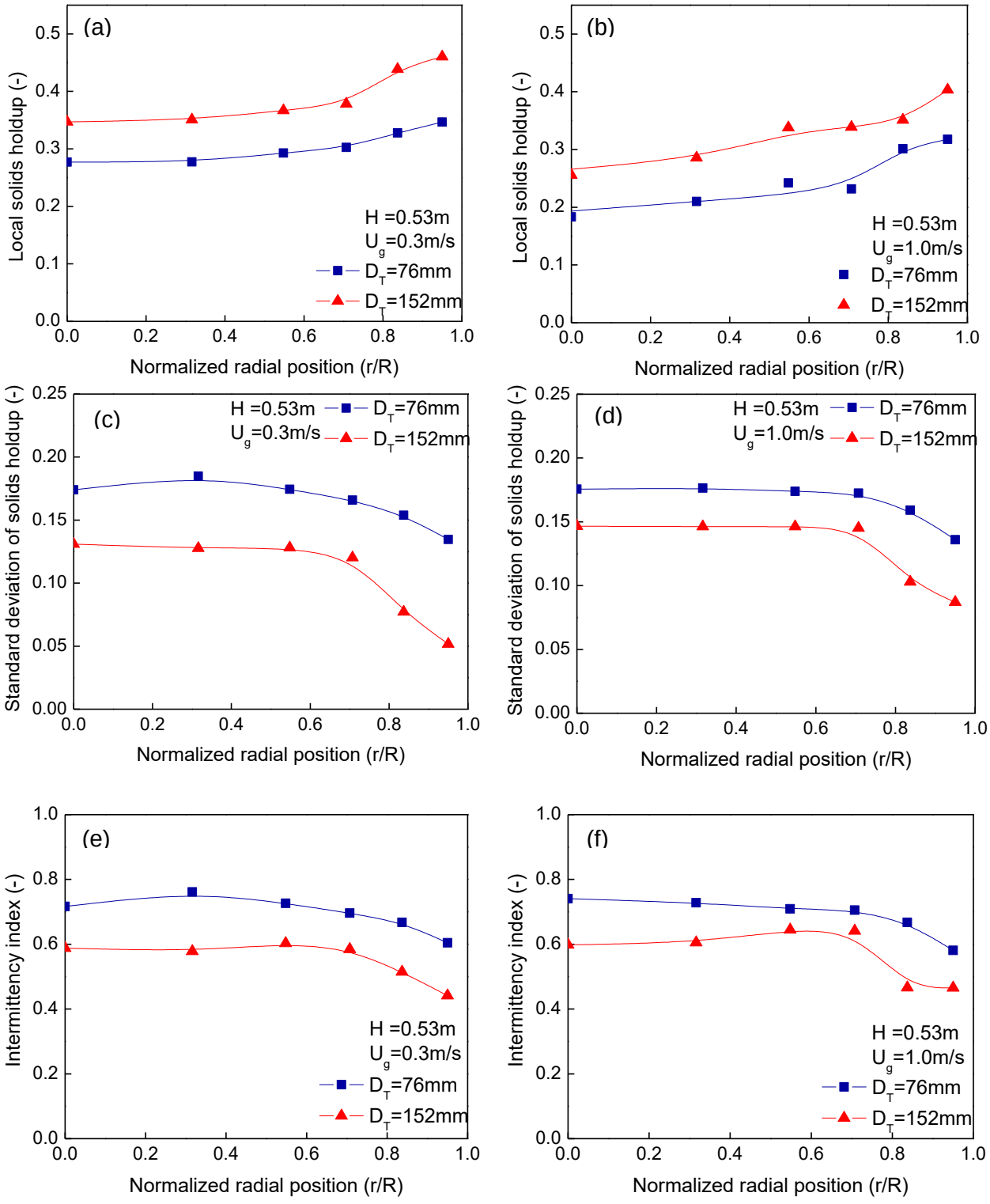

Figure 4.13 Effect of static bed height on radial profiles of solids holdup, standard deviation of solids holdup and intermittency index in the BFB and TFB (H_0=1.0m)

U_g=0.3m/s	r/R=0	r/R=0.95
D_T= 76mm i.d.	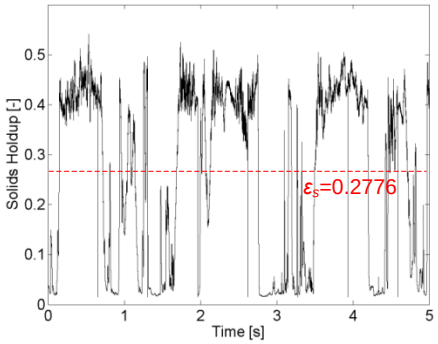	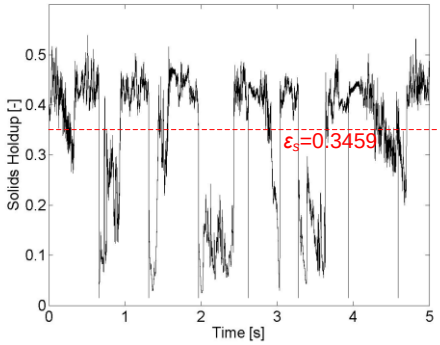
D_T= 152mm i.d.	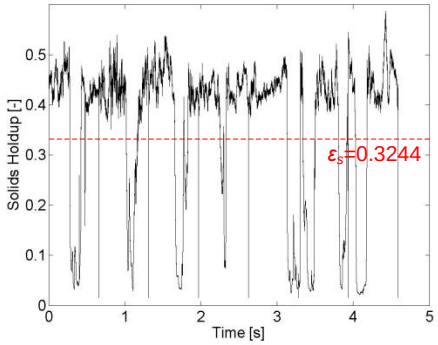	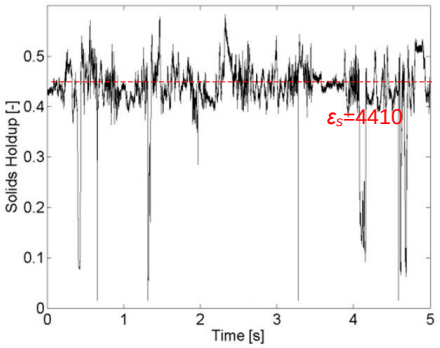
U_g=1.0m/s	r/R=0	r/R=0.95
D_T= 76mm i.d.	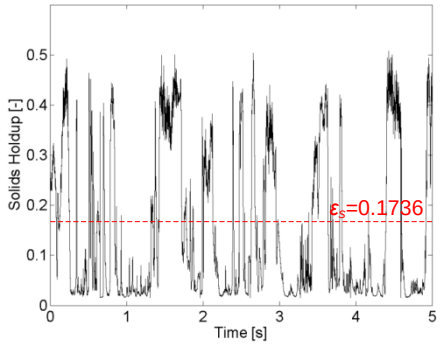	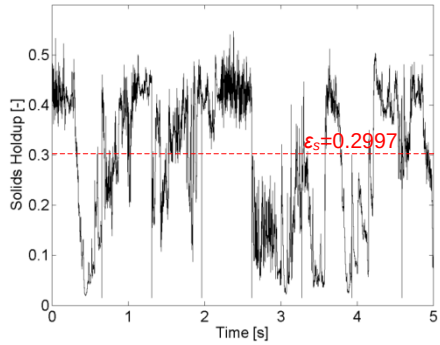
D_T= 152mm i.d.	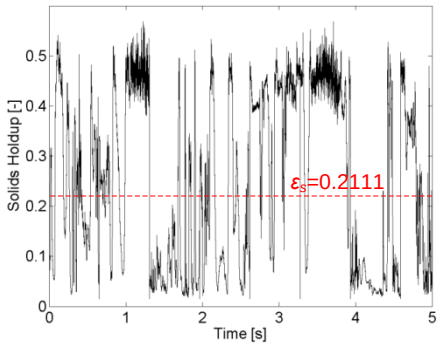	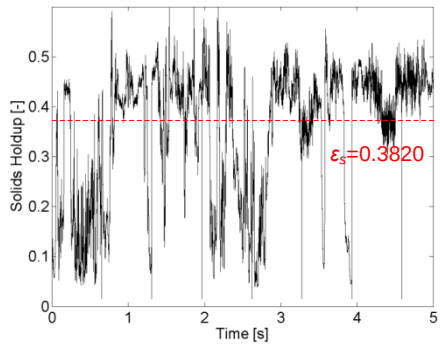

Figure 4.14 Comparison of instantaneous solids holdup signals in the beds of different diameter (H_0=1.0m)

The effect of bed diameter can also be reflected in the instantaneous solids holdup signals in Figure 4.14. The displayed signals were obtained at the radial positions of r/R=0 and 0.95 and at the height of 1.0m. In the BFB (i.e., U_g=0.3 m/s), the bed of larger D_T shows more and narrower signal drops (i.e., passage of bubbles) in the centre, as well as signals of high magnitude in the wall region, when compared with the bed of smaller D_T. This phenomenon indicates the bubbles tend to assemble and rise faster in the central region of the larger bed due to the formation of bubble tracks and solids circulation patterns (Werther 1977). Moreover, the faster bubble movement leads to higher solids holdup if at the same superficial gas velocity. On the other hand, by examining the signals in the TFB (i.e., U_g=1.0 m/s), the difference of fluctuation's frequency and intensity between the two beds becomes closer with the bubbles splitting into much smaller voids with erratic motion. Therefore, scaling-up TFBs could be less troublesome than BFBs, which was also reported by Knowlton, Karri et al. (2005).

4.4. Conclusions

Comprehensive investigations of BFBs and TFBs were conducted both macroscopically and microscopically in terms of flow structure, effect of static bed height and effect of bed diameter in this work.

Differential pressure profiles were studied to reflect the global flow behaviour, showing the overall bed solids holdup reduces with increasing U_g. The standard deviations of differential pressure continuously increased with U_g in the bubbling regime until reaching the maximum at U_g=0.5 m/s, and then turned to decrease gradually. The turning point was used to identify the transition velocity of TFB.

The optical fibre probes were used to measure the local solids holdups. The solids holdup axial and radial distributions in the BFB are more uniform than those in the TFB. The solids holdup of the TFB decreases with increasing elevation due to the considerable solids entrainments. On the other hand, the TFB also shows clear radial gradients in the solids holdup and standard deviation profiles, which become steeper with increasing elevation.

Furthermore, the analysis on instantaneous signals of solids holdup and probability density distributions provided additional information for the local flow structures and interactions

between the gas and solid phases. The results indicate that the BFB is dominated by a two-phase structure of a continuous dense phase and a discrete dilute phase with a few solids inside. The central region has more and larger bubbles, whereas the wall region has less and smaller bubbles. With increasing U_g to the turbulent regime, the dense phase gradually disperses to form a cluster phase, meanwhile more gas entering the dense wall region, which denotes the prevalence of the turbulent gas-solids flow instead of the two-phase structure. The hydrodynamics of TFB is considered to be more favourable to gas-phase catalytic reactions, owing to the excellent gas-solids mixing and contacting.

The scale-up effects, including static bed height and bed diameter, were experimentally studied as well. The results suggest that the higher static bed height leads to denser solids holdups along the entire bed, presumably due to the larger solids loading and the lower bed expansion ratio. The flow fluctuations, however, are not influenced by the change of static bed height. Although the bed of larger diameter has higher overall solids holdup, more vigorous flow fluctuations and phase interactions are found in the bed of smaller diameter. The dynamic feature of the smaller bed is in favour of reactor performance. By further analysing the instantaneous solids holdup signals, the scale-up effect of bed diameter has more significant influence on the BFB than on the TFB.

Nomenclature

D_T	bed diameter [mm]
H	axial coordinate, or distance from gas distributor [m]
H_0	static bed height [m]
r	radial coordinate [m]
R	column radius [m]
r/R	dimensionless sampling position [-]
U_g	superficial gas velocity [m/s]

Greek letters

ε_s	local solids holdup [-]
$\overline{\varepsilon}_s$	mean solids holdup [-]
ρ_p	particle density [kg/m^3]

References

Bai, D., A. Issangya and J. Grace (1999). Characteristics of gas-fluidized beds in different flow regimes. *Industrial & engineering chemistry research* **38**(3): 803-811.

Bai, D. and K. Kato (1995). Saturation carrying capacity of gas and flow regimes in CFB. *Journal of Chemical Engineering of Japan* **28**(2): 179-185.

Bi, H., N. Ellis, I. Abba and J. Grace (2000). A state-of-the-art review of gas–solid turbulent fluidization. *Chemical Engineering Science* **55**(21): 4789-4825.

Bi, H. and L. S. Fan (1992). Existence of turbulent regime in gas‐solid fluidization. *AIChE Journal* **38**(2): 297-301.

Bi, H., J. Grace and K. Lim (1995a). Transition from bubbling to turbulent fluidization. *Industrial & Engineering Chemistry research* **34**(11): 4003-4008.

Bi, H., J. Grace and J. Zhu (1995b). Propagation of pressure waves and forced oscillations in gas-solid fluidized beds and their influence on diagnostics of local hydrodynamics. *Powder Technology* **82**(3): 239-253.

Bi, H. and J. Zhu (1993). Static instability analysis of circulating fluidized beds and concept of high‐density risers. *AIChE Journal* **39**(8): 1272-1280.

Brereton, C. and J. Grace (1993). Microstructural aspects of the behaviour of circulating fluidized beds. *Chemical Engineering Science* **48**(14): 2565-2572.

Chehbouni, A., J. Chaouki, C. Guy and D. Klvana (1994). Characterization of the flow transition between bubbling and turbulent fluidization. *Industrial & Engineering Chemistry Research* **33**(8): 1889-1896.

Cui, H., N. Mostoufi and J. Chaouki (2000). Characterization of dynamic gas–solid distribution in fluidized beds. *Chemical Engineering Journal* **79**(2): 133-143.

Davidson, J., D. Harrison (1963). *Fluidized Particles*. Cambridge, England.

Dry, R., I. Christensen and C. White (1987). Gas—solids contact efficiency in a high-velocity fluidised bed. *Powder Technology* **52**(3): 243-250.

Du, B., W. Warsito and L. S. Fan (2003). Bed nonhomogeneity in turbulent gas‐solid fluidization. *AIChE Journal* **49**(5): 1109-1126.

Foka, M., J. Chaouki, C. Guy and D. Klvana (1996). Gas phase hydrodynamics of a gas-solid turbulent fluidized bed reactor. *Chemical Engineering Science* **51**(5): 713-723.

Grace, J. R. (2000). Reflections on turbulent fluidization and dense suspension upflow. *Powder Technology* **113**(3): 242-248.

Grace, J. R. and H. Bi (1997). Introduction to circulating fluidized beds. Circulating Fluidized Beds, Springer**:** 1-20.

Hailu, L., F. Plaka, R. Clift and J. Davidson (1993). Measurement of gas flow through a two-dimensional bubble in a fluidised bed: particle processing. *Chemical Engineering Research & Design* **71**(4): 382-389.

Halow, J., G. Fasching, P. Nicoletti and J. Spenik (1993). Observations of a fluidized bed using capacitance imaging. *Chemical Engineering Science* **48**(4): 643-659.

Hatano, H., I. A. H. Khattab, K. NAKAMURA and M. ISHIDA (1986). Spatiotemporal measurement of bubble properties in free-bubbling fluidized beds. *Journal of Chemical Engineering of Japan* **19**(5): 425-430.

Knowlton, T., S. Karri and A. Issangya (2005). Scale-up of fluidized-bed hydrodynamics. *Powder Technology* **150**(2): 72-77.

Kunii, D. and O. Levenspiel (1991). Solid Movement: Mixing, Segregation, and Staging. *Fluidization Engineering*: 211-235.

Lee, G. S. and S. D. KIM (1988). Pressure fluctuations in turbulent fluidized beds. *Journal of Chemical Engineering of Japan* **21**(5): 515-521.

Lim, K. and P. K. Agarwal (1992). Bubble velocity in fluidized beds: the effect of non-vertical bubble rise on its measurement using submersible probes and its relationship with bubble size. *Powder Technology* **69**(3): 239-248.

Lim, K., J. Zhu and J. Grace (1995). Hydrodynamics of gas-solid fluidization. *International Journal of Multiphase Flow* **21**: 141-193.

Matsen, J. M. (1997). Design and scale-up of CFB catalytic reactors. *Circulating Fluidized Beds*, Springer**:** 489-503.

Qi, X., H. Zhu and J. Zhu (2009). Demarcation of a new circulating turbulent fluidization regime. *AIChE Journal* **55**(3): 594-611.

Rowe, P. and H. MacGillivray (1980). The Structure of a 15 cm Diameter Gas Fluidised Bed Operated at up to 1 m/s and Seen by X-rays. *Fluidization*, Springer**:** 545-553.

Wang, C., J. Zhu and S. Barghi (2015). Performance evaluation of high density riser and downer: Experimental study using ozone decomposition. *Chemical Engineering Journal* **262**: 478-489.

Werther, J. (1977). Bubble chains in large diameter gas fluidized beds. *International Journal of Multiphase Flow* **3**(4): 367-381.

Werther, J. (1992). Scale-up modeling for fluidized bed reactors. *Chemical Engineering Science* **47**(9): 2457-2462.

Werther, J. and J. Wein (1994). *Expansion behavior of gas fluidized beds in the turbulent regime*. AIChE Symposium Series, New York, NY: American Institute of Chemical Engineers, 1971-c2002.

Yerushalmi, J. and N. Cankurt (1979). Further studies of the regimes of fluidization. *Powder Technology* **24**(2): 187-205.

Zhu, H., J. Zhu, G. Li and F. Li (2008a). Detailed measurements of flow structure inside a dense gas–solids fluidized bed. *Powder Technology* **180**(3): 339-349.

Zhu, H. and J. Zhu (2008b). New investigation in regime transition from bubbling to turbulent fluidization. *The Canadian Journal of Chemical Engineering* **86**(3): 553-562.

Zhu, J., M. Qi and S. Barghi (2013). Identification of the flow structures and regime transition in gas–solid fluidized beds through moment analysis. *AIChE Journal* **59**(5): 1479-1490.

Chapter 5
Hydrodynamics of a circulating turbulent fluidized bed

5.1 Introduction

According to the typical classification, fluidized beds can operate in six regimes: particulate fluidization, bubbling (slugging) fluidization, turbulent fluidization, fast (circulating) fluidization and pneumatic transport (Lim, Zhu et al. 1995). In practice, however, most key commercial applications are using turbulent fluidized beds (TFBs) and circulating fluidized beds (CFBs) by reasons of preferred flow dynamics and favourable operating conditions (Grace 2000). In spite of many advantages, several drawbacks also inherently exist in TFBs and CFBs.

Turbulent fluidization has been widely accepted an individual fluidization regime between bubbling fluidization and fast fluidization so far, owing to the unique hydrodynamics and the popularity in industries, such as FCC regenerators, acrylonitrile, maleic and phthalic anhydride, ethylene dichloride and various ore roasting (Bi, Ellis et al. 2000). Unlike bubbling fluidized beds having a dense-phase flow structure with dispersed bubbles, TFBs have a flow structure with comparable dense (solids) and dilute (voids) phases due to the increased gas velocity. Meanwhile, in TFBs, bubbles break up to smaller and dynamic voids with extensive splitting and coalescence (Bi, Grace et al. 1995). Generally, almost all flow behaviour in TFBs can be characterized to be “turbulent”, e.g., bed surface, local solids holdups, voids and solids motions, and gas-solids mixing. Combining the turbulent flow dynamics with the high solids holdup (~0.25-0.35), TFBs have many advantages in reactor performance, as such high gas-solids contact efficiency, high bed-surface heat transfer efficiency and negligible gas by-passing. However, the low fluidizing gas velocity (~0.5 m/s-2.0 m/s) in TFBs limits the throughput in some applications. Besides, the considerable solids back-mixing possibly results in reduced reaction selectivity when catalysts lose activity shortly.

Circulating fluidized beds (CFBs) have been successfully applied in combustion, gasification and fluid catalytic cracking (FCC), etc. (Grace 1990). They operate in the fast fluidization regime with high fluidizing gas velocities, leading to high gas throughput and reduced gas/solids back-mixing, but lower overall solids holdup. Additionally, the circulating operation is capable of

withdrawing and adding particles continuously, as well as controlling gas and solids fluxes independently. In the early research, the CFBs operated under low operating conditions, such as solids circulation rate $G_s < 200$ kg/m^{2}s, superficial gas velocity $U_g < 5$ m/s and solids holdup $\varepsilon_s < 0.1$. They exhibited a non-uniform flow structure with a dense bottom and a dilute upper region in the axial direction, as well as a dilute core region surrounded by a dense annulus region in the radial direction (Grace and Bi 1997). Such hydrodynamic non-uniformity causes serious gas bypassing through the extreme dilute core region and poor overall gas-solids contact efficiency. More recently, an increasing number of lab-scale investigations were achieved as high operating conditions as those of industrial FCC risers ($G_s \approx 400$~1200 kg/m^{2}s, $U_g \approx 5$~28 m/s, overall $\varepsilon_s > 0.1$) (Issangya, Bai et al. 1999, Pärssinen and Zhu 2001, Wang, Zhu et al. 2014a). These CFBs were defined as high density/flux CFBs (Zhu and Bi 1995). Although it was found that the solids holdup axial distributions became relatively uniform in the high density CFBs, the gas/solids radial segregation still inherently existed, which is unfavourable to gas-solid contacting and reactor performance (Wang, Wang et al. 2014).

A novel circulating turbulent fluidized bed (CTFB) with a distinctive operating mode was developed by Zhu and Zhu (2008a). The word "circulating" in its name suggests it operates with solids circulation, while "turbulent" characterizes the dynamic flow structure. The experimental results (Zhu and Zhu 2008a, Qi, Barghi et al. 2012) demonstrated that the CTFB successfully overcame several disadvantages of TFBs and CFBs, meanwhile integrating their advantages, such as high solids holdup, uniform distribution, favourable gas-solids contacting, reduced solids back-mixing and high solids circulation rates. By comparing the hydrodynamics of CTFB both macroscopically and microscopically with TFBs and CFBs, the circulating turbulent fluidization was identified as a new flow regime (Qi, Zhu et al. 2009).

Although spatial distributions of solids holdup and particle velocity, as well as local behaviour of dense and dilute phases, were reported (Zhu and Zhu 2008a, Zhu and Zhu 2008b, Qi, Barghi et al. 2012, Qi, Zhu et al. 2012), they were obtained in the same experimental system. The investigations of this study have been conducted in a new CTFB apparatus with different dimensions, regarding of axial and radial profiles of solids holdup, flow fluctuations, effect of operating conditions and effect of the gas distributor. The objective is to provide more experimental data for further understanding underlying characteristics and developing numerical

models. Since, for gas-phase catalytic reactions, fluidized-bed reactor performance is closely related to hydrodynamics (Wang, Zhu et al. 2015), the detailed hydrodynamic measurements are necessary to understand the reactor performance of the CTFB.

5.2 Experimental setup

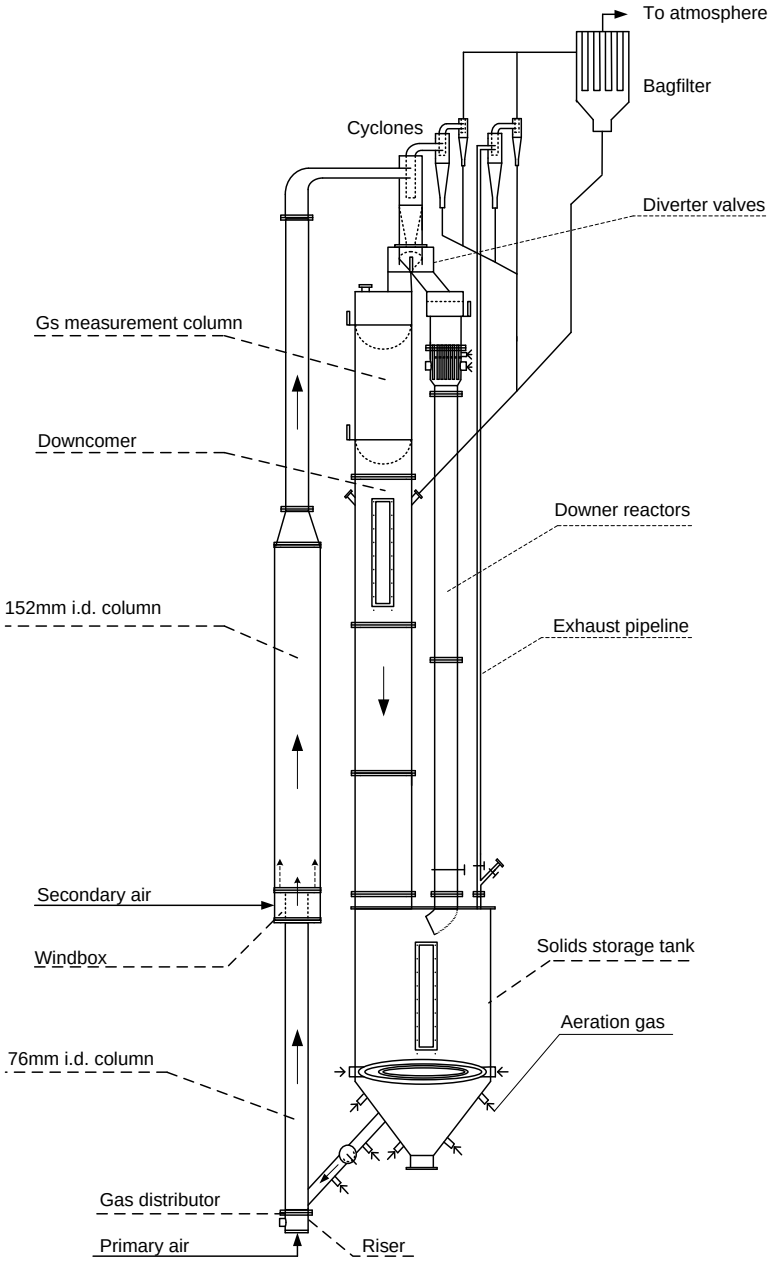

Figure 5.1 Schematic diagram of the CTFB system

The circulating turbulent fluidized bed (CTFB) was operated in the multifunctional fluidized-bed system introduced in Chapter 3. As shown in Figure 5.1, the CTFB riser column is on the left-hand side, which consists of a 76mm i.d. column at the bottom, a 152mm i.d. switchable column in the middle, and another 76mm i.d. column at the top. Each column is 3.0m in height. The bottom column is the main body of the CTFB, so all measurements were conducted in the bottom column. A downcomer on the right of the riser serves for returning solids to a storage tank at its bottom. A gas distributor made of double-layer perforated plates (2mm i.d. hole × 176, 12% opening area) is mounted at the bottom of the riser column. The columns are mainly made of aluminium with some portions made of Acrylic for visual observation. In order to prevent electrostatic charges accumulation and to avoid their influence, the entire system is grounded.

The particles slid down to the gas distributor and were conveyed upwards by the primary air supply with superficial gas velocities (U_g) of 1.0 m/s, 2.0 m/s or 3.0 m/s. The particles were further accelerated by the secondary gas supply with U_g=5.0 m/s in the middle enlarged column. The secondary gas supply was injected through an annular perforated distributor (5mm i.d. hole × 44, 10% opening area). The gas supplies were at 172.4kPa and room temperature (20℃). A mechanical valve was used to control the solids circulation rate (G_s=100, 200 and 300 kg/m^{2}s) in the inclined feeding pipe. At the top of the riser, gas and particles were separated by three cyclones in series. Most particles can be captured within the cyclones and be returned to the downcomer, but those escaping fine particles can be collected by the bagfilter before exhausting. The amount of collected fine particles was very little, so they were recycled periodically. The total FCC particles inventory in the storage tank and downcomer was maintained at 6.0m-high approximately. Such high solids inventory can provide sufficient back pressure head to ensure high solids circulation rates.

Local solids holdups were measured by an optical fibre probe (Model: PV6D) that was manufactured by the Institute of Processing Engineering, Chinese Academy of Science, Beijing, China. The configuration, work mechanism, calibration process and calculations are referred to Section 3.3. In order to map the entire column's solids holdup distribution, several sampling ports were opened at 6 elevations (H=0.25, 0.56, 1.02, 1.47, 1.93 and 2.39m) and 6 radial measuring positions (r/R=0, 0.316, 0.548, 0.707, 0.837 and 0.95) were selected on each axial elevation. At each measuring point, 20 groups of data were collected by the optical fibre probe in

order to ensure accuracy and repeatability. Each group had 32,768 data points detected at the frequency of 50kHz.

FCC particles impregnated with ferric oxide were fluidized in this study and the catalytic ozone decomposition experiments later. The particle's properties are listed in Table 5.1. The particle size distributions before and after the experiments were similar, because the very fine particles were elutriated in the long blending process, see Section 3.7.

Table 5.1 Particle information

Apparent density [kg/m^3]	1780	Bulk density [kg/m^3]	890
d[4,3], [*μm*]	106.3	*d*[3,2], [*μm*]	78.6
Particle size distribution (Vol.%)			
Diameter [*μm*]	Vol.%	Diameter [*μm*]	Vol.%
11.11 - 17.05	0.81	105.24 - 117.13	8.78
17.05 - 23.51	1.32	117.13 - 130.37	8.82
23.51 - 32.41	2.64	130.37 - 145.10	8.34
32.41 - 44.69	5.2	145.10 - 161.5	7.27
44.69 - 55.36	5.88	161.5 - 179.75	5.75
55.36 - 68.58	8.75	179.75 - 200.06	4.02
68.58 - 84.96	12.32	200.06 - 222.66	2.43
84.96 - 94.56	7.53	222.66 - 247.83	1.22
94.56 - 105.24	8.29	247.83 - 307.00	0.63

5.3 Results and discussion

5.3.1 Achieving circulating turbulent fluidization

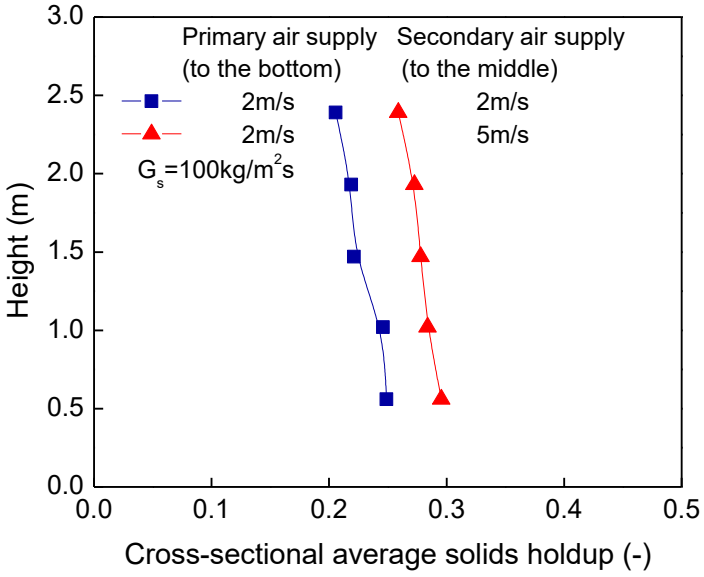

Figure 5.2 Effect of U_g of the secondary air supply on solids holdups in the bottom section of the CTFB

The CTFB has a unique configuration that the 76mm i.d. bottom column connects with a 152mm i.d. enlarged column above it. In addition to the primary air blowing from the bottom at the superficial gas velocity (U_g) up to 3.0 m/s, there is a secondary air being injected to the enlarged column at higher U_g. The effect of U_g of the secondary air on the solids holdup in the CTFB bottom section is clearly shown in Figure 5.2. The cross-sectional average solids holdups were obtained by integrating the local solids holdups of different radial positions based on cross-sectional area. It is seen that the secondary air U_g=5 m/s leads to higher solids holdups than U_g=2 m/s, indicating the higher secondary U_g does help to increase the overall solids holdup. The formation mechanism of this dense upflow can be elaborated by a pressure drop analysis along the entire system (Bi and Zhu 1993). After particles enter the enlarged section, the solids holdup of the flow would be significantly reduced due to space expansion and velocity acceleration, resulting in largely decreased pressure drops in the middle and upper columns. Since the pressure heads of the blower and the solids inventory stay constant during operations, the pressure drop of the bottom column should increase in order to keep the system pressure balanced. As a result, the solids holdup in the bottom column is significantly increased. Thus, the bottom bed is the main body of the CTFB. All measurements were conducted in the bottom column.

When the bottom column and the enlarged column were operated at the same U_g of 2.0 m/s, the solids flow with solids holdup of 0.22 can be identified as the dense bottom of a CFB whose high solids holdup is likely caused by the "U" tube effect. On the other hand, the cross-sectional average solids holdup of CTFB ranges from 0.25-0.30 at U_g=2.0 m/s in Figure 5.2. The result implies the hydrodynamics of CTFB could be different from that of the dense bottom of CFB. It also re-confirms that the well-designed fluidized beds using fine (no-slugging) particles are able to operate over the conditions which are normally considered to induce choking (Zhu and Bi 1995).

5.3.2 Axial profiles of solids holdup

The axial distributions of solids holdup were obtained at various U_g (1.0, 2.0, 3.0 m/s) and G_s (30, 60, 100, 200, 300 kg/m^{2}s) in the CTFB, as shown in Figure 5.3. The axial profiles of all conditions exhibit great uniformity with remarkably high solids holdups ranging from 0.22 to 0.35. A relatively dense bottom region can be observed at the height (H) of 0.25m due to the low particle velocity, which is analogous to the bottoms of CFBs (Wang, Zhu et al. 2014b). However, the bottom region of CTFB is very short, just up to 0.56m, as shown in Figure 5.3, indicating particles accelerate to a stable velocity rapidly. Furthermore, it is found that the solids holdups reasonably increase with increasing G_s.

The effect of U_g on solids holdup axial profiles has been studied at three different G_s as shown in Figure 5.4. The solids holdups decrease with increasing U_g, while the change of solids holdup with U_g becomes less significant with increasing G_s. The result suggests that G_s of 300 kg/m^{2}s could be approaching a "saturation" state. Besides, compared with conventional CFBs, the change of solids holdup with U_g is much less significant, indicating the particle-particle interactions (collision) become comparable or even prevailing to the gas-particle interactions under the high density conditions. Overall, the presented high solids holdups and uniform axial distributions can lead to sufficient gas-solids contacting and high bed-surface heat transfer efficiency. The unique operation of low U_g and high G_s is in favour of the reactions requiring higher solids/gas feed ratio, higher gas-solids contact efficiency and relatively longer residence time (Zhu and Zhu 2008a).

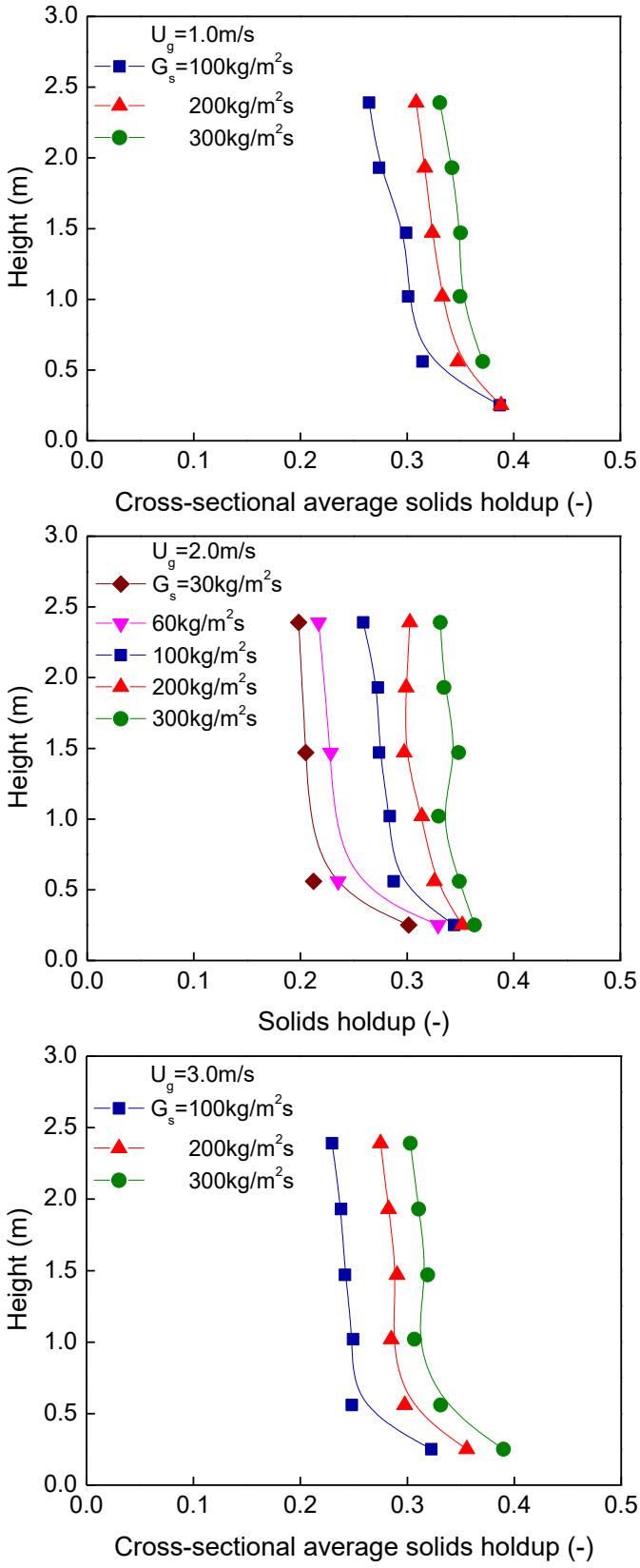

Figure 5.3 Axial profiles of solids holdup at various solids circulation rates in the CTFB

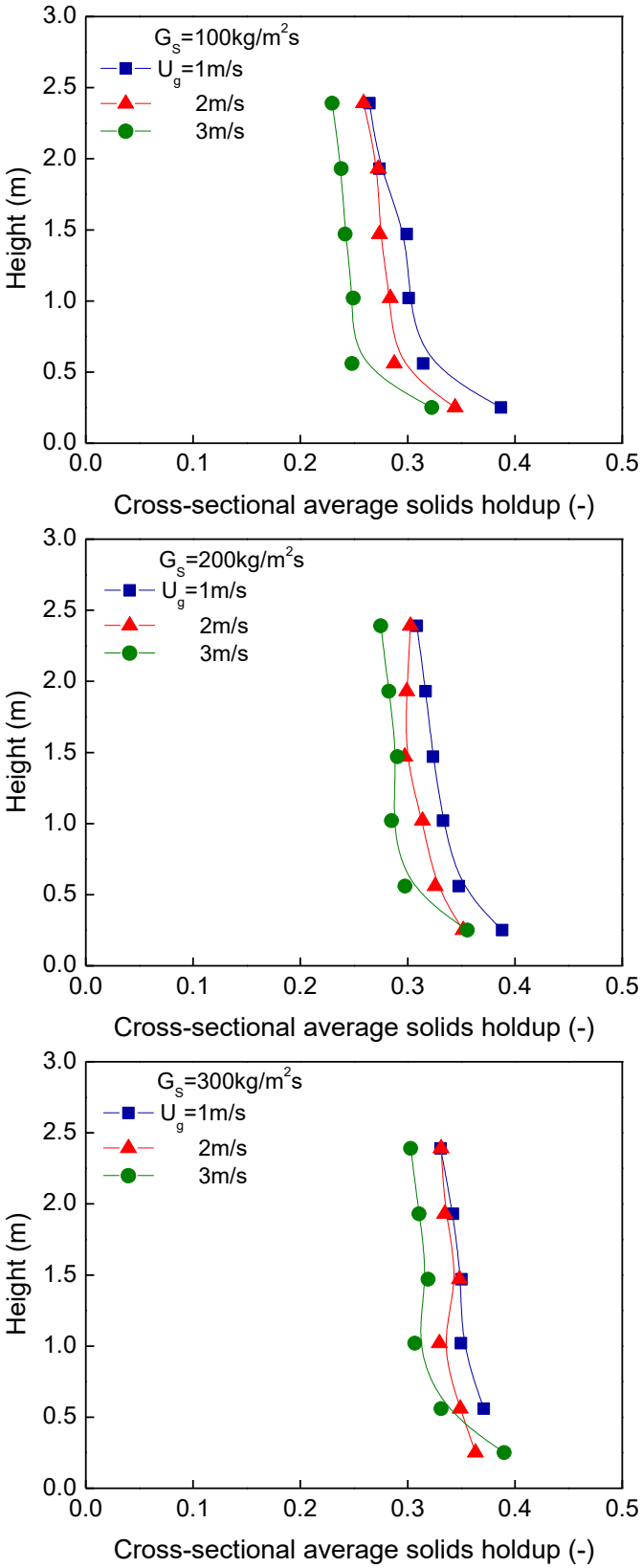

Figure 5.4 Axial profiles of solids holdup at various superficial gas velocities in the CTFB

5.3.3 Radial profiles of solids holdup

The radial profiles of solids holdup at various U_g and G_s were investigated as well. The effect of G_s on the radial profiles of solids holdup at H=1.5m, is shown in Figure 5.5. It is seen that the solids holdups keep increasing from the centre to the wall. For the conditions of $G_s \geq 100$ kg/m^{2}s, the solids holdups in the centre are higher than 0.1, which is a very high level for the fluidized beds with circulating operations. Also, the solids holdups increase with increasing G_s, corresponding to the trend shown in the axial profiles. By detailed observation, the profiles at different G_s display different shapes. For G_s=30 and 60 kg/m^{2}s, the solids holdups stay almost constant from r/R=0 to 0.548, then sharply increase near the wall, which is comparable to the core-annular structure in CFBs. For $G_s \geq 100$ kg/m^{2}s, the profiles show gradually ascending slopes towards the wall, denoting the merging of the dilute core region and the dense annulus region.

The radial profiles of solids holdup at different U_g and H=1.5m are illustrated in Figure 5.6. Basically, the solids holdups decrease as U_g increases, excluding the wall region (r/R≥0.837). The solids holdups in the wall region increase with U_g, possibly because the larger gas flowrate through the central region compresses more solids to the wall region. As a result, the radial gradient becomes increasingly steeper with U_g, showing a tendency in transforming to CFBs.

The development of solids holdup at three radial positions (r/R=0, 0.707 and 0.95) was studied at various U_g but the same G_s of 200 kg/m^{2}s, as shown in Figure 5.7. With U_g increasing, the largest reduction of solids holdup takes place in the centre, whereas the change near the wall (r/R=0.95) is less noticeable. Furthermore, the axial distributions of solids holdup in all radial positions are uniform as well, indicating that the radial gradient of solids holdup does not vary with elevation. In other words, the uniform flow pattern of CTFB fairly resembles a plug flow.

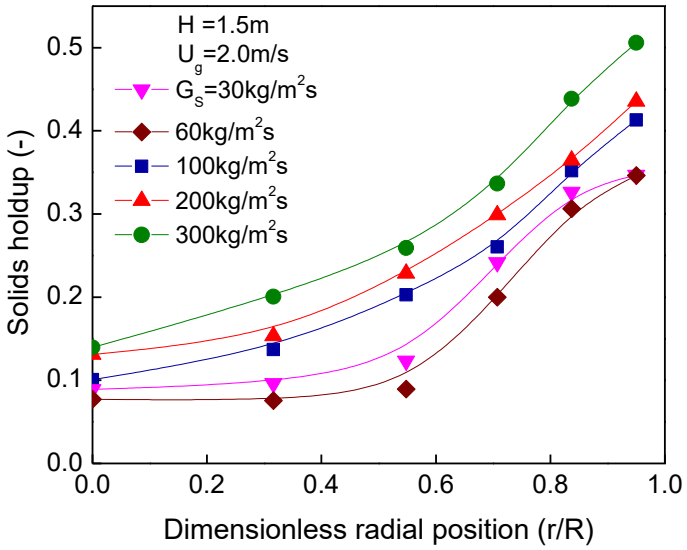

Figure 5.5 Radial profiles of solids holdup at various solids circulation rates in the CTFB

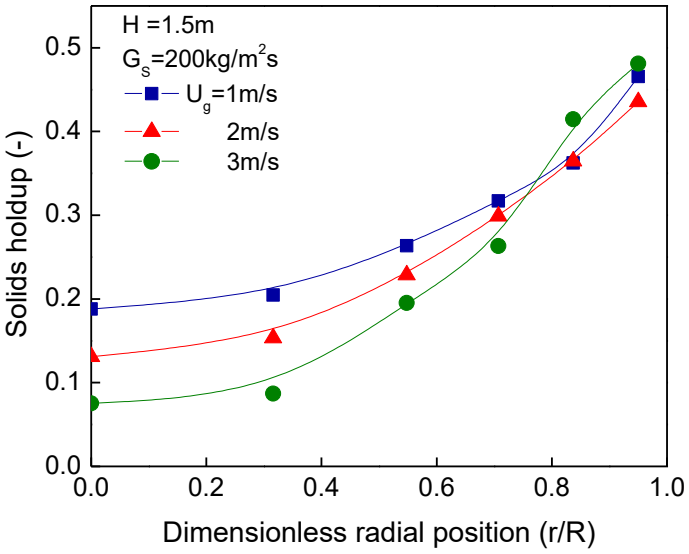

Figure 5.6 Radial profiles of solids holdup at various solids circulation rates in the CTFB

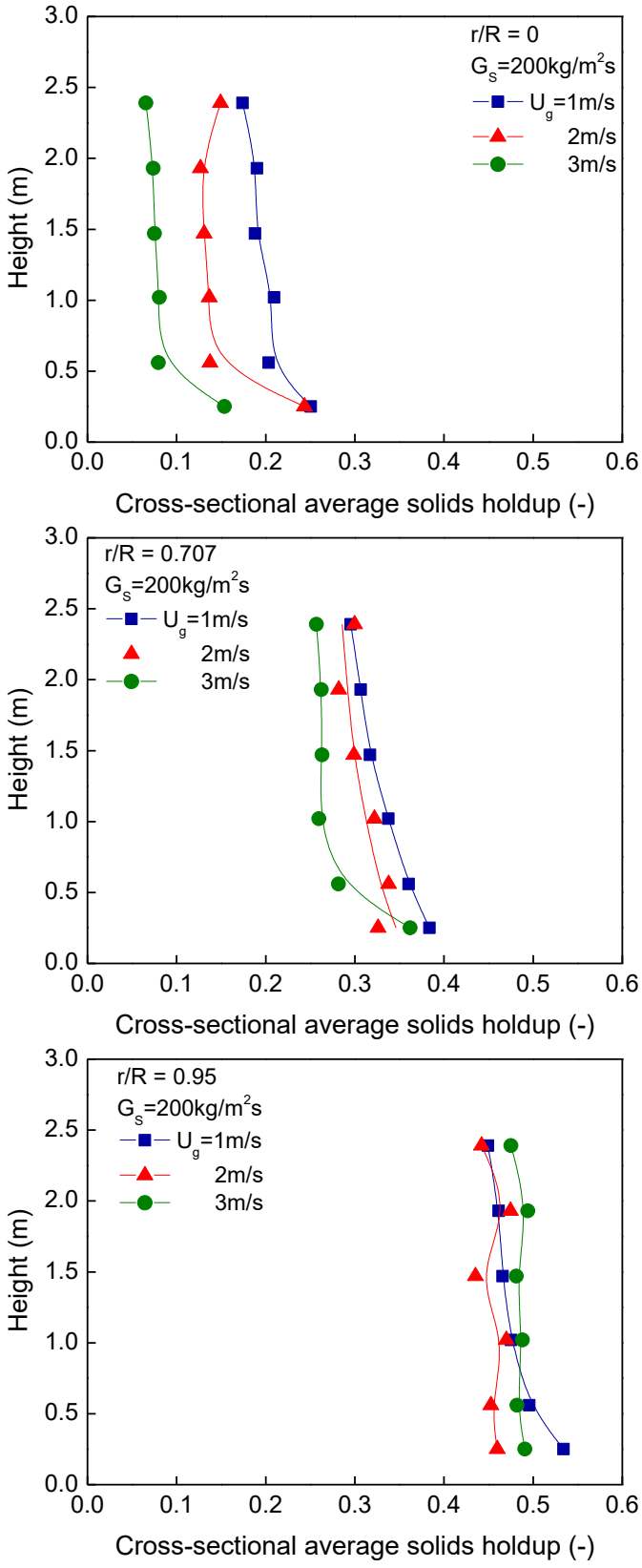

Figure 5.7 Axial profiles of solids holdup at different radial positions at various U_g in the CTFB

5.3.4 Flow fluctuations

The effect of operating conditions on solids holdup, standard deviation and intermittency index was studied, as presented in Figure 5.8. The results were acquired at the height of 1.9m. The radial profiles of standard deviations generally exhibit a convex parabolic shape with a maximum value appearing in the middle (r/R=0.548-0.707), as shown in Figure 5.8(b) and (e). This distribution indicates the most vigorous flow fluctuations occur in the middle region of the radius. Moreover, it is worth noting that U_g and G_s have different effects on the flow fluctuations. At U_g=2.0 m/s, the standard deviations do not vary with G_s significantly. However, at G_s=200 kg/m^{2}s, U_g of 1.0 m/s leads to the highest standard deviations among all the examined U_g, as shown in Figure 5.8(e). U_g of 2.0 m/s and 3.0 m/s have the maximum standard deviations in the middle region (r/R=0.548-0.707), which is different with the profile of 1.0 m/s.

Furthermore, flow fluctuations can be quantified by intermittency indexes of solids holdup proposed by Brereton and Grace (1993) for circulating fluidized beds. Higher intermittency index means more intense fluctuations. Besides, the level of segregation of gas and solids can be evaluated by the intermittency index. The value of the intermittency index equal to one suggests "perfect mixing", while the value is zero if there is "complete segregation", e.g. a bubble with no solids inside surrounded by a dense solids phase. The radial profiles of intermittency index in the CTFB show the similar trends as the profiles of standard deviations in Figure 5.8(c) and (f). By carefully observing, the intermittency indexes slightly increase with G_s. The result suggests that the increasing solids flux and solids holdup hardly intensify the fluctuations of the gas/solids flow, presumable due to the near "saturation" state. On the other hand, the increasing U_g evidently influences the intermittency indexes, which indicates the intensity of gas-solids interaction is effectively controlled by U_g in the CTFB.

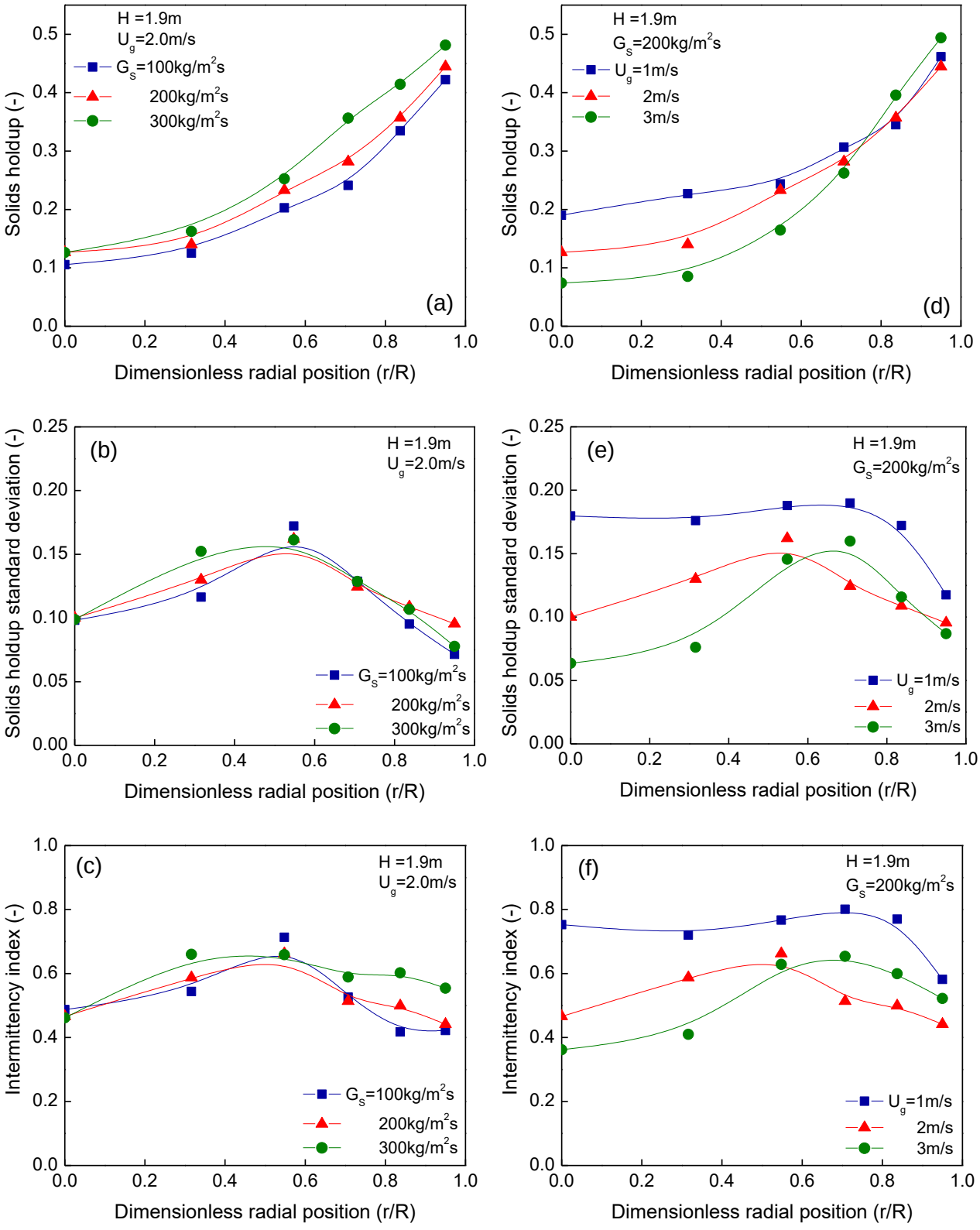

Figure 5.8 Effect of operating conditions on radial profiles of solids holdup, standard deviation and intermittency index

5.3.5 Effect of gas distributor

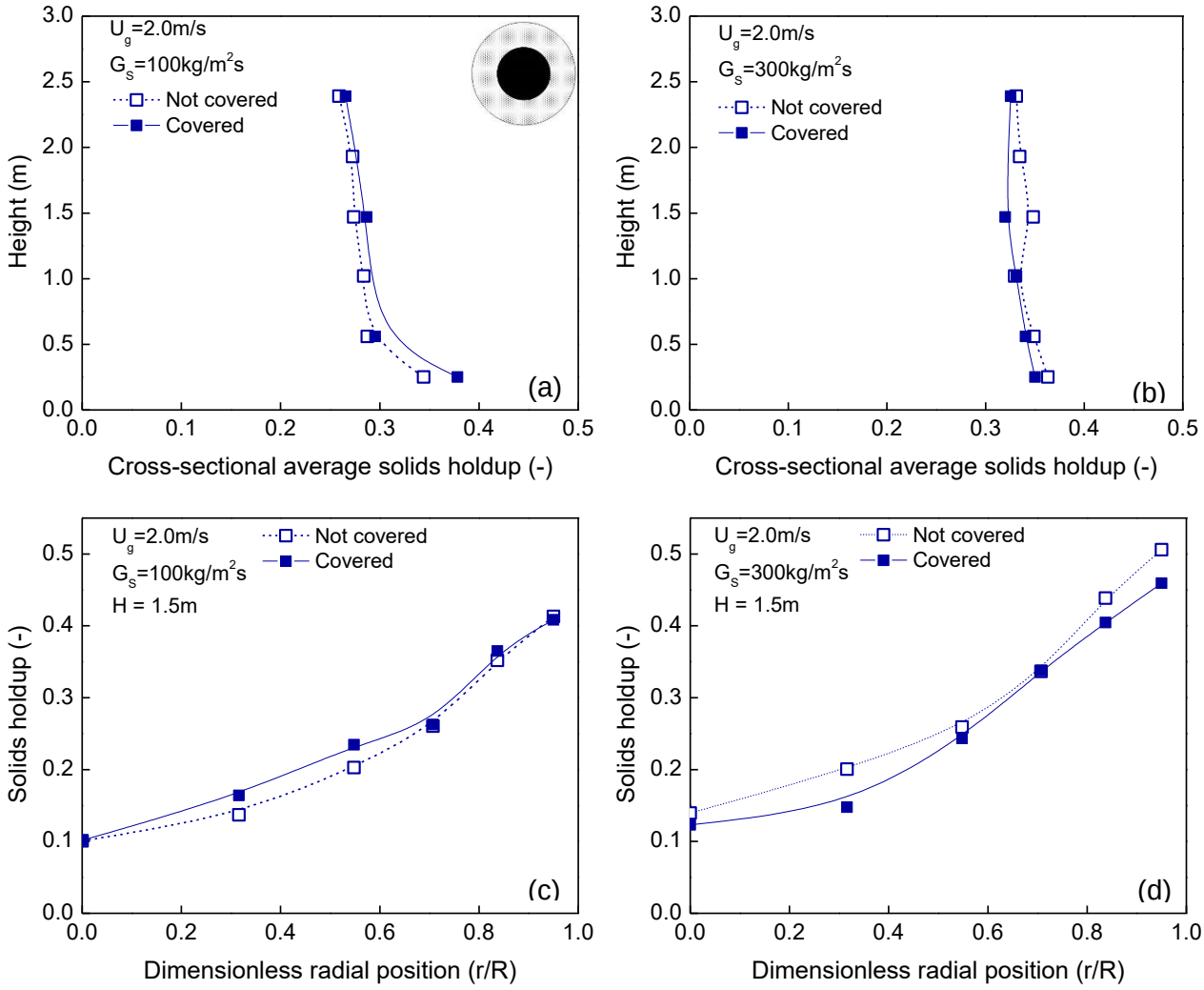

Figure 5.9 Effect of gas distributor on flow structure in the CTFB

The effect of the gas distributor was investigated by covering half of the area of the distributor in the centre, as shown in the upper-right corner of Figure 5.9(a). The results obtained under the conditions of U_g=2.0 m/s and G_s=100, 300 kg/m^{2}s are plotted as the axial and radial profiles in Figure 5.9. It is clearly shown that the flow structure remains almost the same before and after the covering. In other words, the gas distributor designs may have weak influence on the hydrodynamics of CTFB. Therefore, it can be concluded that the non-uniform radial flow structure is an inherent property of CTFB.

5.3.6 Comparison of TFB, CTFB and CFB

Axial profiles of solids holdup

In order to further understand the hydrodynamics of CTFB and highlight its advantages over other fluidized beds, comparisons were conducted among the CTFB, a TFB and a CFB in both macroscopic and microscopic scales. The three types of fluidized beds have the same bed diameter and use the same particles. The operating condition of CTFB is U_g=1.0 m/s and G_s=100 kg/m^{2}s. For the sake of comparison, the U_g of TFB is 1.0 m/s as well. The CFB is separated as low density CFB (LDCFB) and high density CFB (HDCFB) according to different G_s. The LDCFB and HDCFB were operated at U_g=7.0 m/s with G_s=100 kg/m^{2}s and 700 kg/m^{2}s respectively.

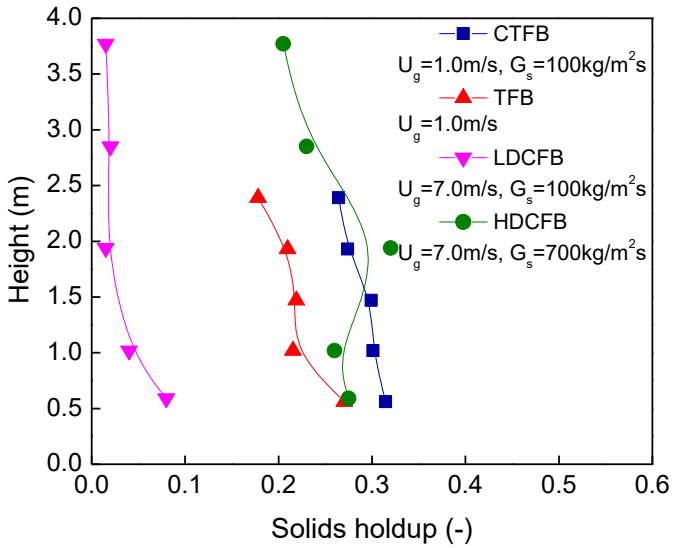

Figure 5.10 Axial profiles of solids holdup in the CTFB, TFB, LDCFB and HDCFB

The axial profiles of solids holdup in the CTFB, TFB, LDCFB and HDCFB are shown in Figure 5.10. Firstly, the CTFB exhibits significantly higher solids holdups (~0.3) than the CFB (<0.1), even though at the same G_s of 100 kg/m^{2}s. In spite of high gas throughput, the gas-solids contact efficiency of CFB is very limited due to the low solids holdup (Dry, Christensen et al. 1987). However, in the HDCFB bottom, it is found to have comparable solids holdups (~0.3) and uniform axial distribution as those in the CTFB. The result suggests that CTFB and HDCFB are two feasible approaches to achieve a highly dense suspension with uniform axial flow structure. Additionally, the TFB gives a similar trend, but lower solids holdups than the CTFB. It should be

noted that the solids holdup profile of TFB only describes the dense bed without the freeboard at a high static bed height (H_0=1.9m). Therefore, the CTFB differs from the TFB in respect of time-mean results.

Radial profiles of solids holdup and flow fluctuation

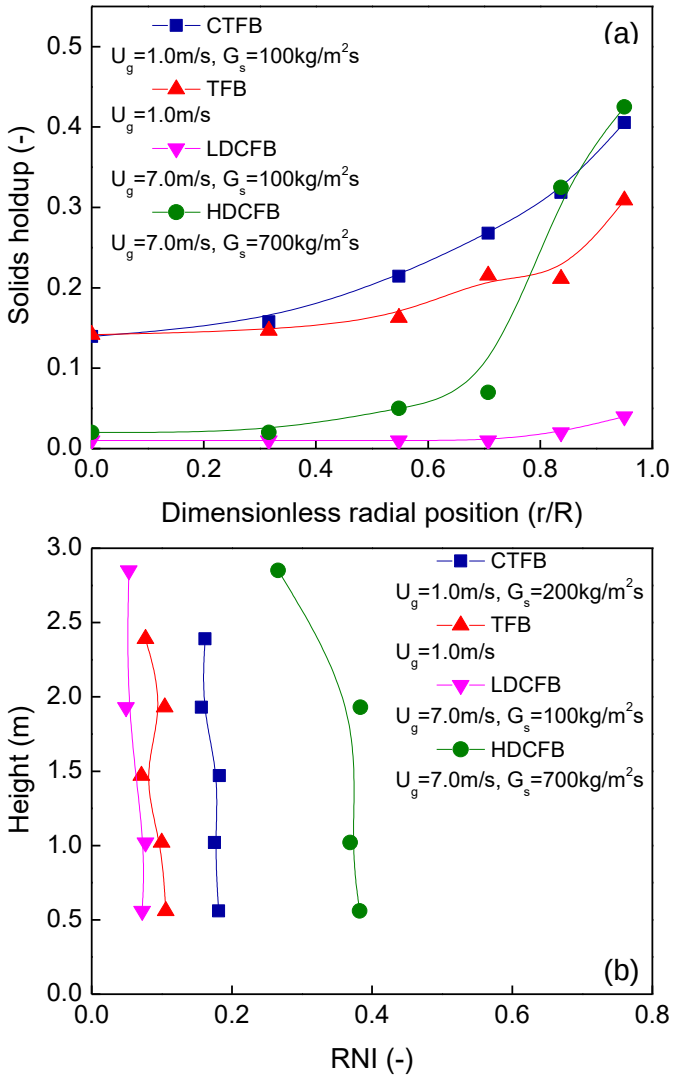

Figure 5.11 Radial profiles of solids holdup and radial non-uniformity index (RNI) in the CTFB, TFB, CFB and HDCFB

The radial profiles of solids holdup in the CTFB, TFB, LDCFB and HDCFB on the same elevation (H=1.9m) and same aforementioned operating conditions are displayed in Figure 5.11(a). It is found that all fluidized beds show monotonically increasing profiles from the centre to the wall. The LDCFB has a uniform radial profile due to the extremely low solids holdups. The HDCFB exhibits more serious radial non-uniformity with an obvious core-annulus structure,

when compared with the CTFB and TFB. In the TFB and CTFB, the solids holdup in the central region is over 0.1, much higher than that in the HDCFB, which is able to effectively improve the heat/mass transfer efficiency and the gas-solids contact efficiency of the entire beds. In addition, the high solids holdup and high solids flux in the CTFB likely make higher effective viscosity of gas-solids suspension (Grace, Issangya et al. 1999), thereby causing strong shear on the descending particles and reducing the probability of solids downflow.

The non-uniformity of solids holdup radial distribution can be quantified by radial non-uniformity indexes (RNI) (Zhu and Manyele 2001). The RNI is defined for each given parameter as the standard deviation of its values in the radial direction, normalized by the maximum possible standard deviation for the same parameter with the same cross-sectional average value. The higher RNI, the less uniform distribution is. The RNIs of solids holdup were calculated at each elevation in the TFB, CTFB, LDCFB and HDCFB, as displayed in Figure 5.11(b). The HDCFB shows the highest RNIs, i.e., most non-uniform radial distributions, because the increased solids holdup mainly contributes to the formation of large clusters near the wall (Wang, Zhu et al. 2014a). The magnitude of RNI in the HDCFB decreases with increasing elevation due to the flow development. On the contrary, the LDCFB has the lowest RNIs resulting from the lower solids holdup in the entire cross section. For the TFB and CTFB, they both exhibit relatively low RNIs, indicating uniform radial distributions of solids holdup. And the uniform flow structure persists along the axial direction, therefore leading to uniform radial distribution of gas and solids residence time. Furthermore, the RNIs of CTFB are slightly higher than those of TFB, likely due to the higher U_g and G_s.

More differences among these fluidized beds can be seen in the profiles of standard deviation of solids holdup, shown in Figure 5.12(a). The standard deviation profile of LDCFB shows a steady core region and a fluctuating annular region, corresponding to its solids holdup profile. In the HDCFB, however, a maximum value is found in the middle region (r/R=0.707), but then the standard deviation sharply drops towards the wall. Moreover, the profiles of TFB and CTFB are at the similar level (H≈1.0m), showing the relatively uniform distributions. Although the standard deviation profile of CTFB also shows a convex parabolic shape like that of the HDCFB to some extent, the values in the central and wall regions are largely increased. This feature indicates that the CTFB has intense gas-solids interaction on the whole cross-section.

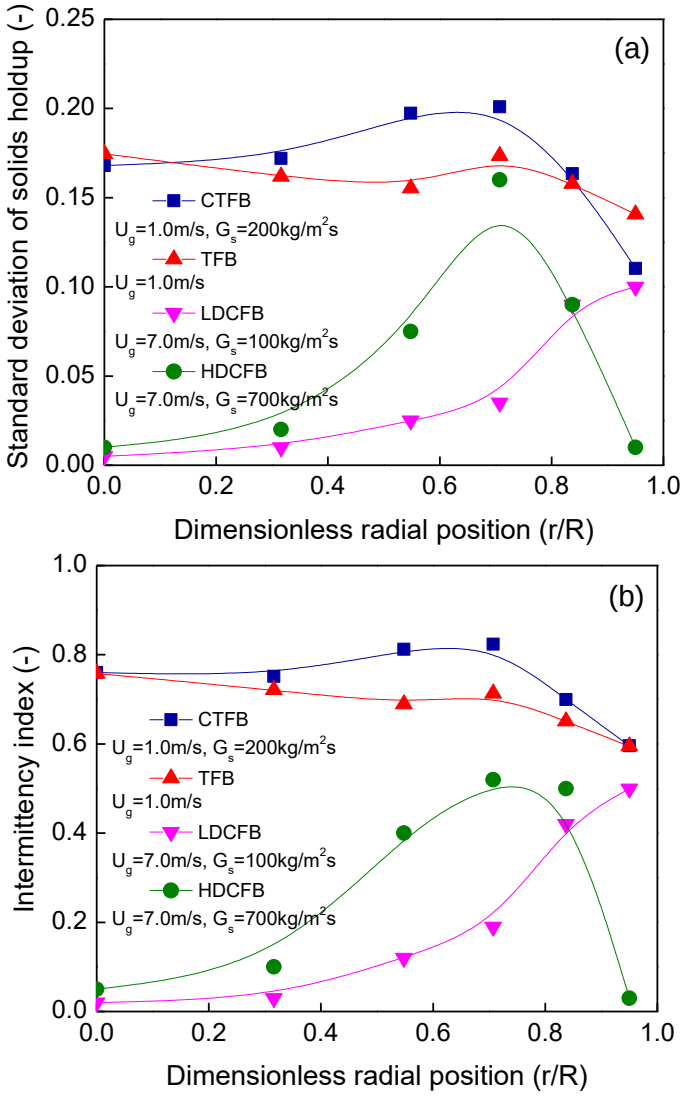

Figure 5.12 Radial profiles of standard deviation of solids holdup and intermittency index in the CTFB, TFB, CFB and HDCFB

As shown in Figure 5.12(b), both LDCFB and HDCFB have a non-uniform radial profile of intermittency index determined by their heterogeneous flow structure. Besides, the intermittency indexes of LDCFB and HDCFB are generally lower than those of the TFB and CTFB, which demonstrates the extent of gas-solids segregation is greater in the CFBs. As a consequence, gas and solids have lower chance to contact and react in the CFBs, further resulting in weak reactor performance (Wang, Zhu et al. 2015). The CTFB shows even higher intermittency indexes than the TFB, indicating more intense flow fluctuation and two-phase interaction. The vigorous gas-solids interaction can improve the reactor performance by means of increasing gas-solids contact efficiency.

Instantaneous solids holdups

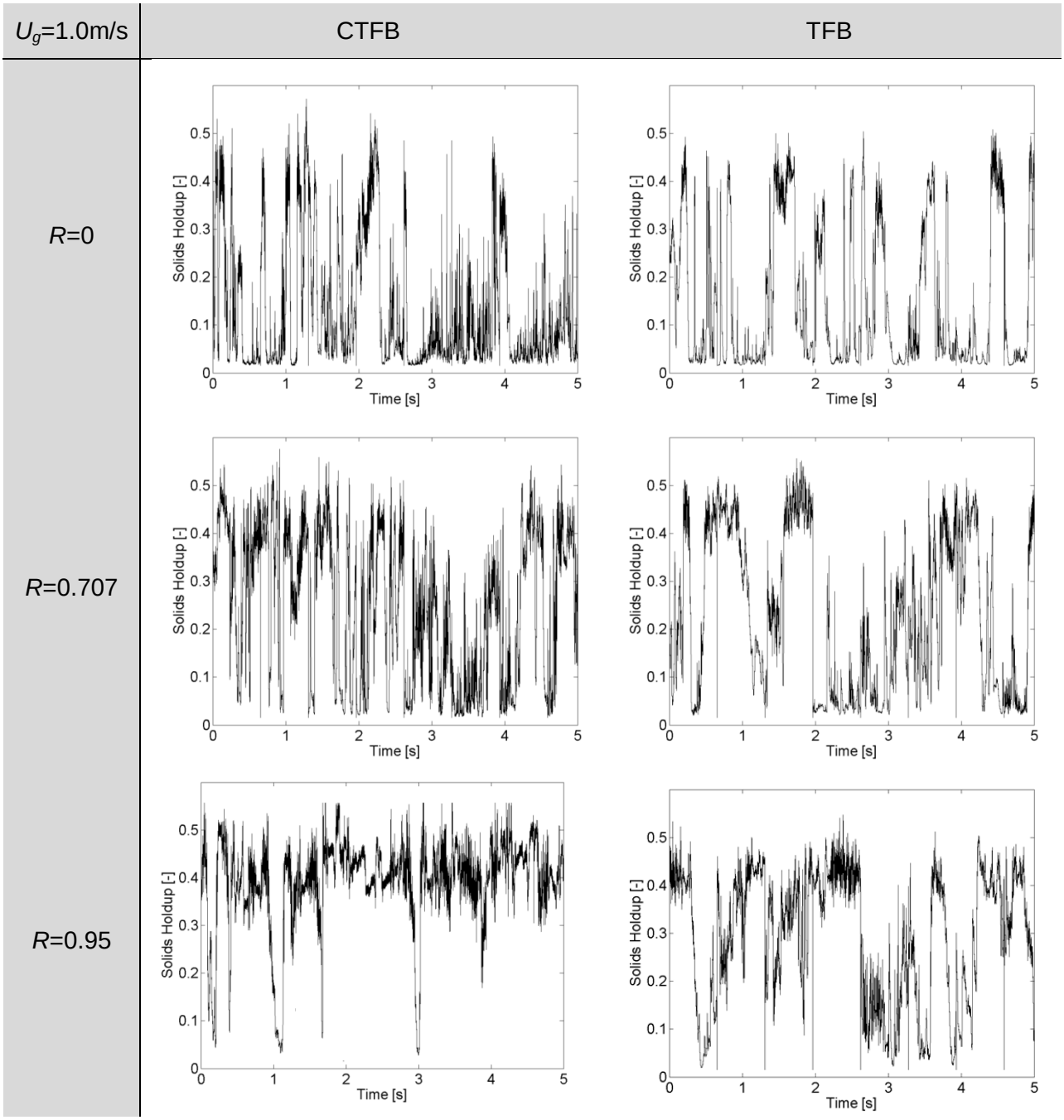

Figure 5.13 Comparison of instantaneous solids holdup signals in the CTFB and TFB

As discussed above, the time-mean results of CTFB, such as average solids holdup, standard deviation and intermittency index, show similar values with those in the TFB. Further study of instantaneous solids holdup signals and the fluctuations reflects the difference between the CTFB and the TFB. Figure 5.13 displays the instantaneous solids holdup signals at different radial positions in the TFB and CTFB. The results were obtained in the same column (76mm i.d.) and at the same superficial gas velocity (U_g=1.0 m/s).

Both CTFB and TFB show numerous peaks with various heights and width at *r/R*=0, indicating a flow structure having a turbulent cluster phase competing with a dilute void phase. In detail, the signal fluctuations in the CTFB are more frequent and intense at *r/R*=0, which becomes more remarkable at *r/R*=0.707. This demonstrates that the cluster phase and the void phase in the CTFB are more homogeneous than those in the TFB, which is favourable to mass transfer between the gas phase and the solid phase. In the wall region (*r/R*=0.95), the average solids holdup of CTFB is higher than that of TFB, suggesting less gas enters the dense wall region. Overall, the CTFB can be distinguished from the TFB in regard of the microscopic flow behaviour.

5.4 Conclusions

A gas/solids upflow with solids circulation rate as high as 300 kg/m^{2}s while maintaining high solids holdup ranging from 0.25 to 0.35 was successfully achieved in the CTFB. CTFB's unique operation of low U_g and high G_s is in favour of the reactions requiring higher solids/gas feed ratio, higher gas-solids contact efficiency and relatively longer residence time. The CTFB shows extremely uniform flow structure in the axial direction under all operating conditions. In contrast, a radial gradient of solids holdup is found to increase from the centre to the wall at each elevation, which is likely attributed to the high solids circulation rate. Nevertheless, the radial non-uniformity is significantly mitigated by the increased solids holdups in the central region, when compared with CFBs. Moreover, the operating conditions affect the flow structure in the CTFB. The solids holdup increases with increasing G_s, but with decreasing U_g. In addition, the configuration of gas distributor does not influence the flow structure, suggesting the aforementioned flow structure is an inherent characteristic.

The flow fluctuations and two-phase interactions were studied in terms of standard deviations of solids holdup and intermittency indexes. The CTFB has intense fluctuations in the whole cross-section at each elevation, which is comparable to a TFB but stronger than a LDCFB and a HDCFB. By analyzing the instantaneous solids holdup signals of the CTFB and TFB, the CTFB has more homogeneously inter-diffused dilute and dense phases, which is an important feature to distinguish CTFB from TFB. Taking all the favourable hydrodynamics into account, The CTFB exhibits high gas-solids contact efficiency and heat/mass transfer efficiency, which are advantageous in reactor performance.

Nomenclature

G_s	solids circulation rate [kg/m^{2}s]
H	axial coordinate, or distance from the gas distributor [m]
H_0	static bed height [m]
r	radial coordinate [m]
R	column radius [m]
r/R	dimensionless radial sampling position [-]
U_g	superficial gas velocity [m/s]

Greek letters

ε_s	local solids holdup [-]
$\overline{\varepsilon_s}$	mean solids holdup [-]
ρ_p	particle density [kg/m^3]

References

Bi, H., N. Ellis, I. Abba and J. Grace (2000). A state-of-the-art review of gas–solid turbulent fluidization. *Chemical Engineering Science* **55**(21): 4789-4825.

Bi, H., J. Grace and K. Lim (1995). Transition from bubbling to turbulent fluidization. *Industrial & Engineering Chemistry research* **34**(11): 4003-4008.

Bi, H. and J. Zhu (1993). Static instability analysis of circulating fluidized beds and concept of high-density risers. *AIChE Journal* **39**(8): 1272-1280.

Brereton, C. and J. Grace (1993). Microstructural aspects of the behaviour of circulating fluidized beds. *Chemical Engineering Science* **48**(14): 2565-2572.

Dry, R., I. Christensen and C. White (1987). Gas—solids contact efficiency in a high-velocity fluidised bed. *Powder Technology* **52**(3): 243-250.

Grace, J. (1990). "High-velocity fluidized bed reactors." *Chemical Engineering Science* **45**(8): 1953-1966.

Grace, J. R. (2000). Reflections on turbulent fluidization and dense suspension upflow. *Powder Technology* **113**(3): 242-248.

Grace, J. R. and H. Bi (1997). Introduction to circulating fluidized beds. *Circulating Fluidized Beds*, Springer**:** 1-20.

Issangya, A., D. Bai, H. Bi, K. Lim, J. Zhu and J. Grace (1999). Suspension densities in a high-density circulating fluidized bed riser. *Chemical Engineering Science* **54**(22): 5451-5460.

Lim, K., J. Zhu and J. Grace (1995). Hydrodynamics of gas-solid fluidization. *International Journal of Multiphase Flow* **21**: 141-193.

Pärssinen, J. and J. X. Zhu (2001). Axial and radial solids distribution in a long and high-flux CFB riser. *AIChE Journal* **47**(10): 2197-2205.

Qi, M., S. Barghi and J. Zhu (2012). Detailed hydrodynamics of high flux gas–solid flow in a circulating turbulent fluidized bed. *Chemical Engineering Journal* **209**: 633-644.

Qi, M., J. Zhu and S. Barghi (2012). Particle velocity and flux distribution in a high solids concentration circulating turbulent fluidized bed. *Chemical Engineering Science* **84**: 437-448.

Qi, X., H. Zhu and J. Zhu (2009). Demarcation of a new circulating turbulent fluidization regime. *AIChE Journal* **55**(3): 594-611.

Wang, C., G. Wang, C. Li, S. Barghi and J. Zhu (2014). Catalytic ozone decomposition in a high density circulating fluidized bed riser. *Industrial & Engineering Chemistry Research* **53**(16): 6613-6623.

Wang, C., J. Zhu and S. Barghi (2015). Performance evaluation of high density riser and downer: Experimental study using ozone decomposition. *Chemical Engineering Journal* **262**: 478-489.

Wang, C., J. Zhu, S. Barghi and C. Li (2014a). Axial and radial development of solids holdup in a high flux/density gas–solids circulating fluidized bed. *Chemical Engineering Science* **108**: 233-243.

Wang, C., J. Zhu, C. Li and S. Barghi (2014b). Detailed measurements of particle velocity and solids flux in a high density circulating fluidized bed riser. *Chemical Engineering Science* **114**: 9-20.

Zhu, H. and J. Zhu (2008a). Gas‐solids flow structures in a novel circulating‐turbulent fluidized bed. *AIChE Journal* **54**(5): 1213-1223.

Zhu, H. and J. Zhu (2008b). Comparative study of flow structures in a circulating-turbulent fluidized bed. *Chemical Engineering Science* **63**(11): 2920-2927.

Zhu, J. X. and H. T. Bi (1995). Distinctions between low density and high density circulating fluidized beds. *The Canadian Journal of Chemical Engineering* **73**(5): 644-649.

Zhu, J. X. J. and S. V. Manyele (2001). Radial nonuniformity index (RNI) in fluidized beds and other multiphase flow systems. *The Canadian Journal of Chemical Engineering* **79**(2): 203-213.

Chapter 6
Reactor performances of low-velocity gas-solids fluidized beds

6.1. Introduction

Gas-solids fluidization can be typically divided into several regimes: particulate fluidization, bubbling (slugging) fluidization, turbulent fluidization, fast (circulating) fluidization, dense suspension upflow and pneumatic transport (Lim, Zhu et al. 1995, Grace 2000). It is commonly accepted that bubbling fluidized beds (BFBs) and turbulent fluidized beds (TFBs) are classified as low-velocity fluidized beds due to the low fluidizing gas velocities (approx. < 2.0 m/s) and high solids holdups (approx. > 0.25), when compared with circulating fluidized beds (CFBs). The hydrodynamics of low-velocity fluidized beds have been extensively studied so far (Lim, Zhu et al. 1995, Bi, Ellis et al. 2000, Grace 2000). However, their reactor performances, especially TFBs, have received much less attention, which hampers modelling development, reactor design, process optimization, etc. As a consequence, designs of commercial fluidized-bed reactors are still mostly based on empirical equations and engineers' experiences (Knowlton, Karri et al. 2005).

Experimental studies with conducting chemical reactions in fluidized beds, also called "hot-model" studies, can reflect reactor performances more directly than other methods. Several reactions were employed as the model reactions to investigate the reactor performances of BFB and TFB, such as NOx decomposition (Shen and Johnstone 1955), ethylene hydrogenation (Lewis, Gilliland et al. 1959), catalytic ammonia oxidation (Massimilla and Johnstone 1961), and catalytic ozone decomposition (Frye, Lake et al. 1958, Chavarie and Grace 1975, Frye and Potter 1976, Lin, Arastoopour et al. 1986, Sun and Grace 1990, Van Lare, Piepers et al. 1990). The catalytic decomposition of ozone was most frequently used to study the reactor performances of not only BFBs and TFBs, but CFBs as well, due to its advantages in lab-scale research. Firstly, ozone can decompose to oxygen in the ambient temperature and pressure by the catalytic effect of some metallic oxides, like ferric oxide. Secondly, since ozone decomposition is a simple and a first-order reaction, the conversions are independent of initial reactant concentrations. Additionally, the reaction has negligible heat effect under a dilute concentration condition, as well as being non-toxic to the catalysts.

For catalytic gas-phase reactions in fluidized beds, the distributions of reactant conversion were found to be closely related to the flow structures (Ouyang, Li et al. 1995, Wang, Zhu et al. 2015), because the hydrodynamics can directly influence gas-solids contacting and mass transfer. In BFBs, the majority of fluidizing gas flows through the particulate bed in the form of bubbles. These bubbles have a low solids concentration inside and a relatively clear boundary with the surrounding dense solid phase, resulting in low gas-solids contact efficiency inside bubbles and high mass transfer resistance between the bubble phase and the solid phase (Chavarie and Grace 1975). In TFBs, voids with smaller sizes prevails instead of bubbles, while splitting and coalescing extensively (Bi, Grace et al. 1995). Also, the chaotic void phase is inter-dispersed with the comparable solid phase (Matsen 1997). Such dynamic flow characteristics lead to vigorous gas-solids interaction, as well as intense heat and mass transfer. This reactor feature was experimentally confirmed by Sun and Grace (1990) based on outlet reaction conversions, but no conversion spatial distribution was provided in TFBs.

The objective of this work is to study the reactor performances of BFBs and TFBs using catalytic ozone decomposition. Detailed measurement of local ozone concentrations has been conducted to depict the complete conversion mappings of the entire bed, which is necessary to comprehensively understand the reactor performances of BFBs and TFBs. The gas-solids contact efficiency is used to evaluate the reactor performances. In addition, the effects of static bed height and bed diameter on reactor performances are investigated as well.

6.2. Experimental setup

Fluidized beds setup

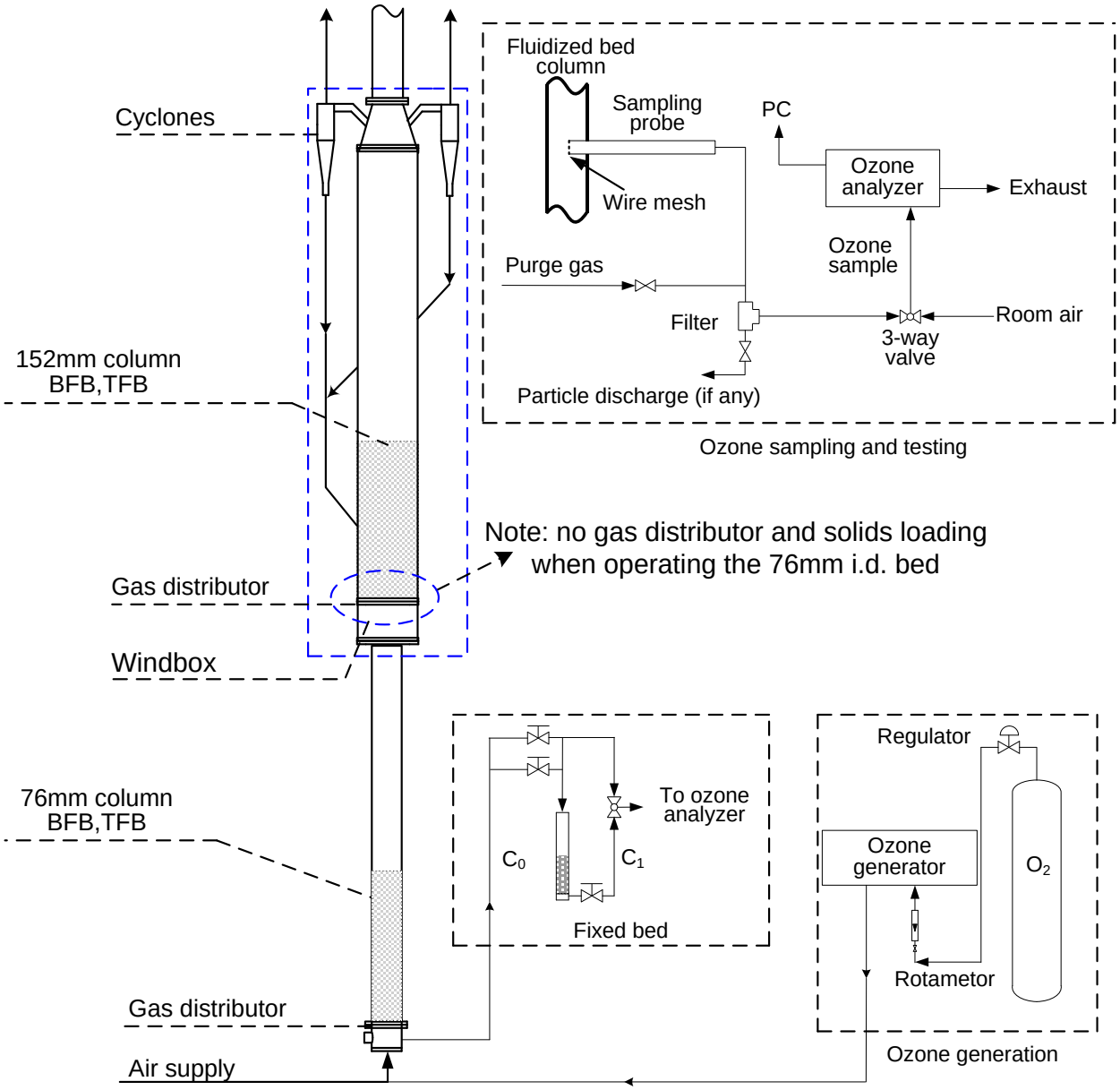

Figure 6.1 Schematic diagrams of BFBs and TFBs and ozone testing system

Each of BFBs and TFBs was respectively operated in either the 76mm i.d. column or the 152mm i.d. column of a multifunctional fluidized-bed system. As shown in Figure 6.1, the bottom column is 76mm i.d. and 3.0m in height, installed with a gas distributor made of perforated plates (2mm i.d. hole × 176, 12% opening area). There was no gas distributor and solids loading

in the middle column, when operating the bottom bed. Therefore, the upper 152mm i.d. column is able to greatly reduce particle velocity, so that the entrained solids can be returned due to loss of velocity. The experiments were performed by loading certain amounts (1.0m and 1.9m static bed height) of particles into the column and introducing fluidizing gas at the velocities of 0.3 m/s-1.2 m/s through the distributor.

The upper column is 152mm i.d. and 3.0m in length. Another perforated-plate gas distributor was installed at its bottom after finishing experiments in the 76mm i.d. column. Additionally, two cyclones were employed in parallel to recycle entrained solids. The amounts of loaded particles were equivalent to the static bed height of 0.79m and 1.0m. The fluidizing gas was introduced from the bottom column in the range of 0.1 m/s to 1.0 m/s.

The multifunctional fluidized-bed system is mainly made of aluminium to avoid the oxidization of ozone, since an inert aluminium oxide layer is formed inside the column. In order to prevent electrostatic charges accumulation, the entire system is grounded.

Measurement of solids holdup

The local solids holdups were measured by an optical fibre probe system (Model: PV6D) that was manufactured by the Institute of Processing Engineering, Chinese Academy of Science, Beijing, China. The diameter of the probe is 3.8mm with a bundle of fibres whose cross-section is a square of $2\times2mm^2$ placed in the centre. The fibre bundle consists of 8000 quartz fibres each with a diameter of $15\mu m$. Half of the quartz fibres are emitting fibres and the others are receiving fibres. They are arranged alternatively. A Plexiglas pad of 0.2mm thickness is covered the probe tip in order to prevent particles from occupying the blind zone (Liu, Grace et al. 2003). By illuminating a small area and measuring the intensity of light reflected by passing particles, the optical fibre probe can correlate local solids holdups with the corresponding voltage signals converted from the light intensity. More particles can reflect more light, i.e., higher light intensity, resulting in higher voltage. The correlation equation between solids holdups and voltage signals requires calibrations. A proper calibration method developed by Zhang, Johnston et al. (1998) was adopted.

Instantaneous local solids holdup $\varepsilon_s(t)$ can be obtained by the calibration equation with voltage data $V(t)$:

$$\varepsilon_s(t) = f\left[V(t)\right] \quad \text{Eq. 6.1}$$

where f is the calibration function.

Time-mean solids holdup ε_s can be calculated by integrating $\varepsilon_s(t)$ over a time span T:

$$\varepsilon_s = \frac{1}{T}\int_0^T \varepsilon_s(t)dt \quad \text{Eq. 6.2}$$

Cross-sectional average solids holdup $\bar{\varepsilon}_s$ can be calculated by integrating ε_s over the cross-sectional area of reactor:

$$\bar{\varepsilon}_s = \frac{1}{\pi R^2}\int_0^R 2\pi r\varepsilon_s \mathrm{d}r = \frac{2}{R^2}\int_0^R \varepsilon_s r\mathrm{d}r \quad \text{Eq. 6.3}$$

At each measuring point, 20 groups of data were collected in order to ensure accuracy and repeatability. Each group had 32,768 data points with detecting frequency of 50kHz.

Ozone generation and testing

An electronic corona discharge ozone generator (Model AE15M, manufactured by Absolute Ozone Inc.) was applied to generate ozone using bottled oxygen as the gas supply in this work. The O_2-O_3 mixture gas produced by the ozone generator was mixed into the primary fluidizing air before entering the fluidized beds, shown in Figure 6.1. After passing a fairly long path and several L-bends in the primary air feeding pipeline, ozone was considered to be mixed thoroughly. The ozone generator's potentiometer setting was fixed and the primary air flowrate was constant in each experimental run, thus the initial ozone concentrations in the fluidizing air can be adjusted effectively by a rotameter in the oxygen supply stream.

In order to prevent ozone decomposing in the sampling process, ozone-inert materials were adopted, e.g. aluminium, brass, stainless steel and Teflon. Although aluminium and brass would be oxidized by ozone, an inert oxide layer can form quickly. The schematic diagram of the ozone sampling system is shown in the upper-right corner of Figure 6.1. Brass tubes (6mm o.d.,

0.36mm wall thickness and 15.0cm length) were inserted horizontally into the column as sampling probes. The tip of the sampling probe is covered with stainless wire mesh to prevent particles leaking to the ozone analyser. There is a vacuum pump inside the ozone analyser to withdraw sample gas continuously. The sampling gas velocity is up to 1.5LPM, low enough to assure minimal disturbance to the gas/solids flow. High pressure purging air of 689.5kPa was used to clean the particle cake possibly formed on the probe tip before every sampling.

An ozone analyser (Model 49i, Thermo Electron Inc.) based on the UV photometric method was used to measure ozone concentrations in the sample gas. The UV light source used in ozone photometers is 253.7nm from a low-pressure Hg discharge lamp. At this wavelength, the absorptivity of ozone is very close to unity and with little interference from other gases (Seinfeld and Pandis 2006). The analyser is a dual-cell photometer, having both sample and reference air flowing at the same time, with the internal surfaces coated with polyvinylidine fluoride (PVDF) to ensure that ozone undergoes no decomposition during testing. A single test lasted 1min and generated 15 data points. Three tests were required at each measuring position.

Preparation of catalysts

Ozone decomposes very slowly at room temperature (20℃) in the absence of catalysts or ultraviolet (Wojtowicz 2005), and the gas residence time is only up to 10s in this study, so catalysts are necessary. It can be assumed that ozone decomposes only when contacting with catalysts.

Ferric oxide was usually used as the catalyst in the previous ozone decomposition research (Jiang, Bi et al. 1991, Ouyang, Li et al. 1995, Wang, Wang et al. 2014), as well as being used in this study. FCC particles (Geldart Group A particles) were chosen as the catalyst carrier due to the wide applications. The FCC particles were first impregnated in a 40wt% $Fe(NO_3)_3$ solution for 12 h, and then the wet particles were dried at 120^{o}C for 6 h in an oven followed by calcination at 450^{o}C for 4 h. After calcination, ferric nitrate converted to ferric oxide loaded on the particles. A ball mill was used to break up the agglomerates formed during calcination. The particles processed by the ball mill were sifted using a sieve with pore opening of 250μm. The impregnated particles were blended with the original FCC particles which have negligible

catalytic activity, in order to adjust the overall catalytic activity. The particle information is shown in Table 6.1.

Table 6.1 Particle information

Apparent density [kg/m^3]	1780	Bulk density [kg/m^3]	890
d[4,3], [*μm*]	106.3	*d*[3,2], [*μm*]	78.6
Particle size distribution (Vol.%)			
Diameter [*μm*]	Vol.%	Diameter [*μm*]	Vol.%
11.11 - 17.05	0.81	105.24 - 117.13	8.78
17.05 - 23.51	1.32	117.13 - 130.37	8.82
23.51 - 32.41	2.64	130.37 - 145.10	8.34
32.41 - 44.69	5.2	145.10 - 161.5	7.27
44.69 - 55.36	5.88	161.5 - 179.75	5.75
55.36 - 68.58	8.75	179.75 - 200.06	4.02
68.58 - 84.96	12.32	200.06 - 222.66	2.43
84.96 - 94.56	7.53	222.66 - 247.83	1.22
94.56 - 105.24	8.29	247.83 - 307.00	0.63

Frye, Lake et al. (1958) reported that the apparent reaction rate constants k_r of a first order reactions can be determined in a small integral reactor (a fixed-bed reactor) by the equation below, if it runs as a plug-flow reactor isothermally with minimal transport gradients.

$$k_r = \frac{Q_g \rho_p}{m_c} \ln \frac{C_{in}}{C_{out}} \qquad \text{Eq. 6.4}$$

where Q_g is the volumetric gas flowrate (m^3/s), ρ_p is the particle density (kg/m^3), and m_c is the mass of catalyst (kg). Therefore, a small fixed-bed reactor (16mm i.d.) made of brass pipe was used to measure the reaction rate constant k_r, as shown in Figure 6.1. A humidity meter and a thermometer were used to monitor the relative humidity and temperature of the air supply respectively. The relative humidity was maintained at 19%, and the temperature remained at 20℃ without significant fluctuation. Therefore, the moisture and temperature would not

influence the reaction rate in the experiments. The k_r of the catalysts in the experiments was 4.2 s^{-1}. The reaction rate constant was tested after every experimental run, showing no obvious variance.

Measuring positions

In order to map the entire column's solids holdup and conversion distributions, several sampling ports were opened at different elevations and 6 radial measuring positions were selected on each axial level (listed in Table 6.2). The optical fibre probes and ozone sampling probes shared these sampling ports.

Table 6.2 Axial and radial sampling locations of the fluidized beds

	Distance from gas distributor [m]	
Port No.	76mm i.d. column	152mm i.d. column
1	0.25	0.22
2	0.56	0.53
3	1.02	0.79
4	1.47	1.04
5	1.93	1.30
6	2.39	1.55
7		1.80
8		2.34

Radial sampling locations, r/R [-]					
0	0.316	0.548	0.707	0.837	0.950

6.3. Results and discussion

6.3.1. Axial profiles of ozone concentration

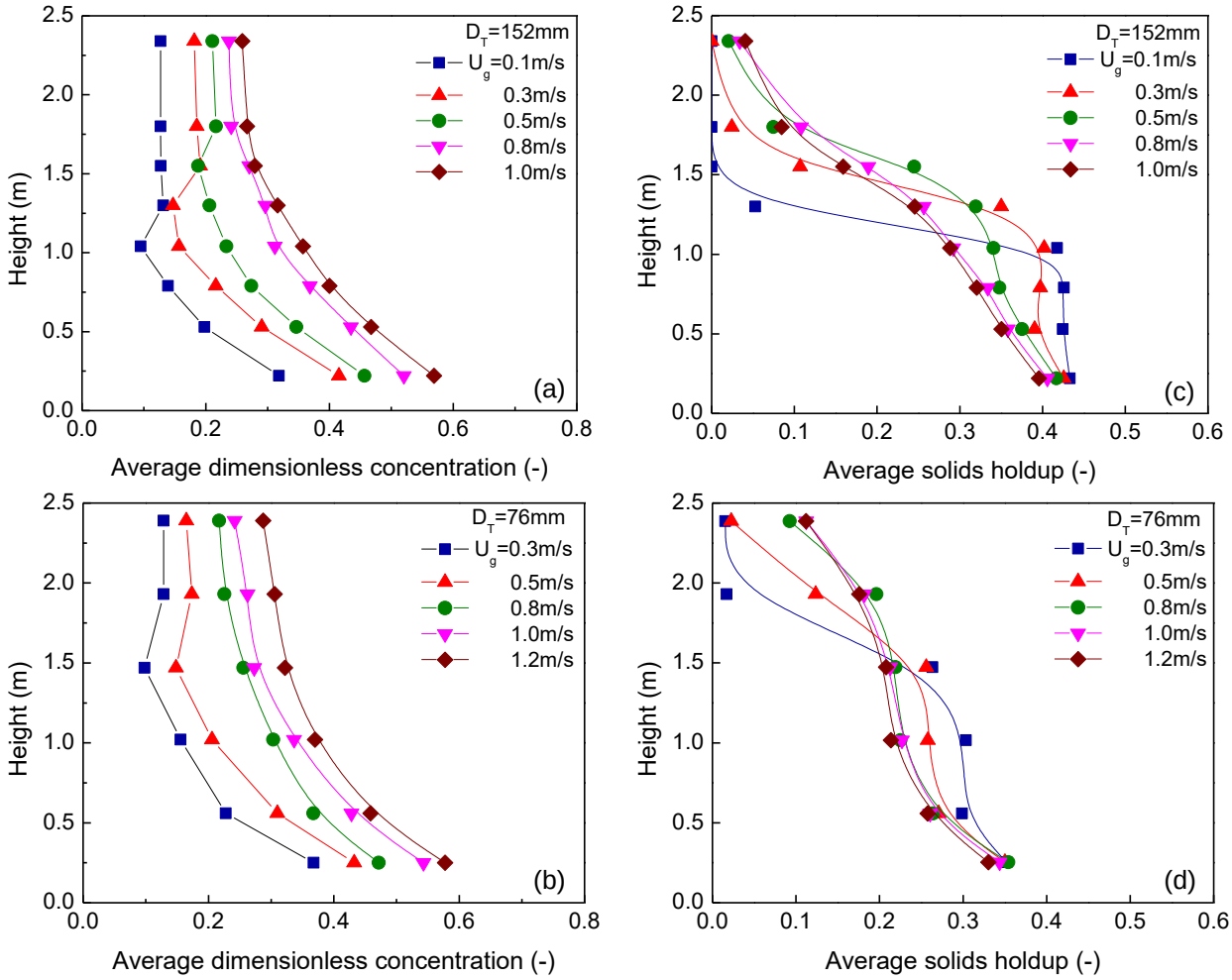

Figure 6.2 Axial profiles of average dimensionless ozone concentration (a, b) and corresponding solids holdup (c, d) at the same static bed height (H_0=1.0m)

The axial profiles of average dimensionless ozone concentration at various superficial gas velocities (U_g) obtained in two columns with different diameters (D_T) are shown in Figure 6.2(a) and (b). The static bed heights were both maintained at 1.0m. The dimensionless ozone concentration (C/C_0) equals the measured ozone concentration over the initial ozone concentration before entering the fluidized beds. So the ozone conversion equals one minus the dimensionless ozone concentration. The corresponding axial profiles of solids holdup (ε_s) are displayed in Figure 6.2(c) and (d). The average values of ozone concentrations and solids

holdups were obtained by integrating the local values of different radial positions based on the cross-sectional area.

Pressure fluctuations represented by standard deviations of differential bed pressure were used to identify the transition from a BFB to a TFB, which is one of the commonly used methods (Yerushalmi and Cankurt 1979). The superficial gas velocity at which the pressure standard deviation reaches its maximum is referred as the transition velocity (U_c) from bubbling fluidization to turbulent fluidization. In this work, it was found that the transition velocity was 0.5 m/s in all cases. Therefore, the fluidized beds operated below U_g=0.5 m/s are considered as BFBs, whereas those operated above U_g=0.5 m/s are identified as TFBs.

The ozone concentrations generally decrease with increasing elevation, except for some positions in the BFBs where sudden jumps take place, as shown in Figure 6.2(a) and (b). Since the phenomenon only occurred in the BFBs, it possibly caused by the distinctive two-phase flow structure that can be revealed from the instantaneous signals and the probability density distributions of solids holdup in Figure 6.3. The results were acquired in the 152mm i.d. fluidized bed at the elevation of 1.3m, at the gas velocities of 0.3 m/s (BFB) and 1.0 m/s (TFB).

In Figure 6.3(a), most transient signals stay on a high level ($\varepsilon_s \approx 0.5$) but with the clear-cut valleys sharply down to the bottom denoting the passing of bubbles. By close examination, the solids holdup inside bubbles is as low as 0.02-0.05. In addition, a conspicuous peak with high magnitude appears at ε_s=0.4-0.5 in Figure 6.3(b), demonstrating the dense phase is dominant in the BFB. The small peak at ε_s=0-0.1 denotes the existence of the bubble phase. Thus, it re-confirms that, in BFBs, the majority of fluidizing gas goes through the particulate bed in the form of bubbles having low solids concentration inside and a clear boundary with the surrounding dense solid phase. This flow structure can cause poor mass transfer of gas between the bubble phase and the solid phase, and insufficient gas-solids contacting inside bubbles. As a result, the ozone concentration within bubbles could be higher than that in the dense solid phase, which was observed by Chavarie and Grace (1975) who measured the ozone concentration in bubbles using a special probe. In this work, however, the measured ozone concentrations in the particulate bed are the time-mean average values of the two phases. Moreover, by analysing the axial profiles of solids holdup, the local jumps of ozone concentration in the BFBs are found to

occur on the bed surface. This evidence indicates that when bubbles burst at the bed surface, the gas of higher concentration released to the freeboard and resulted in an increase of concentration. The result also implies the bubbling behaviour cause bypassing of reactant-gas.

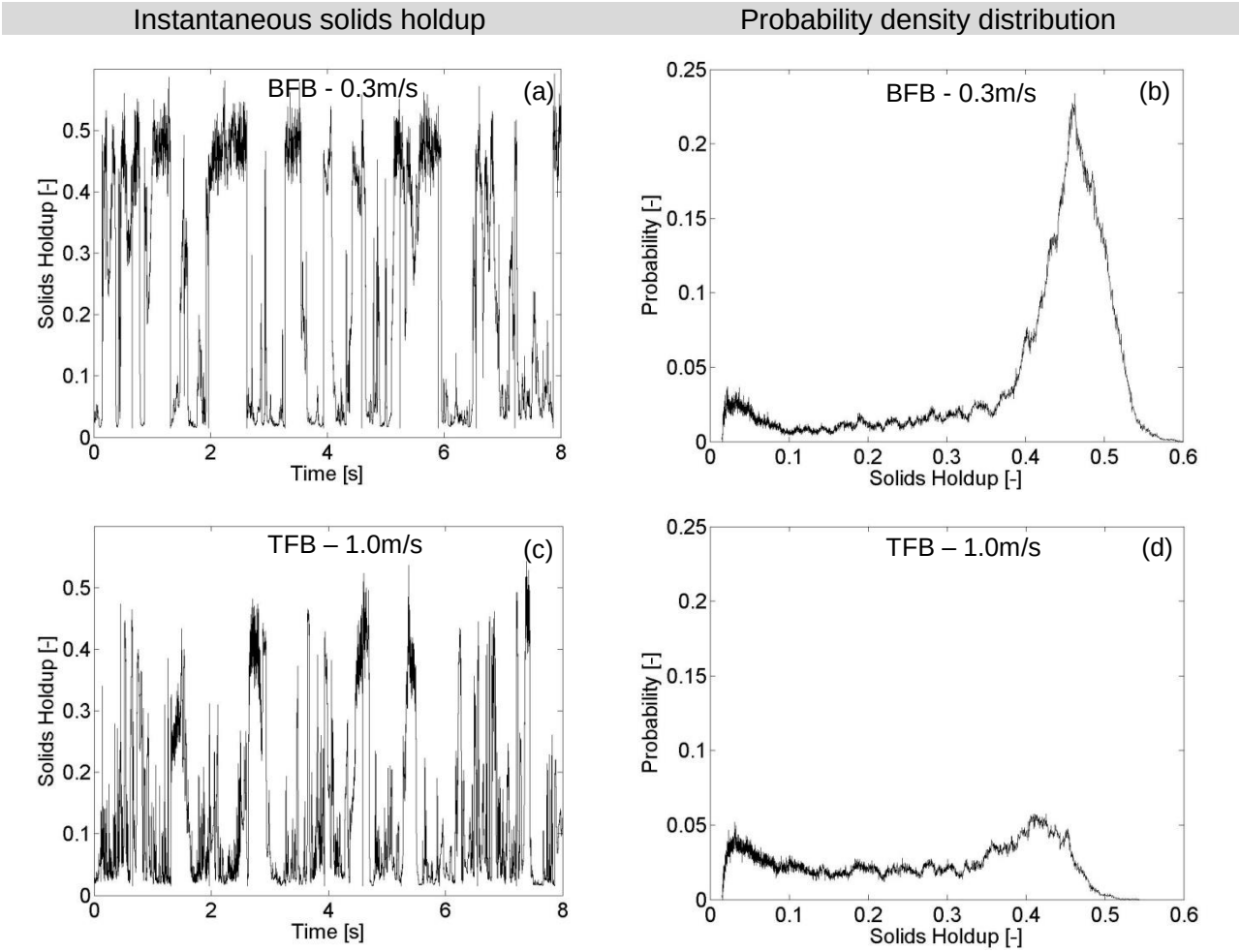

Figure 6.3 Instantaneous solids holdup signals and probability density distributions at 0.3 m/s (BFB) (a, b) and 1.0 m/s (TFB) (c, d)

Unlike BFBs, the ozone concentrations in the TFBs continuously decrease with increasing elevation, as shown in Figure 6.2(a) and (b). Since the dilute phase and the dense phase become comparable and inter-dispersed (revealed by Figure 6.3(c) and (d)), the conversion distribution between the two phases is relatively uniform in the TFBs. Moreover, in Figure 6.2(a) and (b), it is found that the ozone concentration reduces rapidly in the entrance region and the lower section of the TFBs, and the reduction rate decreases with increasing elevation. This trend corresponds to the gradually decreasing solids holdup in the axial direction. Due to the higher solids holdup and smaller void size in the entrance region, there would be more opportunity of contacting

between gas and solids, thereby leading to higher reactant conversions. In addition, although the overall conversions decrease from the BFBs to the TFBs in Figure 6.2(a) and (b), the reactor performances of BFBs and TFBs cannot be simply compared by conversions without considering the reactant-gas residence time. The reactor performances are compared later.

6.3.2. Radial profiles of ozone concentration

The radial profiles of ozone concentration (a, b, c, d) and solids holdup (e, f, g, h) at different elevations (H) and superficial gas velocities (U_g) in the 152mm i.d. column are shown in Figure 6.4. The U_g of 0.1 m/s and 0.3 m/s are considered in the bubbling fluidization regime, whereas 0.8 m/s and 1.0 m/s are in the turbulent fluidization regime.

In the BFB, the radial distributions of ozone concentration at H=0.22m and 0.79m exhibit a gradient slightly decreasing from the centre to the wall. Since more bubbles tend to rise in the central region (Halow, Fasching et al. 1993), the measured ozone concentrations are relatively high in this region due to the higher concentration in bubbles. The solids holdup distributions in Figure 6.4(e) and (f) illustrate the flow pattern as well. Further increasing the elevation beyond 1.30m, the concentration profiles level off due to entering the freeboard with very few solids.

In the TFB, the ozone concentrations keep reducing with increasing elevation, which is consistent with the trend observed in the axial profiles. By comparing the solids holdup radial profiles of the BFB and TFB, less uniform radial distributions can be found in the TFB due to the transition characteristics just about entering the fast fluidization. Even so, in Figure 6.4(c) and (d), the radial distributions of ozone concentration do not show significant radial non-uniformity in the TFBs, due to the erratic motion of voids and the widespread gas/solids turbulent flow.

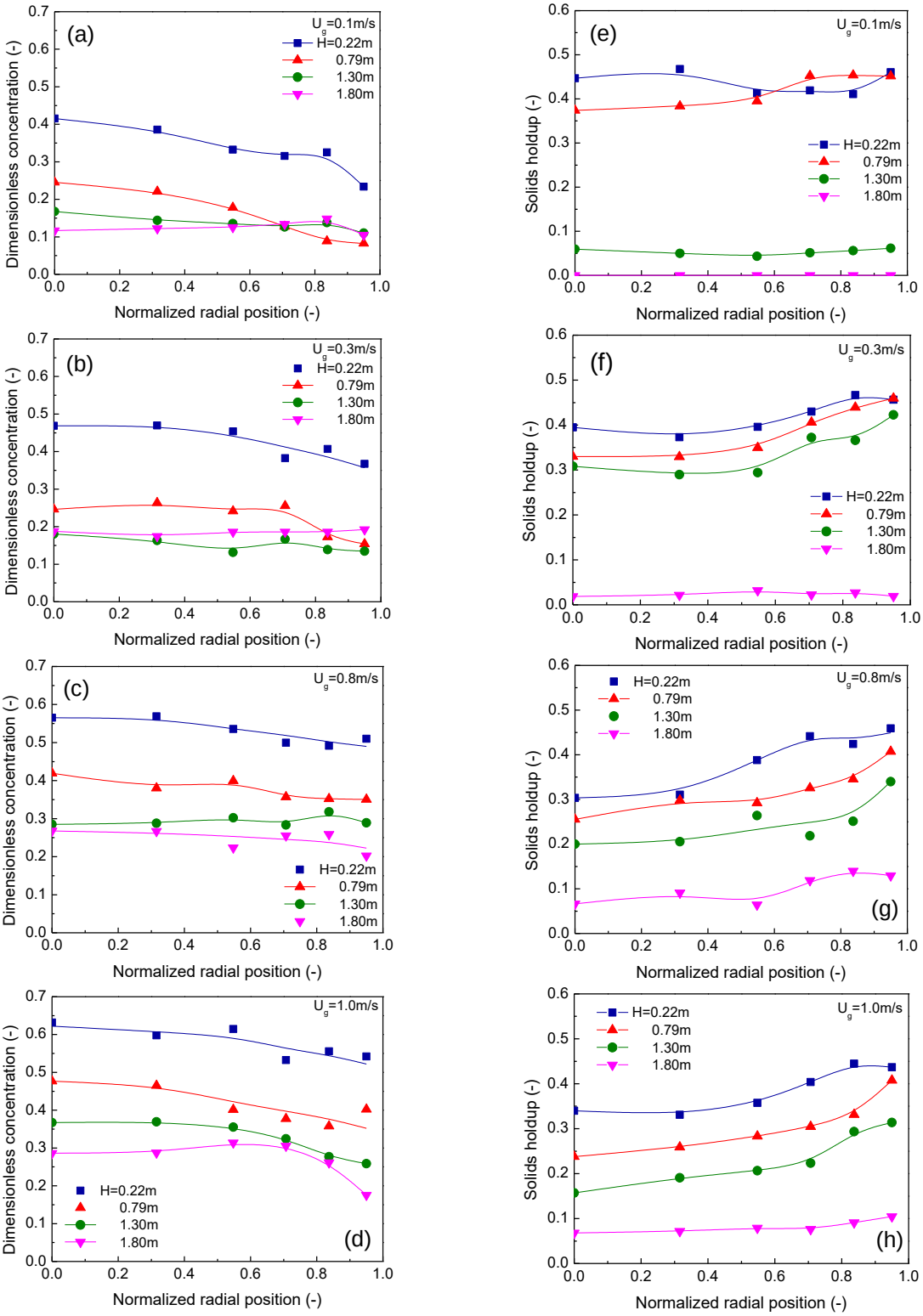

Figure 6.4 Radial profiles of ozone concentration (a,b,c,d) and solids holdup (e,f,g,h) at various U_g (H_0=1.0m, D_T=152mm)

6.3.3. Effect of static bed height on ozone concentration distributions

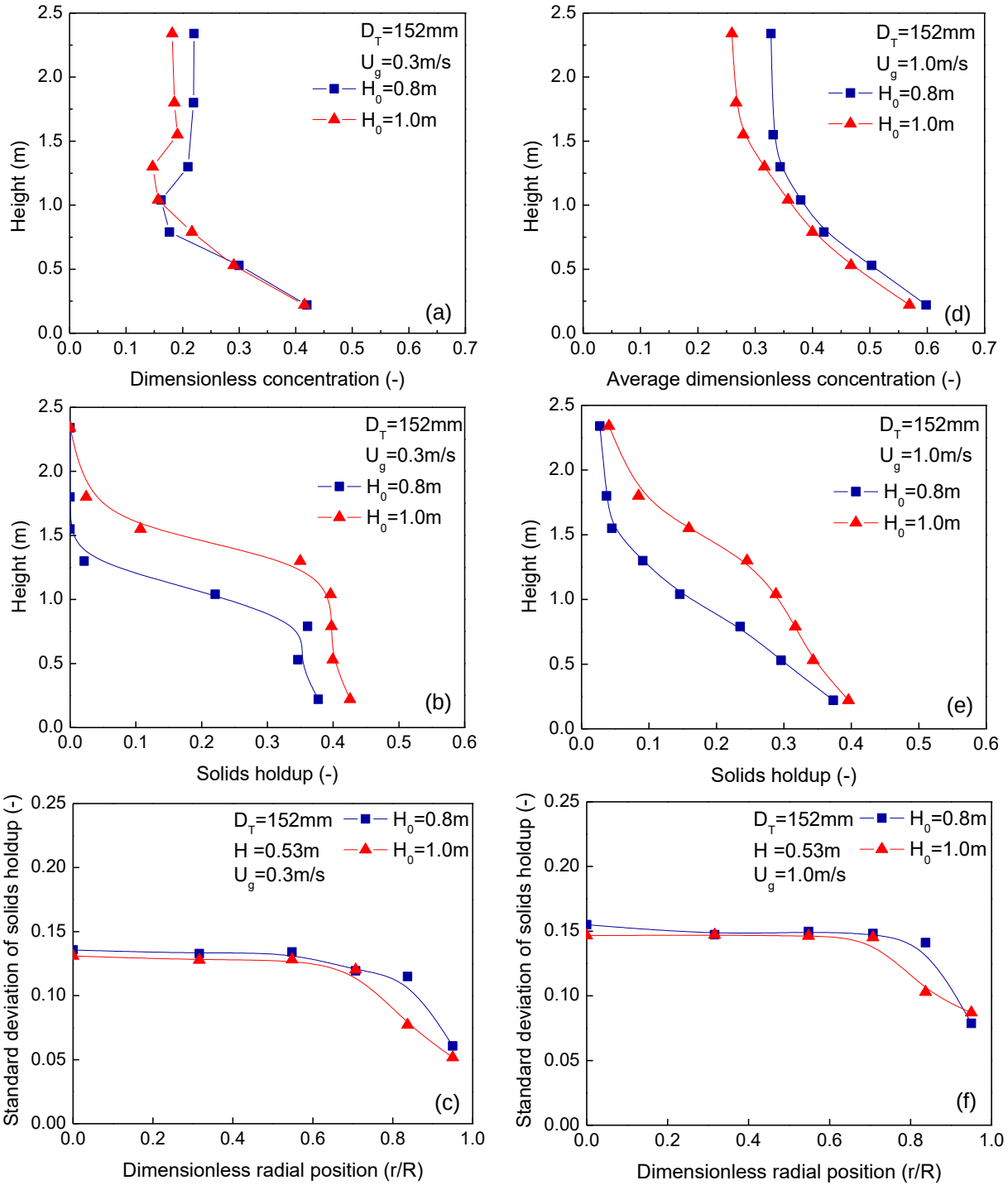

Figure 6.5 Effects of static bed height (H_0) on ozone concentration (a, d), solids holdup (b, e) and standard deviation of solids holdup (c, f) in the BFB and TFB

The effects of static bed height (H_0) on ozone concentration, solids holdup and standard deviation of solids holdup were studied in the BFBs and TFBs. Typical results obtained in the 152mm i.d. column with H_0=0.8m and 1.0m are presented in Figure 6.5.

In the BFB (U_g=0.3 m/s) and TFB (U_g=1.0 m/s), the bed of higher H_0 leads to higher solids holdup in every axial position, but similar standard deviation compared with the bed of lower H_0, as shown in Figure 6.5(b), (e), (c) and (f). The close standard deviations indicate the similar gas-solids interactions in the beds of different H_0, further leading to the similar inter-phase mass transfer of gas. Since the inter-phase mass transfer essentially affects the extent of reaction in the BFB and TFB (Bi, Jiang et al. 1992), the ozone concentration distributions at different static bed heights are very similar in the particulate bed regions, as shown in Figure 6.5(a) and (d). Further increasing the elevation over the bed surface, the bed of higher H_0 produces lower outlet concentration, mainly due to the additional bed height and the longer reactant residence time. Overall, the static bed height has almost no influence on the reactor performance in the particulate bed region, because it has unnoticeable effect on the gas-solids interaction.

6.3.4. Effect of bed diameter on ozone concentration distributions

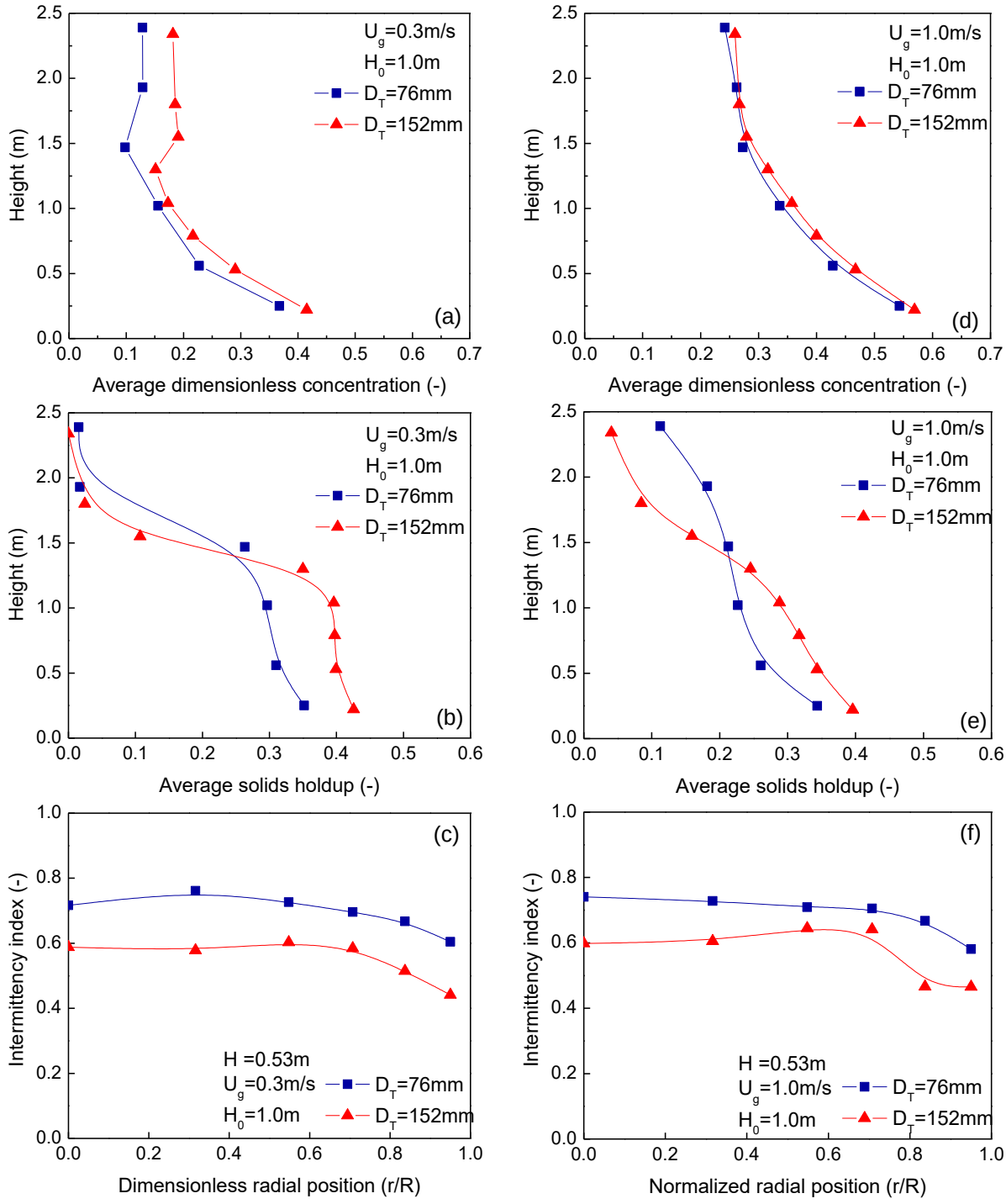

Figure 6.6 Effects of bed dimeter (D_T) on ozone concentration (a, d), solids holdup (b, e) and intermittency index of solids holdup (c, f) in the BFB and TFB

The effects of bed dimeter (D_T) on ozone concentration, solids holdup and intermittency index of solids holdup are illustrated in Figure 6.6. The results were obtained from the beds of D_T=76mm and 152mm at U_g=0.3 m/s (BFB) and 1.0 m/s (TFB). The static bed heights were both maintained at 1.0m.

In the BFB, the bed of smaller D_T has higher ozone conversions than the bed of larger D_T at every elevation, as shown in Figure 6.6(a), which is consistent with the result of Bauer, Werther et al. (1981). Besides, the bed of smaller D_T has lower solids holdups in the particulate bed region, but slightly higher solids holdups in the freeboard, as shown in Figure 6.6(b). Figure 6.6(c) introduces a parameter, intermittency index, to quantify the intensity of flow fluctuations (Brereton and Grace 1993). Higher intermittency index means more intense fluctuations. Besides, the level of segregation of gas and solids can be evaluated by the intermittency index between 0 and 1, indicating "complete segregation" (e.g., a bubble without any solids inside surrounded by dense solids) and "perfect mixing" respectively. Therefore, Figure 6.6(c) demonstrates that the bed of smaller D_T has stronger gas-solids interaction and better gas-solids mixing. In spite of the lower solids holdups in the bed of smaller D_T, the improved inter-phases mass transfer is a great help for increasing the ozone conversions. On the other hand, the bubbles tend to assemble and rise faster along the bubbling tracks in the central region of the bed with larger D_T, as suggested by the simultaneous signals of solids holdup in Chapter 4. The same effect of bed diameter on bubble behaviour was observed by Werther (1977, 1992). As a result, the reactant-gas residence time and conversion reduce in the bed with larger D_T.

In the TFB, the ozone conversions in the bed of smaller D_T show no obvious difference with those in the bed of larger D_T, as displayed in Figure 6.6(d). Nevertheless, the difference between the two profiles is much closer than that in the BFB. As displayed in Figure 6.6(e) and (f), the bed of smaller D_T shows lower solids holdup in the lower section than the bed of larger D_T, but the more vigorous gas-solids interaction indicated by the evidently higher intermittency index compensates the "disadvantage" of dilute solids concentration.

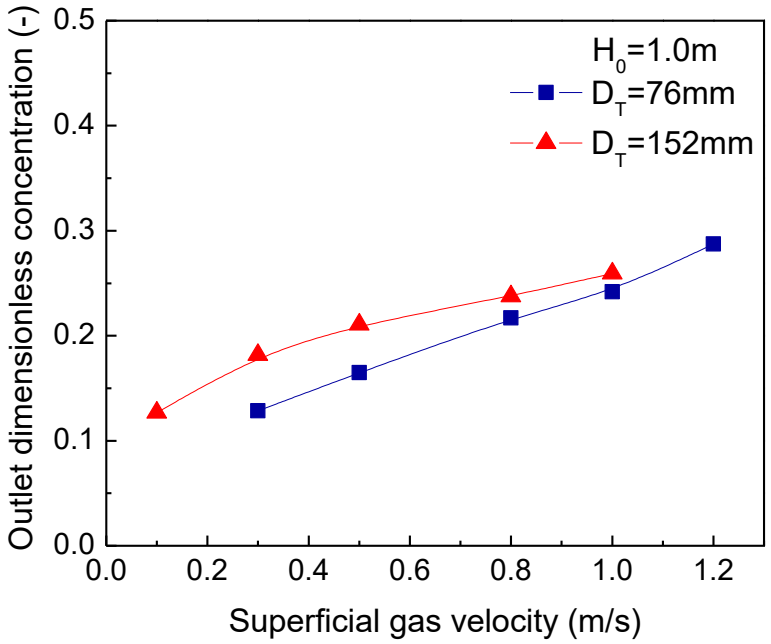

Figure 6.7 Outlet ozone concentrations at various superficial gas velocities in the beds of different diameters

Figure 6.7 compares the outlet ozone concentrations at various U_g in the 76mm i.d. bed and the 152mm i.d. bed. It is found that the effect of bed diameter becomes less significant with increasing U_g, i.e., from the bubbling regime to the turbulent regime. Due to the highly vigorous hydrodynamics in TFBs, the flow structure is less easily influenced by the bed diameter, especially for the reactors using Group A particles (King 1989). Therefore, the scale-up of TFBs using Group A particles may be less complicated than that of BFBs, as illustrated in Figure 6.7.

6.3.5. Correlation between ozone conversions and solids holdups

As discussed before, the ozone conversions are essentially determined by the flow structures that can be partially represented by the solids holdup distributions in the fluidized beds. The relationship between ozone conversions and solids holdups was well correlated in CFB risers and downers (Ouyang, Li et al. 1995, Fan, Zhang et al. 2008, Wang, Zhu et al. 2015). However, limited work has been done in BFBs and TFBs.

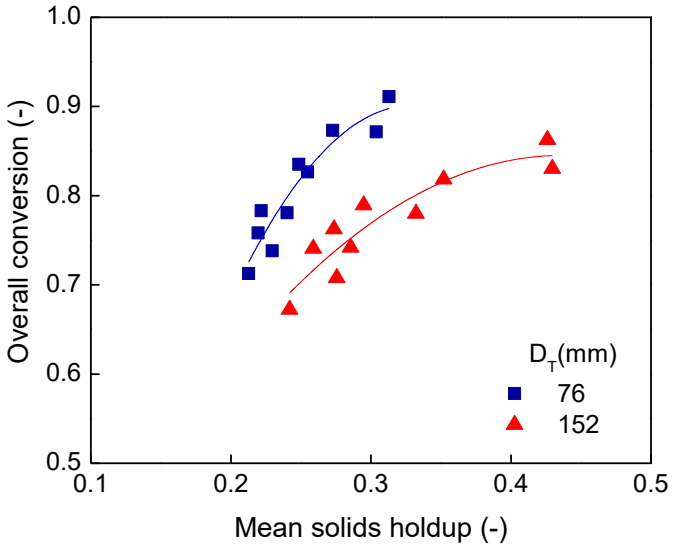

Figure 6.8 Correlation between overall conversions and mean solids holdups in the bed with different diameters

The correlation between the overall conversions and the mean solids holdups of the entire bed is plotted in Figure 6.8. In general, the overall conversion increases with the mean solids holdup in all cases. Unlike the linear relationship showing in CFBs (Wang, Wang et al. 2014), a second order polynomial function best fit the results in the low-velocity fluidized beds. The possible reason is that the fluidized beds experience a change of flow structure from the bubbling regime to the turbulent regime. It indicates that the flow structure, including bubble/void behaviour, gas-solids mixing and contacting, also plays an important role in the reactor performance. Furthermore, the beds of different diameters show different trends. In other words, the total conversion increases faster in the smaller bed than in the larger bed. Due to the better gas-solids mixing reflected by the higher intermittency indexes in the smaller bed, the increased solids holdup can more effectively enhance the gas-solids contacting, thereby increasing more on the conversions. The same explanation also accounts for the trend that the increase rate of conversion gradually slows down with increasing mean solids holdup (from turbulent to bubbling regime). Because of the nature of the two-phase structure in the BFBs, the increase of solids holdup mainly occurs in the dense solid phase, an “inactive zone” where the reactant-gas throughflow is so low.

6.3.6. Reactor performances of BFBs and TFBs

In order to evaluate the reactor performances of the BFBs and TFBs, more comprehensive investigations are needed. As the overall conversions of a gas-phase catalytic reaction are affected by the reactant-gas residence time, reaction kinetics and gas-solids mass transfer collectively, Damköhler numbers ($Da=k_r\varepsilon_s H/U_g$) combining the gas residence time and the reaction rate constant are plotted against the overall conversions in Figure 6.9. Since no well-developed model for BFBs and TFBs is available at the moment, the ideal reactor models, a plug-flow reactor (PFR) and a continuous stirred-tank reactor (CSTR), are adopted as references to assess the reactor performances. The formulas for the conversions in a PFR and a CSTR are derived (Jiang, Bi et al. 1991):

PFR: $$X_{PFR} = 1 - \exp(-Da) \qquad \text{Eq. 6.5}$$

CSTR: $$X_{CSTR} = \frac{Da}{1+Da} \qquad \text{Eq. 6.6}$$

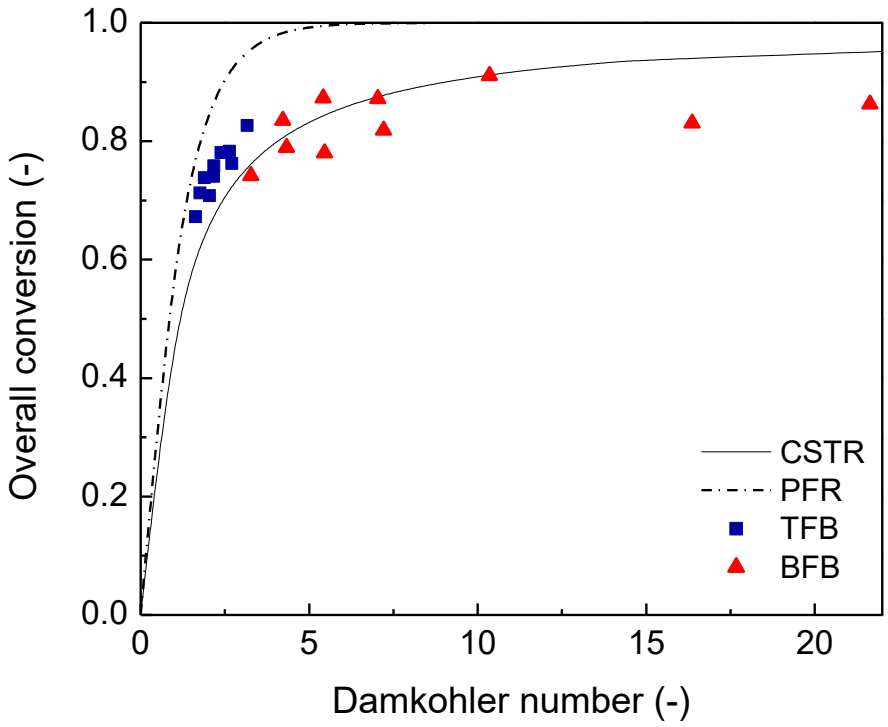

Figure 6.9 Relationship of overall ozone conversions and Damköhler numbers in the BFBs and TFBs

In Figure 6.9, it should be mentioned that the results with low *Da* were normally obtained in the TFBs, while those with high *Da* were from the BFBs. The TFBs show lower conversions than the PFR, but higher conversions than the CSTR. The conversions of BFBs are generally lower than those of the PFR, and most of them are even lower than those of the CSTR. But there are some results from the smaller BFB above or on the CSTR curve. Therefore, the TFBs have better reactor performance than the CSTR but poorer than the PFR, whereas the reactor performance of the BFBs is equivalent or even poorer than that of the CSTR.

The deviation of the TFBs and BFBs from a PFR at a given *Da* can be attributed to the different gas-solids mass transfer or contact efficiency. It is well-known that the two-phase structure in BFBs results in poor gas-solids contact inside bubbles and high mass transfer resistance between the two phases (Chiba and Kobayashi 1970). The bubbles keep a relatively stable state, albeit splitting and coalescing, leading to reactant-gas bypassing to some extent. In addition, the serious solids downflow may cause backmixing of reactant-gas (Du, Fan et al. 2002). The insufficient gas-solids contacting, reactant-gas by-passing and back-mixing of BFBs lead to the poorer reactor performance than that of a CSTR.

With increasing gas velocity beyond the transition velocity, a BFB changes to a TFB accompanied with bubbles transforming to much smaller voids and producing larger total mass transfer area. The voids even lose their identities due to the drastic motion and frequent splitting. Moreover, as the gas fraction increases, the former continuous dense phase takes apart to a cluster phase competing with the dilute phase. This inherent flow structure of TFBs leads to intense gas-solids interaction and improved contact efficiency, making TFBs favourable in industries.

According to the discussion above, the gas-solids contact efficiency is a key effect on the reactor performance for gas-phase catalytic reactions. In order to quantitatively evaluate the gas-solids contact efficiency of TFBs and BFBs, a calculation method was proposed by Sun and Grace (1990). Since the gas-solids contacting and mixing in a fluidized bed deviate from those in a PFR at the same gas velocity, the amount of catalysts ($V_{c,f}$) in a fluidized bed required to achieve the same conversion with the same gas flowrate and reaction rate constant should be larger than the catalyst amount ($V_{c,p}$) in a PFR. Therefore, the ratio of $V_{c,p}/V_{c,f}$ can evaluate the utility efficiency

or contact efficiency of catalysts in different fluidized bed reactors. The higher contact efficiency, the better the reactor performance is, i.e., the less the fluidized bed deviates from a PFR. $V_{c,f}$ comes from experimental values, whereas $V_{c,p}$ is calculated by the following equation in which Q_g is the operating gas flowrate, k_r is the reaction rate constant, C_{in} is the initial ozone concentration and C_{out} is the outlet ozone concentration.

$$V_{c,p} = \frac{Q_g}{k_r} \ln\left(\frac{C_{in}}{C_{out}}\right) \qquad \text{Eq. 6.7}$$

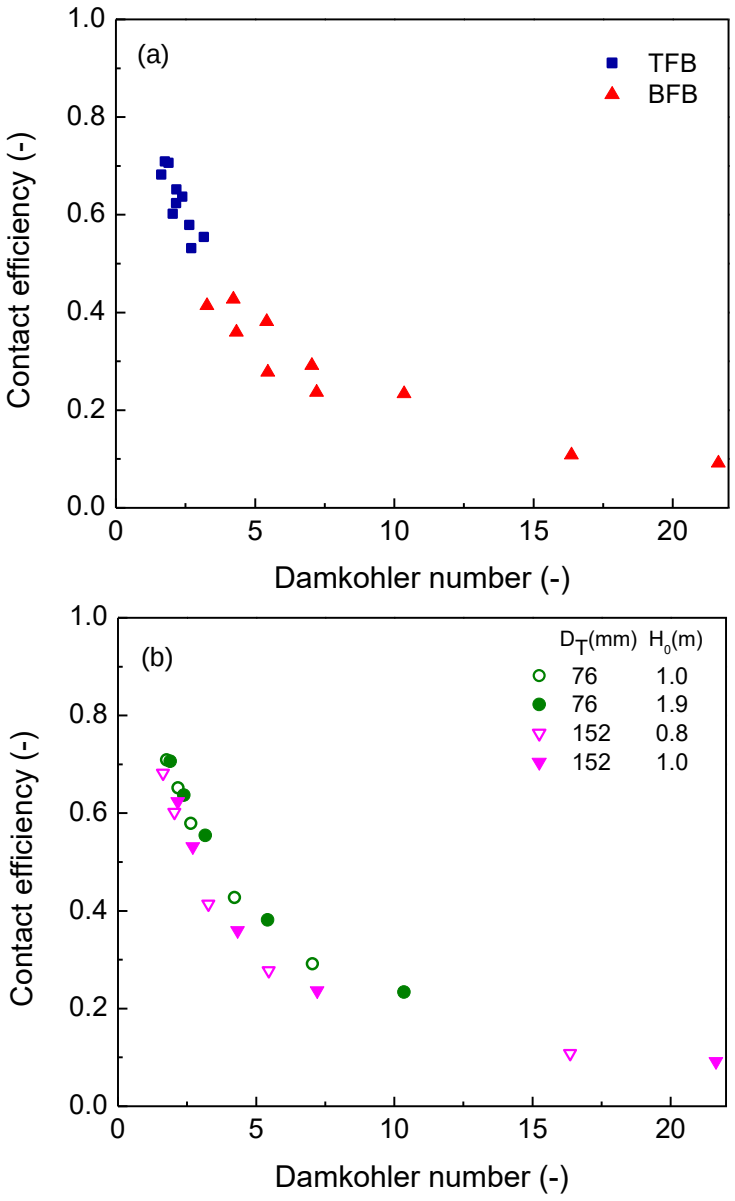

Figure 6.10 Gas-solids contact efficiencies of the TFBs and BFBs

The contact efficiencies of the TFBs and BFBs are compared in Figure 6.10(a). It is clearly shown that the TFBs have higher gas-solids contact efficiency than the BFBs. In the BFBs, most particles are "locked" in the dense phase where little reactant-gas flows through. The segregation between the bubble phase and the solids phase results in the reduction of contact efficiency. In the TFBs, however, the catalyst-solids have high probability to contact with the reactant-gas owing to the strong gas-solids interaction. Furthermore, the contact efficiencies of the fluidized beds with different D_T and H_0 are plotted against Da in Figure 6.10(b). The bed of smaller D_T is found to have higher contact efficiency than the bed of larger D_T. In contrast, the static bed height has almost no influence on the contact efficiency. The results agree with those discussed in the profiles of ozone concentration.

6.4. Conclusions

The catalytic ozone decomposition was used as the model reaction to study the reactor performances of BFBs and TFBs. The ozone concentration distributions were experimentally investigated in both axial and radial directions at U_g ranging from 0.1 m/s to 1.2 m/s. The profiles of concentration were found to be dependent on the flow structures. By analysing the microscopic bubble behaviour in the BFBs, it is suggested that bubbles are able to carry the gas of higher concentration and release to the freeboard, which can be considered as reactant-gas bypassing. For the TFBs, the axial profiles of ozone concentration closely correspond to the axial profiles of solids holdup. Although the TFBs show non-uniform radial profiles of solids holdup, the ozone concentrations distribute uniformly in the radial direction due to the widespread turbulent gas/solids flow on the cross section.

Moreover, the static bed height had almost no effect on the ozone concentration distributions owing to the unchanged flow structure. In contrast, the bed of smaller diameter had higher ozone conversions than the bed of larger diameter, presumably due to the longer gas residence time and better gas-solids mixing. The effect of bed diameter was more significant in the bubbling regime, but it diminished with entering the turbulent regime. This finding suggests that the scale-up of TFBs is likely less troublesome than that of BFBs.

The overall ozone conversions were correlated with the mean solids holdups of the entire bed, indicating not only solids holdup, but also flow structure affects the reaction conversions. Under

the influence of the dynamic flow structures, the increased solids holdup can more effectively increase the conversions in the TFBs than in the BFBs. In addition, the overall ozone concentrations were plotted against Damkohler numbers to evaluate the reactor performances of BFBs and TFBs. It is concluded that the TFBs have better reactor performance than the BFBs, but they both deviate from a PFR. These characteristics are determined by the hydrodynamics of BFBs and TFBs. The reactor performances of BFBs and TFBs were also quantitatively assessed by gas-solids contact efficiencies. It is clearly shown that the TFBs have higher gas-solids contact efficiency than the BFBs by reason of the better mixing and stronger interaction of gas and solids.

Nomenclature

C	local ozone concentration [ppm]
C_0, C_{in}	initial ozone concentration [ppm]
C_{out}	outlet ozone concentration [ppm]
C/C_0	dimensionless ozone concentration [-]
Da	Damkohler number, $k_r\bar{\varepsilon}_s H/U_g$ [-]
D_T	bed diameter [mm]
H	axial coordinate, or distance from the gas distributor [m]
H_0	static bed height [m]
k_r	reaction rate constant based on particle volume, first-order [s^{-1}]
m_c	mass of catalysts [g]
r	radial coordinate [m]
R	column radius [m]
r/R	dimensionless sampling position [-]
U_g	superficial gas velocity [m/s]
$V_{c,f}$	volume of catalyst in a fluidized bed [m^3]
$V_{c,p}$	volume of catalyst in the ideal plug flow reactor [m^3]
Q_g	gas flowrate [m^3/s]

Greek letters

ε_s	local solids holdup [-]
$\bar{\varepsilon}_s$	mean solids holdup [-]
ρ_p	particle density [kg/m^3]

References

Bauer, W., J. Werther and G. Emig (1981). Influence of gas distributor design on the performance of fluidized bed reactor. *Ger. Chem. Eng* **4**: 291-298.

Bi, H., N. Ellis, I. Abba and J. Grace (2000). A state-of-the-art review of gas–solid turbulent fluidization. *Chemical Engineering Science* **55**(21): 4789-4825.

Bi, H., J. Grace and K. Lim (1995). Transition from bubbling to turbulent fluidization. *Industrial & Engineering Chemistry research* **34**(11): 4003-4008.

Bi, H., P. Jiang, R.-H. Jean and L.-S. Fan (1992). Coarse-particle effects in a multisolid circulating fluidized bed for catalytic reactions. *Chemical Engineering Science* **47**(12): 3113-3124.

Brereton, C. and J. Grace (1993). Microstructural aspects of the behaviour of circulating fluidized beds. *Chemical Engineering Science* **48**(14): 2565-2572.

Chavarie, C. and J. R. Grace (1975). Performance analysis of a fluidized bed reactor. II. Observed reactor behavior compared with simple two-phase models. *Industrial & Engineering Chemistry Fundamentals* **14**(2): 79-86.

Chiba, T. and H. Kobayashi (1970). Gas exchange between the bubble and emulsion phases in gas-solid fluidized beds. *Chemical Engineering Science* **25**(9): 1375-1385.

Du, B., L. S. Fan, F. Wei and W. Warsito (2002). Gas and solids mixing in a turbulent fluidized bed. *AIChE Journal* **48**(9): 1896-1909.

Fan, C., Y. Zhang, X. Bi, W. Song, W. Lin and L. a. Luo (2008). Evaluation of downer reactor performance by catalytic ozone decomposition. *Chemical Engineering Journal* **140**(1): 539-554.

Frye, C., W. Lake and H. Eckstrom (1958). Gas-solid contacting with ozone decomposition reaction. *AIChE Journal* **4**(4): 403-408.

Frye, C. and O. E. Potter (1976). Experimental investigation of models for fluidized bed catalytic reactors. *AIChE Journal* **22**(1): 38-47.

Grace, J. R. (2000). Reflections on turbulent fluidization and dense suspension upflow. *Powder Technology* **113**(3): 242-248.

Halow, J., G. Fasching, P. Nicoletti and J. Spenik (1993). Observations of a fluidized bed using capacitance imaging. *Chemical Engineering Science* **48**(4): 643-659.

Jiang, P., H. Bi, R. H. Jean and L. S. Fan (1991). Baffle effects on performance of catalytic circulating fluidized bed reactor. *AIChE Journal* **37**(9): 1392-1400.

King, D. (1989). Estimation of dense bed voidage in fast and slow fluidized beds of FCC catalyst. *Fluidization VI*: 1-8.

Knowlton, T., S. Karri and A. Issangya (2005). Scale-up of fluidized-bed hydrodynamics. *Powder Technology* **150**(2): 72-77.

Lewis, W., E. Gilliland and W. Glass (1959). Solid‐catalyzed reaction in a fluidized bed. *AIChE Journal* **5**(4): 419-426.

Lim, K., J. Zhu and J. Grace (1995). Hydrodynamics of gas-solid fluidization. *International Journal of Multiphase Flow* **21**: 141-193.

Lin, S.-C., H. Arastoopour and H. Kono (1986). Experimental and theoretical study of a multistage fluidized-bed reactor. *Powder Technology* **48**(2): 125-140.

Liu, J., J. R. Grace and X. Bi (2003). Novel multifunctional optical‐fiber probe: I. Development and validation. *AIChE Journal* **49**(6): 1405-1420.

Massimilla, L. and H. Johnstone (1961). Reaction kinetics in fluidized beds. *Chemical Engineering Science* **16**(1): 105-112.

Matsen, J. M. (1997). Design and scale-up of CFB catalytic reactors. *Circulating Fluidized Beds*, Springer**:** 489-503.

Ouyang, S., X. G. Li and O. Potter (1995). Circulating fluidized bed as a catalytic reactor: experimental study. *AIChE Journal* **41**(6): 1534-1542.

Seinfeld, J. and S. Pandis (2006). Atmospheric Chemistry and Physics, A Wiley-Inter Science Publication, John Wiley & Sons Inc, New York.

Shen, C. and H. Johnstone (1955). Gas‐solid contact in fluidized beds. *AIChE Journal* **1**(3): 349-354.

Sun, G. and J. R. Grace (1990). The effect of particle size distribution on the performance of a catalytic fluidized bed reactor. *Chemical Engineering Science* **45**(8): 2187-2194.

Van Lare, C., H. Piepers and D. Thoenes (1990). Scaling and particle size optimization of mass transfer in gas fluidized beds. *Chemical Engineering Science* **45**(8): 2211-2217.

Wang, C., G. Wang, C. Li, S. Barghi and J. Zhu (2014). Catalytic ozone decomposition in a high density circulating fluidized bed riser. *Industrial & Engineering Chemistry Research* **53**(16): 6613-6623.

Wang, C., J. Zhu and S. Barghi (2015). Performance evaluation of high density riser and downer: Experimental study using ozone decomposition. *Chemical Engineering Journal* **262**: 478-489.

Werther, J. (1977). Bubble chains in large diameter gas fluidized beds. *International Journal of Multiphase Flow* **3**(4): 367-381.

Werther, J. (1992). Scale-up modeling for fluidized bed reactors. *Chemical Engineering Science* **47**(9): 2457-2462.

Wojtowicz, J. A. (2005). Ozone. *Encyclopedia of Chemical Technology*. Kirk-Othmer, John Wiley & Sons.

Yerushalmi, J. and N. Cankurt (1979). Further studies of the regimes of fluidization. *Powder Technology* **24**(2): 187-205.

Zhang, H., P. Johnston, J.-X. Zhu, H. De Lasa and M. Bergougnou (1998). A novel calibration procedure for a fiber optic solids concentration probe. *Powder Technology* **100**(2): 260-272.

Chapter 7
Reactor performance of a circulating turbulent fluidized bed

7.1. Introduction

According to the typical fluidization regime classification, fluidized beds can be operated in particulate fluidization, bubbling (slugging) fluidization, turbulent fluidization, dense suspension upflow, fast (circulating) fluidization and pneumatic transport (Lim, Zhu et al. 1995, Grace 2000). In practice, however, most key commercial applications are using turbulent fluidized beds (TFBs) and circulating fluidized beds (CFBs) by reason of preferred fluidizing characteristics and favourable operating conditions (Grace 2000). In spite of their advantages, several drawbacks also inherently exist in TFBs and CFBs.

Turbulent fluidized beds (TFBs) have a dynamic gas/solids flow with intense dense and dilute phases interaction (Bi, Ellis et al. 2000). The dilute phase in TFBs mainly exists of voids having erratic motion and extensive splitting and coalescence. Turbulent fluidized beds offer many hydrodynamic advantages over bubbling and circulating fluidized beds, such as high gas-solids contact efficiency, favourable mass transfer of gas between the voids and the dense phase, negligible gas bypassing, and relatively high overall solids holdup (approx. 0.25-0.35). Nevertheless, the low fluidizing gas velocity (approx. 0.5 m/s-2.0 m/s) of TFBs limits the throughput when compared with CFBs. The gas/solids back-mixing results in reduced selectivity of the reaction when catalysts lose activity shortly in gas-phase catalytic reactions.

Circulating fluidized beds (CFBs) have many successful industrial applications, such as combustion, gasification and fluid catalytic cracking (FCC) (Reh 1995). They are operated in the fast fluidization regime with high fluidizing gas velocities, resulting in higher gas throughput and reduced gas/solids back-mixing, but lower overall solids holdup, when compared with TFBs. Additionally, the circulating operation is capable of continuously withdrawing and adding large quantity of particles, independently controlling gas and solids flux, and operating in large scales. In the early research, CFBs were operated under low conditions, such as solids circulation rate G_s < 200 kg/m^{2}s, superficial gas velocity U_g < 10 m/s and solids holdup ε_s < 0.1. They exhibit a non-uniform flow structure with a dense bottom and a dilute upper region in the axial direction, as

well as a dilute core region surrounded by a dense annulus region in the radial direction (Grace and Bi 1997). Such hydrodynamic non-uniformity causes gas bypassing through the extreme dilute core region and poor overall gas-solids contact efficiency. More recently, an increasing number of lab-scale investigations have been conducted at high operating conditions like those of industrial FCC risers ($G_s \approx$ 400~1200 kg/m^{2}s, $U_g \approx$ 5~28 m/s, overall $\varepsilon_s > 0.1$) (Issangya, Bai et al. 1999, Pärssinen and Zhu 2001, Wang, Zhu et al. 2014). These CFBs were defined as high density CFBs (Zhu and Bi 1995). Although it was found that the solids holdup axial distributions became relatively uniform in high density CFBs, the radial segregation of gas and solids still inherently existed, which is unfavourable to gas-solid contacting and further reactor performance (Wang, Wang et al. 2014).

A novel circulating turbulent fluidized bed (CTFB) with a distinctive operating mode was recently developed by Zhu and Zhu (2008). The word "circulating" in its name suggests it operates with solid circulation, while "turbulent" characterizing the dynamic flow structure. The experimental results (Zhu and Zhu 2008, Qi, Barghi et al. 2012) demonstrated that the CTFB successfully overcame several disadvantages of TFBs and CFBs, meanwhile integrating their advantages, such as high solids holdup, uniform distribution, favourable gas-solids mixing and contacting, reduced solids back-mixing, and high solids circulation rates. By comparing the hydrodynamics of CTFB both macroscopically and microscopically with TFBs and CFBs, the circulating turbulent fluidization was identified as a new flow regime (Qi, Zhu et al. 2009, Zhu, Qi et al. 2013).

Experimental studies with chemical reactions in fluidized beds, also called "hot-model" studies, can reflect reactor performance more directly than other methods. Several "hot-model" studies were conducted in bubbling fluidized beds (BFBs), TFBs and CFBs (Chavarie and Grace 1975, Frye and Potter 1976, Sun and Grace 1990, Jiang, Bi et al. 1991, Ouyang, Li et al. 1995, Wang, Zhu et al. 2015), however, no one reported the reactor performance of CTFBs before this work. The catalytic decomposition of ozone is the most used model reaction to study the reactor performances of fluidized beds due to its advantages in lab-scale research. Firstly, ozone can decompose to oxygen in the ambient temperature and pressure by the catalytic effect of some metallic oxides, like ferric oxide. Secondly, since ozone decomposition is a simple and a first-

order reaction, the conversions are independent of initial reactant concentrations (Frye, Lake et al. 1958). Additionally, the reaction has negligible effect, as well as being non-toxic to the catalysts.

This work aims to study the reactor performance of CTFB for the first time by using an ozone decomposition reaction. The axial and radial profiles of ozone concentration have been provided under various operating conditions. To have an in-depth understanding of the reactor performance, the complete mapping of solids holdup has been investigated as well. Furthermore, the gas-solids contact efficiency is used to evaluate the reactor performance of CTFB.

7.2. Experimental setup

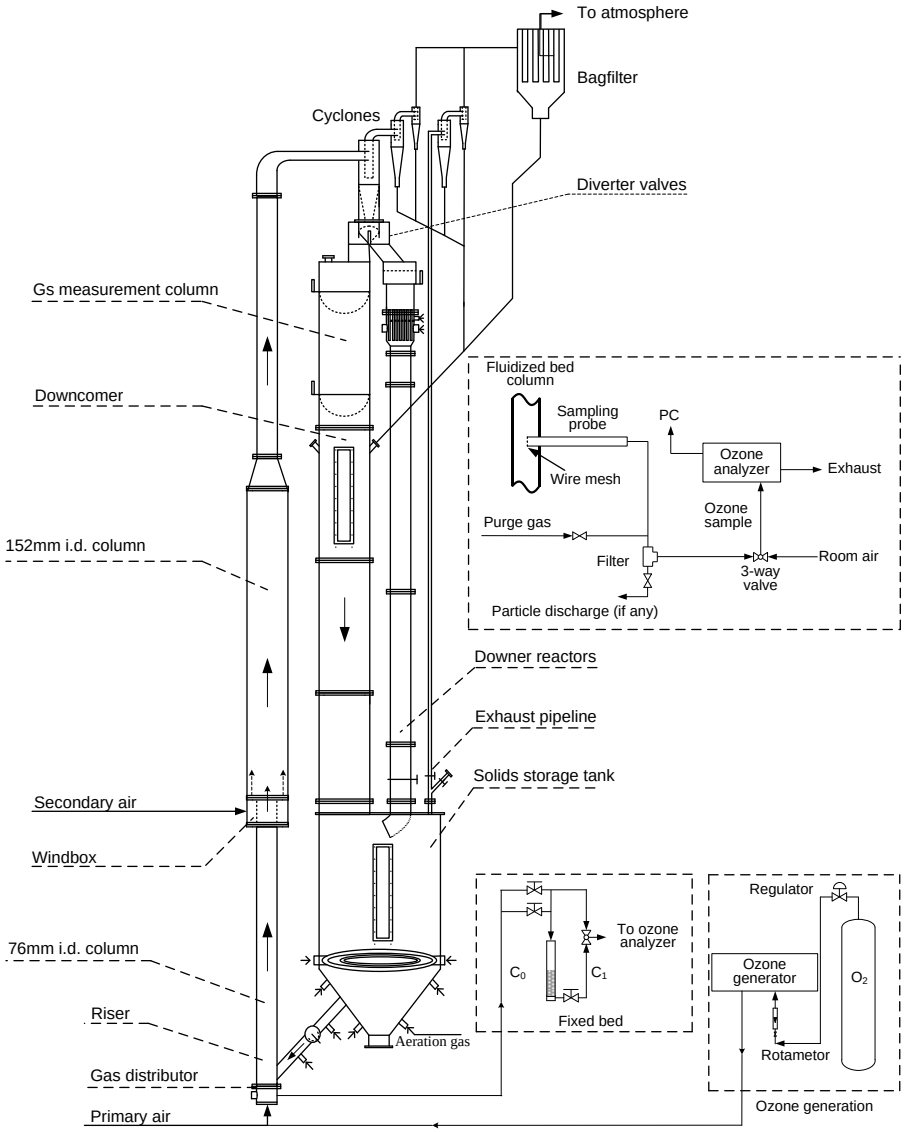

Figure 7.1 Schematic diagrams of a CTFB and an ozone testing system

Fluidized bed setup

A circulating turbulent fluidized bed (CTFB) was operated in a multifunctional fluidized-bed system, introduced in Chapter 3. As shown in Figure 7.1, the CTFB riser column is on the left-hand side, which consists of a 76mm i.d. column at the bottom, a 152mm i.d. column in the middle, and another 76mm i.d. column at the top. Each column is 3.0m in height. The bottom column is the main body of the CTFB, so all measurements were conducted in the bottom column. A gas distributor made of double-layer perforated plates (2mm i.d. hole × 176, 12% opening area) is mounted at the bottom of the riser column. A downcomer of 203mm i.d., on the right of the riser, serves for returning solids to a storage tank at its bottom. The column on the right of the downcomer is a downer reactor which is not studied in this work. The columns are mainly made of aluminium in order to avoid the oxidization of ozone, since an inert aluminium oxide layer is formed inside the column. To prevent electrostatic charges accumulation, the entire system is grounded.

The particles slid down to the gas distributor and were conveyed upwards by the primary air supply with superficial gas velocities (U_g) of 1.0 m/s, 2.0 m/s or 3.0 m/s. The particles were further accelerated by the secondary gas supply with U_g=5.0 m/s in the middle enlarged column. The secondary gas supply was injected through an annular perforated distributor (5mm i.d. hole × 44, 10% opening area). The gas supplies were at 172.4kPa and room temperature (20℃). A mechanical valve in the inclined feeding pipe was used to control the solids circulation rate (G_s=100, 200 and 300 kg/m^{2}s). A measurement section installed at the top of the downcomer was used to measure solids circulation rates. At the top of the riser, gas and particles were separated by three cyclones in series. Most particles can be captured within the cyclones and be returned to the downcomer, but the escaping fine particles can be collected by the bagfilter before exhausting. The amount of collected fine particles was very little, so they were recycled periodically. The total FCC particles inventory in the storage tank and downcomer was maintained at 6.0m-high approximately. Such high solids inventory can provide sufficient back pressure head to ensure high solids circulation rates.

Measurement of solids holdup

The local solids holdups were measured by an optical fibre probe system (Model: PV6D) that was manufactured by the Institute of Processing Engineering, Chinese Academy of Science, Beijing, China. The diameter of the probe is 3.8mm with a bundle of fibres whose cross-section is a square of $2\times2mm^2$ placed in the centre. The fibre bundle consists of 8000 quartz fibres each with a diameter of $15\mu m$. Half of the quartz fibres are emitting fibres and the others are receiving fibres. They are arranged alternatively. A Plexiglas pad of 0.2mm thickness is covered the probe tip in order to prevent particles from occupying the blind zone (Liu, Grace et al. 2003). By illuminating a small area and measuring the intensity of light reflected by passing particles, the optical fibre probe can correlate local solids holdups with the corresponding voltage signals converted from the light intensity. More particles can reflect more light, i.e., higher light intensity, resulting in higher voltage. The correlation equation between solids holdups and voltage signals requires calibrations. A proper calibration method developed by Zhang, Johnston et al. (1998) was adopted.

Instantaneous local solids holdup $\varepsilon_s(t)$ can be obtained by the calibration equation with voltage data $V(t)$:

$$\varepsilon_s(t) = f\left[V(t)\right] \qquad \text{Eq. 6.1}$$

where f is the calibration function.

Time-mean solids holdup ε_s can be calculated by integrating $\varepsilon_s(t)$ over a time span T:

$$\varepsilon_s = \frac{1}{T}\int_0^T \varepsilon_s(t)dt \qquad \text{Eq. 6.2}$$

Cross-sectional average solids holdup $\bar{\varepsilon}_s$ can be calculated by integrating ε_s over the cross-sectional area of reactor:

$$\bar{\varepsilon}_s = \frac{1}{\pi R^2}\int_0^R 2\pi r\varepsilon_s \mathrm{d}r = \frac{2}{R^2}\int_0^R \varepsilon_s r\mathrm{d}r \qquad \text{Eq. 6.3}$$

At each measuring point, 20 groups of data were collected in order to ensure accuracy and repeatability. Each group had 32,768 data points with detecting frequency of 50kHz.

Ozone generation and testing

Electronic corona discharge ozone generator (Model AE15M, manufactured by Absolute Ozone Inc.) was applied to generate ozone using bottled oxygen as the gas supply in this work. The O_2-O_3 mixture gas produced by the ozone generator was mixed into the primary fluidizing air before entering the fluidized beds, shown in Figure 7.1. After passing a fairly long path and several L-bends in the primary air feeding pipeline, ozone was considered to be mixed thoroughly. The ozone generator's potentiometer setting was fixed and the primary air flowrate was constant in each experimental run. Thus the initial ozone concentrations in the fluidizing air can be adjusted effectively by a rotameter in the oxygen supply stream.

In order to prevent ozone decomposing in the sampling process, ozone-inert materials were adopted, e.g., aluminium, brass, stainless steel and Teflon. Although aluminium and brass would be oxidized by ozone, an inert oxide layer can form quickly. The schematic diagram of the ozone sampling system is shown in the upper-right corner of Figure 7.1. Brass tubes (6mm o.d., 0.36mm wall thickness and 15.0cm length) were inserted horizontally into the column as sampling probes. The tip of the sampling probe is covered with stainless wire mesh to prevent particles leaking to the ozone analyser. There is a vacuum pump inside the ozone analyser to withdraw sample gas continuously. The sampling gas velocity is up to 1.5LPM, low enough to assure minimal disturbance to the gas/solids flow. High pressure purging air of 689.5kPa was used to clean the particle cake possibly formed on the probe tip before every sampling.

An ozone analyser (Model 49i, Thermo Electron Inc.) based on the UV photometric method was used to measure ozone concentrations in the sample gas. The UV light source used in ozone photometers is 253.7nm from a low-pressure Hg discharge lamp. At this wavelength, the absorptivity of ozone is very close to unity and with little interference from other gases (Seinfeld and Pandis 2006). The analyser is a dual-cell photometer, having both sample and reference air flowing at the same time, with the internal surfaces coated with polyvinylidine fluoride (PVDF) to ensure that ozone undergoes no decomposition during testing. A single test lasted 1min and generated 15 data points. Five tests were required at each measuring position in order to ensure accuracy and repeatability.

Preparation of catalysts

Ozone decomposes very slowly at room temperature (20℃) in the absence of catalysts or ultraviolet (Wojtowicz 2005), and the gas residence time is only up to 3s in this study. so catalysts are necessary. It can be assumed that ozone decomposes only when contacting with catalysts.

Ferric oxide was usually used as the catalyst in the previous ozone decomposition research (Jiang, Bi et al. 1991, Ouyang, Li et al. 1995, Wang, Wang et al. 2014), as well as being used in this study. FCC particles (Geldart Group A particles) were chosen as the catalyst carriers due to their wide applications. The FCC particles were first impregnated in a 40wt% $Fe(NO_3)_3$ solution for 12 h, and then the wet particles were dried at 120^{o}C for 6 h in an oven followed by calcination at 450^{o}C for 4 h. After calcination, ferric nitrate converted to ferric oxide loaded on the particles. A ball mill was used to break up the agglomerates formed during calcination. The particles processed by the ball mill were sifted using a sieve with pore opening of 250μm. The impregnated particles were blended with the original FCC particles which have negligible catalytic activity, in order to adjust the overall catalytic activity. The particle information is shown in Table 7.1.

Table 7.1 Particle information

Apparent density [kg/m^3]	1780	Bulk density [kg/m^3]	890
d[4,3], [*μm*]	106.3	*d*[3,2], [*μm*]	78.6
Particle size distribution (Vol.%)			
Diameter [*μm*]	Vol.%	Diameter [*μm*]	Vol.%
11.11 - 17.05	0.81	105.24 - 117.13	8.78
17.05 - 23.51	1.32	117.13 - 130.37	8.82
23.51 - 32.41	2.64	130.37 - 145.10	8.34
32.41 - 44.69	5.2	145.10 - 161.5	7.27
44.69 - 55.36	5.88	161.5 - 179.75	5.75
55.36 - 68.58	8.75	179.75 - 200.06	4.02
68.58 - 84.96	12.32	200.06 - 222.66	2.43
84.96 - 94.56	7.53	222.66 - 247.83	1.22
94.56 - 105.24	8.29	247.83 - 307.00	0.63

Frye, Lake et al. (1958) reported that the apparent reaction rate constants k_r of a first order reactions can be determined in a small integral reactor (a fixed-bed reactor) by the equation below, if it runs as a plug-flow reactor isothermally with minimal transport gradients.

$$k_r = \frac{Q_g \rho_p}{m_c} \ln \frac{C_{in}}{C_{out}} \qquad \text{Eq. 7.4}$$

where Q_g is the volumetric gas flowrate (m^3/s), ρ_p is the particle density (kg/m^3), and m_c is the mass of catalyst (kg) and C_{in}, C_{out} are inlet and outlet ozone concentrations. Therefore, a small fixed-bed reactor (16mm i.d.) made of brass pipe was used to measure the reaction rate constant k_r, shown in Figure 7.1. A humidity meter and a thermometer were used to monitor the relative humidity and temperature of the air supply respectively. The relative humidity was maintained at 19%, and the temperature remained at 20℃ without significant fluctuation. Therefore, the moisture and temperature would not influence the reaction rate in the experiments. The k_r of the catalysts in the experiments was 4.2 s^{-1}. The reaction rate constant was tested after every experimental run, showing no obvious variance.

Measuring positions

In order to map the entire column's solids holdup and conversion distributions, several sampling ports were opened at different elevations and 6 radial measuring positions were selected on each axial level (listed in Table 7.2). The optical fibre probes and ozone sampling probes shared these sampling ports.

Table 7.2 Axial and radial sampling locations of the fluidized beds

	Distance from gas distributor [m]	
Port No.	76mm i.d. column	152mm i.d. column
1	0.25	0.22
2	0.56	0.53
3	1.02	0.79
4	1.47	1.04
5	1.93	1.30
6	2.39	1.55
7		1.80
8		2.34

Radial sampling locations, r/R [-]					
0	0.316	0.548	0.707	0.837	0.950

7.3. Results and discussion

7.3.1. Axial and radial profiles of ozone concentration

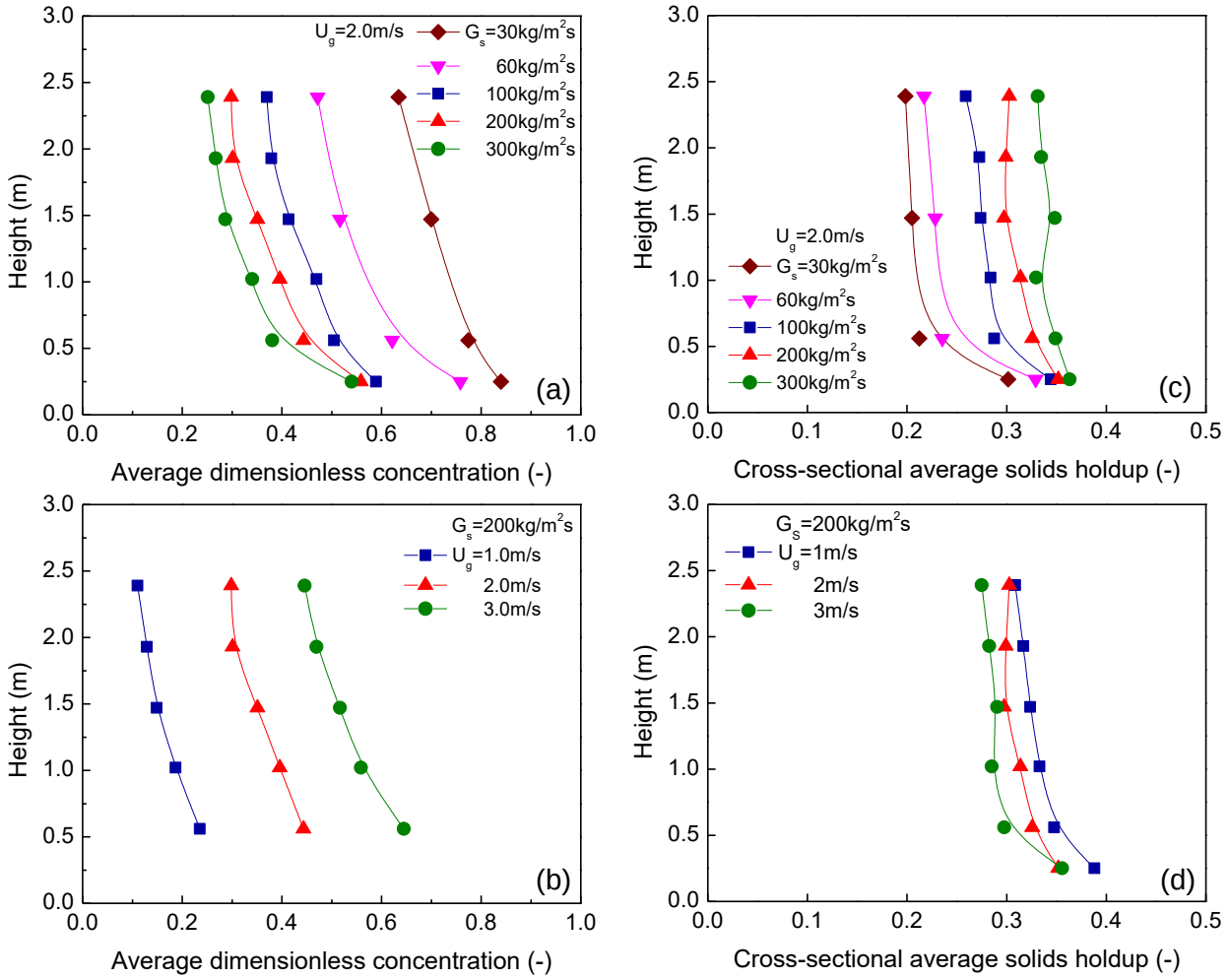

Figure 7.2 Axial profiles of average dimensionless ozone concentration (a, b) and corresponding solids holdup (c, d)

Axial profiles of ozone concentration and solids holdup at various superficial gas velocities (U_g) and solids circulation rates (G_s) are displayed in Figure 7.2. The cross-sectional average values of ozone concentrations and solids holdups were obtained by integrating the local values of all the radial positions based on the cross-sectional area. As shown in Figure 7.2(c) and (d), the CTFB successfully achieved a gas/solids flow with high G_s up to 300 kg/m^{2}s, while maintaining dense solids holdup ranging from 0.2 to 0.35. The axial distributions of solids holdup are significantly uniform, when G_s is larger than 100 kg/m^{2}s. The formation mechanism of this dense upflow can be elaborated by a pressure drop analysis along the entire system (Bi and Zhu 1993).

After particles enter the enlarged column, the flow's solids holdup would be significantly reduced due to space expansion and velocity acceleration, resulting in a largely decreased pressure drop in the middle and upper columns. Since the pressure heads of the blower and the solids inventory remain constant during operation, the pressure drop of the bottom column should increase in order to keep the system pressure balance. As a result, the solids holdup in the bottom column can be considerably increased. The dense gas/solids upflow in the bottom column could have highly efficient gas-solids contacting and favourable mass transfer characteristics, so it should receive more research in respect of reactor performance.

The dimensionless ozone concentration (C/C_0) equals the measured ozone concentration over the initial ozone concentration before entering the fluidized bed. So the ozone conversion equals one minus the dimensionless ozone concentration. The axial profiles of ozone concentration are shown in Figure 7.2(a) and (b). It is seen that the ozone concentrations decrease with increasing elevation in all conditions. In detail, the ozone concentrations decrease dramatically in the bottom region from the distributor to the height of 0.5m, presumably due to the entrance effect of vigorous gas-solids contacting and high reactant concentration.

Furthermore, the operating conditions (G_s and U_g) affect the distributions of ozone concentration. For instance, the concentrations decrease with increasing G_s and the associated solids holdup. Under the condition of higher solids holdup, the reactant-gas would have more opportunity to contact with the catalyst-solids, resulting in lower ozone concentrations (i.e., higher ozone conversions). The results indicate that there exists a relationship between the ozone concentrations and the solids holdups in the CTFB, like CFB risers and downers (Ouyang, Li et al. 1995, Wang, Zhu et al. 2015). The clear correlation between the ozone conversions and the solids holdups are studied next.

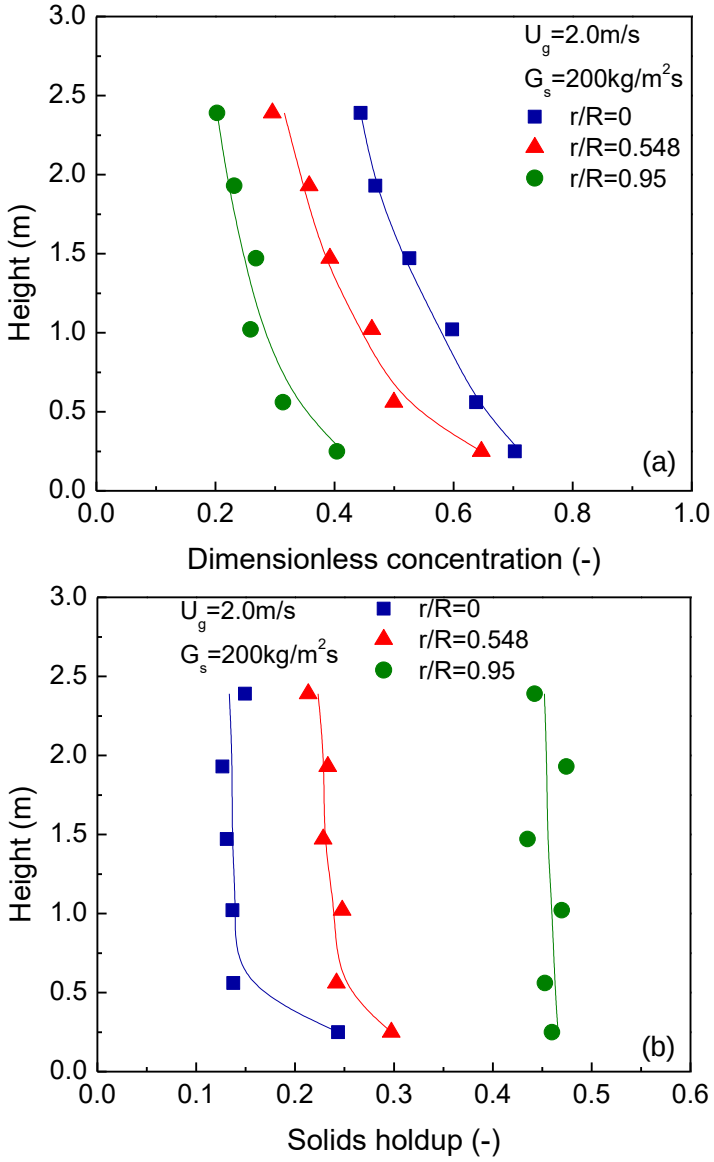

Figure 7.3 Axial distributions of local ozone concentration (a) and corresponding solids holdup (b) at different radial positions

The typical axial profiles of local ozone concentration and corresponding solids holdup at different radial positions for U_g of 2.0 m/s and G_s of 200 kg/m^{2}s are presented in Figure 7.3. These three radial positions (r/R=0, 0.548 and 0.95) represent the central, middle and wall regions respectively. As shown in Figure 7.3(a), the central region shows the highest ozone concentrations on every elevation, followed by the middle region, whereas the wall region shows the lowest ozone concentrations.

The ozone concentration distributions are related to the solids holdup distributions in the CTFB. Figure 7.3(b) illustrates that the solids holdup increases from the centre to the wall, corresponding to the radial gradient of ozone conversion. In the central region, the solids holdups are lower, so that the unconverted ozone concentrations are relatively higher. On the contrary, the higher solids holdups lead to the lower concentrations in the wall region. Moreover, it is also found that the axial distribution of local solids holdup at each radial position is generally uniform above the bottom section.

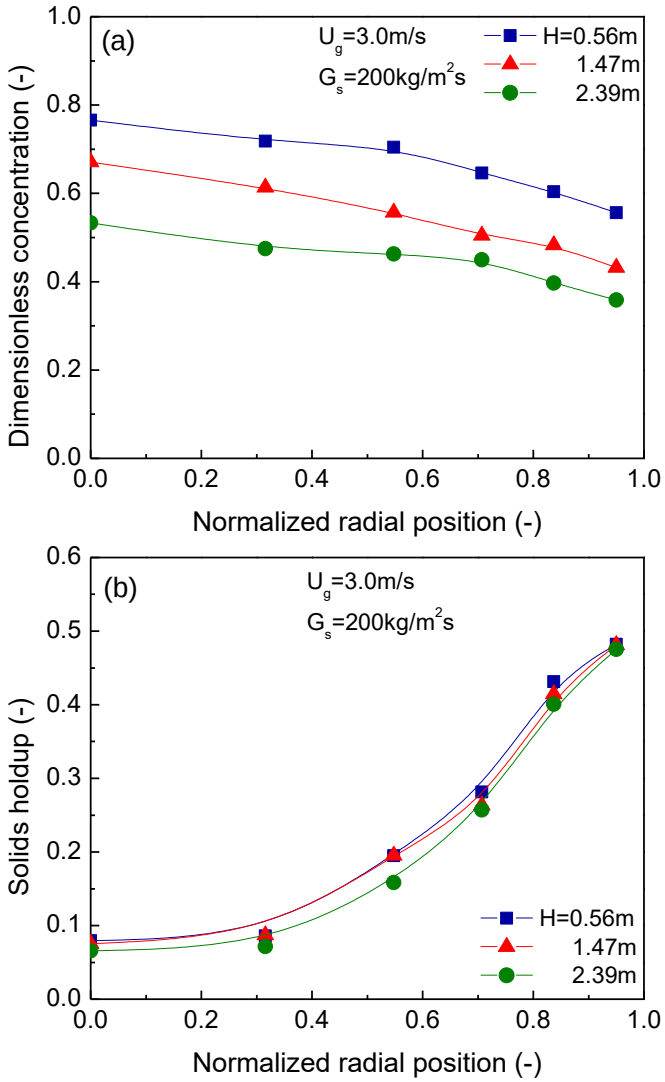

Figure 7.4 Radial profiles of ozone concentration (a) and corresponding solids holdup (b) at different elevations

The radial profiles of ozone concentration at different elevations for U_g of 3.0 m/s and G_s of 200 kg/m^{2}s are presented in Figure 7.4(a). It is shown that the ozone concentration continuously decreases from the centre to the wall on every elevation. Also, the local ozone concentrations decrease with increasing elevation at all radial positions, which is consistent with the trend in Figure 7.3(a). As the same as the axial profiles, the radial profiles of ozone concentration can be explained by the solids holdup distributions as well. Figure 7.4(b) shows the radial profiles of solids holdup at the same positions and operating conditions as those in the ozone concentration profiles. It is seen that the solids holdups monotonically increase from the centre to the wall. The lower solids holdups in the core region result in higher unconverted ozone concentrations, whereas the higher solids holdups near the wall lead to lower ozone concentrations. It is noted that CFB risers also have non-uniform radial solids holdup distributions which possibly causes a "shielding effect" in the dense wall region, hampering the reactant-gas throughflow (Bi, Jiang et al. 1992). Consequently, the ozone concentration in the wall region stays at low values and slightly decreases with increasing elevation (Ouyang, Li et al. 1995, Wang, Wang et al. 2014). However, unlike CFB risers, the ozone concentration exhibits an appreciable change in the wall region of the CTFB, likely due to the widely expanded turbulent flow in the whole cross-section and the lateral gas exchange.

7.3.2. Effect of operating conditions on ozone concentration

The effect of solids circulation rate (G_s) on the radial distributions of ozone concentration and solids holdup is shown in Figure 7.5. The radial profiles of ozone concentration were obtained at three different elevations at U_g of 2.0 m/s. Since the axial flow structure of CTFB is uniform as discussed above, the radial profiles of solids holdup at one elevation are presented.

Generally, the ozone concentrations decrease from the centre towards the wall, as shown in Figure 7.5(a) (b) and (c). In detail, the ozone concentration profiles at G_s=30 kg/m^{2}s and 60 kg/m^{2}s remain nearly constant in the core region, while dropping sharply closing to the wall. It is attributed to the radial profiles of solids holdup that have a flat core region and a clear-cut wall region, as shown in Figure 7.5(d). In contrast, when $G_s \geq$100 kg/m^{2}s, the ozone concentrations decrease towards the wall at an almost constant rate due to the steady increasing solids holdups.

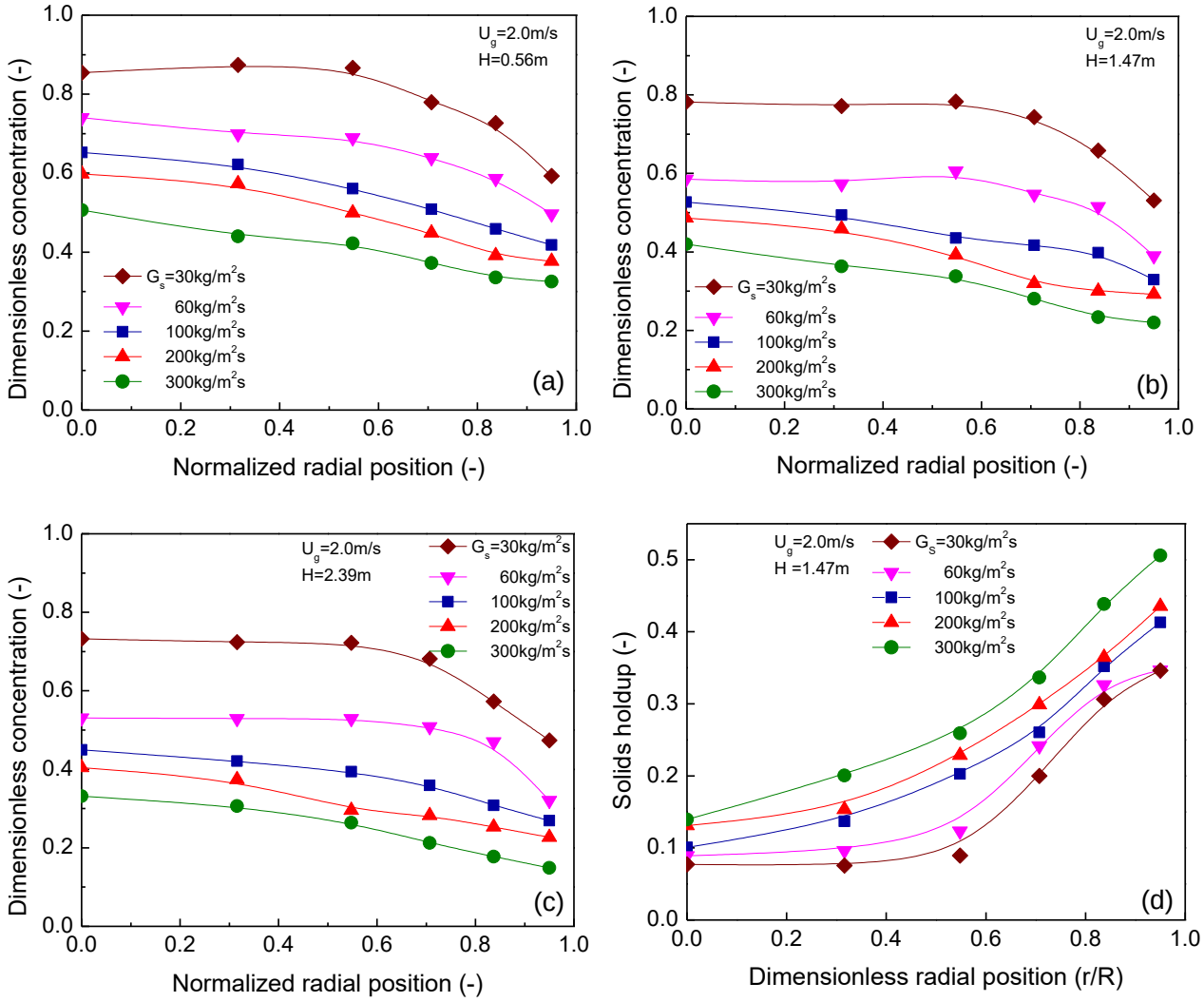

Figure 7.5 Effect of solids circulation rate on the distributions of ozone concentration (a, b, c) and solids holdup (d)

Furthermore, the ozone concentrations are found to decrease (i.e. the conversions increase) with increasing G_s and the associated solids holdup on all elevations. At higher G_s, The total gas-solids contacting area is larger due to the higher solids holdup, leading to lower ozone concentrations. In addition, it is found that the concentration decreasing rate slows down with increasing G_s. As reported by Zhu and Zhu (2008), the dense upflow in CTFB is considered to reach a "saturation" state, and the increase of G_s is mainly due to the increase of particle upward velocity, not the increase of solids holdup. Accordingly, the gas-solids contacting presumably approaches a maximum under the extremely dense conditions. Therefore, the effect of G_s on ozone conversions turns out to be less significant at larger G_s.

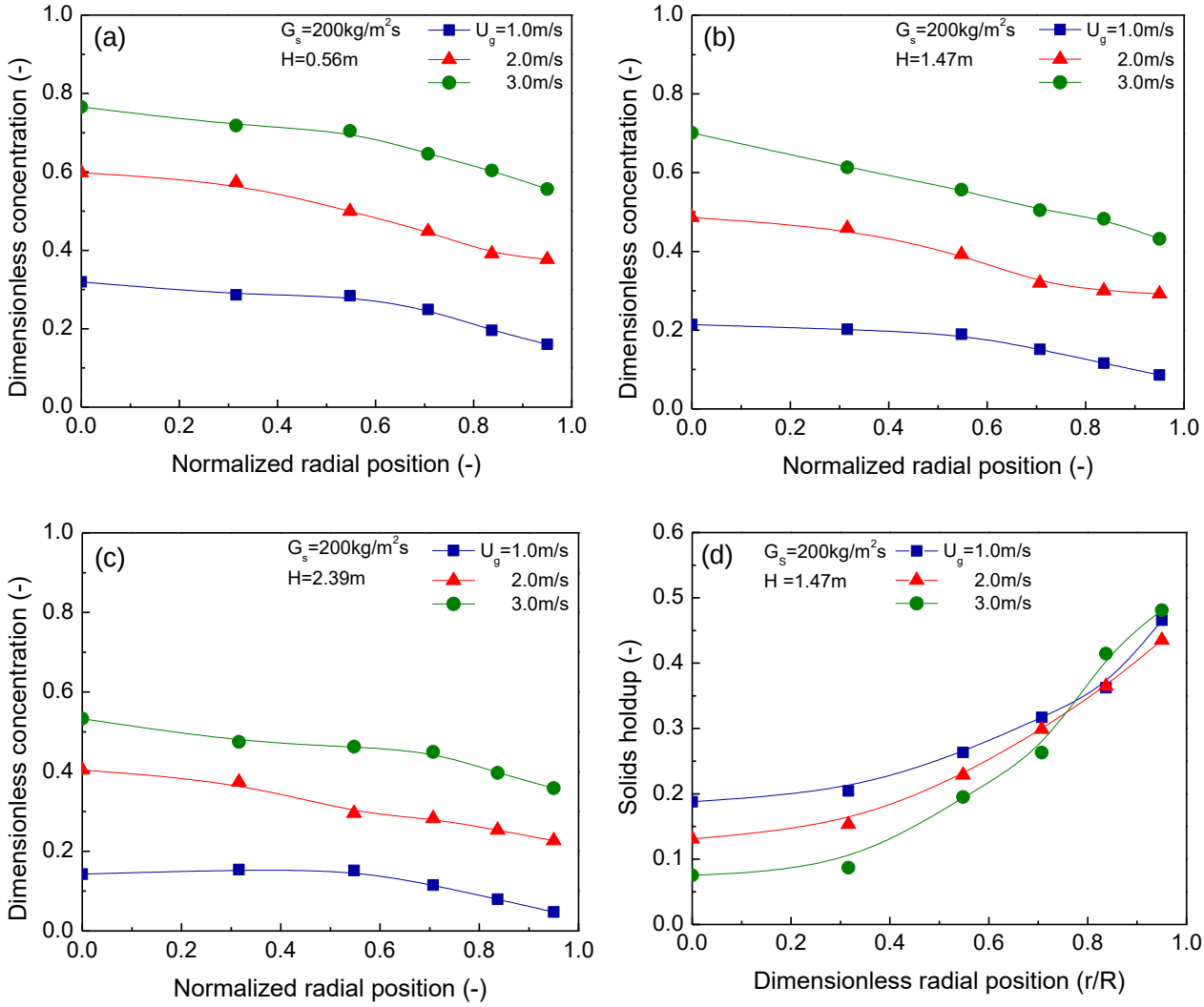

Figure 7.6 Effect of superficial gas velocity on the distributions of ozone concentration (a, b, c) and solids holdup (d)

The effect of U_g on the ozone concentration radial distributions at three different elevations is displayed in Figure 7.6(a) (b) and (c). The representative radial profile of solids holdup under the given condition is shown in Figure 7.6(d). In general, the unconverted ozone concentrations increase with increasing U_g on all elevations. It is mainly because the reactant-gas residence time becomes shorter with increasing U_g, thereby lower ozone conversions. Moreover, by comparing the ozone concentration profiles in Figure 7.5 and Figure 7.6, the variation of ozone concentration with U_g is found to be larger than that with G_s in the range of 100 - 300 kg/m^{2}s. It suggests that the effect of U_g is more significant than the effect of G_s in the CTFB for a gas-phase catalytic reaction.

7.3.3. Correlation between ozone conversions and solids holdups

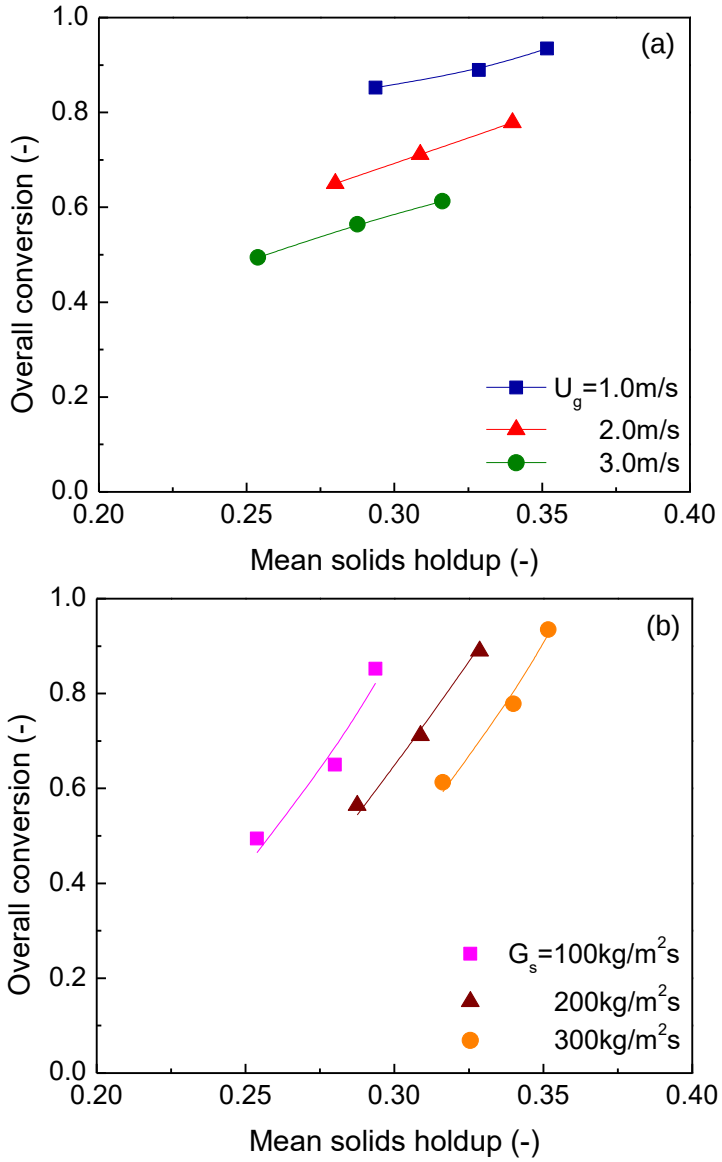

Figure 7.7 Correlation between overall ozone conversions and mean solids holdups

As discussed above, the ozone concentrations are strongly related with the solids holdups in the CTFB. The correlations between the overall conversions and the mean solids holdups of the entire bed at different U_g are shown in Figure 7.1(a). It is seen that the ozone conversions increase with increasing mean solids holdups at all U_g. In detail, there appears to be a linear relationship between them when G_s is beyond 100 kg/m^{2}s. In addition, the correlation line moves downwards with increasing U_g, due to the decreasing gas residence time and solids holdup. The slope of the linear fitting remains nearly the same for the different gas velocities, suggesting similar flow structures.

Figure 7.1(b) exhibits the correlations at various G_s ranging from 100 kg/m^{2}s to 300 kg/m^{2}s. The overall conversions increase almost linearly with the mean solids holdups under all conditions. The slopes of the fittings are consistent with varying G_s as well. However, the magnitude of the slope at a given G_s is larger than that at a given U_g, implying U_g affects the ozone conversions more effectively than G_s in the CTFB.

7.3.4. Reactor performance of CTFB

In order to evaluate the reactor performance of the CTFB, more comprehensive investigations are needed. As the conversions of a gas-phase catalytic reaction are affected by the reactant-gas residence time, reaction kinetics and gas-solids mass transfer collectively, Damköhler numbers ($Da=k_r\varepsilon_s H/U_g$) combining the gas residence time and the reaction rate constant are plotted against the overall conversions in Figure 7.8. Since no well-developed numerical model for CTFBs is available at the moment, the ideal reactor models, a plug-flow reactor (PFR) and a continuous stirred-tank reactor (CSTR), are adopted as references to assess the reactor performance. The formulas for the conversions in a PFR and a CSTR are derived (Jiang, Bi et al. 1991):

PFR: $$X_{PFR}=1-\exp(-Da) \quad \text{Eq. 7.5}$$

CSTR: $$X_{CSTR}=\frac{Da}{1+Da} \quad \text{Eq. 7.6}$$

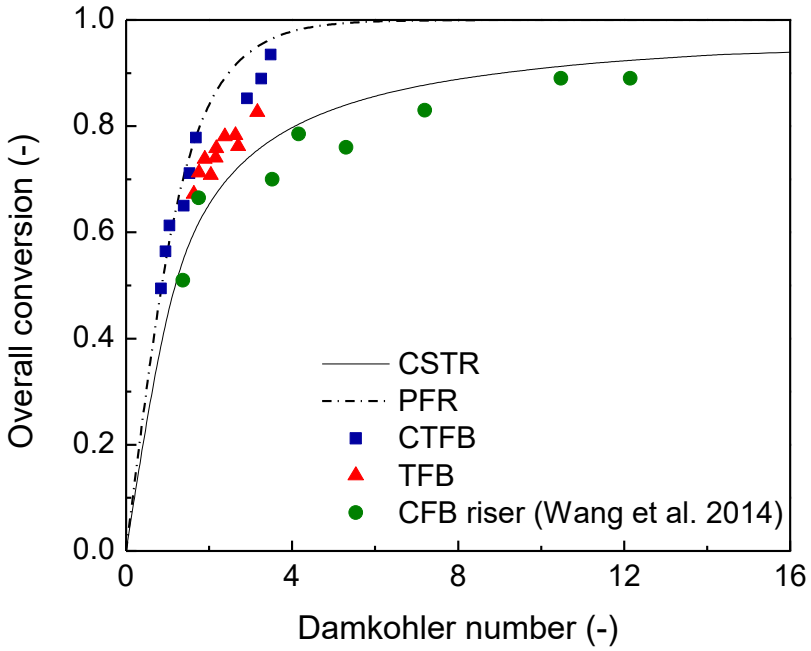

Figure 7.8 Relationship of overall ozone conversions and Damköhler numbers in the CTFB

In Figure 7.8, the CTFB has slightly lower conversions than the PFR, but significantly higher conversions than the CSTR. In other words, the reactor performance of CTFB is very close to that of the PFR, while being evidently better than that of the CSTR. The deviation of the CTFB from a PFR at a given *Da* can be attributed to different gas-solids mass transfer rate and contact efficiency that are greatly affected by the hydrodynamics. As stated before, the CTFB exhibits a uniform flow pattern in the axial direction, which is one of the typical characteristics of a PFR. In spite of the non-uniform radial distribution of solids holdup, the relatively high solids holdup in the central region provides sufficient gas-solids contacting area, while eliminating reactant-gas bypassing. Furthermore, unlike BFBs, TFBs and CFB risers that have obvious gas/solids back-mixing, CTFBs have almost no net downward solids flux (Qi, Barghi et al. 2012), which likely avoids axial dispersion of gas carried by the solids downflow. These hydrodynamic features of the CTFB fairly fit the characteristics of a PFR, thereby resulting in the similar reactor performance to that of a PFR.

The conversions of a TFB and a CFB riser are also plotted against *Da* in Figure 7.8 for comparison. The results of the CFB riser are cited from the work of Wang, Wang et al. (2014). Although the vigorous gas-solids interaction in the TFB leads to relatively favourable reactor performance, the TFB deviates from a PFR due to the reactant-gas back-mixing caused by the severe solids downflow (Du, Fan et al. 2002). On the other hand, in the CFB riser, the reactant-gas flowing through the extremely dilute core region at high velocity is considered as bypassing to some extent. Despite the reduction of gas/solids back-mixing in the central region, the gas back-mixing still exists in the wall region due to the noticeable downflowing solids (Liu, Grace et al. 1999). As a consequence, the reactor performance of CFBs is much poorer than that of a PFR.

The reactor performance of a fluidized bed for gas-phase catalytic reactions is essentially determined by the mass transfer, or to be more specific, the gas-solids contacting. Therefore, the reactor performance can be quantitatively evaluated by the gas-solids contact efficiency (Jiang, Bi et al. 1991, Ouyang, Li et al. 1995, Wang, Wang et al. 2014). Sun and Grace (1990) proposed a calculation method for gas-solids contact efficiency. Since the gas-solids contacting and mixing in a fluidized bed deviate from those in a PFR at the same gas velocity, the amount of catalysts ($V_{c,f}$) in a fluidized bed required to achieve the same conversion with the same gas

flowrate and reaction rate constant should be larger than the catalyst amount ($V_{c,p}$) in a PFR. Therefore, the ratio of $V_{c,p}/V_{c,f}$ can evaluate the utility efficiency or contact efficiency of catalysts in different fluidized bed reactors. The higher contact efficiency, the better the reactor performance is, i.e., the less the fluidized bed deviates from a PFR. $V_{c,f}$ comes from experimental values, whereas $V_{c,p}$ is calculated by the following equation in which Q_g is the operating gas flowrate, k_r is the reaction rate constant, C_{in} is the initial ozone concentration and C_{out} is the outlet ozone concentration.

$$V_{c,p} = \frac{Q_g}{k_r} \ln\left(\frac{C_{in}}{C_{out}}\right) \qquad \text{Eq. 7.7}$$

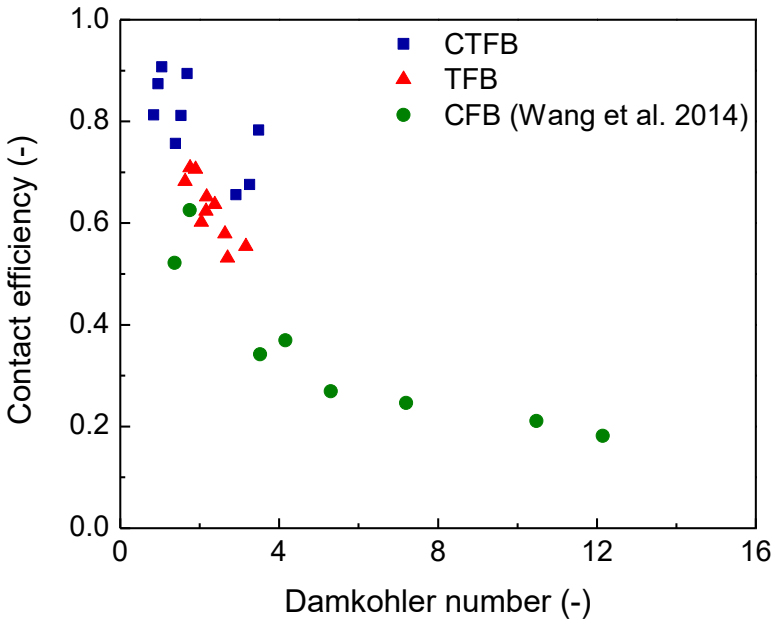

Figure 7.9 Gas-solids contact efficiencies of CTFB, TFB and CFB riser

The gas-solids contact efficiencies of the CTFB are presented and compared with those of a TFB and a CFB riser in Figure 7.9. It is clearly shown that the CTFB has the highest contact efficiency due to the dense solids concentration and homogeneous gas/solids mixing. The contact efficiencies of the TFB are lower but close to those of the CTFB. By analysing the instantaneous solids holdup signals in the CTFB and TFB, the CTFB has even more intense gas-solids interactions than the TFB, as discussed in Chapter 5. Besides, the continuous distribution of the magnitude of transient solids holdups in the CTFB suggests that the dense phase contains more

gas, and more solids disperse into the void, when compared the TFB. These hydrodynamic distinctions make the reactor performance of TFB poorer than that of CTFB. Moreover, in the CFB riser, the formation of clusters and the severe lateral segregation of gas and solids greatly reduce the amount of particles available for the reaction, accordingly lowering the gas-solids contact efficiency. Overall, the outstanding reactor performance of CTFB further proves the circulating turbulent fluidization as an individual flow regime that is distinctive to the other types of fluidized beds (Qi, Zhu et al. 2009, Zhu 2010).

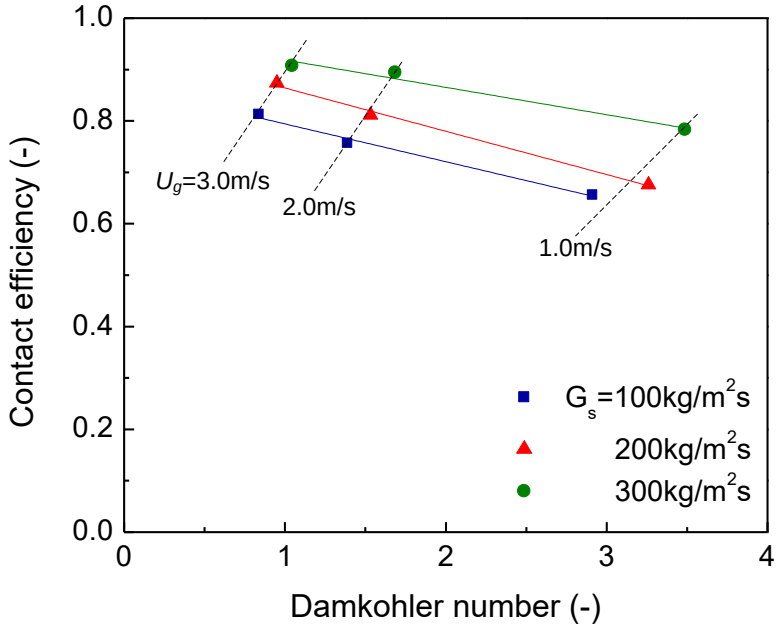

Figure 7.10 Gas-solids contact efficiencies of CTFB under various operating conditions

The effects of superficial gas velocity and solids circulation rate on the gas-solids contact efficiency of CTFB are shown in Figure 7.10. The contact efficiency is found to increase with increasing G_s. As the solids holdup increases with G_s in the CTFB, the increased solids holdup leads to enlarged gas-solids contacting area, i.e., higher contact efficiency. Furthermore, the higher G_s may provide more momentum to compel particles to flow upwards by the stronger particle-particle interaction (collision) in the CTFB. The increased solids holdup is considered to increase the effective viscosity of the upflowing suspension, thereby imposing more shear force to reduce the tendency of particles downflowing (Grace, Issangya et al. 1999). Therefore, there is no net downward solids flux in CTFBs (Qi, Barghi et al. 2012), which is favourable for the reactor performance.

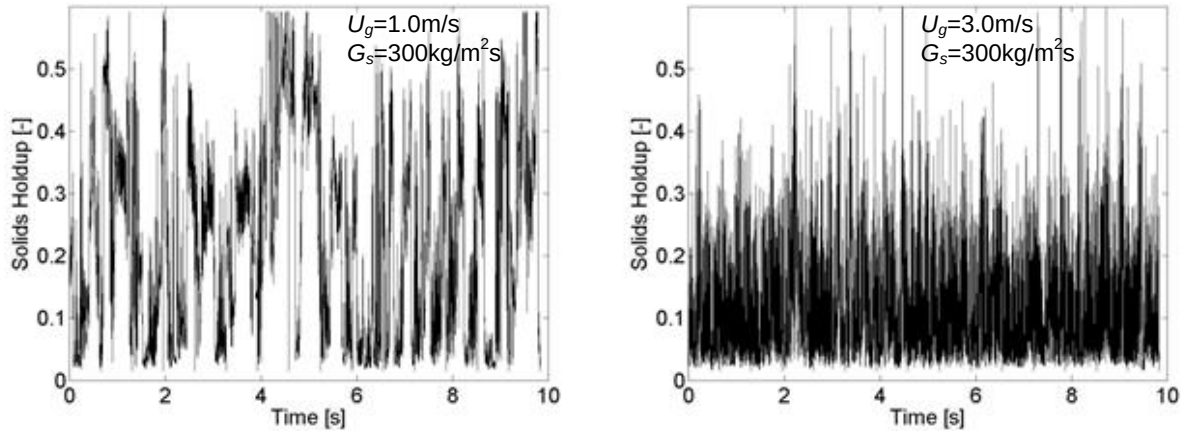

Figure 7.11 Instantaneous solids holdup signals in the CTFB at U_g=1.0 m/s and 3.0 m/s, and G_s=300 kg/m^{2}s

In Figure 7.10, it is also illustrated that the gas-solids contact efficiency increases with increasing U_g, due to the decreasing cluster size. The difference between the clusters at low and high gas velocities can be seen from the instantaneous solids holdup signals in Figure 7.11. The signals were acquired at G_s=300 kg/m^{2}s and U_g of 1.0 m/s and 3.0 m/s respectively. The cluster phase can be clearly observed at U_g=1.0 m/s in the form of individual peaks with noticeable width. In contrast, at U_g=3.0 m/s, the signals fluctuate at an extremely high frequency, indicating the homogeneously inter-diffused void phase and cluster phase. At low U_g, e.g., 1.0 m/s, the clusters hamper the gas-solids contacting, since some particles are "locked" in the clusters. At high U_g, e.g., 3.0 m/s, the clusters are reduced in size, or even broken down to dispersed particles by the stronger shear force, thereby enhancing the gas-solids contact efficiency.

7.4. Conclusions

The reactor performance of CTFB was studied for the first time in this work using the catalytic decomposition of ozone. The axial and radial profiles of ozone concentration were investigated at U_g of 1.0-3.0 m/s and G_s up to 300 kg/m^{2}s. In the axial direction, the unconverted ozone concentration decreased (i.e., the conversion increased) with increasing elevation. A large portion of reaction took place in the bottom region, due to the entrance effect. In the radial direction, the ozone concentration continuously decreased from the centre to the wall, which is determined by the non-uniform radial distribution of solids holdup.

The effects of operating conditions on the ozone concentration distributions were studied as well. The ozone concentration decreased (i.e., the conversion increased) with increasing G_s. This trend is attributed to the increase of solids holdup with increasing G_s, accordingly providing more gas-solids (reactant-catalysts) contacting area for the reaction. On the other hand, the ozone concentration increased with increasing U_g, mainly due to the decreasing reactant-gas residence time.

The overall conversions were clearly correlated with the mean solids holdup of the entire bed under various operating conditions. The relationship between them appears to be linear under all conditions, resulting from the homogeneous flow structure in the CTFB. The variation of ozone concentration with U_g is greater than that with G_s, indicating U_g is more influential in the CTFB for gas-phase catalytic reactions.

Furthermore, the overall ozone conversions were plotted against Damköhler numbers to evaluate the reactor performance of CTFB. The CTFB has outstanding reactor performance that is very close to a plug-flow reactor, owing to the advantageous hydrodynamics of CTFB, such as uniform flow structure, no reactant-gas bypassing and negligible gas back-mixing. The reactor performance was also quantitatively assessed by the gas-solids contact efficiency. It is clearly shown that the contact efficiency of CTFB is evidently higher than other types of fluidized beds. Thus, CTFBs would draw great interest from fluidization research and industrial applications.

Nomenclature

C	local ozone concentration [ppm]
C_0, C_{in}	initial ozone concentration [ppm]
C_{out}	outlet ozone concentration [ppm]
C/C_0	dimensionless ozone concentration [-]
Da	Damkohler number, $k_r\bar{\varepsilon}_s H/U_g$ [-]
D_T	bed diameter [mm]
G_s	solids circulation rate [kg/m^{2}s]
H	axial coordinate, or distance from the gas distributor [m]
H_0	static bed height [m]
k_r	reaction rate constant based on particle volume, first-order [s^{-1}]
m_c	mass of catalysts [g]
r	radial coordinate [m]
R	column radius [m]
r/R	dimensionless sampling position [-]
U_g	superficial gas velocity [m/s]
$V_{c,f}$	volume of catalyst in a fluidized bed [m^3]
$V_{c,p}$	volume of catalyst in the ideal plug flow reactor [m^3]
Q_g	gas flowrate [m^3/s]
Greek letters	
ε_s	local solids holdup [-]
$\bar{\varepsilon}_s$	mean solids holdup [-]
ρ_p	particle density [kg/m^3]

References

Bi, H., N. Ellis, I. Abba and J. Grace (2000). A state-of-the-art review of gas–solid turbulent fluidization. *Chemical Engineering Science* **55**(21): 4789-4825.

Bi, H., P. Jiang, R.-H. Jean and L.-S. Fan (1992). Coarse-particle effects in a multisolid circulating fluidized bed for catalytic reactions. *Chemical Engineering Science* **47**(12): 3113-3124.

Bi, H. and J. Zhu (1993). Static instability analysis of circulating fluidized beds and concept of high‐density risers. *AIChE Journal* **39**(8): 1272-1280.

Chavarie, C. and J. R. Grace (1975). Performance analysis of a fluidized bed reactor. II. Observed reactor behavior compared with simple two-phase models. *Industrial & Engineering Chemistry Fundamentals* **14**(2): 79-86.

Du, B., L. S. Fan, F. Wei and W. Warsito (2002). Gas and solids mixing in a turbulent fluidized bed. *AIChE Journal* **48**(9): 1896-1909.

Frye, C., W. Lake and H. Eckstrom (1958). Gas‐solid contacting with ozone decomposition reaction. *AIChE Journal* **4**(4): 403-408.

Frye, C. and O. E. Potter (1976). Experimental investigation of models for fluidized bed catalytic reactors. *AIChE Journal* **22**(1): 38-47.

Grace, J. R. (2000). Reflections on turbulent fluidization and dense suspension upflow. *Powder Technology* **113**(3): 242-248.

Grace, J. R. and H. Bi (1997). Introduction to circulating fluidized beds. *Circulating Fluidized Beds*, Springer**:** 1-20.

Issangya, A., D. Bai, H. Bi, K. Lim, J. Zhu and J. Grace (1999). Suspension densities in a high-density circulating fluidized bed riser. *Chemical Engineering Science* **54**(22): 5451-5460.

Jiang, P., H. Bi, R. H. Jean and L. S. Fan (1991). Baffle effects on performance of catalytic circulating fluidized bed reactor. *AIChE Journal* **37**(9): 1392-1400.

Lim, K., J. Zhu and J. Grace (1995). Hydrodynamics of gas-solid fluidization. *International Journal of Multiphase Flow* **21**: 141-193.

Liu, J., J. R. Grace, H. Bi, H. Morikawa and J. Zhu (1999). Gas dispersion in fast fluidization and dense suspension upflow. *Chemical Engineering Science* **54**(22): 5441-5449.

Liu, J., J. R. Grace and X. Bi (2003). Novel multifunctional optical‐fiber probe: I. Development and validation. *AIChE Journal* **49**(6): 1405-1420.

Ouyang, S., X. G. Li and O. Potter (1995). Circulating fluidized bed as a catalytic reactor: experimental study. *AIChE Journal* **41**(6): 1534-1542.

Pärssinen, J. and J. X. Zhu (2001). Axial and radial solids distribution in a long and high‐flux CFB riser. *AIChE Journal* **47**(10): 2197-2205.

Qi, M., S. Barghi and J. Zhu (2012). Detailed hydrodynamics of high flux gas–solid flow in a circulating turbulent fluidized bed. *Chemical Engineering Journal* **209**: 633-644.

Qi, X., H. Zhu and J. Zhu (2009). Demarcation of a new circulating turbulent fluidization regime. *AIChE Journal* **55**(3): 594-611.

Reh, L. (1995). New and efficient high‐temperature processes with circulating fluid bed reactors. *Chemical Engineering & Technology* **18**(2): 75-89.

Seinfeld, J. and S. Pandis (2006). Atmospheric Chemistry and Physics, A Wiley-Inter Science Publication, John Wiley & Sons Inc, New York.

Sun, G. and J. R. Grace (1990). The effect of particle size distribution on the performance of a catalytic fluidized bed reactor. *Chemical Engineering Science* **45**(8): 2187-2194.

Wang, C., G. Wang, C. Li, S. Barghi and J. Zhu (2014). Catalytic ozone decomposition in a high density circulating fluidized bed riser. *Industrial & Engineering Chemistry Research* **53**(16): 6613-6623.

Wang, C., J. Zhu and S. Barghi (2015). Performance evaluation of high density riser and downer: Experimental study using ozone decomposition. *Chemical Engineering Journal* **262**: 478-489.

Wang, C., J. Zhu, S. Barghi and C. Li (2014). Axial and radial development of solids holdup in a high flux/density gas–solids circulating fluidized bed. *Chemical Engineering Science* **108**: 233-243.

Wojtowicz, J. A. (2005). Ozone. *Encyclopedia of Chemical Technology*. Kirk-Othmer, John Wiley & Sons.

Zhang, H., P. Johnston, J.-X. Zhu, H. De Lasa and M. Bergougnou (1998). A novel calibration procedure for a fiber optic solids concentration probe. *Powder Technology* **100**(2): 260-272.

Zhu, H. and J. Zhu (2008). Gas‐solids flow structures in a novel circulating‐turbulent fluidized bed. *AIChE Journal* **54**(5): 1213-1223.

Zhu, J. (2010). Circulating turbulent fluidization—a new fluidization regime or just a transitional phenomenon. *Particuology* **8**(6): 640-644.

Zhu, J., M. Qi and S. Barghi (2013). Identification of the flow structures and regime transition in gas–solid fluidized beds through moment analysis. *AIChE Journal* **59**(5): 1479-1490.

Zhu, J. X. and H. T. Bi (1995). Distinctions between low density and high density circulating fluidized beds. *The Canadian Journal of Chemical Engineering* **73**(5): 644-649.

Chapter 8
Comparative study on reactor performances of various fluidized beds

8.1. Introduction

Many industrial processes use gas-solid fluidized-bed reactors (Zhu and Cheng 2006). With fluidizing gas velocity increasing, the gas-solid fluidization can be generally divided into several regimes: particulate fluidization, bubbling fluidization (bubbling fluidized bed, BFB), turbulent fluidization (turbulent fluidized bed, TFB), fast fluidization (circulating fluidized bed, CFB) and pneumatic transport (Lim, Zhu et al. 1995). In addition, new flow regimes, e.g., dense suspension upflow (DSU) (Grace, Issangya et al. 1999) and circulating turbulent fluidization (Qi, Zhu et al. 2009), have been proposed and situated on typical regime maps based on the distinctive hydrodynamic characteristics and the unique operating processes. In contrast with the conventional CFB risers where gas and solids flow upwards co-currently, the recently proposed CFB downers adopt co-current gas/solids downflow (Zhu, Yu et al. 1995).

A good understanding of fluidized-bed reactor performance is very necessary to design and optimize commercial fluidization processes. Experimental studies using chemical reactions can provide more direct and reliable information on fluidized-bed reactor performance than other methods (Li, Ray et al. 2013). However, to the author's knowledge, insufficient research has been done in this aspect, which hampers the development of modelling work. As a consequence, designs of industrial fluidized beds are still mostly based on empirical equations and engineers' experiences (Knowlton, Karri et al. 2005). The lab-scale research of reactor performance has been mostly using catalytic ozone decomposition as the model reaction due to its simplicity in reaction kinetics (i.e., a first order reaction happening in ambient conditions) and negligible heat effect (Ouyang, Li et al. 1995).

For the gas-phase catalytic reactions in a gas-solid fluidized-bed, the reactor performance is considered to be not only affected by the reaction kinetics, but also by the hydrodynamics that can essentially influence the gas-solids mass transfer and contacting. For instance, it is well-known that BFBs have a dense phase flow structure with dispersed bubbles, resulting in high mass transfer resistance between the bubble phase and the dense phase. Besides, there are much

less particles inside the bubbles than the surrounding dense solid phase, leading to lower reactant conversion in the bubbles (Chavarie and Grace 1975). More experimental reactor performance studies of BFBs have been done by Frye, Lake et al. (1958), Lin, Arastoopour et al. (1986), Van Lare, Piepers et al. (1990).

Turbulent fluidization is regarded as an individual flow regime (Bi and Fan 1992) due to many distinct features and wide applications, such as Fischer-Tropsch synthesis, acrylonitrile, maleic and phthalic anhydride, ethylene dichloride and various ore roasting (Bi, Ellis et al. 2000). TFBs have vigorous interactions between the comparable dilute and dense phases, so that the mass transfer tend to reach a maximum, likely further leading to favourable reactor performance (Grace 1990). However, very few studies have experimentally proven the advantage of TFB reactor performance. Sun and Grace (1990) investigated the reactor performance of a TFB based on the outlet reactant conversions, but no spatial conversion distribution was provided.

Circulating fluidized beds (commonly representing CFB risers) have been successfully applied in combustion, gasification, fluid catalytic cracking (FCC) and so on (Reh 1995). The typical FCC riser reactors are high-density/flux circulating fluidized beds (HDCFBs) operated at high gas velocities from 6 to 28 m/s and high solids circulation rates from 400 to 1200 kg/m^{2}s with relatively high solids holdups of typically 0.1-0.2 (Zhu and Bi 1995). To distinguish from HDCFBs, those operated at low gas velocities and low solids circulation rates are named as low density circulating fluidized beds (LDCFB). Both LDCFBs and HDCFBs have non-uniform radial flow structures (Issangya, Bai et al. 1999, Wang, Zhu et al. 2014), likely resulting in reactant-gas bypassing through the dilute core region and obvious solids back-mixing in the dense wall region. In spite of these disadvantages, CFBs possess many advantages, such as high gas/solids throughputs, high turndown ratios and independent control of gas and solids. The reactor performance of LDCFBs was studied by Ouyang, Li et al. (1995) and Li, Ray et al.(2013) with low solids circulation rates ranging from 50 to 200 kg/m^{2}s. The reactor performance of a HDCFB riser was reported by Wang et al. (2014a) for the first time, providing conversion distributions at gas velocities of 5-9 m/s and solids circulation rates of 100-1000 kg/m^{2}s.

A novel fluidized bed, circulating turbulent fluidized bed (CTFB), with a distinctive operating mode was recently developed by Zhu and Zhu (2008a). The word “circulating” in its name

suggests that it operates with solids circulations, while "turbulent" characterizing the comparable hydrodynamics to TFBs, e.g., high solids holdup and vigorous gas-solids interaction. The experimental results (Zhu and Zhu 2008a, Qi, Barghi et al. 2012) demonstrated that the CTFB successfully overcame several disadvantages of TFBs and CFBs, meanwhile integrating their advantages, such as reduced solids back-mixing, high solids circulation rates and uniform solids holdup distributions. The reactor performance study of a CTFB using ozone decomposition is presented in Chapter 7.

Co-current downflow fluidized beds, so-called downer reactors, also have drawn extensive attention, because of the uniform axial and radial distributions of the gas/solids flow (Zhu, Yu et al. 1995). A few efforts have been made to overcome an inherent inferior feature of downers—low solids holdups, by achieving high density/flux conditions (Chen and Li 2004, Song, Bi et al. 2005, Wang, Li et al. 2015). The reactor performance of downer reactors were reported by Fan et al. (2008) and Li, Zhu et al. (2011), but the studied solids fluxes were just up to 100 kg/m^{2}s which was too small for any meaningful industrial processes. More recently, Wang et al. (2014b) reported the axial and radial conversion distributions in a downer at high solids fluxes of 100-700 kg/m^{2}s.

In the previous literature, almost all reactor performance studies were conducted only in each individual type of fluidized bed with different reactor dimensions and catalyst particles. Consequently, the advantages and drawbacks of the various fluidized beds are difficult to identify. Therefore, a comprehensive study covering the full fluidization regime is needed. In this work, the reactor performances of a BFB, a TFB, a CTFB, a CFB riser and a downer are investigated in a multifunctional fluidized-bed system (introduced in Chapter 3) using an ozone decomposition reaction, the same catalyst particles and the same reactor diameter for sake of reliability and convenience of comparisons. Both axial and radial profiles of ozone conversion of these fluidized beds are provided over a wide range of operating conditions. In order to understand the reactor performances, the solids holdup distributions have been measured as well. The results of the CFB riser and downer were obtained by Wang et al. (2014a and 2014b). Furthermore, the reactor performances of all the fluidized beds are comprehensively evaluated.

8.2. Experimental setup

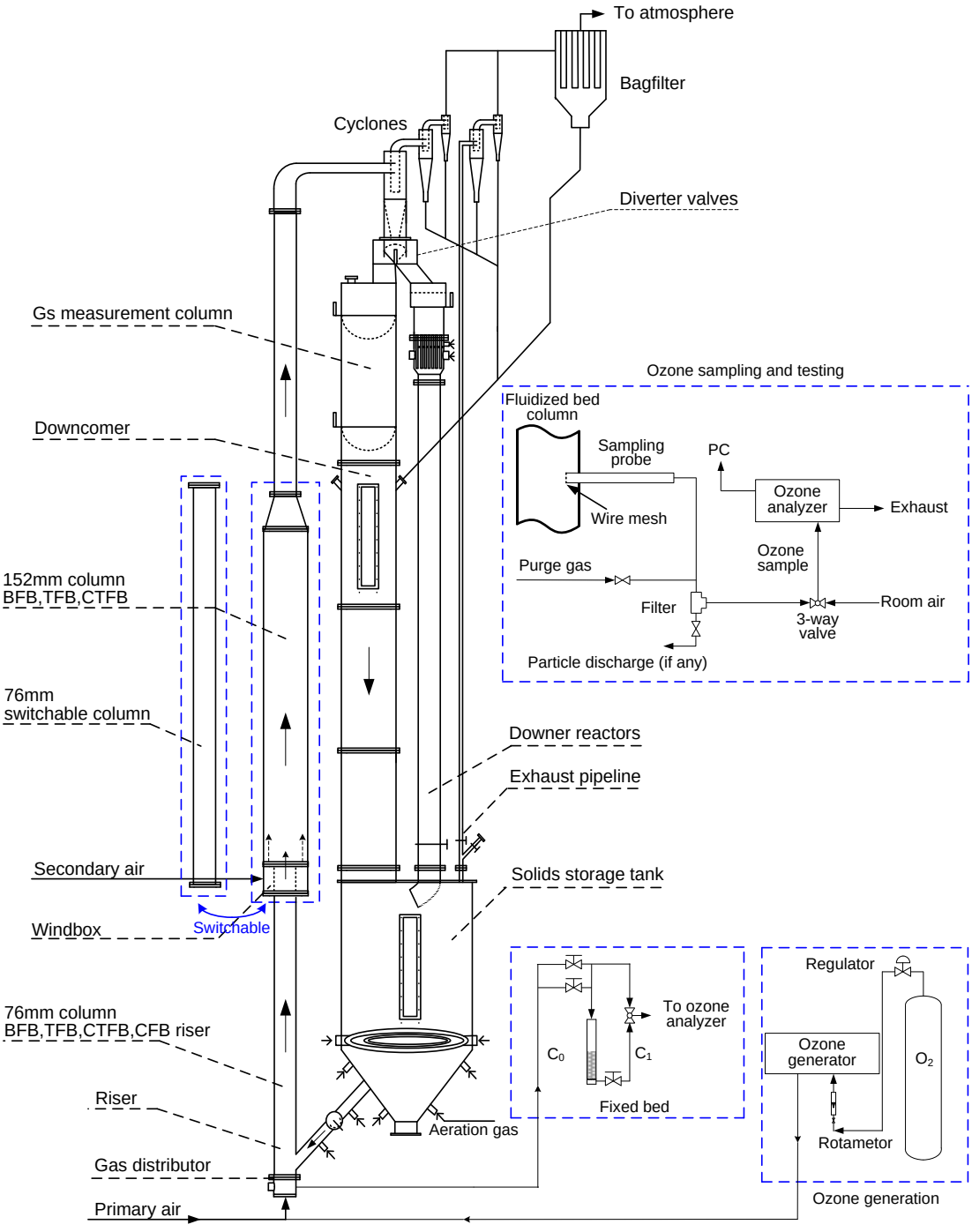

Figure 8.1 Schematic diagrams of a multi-functional fluidized-bed system and an ozone testing system

Fluidized bed setup

The various fluidized beds were operated in a multifunctional fluidized-bed system. As shown in Figure 8.1, a CTFB is on the left-hand side, which consists of a 76mm i.d. column at the bottom, a 152mm i.d. column in the middle, and another 76mm i.d. column at the top. Each column is 3.0m in height. The middle section can be switched to a 76mm i.d. column in order to operate a CFB riser. A gas distributor made of double-layer perforated plates (2mm i.d. hole × 176, 12% opening area) is mounted at the bottom of the riser column. On the right of the CTFB is a 203mm i.d. downcomer serving for returning solids to a storage tank at its bottom. A measurement section is installed at the top of the downcomer to measure solids circulation rates. A downer reactor of 76mm i.d. and 5.8m high is on the right-hand side of the downcomer. Both downcomer and storage tank are used for storing solids. The total solids inventory was maintained at approximately 6.0m-high. Such high solids inventory can provide sufficient back pressure head to ensure high solids circulation rates. The columns are mainly made of aluminium in order to avoid the oxidization of ozone, since an inert aluminium oxide layer is formed inside the column. To prevent electrostatic charges accumulation, the entire system is grounded. The detailed operations of the CTFB are introduced in Chapter 7, and those of the CFB riser and the downer are referred to Wang et al. (2014c) and Wang, Li et al. (2015).

The system should be briefly modified in order to operate BFB and TFB. Each of BFB and TFB was respectively operated in either the 76mm i.d. bottom column or the 152mm i.d. middle column, as shown in Figure 8.1. The bottom column is installed with a gas distributor made of perforated plates (2mm i.d. hole × 176, 12% opening area). There was no gas distributor and solids loading in the middle column, when operating the bottom bed. Therefore, the enlarged middle column is able to greatly reduce particle velocity, so that the entrained solids can be returned due to loss of velocity. The experiments were performed by loading certain amounts (equiv. to 1.0m and 1.9m static bed height) of particles into the column and introducing fluidizing gas at the superficial velocities of 0.3 m/s-1.2 m/s through the gas distributor. Another perforated-plate gas distributor (5mm i.d. hole × 89, 10% opening area) was installed at the bottom of the 152mm i.d. column, after finishing experiments in the bottom column. The connection between the middle column and the upper column was blocked. Additionally, two cyclones were employed in parallel to recycle entrained solids. The amounts of loaded particles

were equivalent to the static bed height of 0.79m and 1.0m. The fluidizing gas was introduced from the bottom column in the range of 0.1 m/s to 1.0 m/s. The detailed operations are described in Chapter 6.

Measurement of solids holdup

The local solids holdups were measured by an optical fibre probe system (Model: PV6D) that was manufactured by the Institute of Processing Engineering, Chinese Academy of Science, Beijing, China. The probe has a fibre bundle consisting of 8000 quartz fibres each with a diameter of 15μm. Half of the quartz fibres are emitting fibres and the others are receiving fibres. They are arranged alternatively. A Plexiglas pad of 0.2mm thickness is covered the probe tip in order to prevent particles from occupying the blind zone (Liu, Grace et al. 2003). By illuminating a small area and measuring the intensity of light reflected by passing particles, the optical fibre probe can correlate local solids holdups with corresponding voltage signals converted from the light intensity. More particles can reflect more light, i.e., higher light intensity, resulting in higher voltage. The correlation equation between solids holdups and voltage signals requires calibrations. A proper calibration method developed by Zhang, Johnston et al. (1998) was adopted. 20 groups of data were collected at each measuring point, in order to ensure accuracy and repeatability. Each group had 32,768 data points with detecting frequency of 50kHz

Ozone generation and testing

Electronic corona discharge ozone generator (Model AE15M, manufactured by Absolute Ozone Inc.) was applied to generate ozone using bottled oxygen as the gas supply in this work. The O_2-O_3 mixture gas produced from the ozone generator was mixed into the primary fluidizing air before entering the fluidized beds, shown in Figure 8.1. After passing a fairly long path and several L-bends in the primary air feeding pipeline, ozone was considered to be mixed thoroughly with the primary air. The ozone generator's potentiometer setting was fixed and the primary air flowrate was constant in each experimental run, thus the initial ozone concentrations in the fluidizing air can be adjusted effectively by a rotameter in the oxygen supply stream.

In order to prevent ozone decomposing in the sampling process, ozone-inert materials were adopted, e.g., aluminium, brass, stainless steel and Teflon. Although aluminium and brass would

be oxidized by ozone, an inert oxide layer can form quickly. The schematic diagram of the ozone sampling system is shown in the upper-right corner of Figure 8.1. Brass tubes (6mm o.d., 0.36mm wall thickness and 15.0cm length) were inserted horizontally into the column as sampling probes. The tip of the sampling probe is covered with stainless wire mesh to prevent particles leaking to the ozone analyser. There is a vacuum pump inside the ozone analyser to withdraw sample gas continuously. The sampling gas velocity is up to 1.5LPM, low enough to assure minimal disturbance to the gas/solids flow. High pressure purging air of 100psi was used to purge the particle cake possibly formed on the probe tip before every sampling.

An ozone analyser (Model 49i, Thermo Electron Inc.) based on the UV photometric method was used to measure ozone concentrations in the sample gas. The UV light source used in ozone photometers is 253.7nm from a low-pressure Hg discharge lamp. At this wavelength, the absorptivity of ozone is very close to unity and with little interference from other gases (Seinfeld and Pandis 2006). The analyser is a dual-cell photometer, having both sample and reference air flowing at the same time, with the internal surfaces coated with polyvinylidine fluoride (PVDF) to ensure that ozone undergoes no decomposition during testing. A single test lasted 1min and generated 15 data points. Five tests were required at each measuring position in order to ensure accuracy and repeatability.

Preparation of catalysts

Ozone decomposes very slowly at room temperature (20℃) in the absence of catalysts or ultraviolet (Wojtowicz 2005), and the gas residence time is only up to 10s in this study, so catalysts are necessary. It can be assumed that ozone decomposes only when contacting with catalysts.

Ferric oxide was usually used as the catalytic component in the previous ozone decomposition research (Jiang, Bi et al. 1991, Ouyang, Li et al. 1995, Wang et al. 2014a), as well as being used in this study. FCC particles (Geldart Group A particles) were chosen as the catalyst carriers due to their wide applications. The FCC particles were first impregnated in a 40wt% $Fe(NO_3)_3$ solution for 12 h, and then the wet particles were dried at 120^{o}C for 6 h in an oven followed by calcination at 450^{o}C for 4 h. After calcination, ferric nitrate converted to ferric oxide loaded on the particles. A ball mill was used to break up the agglomerates formed during calcination. The

particles processed by the ball mill were sifted using a sieve with pore opening of 250μm. The impregnated particles were blended with the original FCC particles which have negligible catalytic activity, in order to modify the overall catalytic activity. The particle information is shown in Table 8.1.

Table 8.1 Particle information

Apparent density [kg/m^3]	1780	Bulk density [kg/m^3]	890
d[4,3], [*μm*]	106.3	*d*[3,2], [*μm*]	78.6
Particle size distribution (Vol.%)			
Diameter [*μm*]	Vol.%	Diameter [*μm*]	Vol.%
11.11 - 17.05	0.81	105.24 - 117.13	8.78
17.05 - 23.51	1.32	117.13 - 130.37	8.82
23.51 - 32.41	2.64	130.37 - 145.10	8.34
32.41 - 44.69	5.2	145.10 - 161.5	7.27
44.69 - 55.36	5.88	161.5 - 179.75	5.75
55.36 - 68.58	8.75	179.75 - 200.06	4.02
68.58 - 84.96	12.32	200.06 - 222.66	2.43
84.96 - 94.56	7.53	222.66 - 247.83	1.22
94.56 - 105.24	8.29	247.83 - 307.00	0.63

Frye, Lake et al. (1958) has reported that the apparent reaction rate constant k_r of ozone decomposition (a first order reaction) can be determined in a small integral reactor (a fixed-bed reactor) by the equation below, if it runs as a plug-flow reactor isothermally with minimal transport gradients.

$$k_r = \frac{Q_g \rho_p}{m_c} \ln \frac{C_{in}}{C_{out}} \qquad \text{Eq. 8.1}$$

where Q_g is the volumetric gas flowrate (m^3/s), ρ_p is the particle density (kg/m^3), m_c is the mass of catalyst (kg) and C_{in}, C_{out} are inlet and outlet ozone concentrations. Therefore, a small fixed-bed reactor (16mm i.d.) made of brass pipe was used to measure the reaction rate constant k_r, shown in Figure 8.1. A humidity meter and a thermometer were used to monitor the relative humidity and temperature of the air supply respectively. The relative humidity was maintained at

19%, and the temperature remained at 20℃ without significant fluctuation. Therefore, the moisture and temperature would not influence the reaction rate in the experiments. The k_r of the catalysts in the experiments was 4.2 s^{-1}. The reaction rate constant was tested after every experimental run, showing no obvious variance.

8.3. Results and discussion

8.3.1. Axial profiles of ozone concentration

Axial profiles of unconverted ozone concentration and solids holdup in the BFB, TFB, CTFB, CFB riser (LDCFB and HDCFB) and downer are shown in Figure 8.2. The results of the CFB riser and downer were obtained by Wang et al. (2014a) and Wang et al. (2014b) respectively. The cross-sectional average value of ozone concentration or solids holdup is calculated by integrating the local value of every radial position based on the cross-sectional area. The dimensionless ozone concentrations (C/C_0) equals to the ratio of the measured ozone concentration over the initial ozone concentration before entering the fluidized beds. So the ozone conversion equals one minus the dimensionless ozone concentration.

Results of BFB and TFB obtained in the 76mm i.d. bottom column with the static bed height of 1.0m are shown in Figure 8.2(a)-(d). Pressure fluctuations represented by standard deviations of differential bed pressure were used to identify the transition from a BFB to a TFB, which is one of the commonly used methods (Yerushalmi and Cankurt 1979). The superficial gas velocity (U_g) at which the pressure standard deviation reaches the maximum is referred as the transition velocity (U_c) from bubbling fluidization to turbulent fluidization. In this work, the transition velocity was found to be 0.5 m/s in all cases. Therefore, the fluidized bed operated below U_g=0.5 m/s is considered as a BFB, whereas one operated above U_g=0.5 m/s is identified as a TFB.

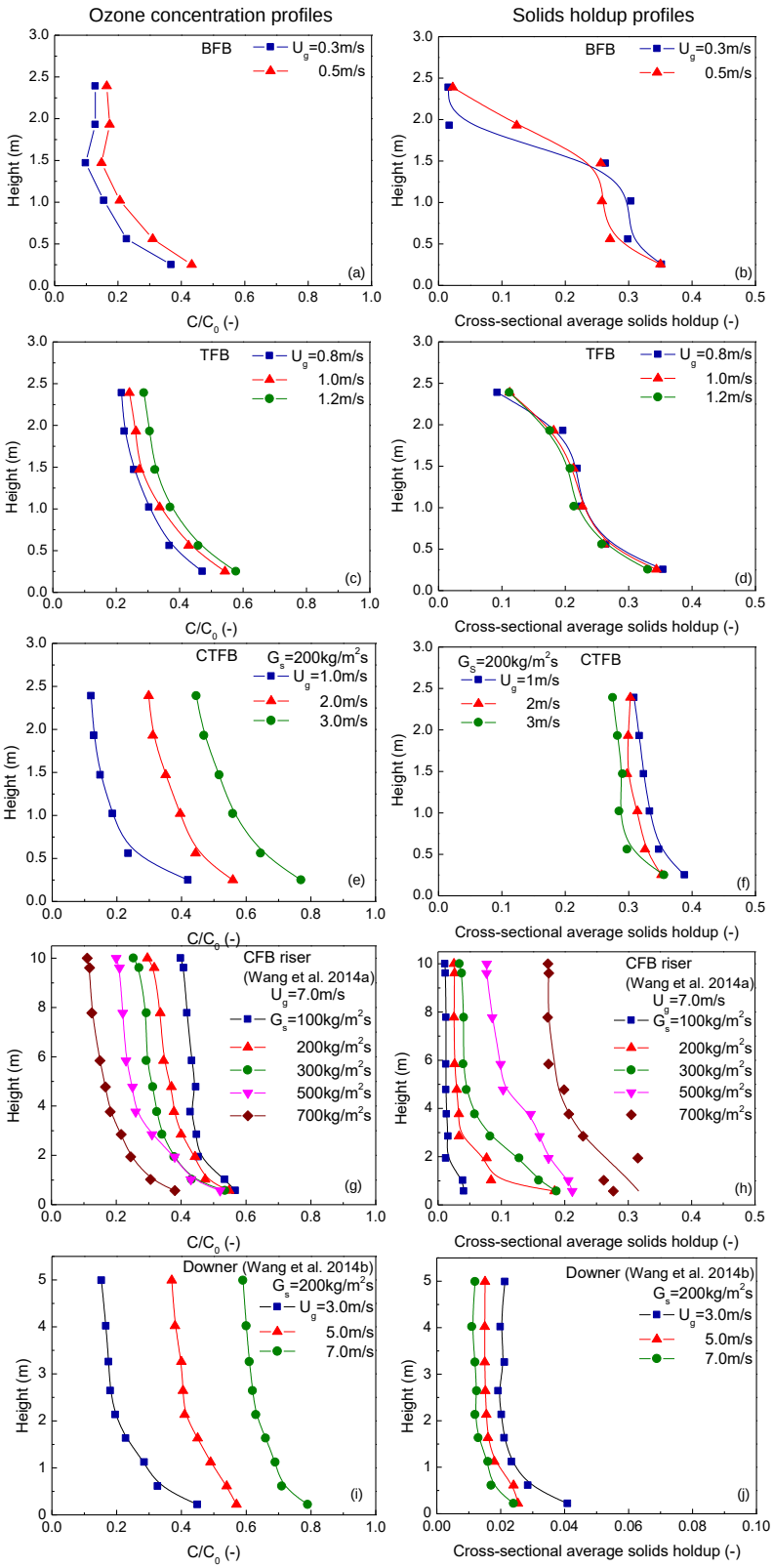

Figure 8.2 Axial profiles of ozone concentration and solids holdup in various fluidized beds

For the TFB, the ozone concentration monotonically decreases with increasing elevation as displayed in Figure 8.2(c) and (d). Since TFBs have vigorous interactions between the dilute and dense phases, the mass transfer between them is greatly improved, thereby leading to the continuous change of concentration. Further analysing the ozone concentration profile of the TFB, the reaction rate is found to decrease from the bottom to the top, which corresponds to the gradually decreasing solids holdup in the axial direction. Due to the higher solids holdup and the smaller void size in the region close to the distributor, the reactant-gas and the catalyst-solids have more contact in the bottom region than elsewhere, further resulting in the higher reaction rate.

For the CTFB, the ozone concentration and solids holdup profiles are shown in Figure 8.2(e) and (f), which were obtained at solids circulation rate (G_s) of 200 kg/m^{2}s and superficial gas velocity (U_g) of 1.0-3.0 m/s. The ozone decomposes dramatically from the distributor to the height of 0.5m, possibly owing to the "entrance effect" (Ouyang, Li et al. 1995).

For the CFB riser, the axial distributions of ozone concentration and solids holdup are presented in Figure 8.2(g) and (h). The ozone concentration reduces drastically in the entrance region as well, like the CTFB. While, above the entrance region, the concentration turns to decrease gradually with increasing elevation. This trend can be explained by the non-uniform axial distribution of solids holdup. The dense bottom region could provide more gas-solids contact area, resulting in more conversion than the upper region. In addition, the solids holdup is considerably increased at high solids circulation rates (i.e., HDCFB). As a result, the ozone concentration decreases more significantly in the HDCFB, when compared with the LDCFB.

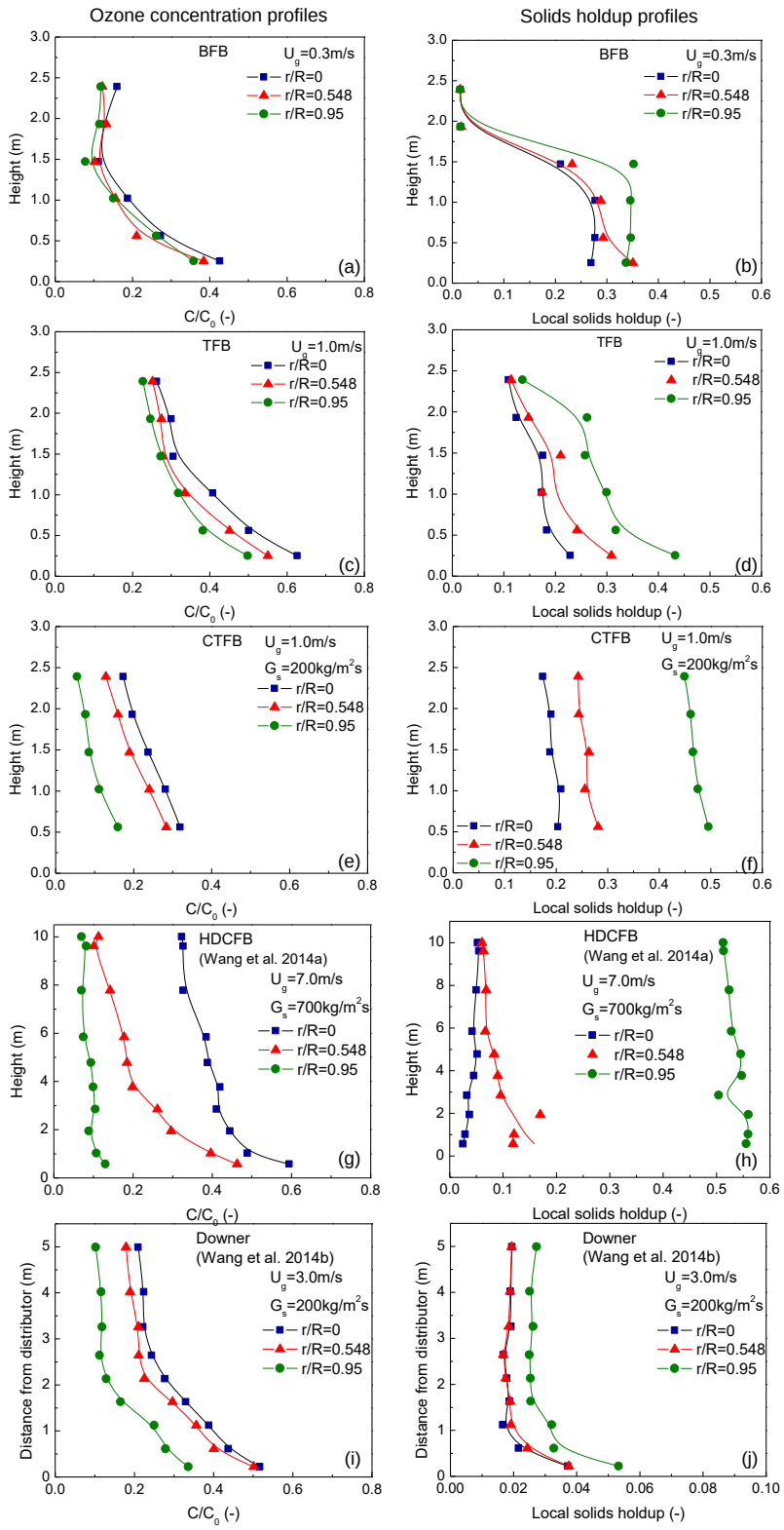

Figure 8.3 Axial distributions of ozone concentration and solids holdup at different radial positions in various fluidized beds

For the downer, the profiles of ozone concentration and solids holdup are displayed in Figure 8.2(i) and (j). It is found that the ozone concentration decreases considerably from the distributor down to the position of 1.0m, then gradually decreases until 3.0m and eventually keeps unchanged down to the outlet. The change of the ozone concentration closely corresponds to the three solid flow regions along the axial direction in the downer, which are the first acceleration zone, the second acceleration zone and the developed zone (Zhang, Huang et al. 2001, Wang, Li et al. 2015). The solids holdup profile in Figure 8.2(j) can reveal the flow development and also exhibit a similar trend with the concentration profile.

The axial distributions of ozone concentration and solids holdup at three different radial positions (r/R=0, 0.548 and 0.95) which represent the central, middle and wall regions respectively are shown in Figure 8.3. For the BFB and the TFB, the axial profile of ozone concentration at each radial position exhibits a similar trend with close magnitude, because of the uniform radial flow structure, as shown in Figure 8.3(a) and (c). Also, the trend is consistent with that of the cross-sectional average ozone concentration. On the other hand, the same phenomenon are demonstrated in the solids holdup profiles in Figure 8.3(b) and (d), implying the direct relationship between the distributions of reactant concentration and solids holdup.

For the CTFB, the typical axial profiles of local ozone concentration and corresponding solids holdup at different radial positions at U_g of 1.0 m/s and G_s of 200 kg/m^{2}s are shown in Figure 8.3(e) and (f). The central region has the highest ozone concentrations (i.e., lowest conversions), followed by the middle region, whereas the wall region gives the lowest concentrations. The difference of ozone concentrations among the radial positions is attributed to the radial gradient of solids holdup shown in Figure 8.3(f). To be specific, the relatively high solids holdup in the wall region leads to larger overall gas-solids contact area, further resulting in lower ozone concentration. In spite of the high solids holdup, it cannot prevent the reactant-gas flowing through the wall region by the fact that the ozone concentration obviously decreases with increasing elevation in this region.

For the HDCFB riser, Figure 8.3(g) illustrates the ozone concentration profiles at different radial positions at U_g of 7.0 m/s and G_s of 700 kg/m^{2}s. In the central and middle regions, the ozone decomposes dramatically in the lower section (below 4.0m) which is also the distributor-

controlled and developing zones for the gas/solids flow identified by the solids holdup profile (Wang et al. 2014d). Beyond the lower section, the ozone reduction rate progressively slows down in the developed zone. In contrast, the ozone concentration remains almost unchanged in the wall region. It is well-known that HDCFB risers have a dilute core-dense annulus flow structure as reflected in Figure 8.3(h). The reactant-gas may hardly flow through the dense wall region due to the "shielding" effect, so this region contributes only a slight portion to the overall conversion.

The CFB downer's profiles of ozone concentration and solids holdup at U_g of 3.0 m/s and G_s of 200 kg/m^{2}s are shown in Figure 8.3(i) and (j). The local ozone concentrations at different radial positions show parallel profiles along the axial direction, which corresponds to the local solids holdups. Besides, the radial flow structure and concentration distribution keep relatively uniform along the axial direction, inferring a uniform residence time distribution.

8.3.2. Radial profiles of ozone concentration

Some typical radial profiles of ozone concentration and solids holdup in the various fluidized beds are presented in Figure 8.4. In the BFB and the TFB, the profiles at the height of 1.0m are shown in Figure 8.4(a). The radial profiles of ozone concentration and solids holdup are fairly flat in both BFB and TFB. One should note that, in the gas-solid fluidized beds, the conversions are determined by the reactant residence time and the two-phase flow structure at a given reaction rate constant. Based on the previous discussion about the flow structures of the BFB and TFB, the TFB is expected to have more favourable gas-solids contacting. Therefore, the lower ozone concentration (i.e., the higher conversion) of the BFB compared to that of the TFB, as shown in Figure 8.4(a), is mainly attributed to the longer reactant residence time, which can be confirmed by the quantitative evaluations next.

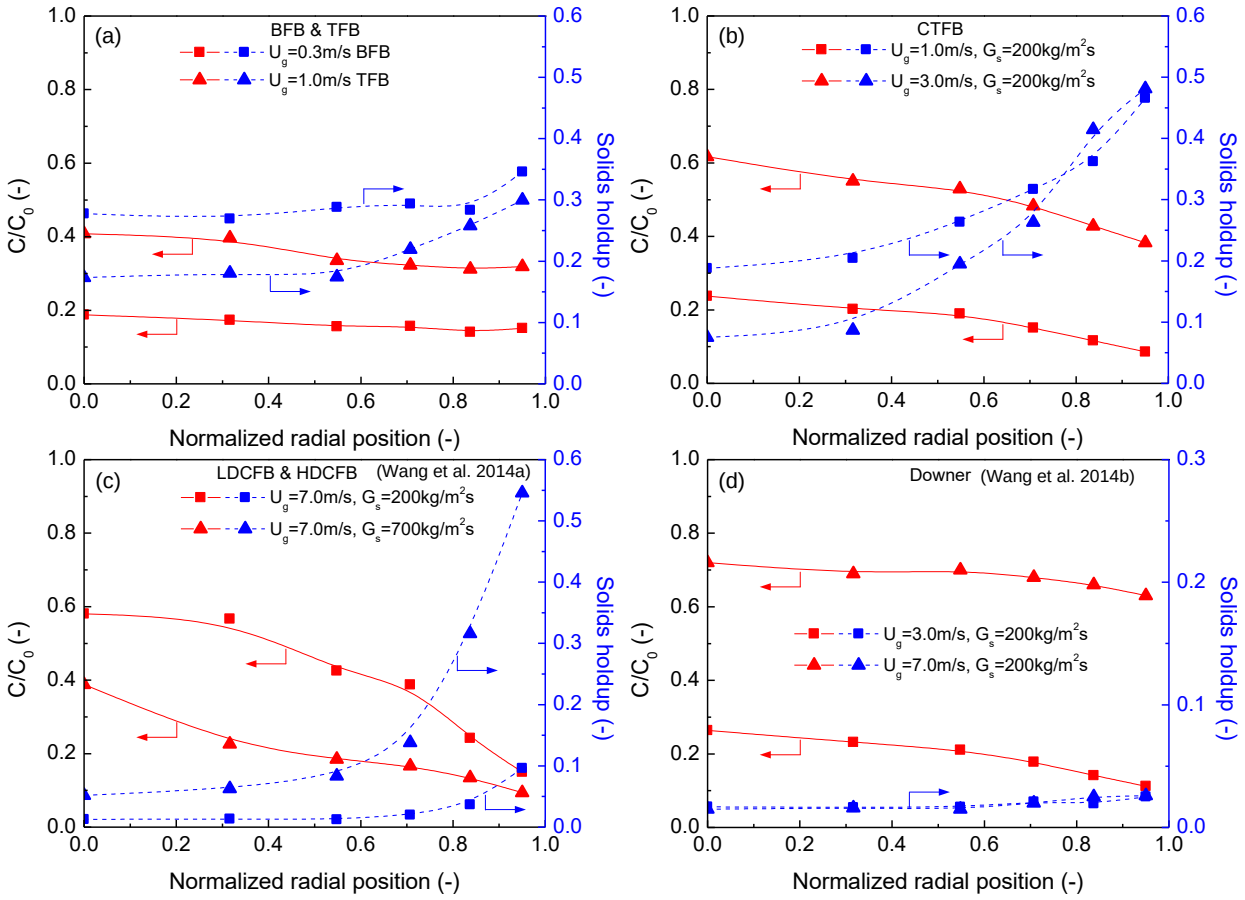

Figure 8.4 Radial profiles of ozone concentration and solids holdup in various fluidized beds at the height of 1.0m

In Figure 8.4(b), the CTFB exhibits non-uniform radial distributions of solids holdup with increasing magnitude from the centre to the wall due to the solid upflow and the wall-boundary effect. The radial gradient of solids holdup becomes even steeper with increasing U_g. Inversely, the ozone concentration continuously decreases from the centre to the wall, which is understandable. Given the greatly inter-dispersed gas/solid phases in CTFBs (Zhu and Zhu 2008b), the lower solids holdup in the core region results in less reactant-catalysts contact area and thereby higher ozone concentration, whereas the higher solids holdup near the wall leads to lower ozone concentration. Nevertheless, the radial non-uniformity of ozone concentration is mitigated compared with that of solids holdup.

Figure 8.4(c) presents the typical radial profiles of ozone concentration and solids holdup at the solids circulation rates (G_s) of 200 kg/m^{2}s and 700 kg/m^{2}s which represents the low density/flux CFB riser and the high density/flux CFB riser respectively. As G_s increases, the solids holdup significantly increases, especially in the wall region, showing a conspicuous "dilute core-dense annulus" structure. This flow structure makes the ozone concentration radial distribution stay high in the core region but drop sharply towards the wall.

In the downer reactor, the radial distribution of solids holdup is extremely uniform due to the same flow direction with the gravity (Zhu, Yu et al. 1995). Therefore, the downer exhibits more uniform radial distribution of ozone concentration compared with the CFB riser. Moreover, the solids holdup does not obviously vary with superficial gas velocity (U_g). The U_g affects the ozone concentration mainly based on the change of reactant-gas residence time.

To quantitatively evaluate the non-uniformity of radial profiles, the radial non-uniformity indexes (RNIs) of solids holdup (ε_s) and ozone concentration (C/C_0) are investigated here. The RNI is defined for each given parameter as the standard deviation of its values in the radial direction, normalized by the maximum possible standard deviation for the same parameter with the same average cross-sectional value (Zhu and Manyele 2001). The values of RNIs(ε_s) and RNIs(C/C_0) are between 0 and 1, indicating the perfectly uniform distribution of the gas/solids flow on the cross-section and the complete segregation of the gas/solid flows, respectively.

The BFB's and TFB's RNIs(C/C_0) and RNIs(ε_s) are shown in Figure 8.5(a) and (b). It is seen that the RNIs(ε_s) of BFB and TFB are generally smaller than 0.4. In detail, the radial distribution of solids holdup in the TFB becomes less uniform than that in the BFB, presumably due to the increased U_g. On the other hand, however, the TFB exhibits similar RNIs(C/C_0) with the BFB, revealing very uniform distributions, which may be attributed to the lateral gas and solids dispersion (Du, Fan et al. 2002).

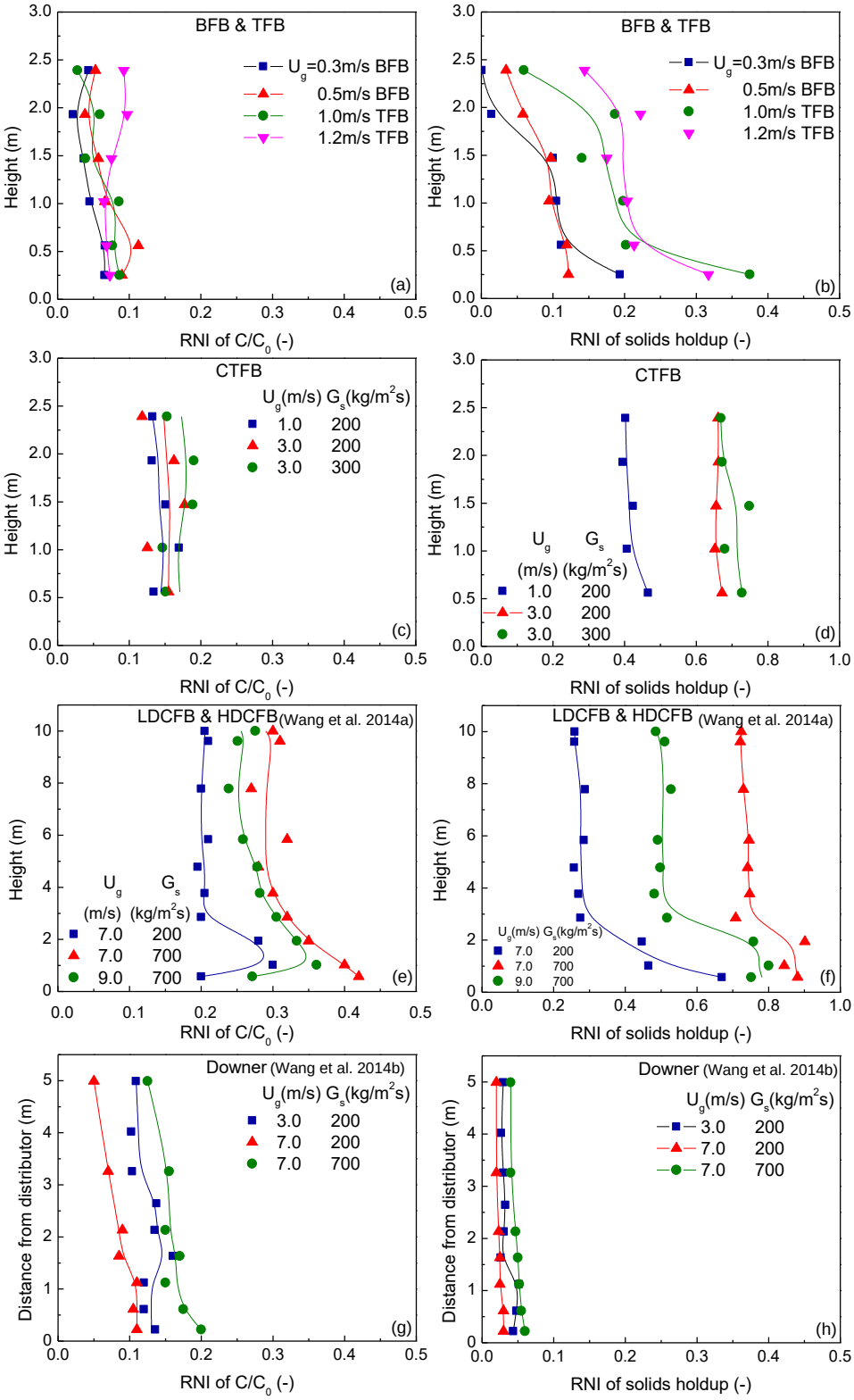

Figure 8.5 Radial non-uniformity indexes (RNIs) of ozone concentration and solids holdup in various fluidized beds

For the CTFB as shown in Figure 8.5(d), the RNIs (ε_s) range from 0.4 to 0.8 which is higher than those of the TFB, mainly due to the large solids flux in the CTFB. The radial non-uniformity increases with superficial gas velocity (U_g), since the increased gas velocity in the core region can significantly reduce the local solids holdup. In Figure 8.5(c), the RNIs(C/C_0) are between 0.1 and 0.2 which is smaller than the RNIs(ε_s), indicating the adequate gas exchange in the radial direction. It is likely accounted for the widely expanded turbulent flow in CTFBs (see Chapter 7). Additionally, the RNI(C/C_0) is found to increase with increasing U_g and G_s.

The CFB riser's RNIs(C/C_0) and RNIs(ε_s) are presented in Figure 8.5(e) and (f) respectively. It is demonstrated that the RNIs(ε_s) are significantly increased under the high density/flux condition (G_s=700 kg/m^{2}s), because the increased solids holdup primarily exists in the wall region. Under the high flux condition, the RNIs(ε_s) decrease with increasing U_g due to the thinner dense annulus region attenuated by the higher shear force. For the radial distribution of ozone concentration in the CFB riser, the RNIs(C/C_0) range from 0.2 to 0.4, the largest among the fluidized beds. This severe non-uniformity of concentration is due to the aforementioned core-annulus flow structure. Besides, the RNIs(C/C_0) decrease with increasing elevation above the distributor-controlled region, and then remain constant in the developed flow region. Additionally, the variation of RNI(C/C_0) with operating conditions is consistent with that of RNI(ε_s), further suggesting the close relationship between solids holdups and reactant concentrations.

As shown in Figure 8.5(h), the downer has the most uniform radial distribution of solids holdup among all the fluidized beds, because the formation of particle clusters in the wall region can be inhibited in the downer (Wang, Li et al. 2015). In Figure 8.5(g), the RNIs(C/C_0) are between 0.1 and 0.2 which are comparable to those of the CTFB, but higher than those of the BFB and TFB. The RNIs(C/C_0) decrease with increasing distance downwards, revealing the flow development in the downer. Furthermore, the RNIs(C/C_0) are found to increase with increasing G_s but decreasing U_g, which corresponds to the trend of RNIs(ε_s).

8.3.3. Correlations between ozone concentrations and solids holdups

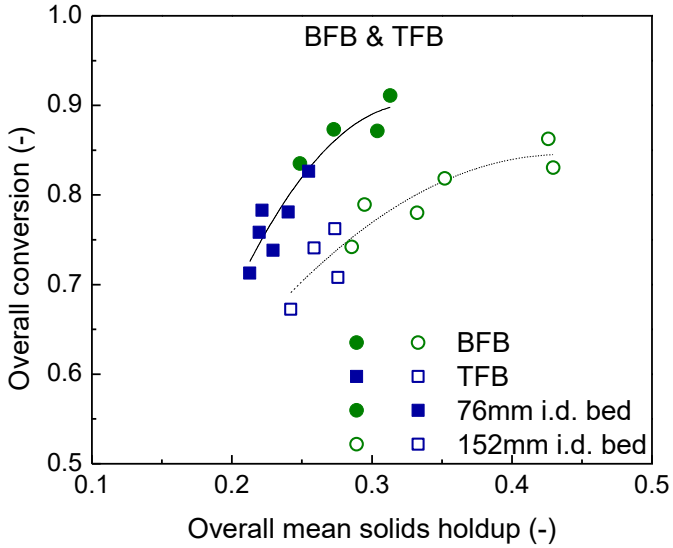

Figure 8.6 Correlation between the overall conversions and the mean solids holdups in the BFB and TFB

As discussed above, the ozone conversions are essentially affected by the flow structures that can be partially represented by the profiles of solids holdup in the fluidized beds. For the BFB and TFB, the overall conversions are plotted against the mean solids holdups of the entire bed in the two reactors with different bed diameter, as shown in Figure 8.6. A second order polynomial function best fits the results in each case. The overall conversion increases with the mean solids holdup, while the increasing rate gradually slows down with entering the bubbling regime, which is likely attributed to the different gas/solids flow structures of the BFB and the TFB. In the BFB, due to the aggregation of gas as the bubbles, the reactant-gas throughflow is relatively low in the dense phase which can be regarded as an "inactive zone". As a result, the total gas-solids contact area cannot be effectively enlarged as the solids holdup increases. While in the TFB, the voids with smaller sizes are considered to split and coalesce frequently and extensively, even lose their identities (Zhu, Zhu et al. 2008c), leading to significant mass transfer between the gas phase and the solid phase. Thus, the solids in the TFB can more efficiently affect the reaction.

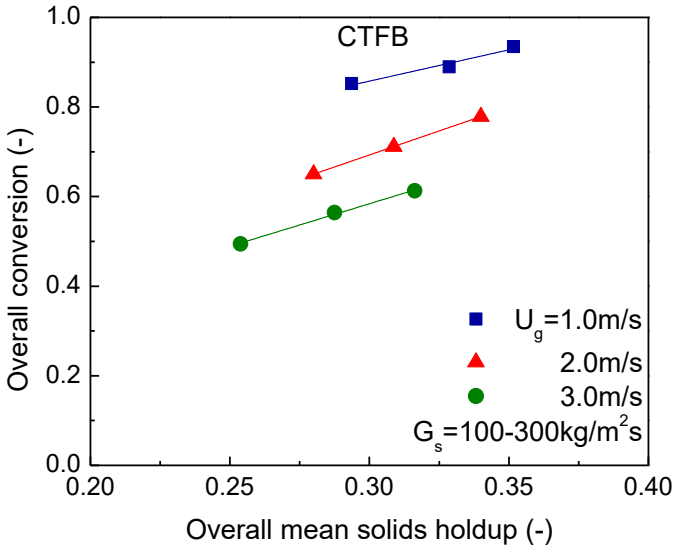

Figure 8.7 Correlation between the overall conversions and the mean solids holdups in the CTFB

For the CTFB, Figure 8.7 shows the correlation between the overall conversions and the mean solids holdups at U_g of 1.0-3.0 m/s and G_s of 100-300 kg/m^{2}s. The ozone conversion increases as a linear function with increasing solids holdup under each condition, indicating the uniform flow structure. The slopes of the linear fittings are almost the same, suggesting the similar flow structures at different U_g. Besides, the correlation curve moves downwards with increasing U_g, due to the reduction of reactant-gas residence time and solids holdup.

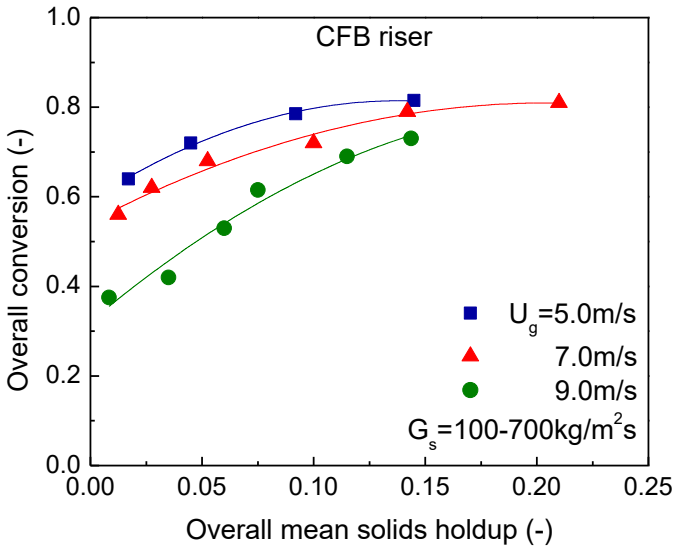

Figure 8.8 Correlation between the overall conversions and the mean solids holdups in the CFB riser (Wang et al. 2014a)

For the CFB riser, the relationship between the overall conversions and the mean solids holdups is demonstrated in Figure 8.8. The data were obtained at the U_g of 5.0-9.0 m/s and G_s of 100-700 kg/m^{2}s covering both LDCFB and HDCFB. It is found that the second order polynomial functions fit the results very well, indicating the change of the flow structure. As reported about the CFB riser, the mean solids holdup increases and the wall region becomes increasingly dense and thick with increasing G_s (Wang et al. 2014c). The growing dense wall region reduces the catalyst-particles available for the reaction. Thus, the increased solids holdup in the HDCFB riser less effectively improves the overall conversion compared with the LDCFB, which is reflected by the reducing slope with the mean solids holdup. In addition, the increasing rate of conversion is the highest at U_g of 9.0 m/s. Since the high gas velocity is able to exert strong shear force onto the solid clusters, the clusters potentially can break down to smaller ones or even individual particles. The mass transfer between the gas and the dispersed particles is superior to that within the clusters. Therefore, the overall conversion increases faster with the mean solids holdup at the high U_g than that at the low U_g, particularly at low solids circulation rates.

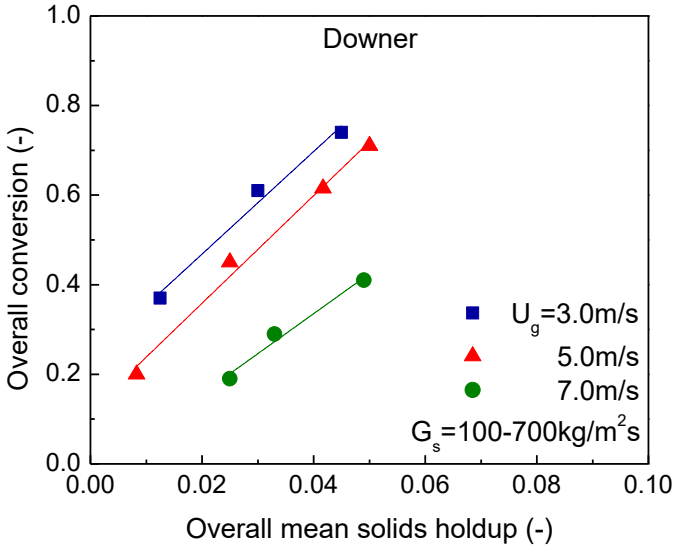

Figure 8.9 Correlation between the overall conversions and the mean solids holdups in the downer (Wang et al. 2014b)

In the downer reactor, the effect of mean solids holdup on the overall ozone conversion at U_g of 3.0-7.0 m/s and G_s of 100-700 kg/m^{2}s is illustrated in Figure 8.9. The overall conversion increases linearly with the mean solids holdup at every U_g, which is similar to the relationship in the CTFB. This trend is attributed to the uniform gas/solids flow in the downer. Besides, the similar slopes of the fitting lines suggest the identical flow structures at various U_g.

8.3.4. Reactor performances of various fluidized beds

As the conversions of a gas-phase catalytic reaction are affected by the reactant-gas residence time, reaction kinetics and gas-solids mass transfer collectively, the overall conversions are plotted against the Damköhler numbers ($Da=k_r\varepsilon_s H/U_g$) that combines the gas residence time and the reaction rate constant, as shown in Figure 8.10. Since no well-developed numerical model is available at the moment, the ideal reactor models of a plug-flow reactor (PFR) and a continuous stirred-tank reactor (CSTR) are adopted as references to assess the reactor performances. The formulas for the conversions in a PFR and a CSTR are derived (Jiang, Bi et al. 1991):

PFR: $$X_{PFR} = 1 - \exp(-Da) \quad (1)$$

CSTR: $$X_{CSTR} = \frac{Da}{1+Da} \quad (2)$$

In Figure 8.10(a), the conversions of the CTFB are the closest to those of the PFR at given Damköhler numbers. The performance of the TFB is not as good as that of the CTFB, but it is better than that of the BFB. As shown in Figure 8.10(b), the performance of the downer reactor is close to that of the PFR as well, which resembles the CTFB. On the other hand, the CFB riser evidently deviates from the PFR, similar to the BFB.

The deviation of the fluidized beds from a PFR can be attributed to the different gas-solids mass transfer rates and contact efficiencies that are greatly affected by the hydrodynamics. It is well accepted that BFBs are dominated by a continuous dense phase with a discrete bubble phase. The bubbles have few particles inside and a distinguishable boundary with the surrounding dense phase, which could result in high mass transfer resistance between the two phases and inadequate gas-solids contacting inside bubbles (Chiba and Kobayashi 1970). Therefore, the bubbles pass through the particulate bed carrying unconverted reactant-gas, albeit splitting and coalescing, leading to gas bypassing to some extent. Besides, the gas back-mixing exists caused by the severe solids downflow in the BFB (Du, Fan et al. 2002). Overall, the insufficient gas-solids contacting, reactant-gas bypassing and back-mixing result in poorer reactor performance of the BFB than that of the PFR.

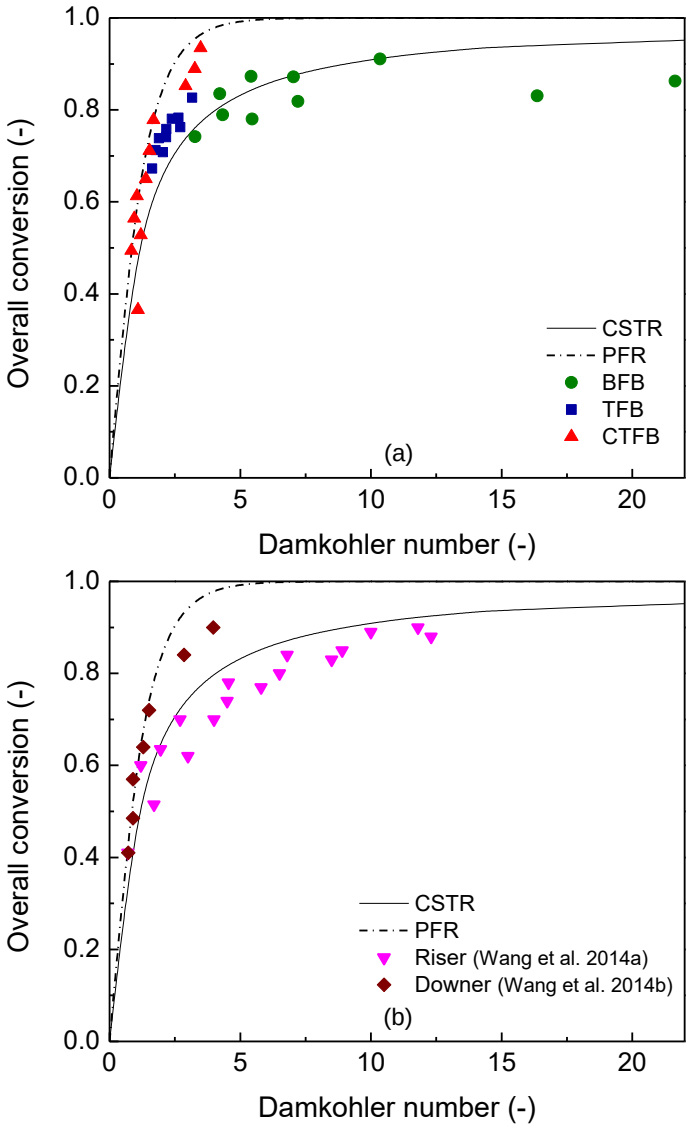

Figure 8.10 Relationship of overall conversions and Damköhler numbers in the various fluidized beds

As the gas fraction increases, TFBs have the comparable dense (solids) phase and dilute (gas) phase (Bi, Grace et al. 1995), leading to homogeneous mixing, intense interaction and efficient contact between the gas and solids. As a result, the reactor performance of TFB is better than that of BFB. However, the gas back-mixing in the TFB cannot be neglected (Du, Fan et al. 2002), which makes the TFB deviate from the PFR.

For the CTFB, its advantageous flow structure accounts for the outstanding reactor performance. First, the CTFB exhibits a uniform flow pattern in the axial direction, which is one of the typical characteristics of a PFR. Secondly, despite the non-uniform radial distribution of the solids flow,

the core region still has fairly high solids holdup providing adequate gas-solids contacting area, which minimizes reactant-gas bypassing. Moreover, almost no net downward solid flux appears in CTFBs (Qi, Barghi et al. 2012), which leads to negligible back-mixing of reactant-gas. These hydrodynamic features of CTFBs reasonably coincide with the characteristics of a PFR, thereby leading to the similar reactor performance.

In the downer reactor, since the gas and solids flow co-currently in the gravity direction, there appears no gas/solids back-mixing. Besides, the solids flow distributes uniformly on the cross-section (Zhu, Yu et al. 1995), so the gas residence time distribution is narrow in the downer. Owing to these preferable hydrodynamics, the reactor performance of the downer is also close to that of the PFR, as shown in Figure 8.10(b).

The reactor performance of the CFB riser is not as good as that of the CSTR, as shown in Figure 8.10(b), probably due to the segregation of gas and solids. Theoretically, the reactant-gas is considered to merely pass through the dilute core region in a high velocity according to the "core-annulus" model, resulting in gas bypassing. Moreover, in spite of the reduction of solids back-mixing in the HDCFBs (Wang et al. 2014d), the gas back-mixing carried by the noticeable downflowing solids still occurs in the dense annulus region. Nevertheless, CFB risers have very high throughputs of gas-product, which is attractive to commercial applications.

The reactor performance of a fluidized bed for gas-phase catalytic reactions is essentially influenced by the mass transfer, particularly the gas-solids contacting. Therefore, the reactor performances of the various fluidized beds can be quantitatively evaluated by the gas-solids contact efficiency. Sun and Grace (1990) proposed a calculation method for gas-solids contact efficiency. Since the gas-solids contacting and mixing in a fluidized bed deviate from those in a PFR at the same gas velocity, the amount of catalysts ($V_{c,f}$) in a fluidized bed required to achieve the same conversion with the same gas flowrate and reaction rate constant should be larger than the catalyst amount ($V_{c,p}$) in a PFR. Therefore, the ratio of $V_{c,p}/V_{c,f}$ can evaluate the utility efficiency or contact efficiency of catalysts in different fluidized bed reactors. The higher contact efficiency, the better the reactor performance is, i.e., the less the fluidized bed deviates from the PFR. $V_{c,f}$ comes from experimental values, whereas $V_{c,p}$ is calculated by the following equation

in which Q_g is the operating gas flowrate, k_r is the reaction rate constant, C_{in} is the initial ozone concentration and C_{out} is the outlet ozone concentration.

$$V_{c,p} = \frac{Q_g}{k_r} \ln\left(\frac{C_{in}}{C_{out}}\right) \tag{3}$$

$$\text{Contact efficiency} = \frac{V_{c,p}}{V_{c,f}} \tag{4}$$

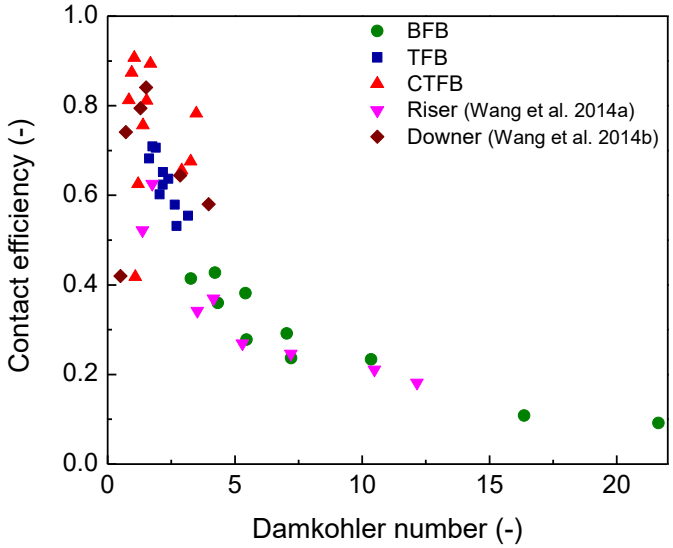

Figure 8.11 Gas-solids contact efficiencies of the various fluidized beds

The gas-solids contact efficiencies of the various fluidized beds are shown in Figure 8.11. The contact efficiency of the CTFB is the highest among all the fluidized beds, due to the uniform axial distribution of solids holdup, homogenous gas/solids mixing and high solids flow density. The contact efficiency of the TFB is lower but close to that of the CTFB, which can be explained by the differences between their microscopic behaviour. The CTFB has even more vigorous gas-solids interactions, revealed by the transient signals of solids holdup (Qi, Zhu et al. 2009). Besides, the continuous distribution of the magnitude of solids holdup in the CTFB infers that the dense phase contains more gas, and more solids disperse into the voids, when compared with the TFB. Overall, the superior reactor performance and the distinctive hydrodynamics can further prove the circulating turbulent fluidization as an individual flow regime (Zhu 2010).

The downer reactor exhibits fairly high gas-solids contact efficiency between the CTFB and the TFB, which is mainly attributed to the uniform solids distribution in both macroscopic scale (i.e., radial distributions) and microscopic scale (i.e., tiny solid clusters or even scattered particles). When the particles move downwards faster than the gas flow in the developed region of the

downer, the upward drag force with reversed direction to the gravity and particle movement restricts the formation of particle clusters (Zhang and Zhu 2000). The potentially formed clusters with increased size and weight could travel faster due to the increased gravitational acceleration. Accordingly, the increased slip velocity causes higher shear force imposed on the clusters, which augments the tendency to break up. Therefore, this hydrodynamic advantage leads to the efficient contact between the gas and scattered particles. Nevertheless, the relatively low solids holdup in the downer limits the contact efficiency to be perfect.

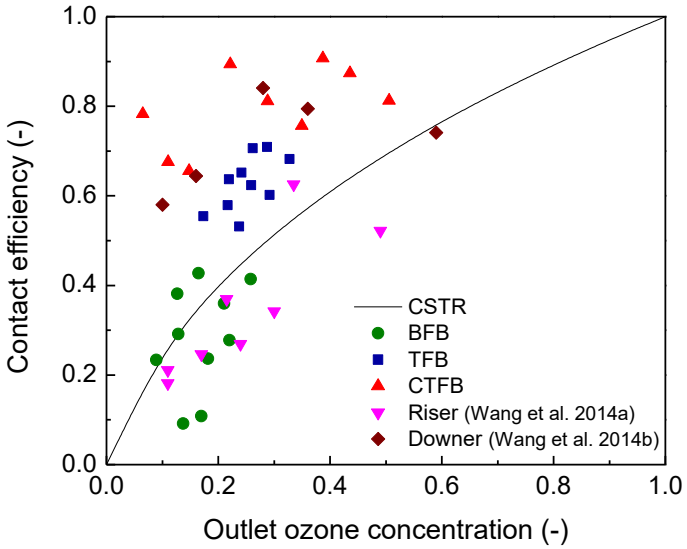

Figure 8.12 Relationship between contact efficiencies and outlet ozone concentrations in the various fluidized beds

As shown in Figure 8.11, the BFB and the CFB riser present relatively low contact efficiencies, which is attributed to the segregation of the gas and solid phases. In the BFB, a large part of reactant-gas aggregates in the form of bubbles having less opportunity to contact with the catalyst-particles. In the CFB riser, a large amount of particles are "locked" in the dense annulus region, leading to a reduction of catalyst-particles available for the reaction. Moreover, in the riser, the large clusters travel even slower, resulting in less shear force and enhanced stability. The compact clusters are considered to have low gas-solids contact efficiency, as the gas is difficult to penetrate through.

The contact efficiencies of these fluidized beds are also plotted against the outlet ozone concentrations in Figure 8.12. It is clearly illustrated that the CTFB shows the highest contact efficiency, closely followed by the downer and the TFB at certain outlet ozone concentrations. In

addition, the BFB and the CFB riser exhibit the comparable contact efficiencies, but which are generally lower than the efficiency of a CSTR.

8.4. Conclusions

The reactor performances of various fluidized beds, including BFB, TFB, CTFB, CFB riser and downer with the same bed diameter and the same catalyst-particles, were studied by using catalytic ozone decomposition in a wide range of operating conditions.

By investigating the axial and radial profiles, the distributions of ozone concentration are affected by those of solids holdup. The ozone concentrations generally decrease with increasing elevation in all the fluidized beds. High ozone conversions in the entrances of the fluidized beds indicate that the initial gas-solids interactions play an important role in the whole reaction. The BFB and the TFB show the most uniform radial distribution of ozone concentration, followed by the CTFB and the downer, whereas the CFB riser has the most severe radial non-uniformity.

The overall ozone conversions and the mean solids holdups are clearly correlated. It is found that the overall conversions increase with the mean solids holdups but as different functions in the various fluidized beds, which indicates the flow structures, e.g., the gas/solids behaviour and distributions, also essentially influence the ozone decomposition reaction.

The CTFB and the downer show the comparable reactor performances which are very close to that of a plug-flow reactor, which is attributed to their favourable flow structures. The TFB also exhibits good reactor performance, mainly due to the relatively vigorous turbulence and intense gas-solids interaction. However, the inevitable gas back-mixing likely makes the TFB deviate from the CTFB. The performances of the BFB and the CFB riser are far away from that of a plug-flow reactor, due to the bypassing and back-mixing of reactant-gas.

The reactor performances of the fluidized beds were also quantitatively assessed by the gas-solids contact efficiencies. The CTFB generally has the highest contact efficiency because of the dense solids concentration, vigorous flow structure and homogeneous gas/solids mixing. The contact efficiency of the downer reactor is equivalent or slightly lower than that of the CTFB. Moreover, the TFB also demonstrates fairly high contact efficiency following the CTFB and the

downer. By reason of the obvious gas/solids segregation in the BFB and the CFB riser, their contact efficiencies are significantly reduced.

Nomenclature

C	local ozone concentration [ppm]
C_0, C_{in}	initial ozone concentration [ppm]
C_{out}	outlet ozone concentration [ppm]
C/C_0	dimensionless ozone concentration [-]
Da	Damkohler number, $k_r\bar{\varepsilon}_s H/U_g$ [-]
d_p	particle size [mm]
G_s	solids circulation rate [kg/m^{2}s]
k_r	reaction rate constant based on particle volume, first-order [s^{-1}]
m_c	mass of catalysts [g]
r	radial coordinate [m]
R	column radius [m]
r/R	dimensionless sampling position [-]
U_g	superficial gas velocity [m/s]
$V_{c,f}$	volume of catalyst in a fluidized bed [m^3]
$V_{c,p}$	volume of catalyst in the ideal plug flow reactor [m^3]
Q_g	gas flowrate [m^3/s]
X	conversion [-]
Greek letters	
ε_s	local solids holdup [-]
ρ_p	particle density [kg/m^3]
Abbreviations	
BFB	bubbling fluidized bed
CFB	circulating fluidized bed
CSTR	continous stired tank reactor
CTFB	circulating turbulent fluidized bed
HDCFB	high density circulating fluidized bed
PFR	plug flow reactor
RNI	radial non-uniformity index
TFB	turbulent fluidized bed

References

Bi, H., N. Ellis, I. Abba and J. Grace (2000). A state-of-the-art review of gas–solid turbulent fluidization. *Chemical Engineering Science* **55**(21): 4789-4825.

Bi, H. and L. S. Fan (1992). Existence of turbulent regime in gas‐solid fluidization. *AIChE Journal* **38**(2): 297-301.

Bi, H., J. Grace and K. Lim (1995). Transition from bubbling to turbulent fluidization. *Industrial & Engineering Chemistry research* **34**(11): 4003-4008.

Chavarie, C. and J. R. Grace (1975). Performance analysis of a fluidized bed reactor. II. Observed reactor behavior compared with simple two-phase models. *Industrial & Engineering Chemistry Fundamentals* **14**(2): 79-86.

Chen, H. and H. Li (2004). Characterization of a high-density downer reactor. *Powder Technology* **146**(1): 84-92.

Chiba, T. and H. Kobayashi (1970). Gas exchange between the bubble and emulsion phases in gas-solid fluidized beds. *Chemical Engineering Science* **25**(9): 1375-1385.

Du, B., L. S. Fan, F. Wei and W. Warsito (2002). Gas and solids mixing in a turbulent fluidized bed. *AIChE Journal* **48**(9): 1896-1909.

Fan, C., Y. Zhang, X. Bi, W. Song, W. Lin and L. a. Luo (2008). Evaluation of downer reactor performance by catalytic ozone decomposition. *Chemical Engineering Journal* **140**(1): 539-554.

Frye, C., W. Lake and H. Eckstrom (1958). Gas‐solid contacting with ozone decomposition reaction. *AIChE Journal* **4**(4): 403-408.

Grace, J. (1990). High-velocity fluidized bed reactors. *Chemical Engineering Science* **45**(8): 1953-1966.

Grace, J. R., A. S. Issangya, D. Bai, H. Bi and J. Zhu (1999). Situating the high‐density circulating fluidized bed. *AIChE Journal* **45**(10): 2108-2116.

Issangya, A., D. Bai, H. Bi, K. Lim, J. Zhu and J. Grace (1999). Suspension densities in a high-density circulating fluidized bed riser. *Chemical Engineering Science* **54**(22): 5451-5460.

Jiang, P., H. Bi, R. H. Jean and L. S. Fan (1991). Baffle effects on performance of catalytic circulating fluidized bed reactor. *AIChE Journal* **37**(9): 1392-1400.

Knowlton, T., S. Karri and A. Issangya (2005). Scale-up of fluidized-bed hydrodynamics. *Powder Technology* **150**(2): 72-77.

Li, D., A. K. Ray, M. B. Ray and J. Zhu (2013). Catalytic reaction in a circulating fluidized bed riser: Ozone decomposition. *Powder Technology* **242**: 65-73.

Li, D., J. Zhu, M. B. Ray and A. K. Ray (2011). Catalytic reaction in a circulating fluidized bed downer: ozone decomposition. *Chemical Engineering Science* **66**(20): 4615-4623.

Lim, K., J. Zhu and J. Grace (1995). Hydrodynamics of gas-solid fluidization. *International Journal of Multiphase Flow* **21**: 141-193.

Lin, S.-C., H. Arastoopour and H. Kono (1986). Experimental and theoretical study of a multistage fluidized-bed reactor. *Powder Technology* **48**(2): 125-140.

Liu, J., J. R. Grace and X. Bi (2003). Novel multifunctional optical‐fiber probe: I. Development and validation. *AIChE Journal* **49**(6): 1405-1420.

Ouyang, S., X. G. Li and O. Potter (1995). Circulating fluidized bed as a catalytic reactor: experimental study. *AIChE Journal* **41**(6): 1534-1542.

Qi, M., S. Barghi and J. Zhu (2012). Detailed hydrodynamics of high flux gas–solid flow in a circulating turbulent fluidized bed. *Chemical Engineering Journal* **209**: 633-644.

Qi, X., H. Zhu and J. Zhu (2009). Demarcation of a new circulating turbulent fluidization regime. *AIChE Journal* **55**(3): 594-611.

Reh, L. (1995). New and efficient high‐temperature processes with circulating fluid bed reactors. *Chemical Engineering & Technology* **18**(2): 75-89.

Seinfeld, J. and S. Pandis (2006). Atmospheric Chemistry and Physics, A Wiley-Inter Science Publication, John Wiley & Sons Inc, New York.

Song, X., X. T. Bi and Y. Bolkan (2005). Hydrodynamics of high-density downer reactors using a novel solids feeder. *International Journal of Chemical Reactor Engineering* **3**(1).

Sun, G. and J. R. Grace (1990). The effect of particle size distribution on the performance of a catalytic fluidized bed reactor. *Chemical Engineering Science* **45**(8): 2187-2194.

Van Lare, C., H. Piepers and D. Thoenes (1990). Scaling and particle size optimization of mass transfer in gas fluidized beds. *Chemical Engineering Science* **45**(8): 2211-2217.

Wang, C., G. Wang, C. Li, S. Barghi and J. Zhu (2014a). Catalytic ozone decomposition in a high density circulating fluidized bed riser. *Industrial & Engineering Chemistry Research* **53**(16): 6613-6623.

Wang, C., S. Barghi and J. Zhu (2014b). Hydrodynamics and reactor performance evaluation of a high flux gas‐solids circulating fluidized bed downer: Experimental study. *AIChE Journal* **60**(10): 3412-3423.

Wang, C., J. Zhu, S. Barghi and C. Li (2014c). Axial and radial development of solids holdup in a high flux/density gas–solids circulating fluidized bed. *Chemical Engineering Science* **108**: 233-243.

Wang, C., J. Zhu, C. Li and S. Barghi (2014d). Detailed measurements of particle velocity and solids flux in a high density circulating fluidized bed riser. *Chemical Engineering Science* **114**: 9-20.

Wang, C., C. Li and J. Zhu (2015). Axial solids flow structure in a high density gas–solids circulating fluidized bed downer. *Powder Technology* **272**: 153-164.

Wojtowicz, J. A. (2005). Ozone. *Encyclopedia of Chemical Technology*. Kirk-Othmer, John Wiley & Sons.

Yerushalmi, J. and N. Cankurt (1979). Further studies of the regimes of fluidization. *Powder Technology* **24**(2): 187-205.

Zhang, H., W. X. Huang and J. X. Zhu (2001). Gas‐solids flow behavior: CFB riser vs. downer. *AIChE Journal* **47**(9): 2000-2011.

Zhang, H., P. Johnston, J.-X. Zhu, H. De Lasa and M. Bergougnou (1998). A novel calibration procedure for a fiber optic solids concentration probe. *Powder Technology* **100**(2): 260-272.

Zhang, H. and J.-X. Zhu (2000). Hydrodynamics in downflow fluidized beds (2): particle velocity and solids flux profiles. *Chemical Engineering Science* **55**(19): 4367-4377.

Zhu, H. and J. Zhu (2008a). Gas‐solids flow structures in a novel circulating‐turbulent fluidized bed. *AIChE Journal* **54**(5): 1213-1223.

Zhu, H. and J. Zhu (2008b). Comparative study of flow structures in a circulating-turbulent fluidized bed. *Chemical Engineering Science* **63**(11): 2920-2927.

Zhu, H., J. Zhu, G. Li and F. Li (2008c). Detailed measurements of flow structure inside a dense gas–solids fluidized bed. *Powder Technology* **180**(3): 339-349.

Zhu, J. (2010). Circulating turbulent fluidization—a new fluidization regime or just a transitional phenomenon. *Particuology* **8**(6): 640-644.

Zhu, J. and Y. Cheng (2006). Fluidized-bed reactors and applications. *CRC Press, Boca Raton*.

Zhu, J. X. and H. T. Bi (1995). Distinctions between low density and high density circulating fluidized beds. *The Canadian Journal of Chemical Engineering* **73**(5): 644-649.

Zhu, J. X., Z. Q. Yu, Y. Jin, J. Grace and A. Issangya (1995). Cocurrent downflow circulating fluidized bed (downer) reactors—a state of the art review. *The Canadian Journal of Chemical Engineering* **73**(5): 662-677.

Zhu, J. X. J. and S. V. Manyele (2001). Radial nonuniformity index (RNI) in fluidized beds and other multiphase flow systems. *The Canadian Journal of Chemical Engineering* **79**(2): 203-213.

Chapter 9 Conclusions

This study comprehensively investigated the hydrodynamics and reactor performances of a bubbling fluidized bed (BFB), a turbulent fluidized bed (TFB) and a newly identified circulating turbulent fluidized bed (CTFB) in a multifunctional fluidized-bed system.

The hydrodynamic study of the fluidized beds was conducted in terms of macroscopic behaviour, such as axial/radial distributions of solids holdup and flow fluctuations, and of microscopic behaviour, such as gas-solids mixing and interactions. For the BFBs and TFBs, their hydrodynamic characteristics were confirmed to be consistent with literature results. Both BFB and TFB exhibited relatively uniform axial and radial profiles of solids holdup. The BFB has a continuous dense particulate phase with small portions of gas and a discrete dilute bubble phase containing a few particles. The TFB has a dilute phase vigorously interacting with a comparable dense phase, which is in favour of gas-solids mixing and contacting. The effects of static bed height and bed diameter on flow structures were also investigated. Higher static bed height led to higher solids holdups in the entire bed, but similar flow fluctuations compared with lower static bed height. Additionally, more vigorous flow fluctuations and two-phase interactions were observed in the bed of smaller diameter in spite of lower solids holdup, when compared with the bed of larger diameter.

The CTFB successfully achieved a gas/solids upflow with solids circulation rates as high as 300 kg/m^{2}s while maintaining high solids holdup ranging from 0.25 to 0.35. A radial gradient of solids holdup was shown at each elevation with increasing magnitude from the centre to the wall, likely due to the high solids circulation rates. However, the non-uniformity was significantly mitigated by the increased solids holdup in the central region of the bed, when compared with that in CFBs. Furthermore, the solids holdup's radial distribution remained constant with the bed elevation, indicating a uniform axial flow structure similar to a plug flow. By analysing the standard deviations of solids holdup, intermittency indexes and transient signals, the CTFB showed vigorous fluctuations and homogeneously inter-diffused dilute and dense phases, suggesting favourable heat/mass transfer and highly efficient gas-solids contacting.

The reactor performances of the BFB, TFB and CTFB were studied by using catalytic ozone decomposition. For both BFB and TFB, the ozone conversions generally increased with

increasing elevation, and they exhibited fairly uniform radial distributions of ozone conversion, the same as those of solids holdup. Furthermore, the static bed height has almost no effect on conversion distributions due to the unchanged flow structure. In contrast, the bed diameter does affect conversion distributions. The bed of smaller diameter led to higher ozone conversions than the bed of larger diameter, presumably due to the increased mass transfer efficiency and better gas-solids mixing. Such scale-up effect was more significant in the bubbling regime, but it diminished after entering the turbulent regime. This finding indicated that the scale-up for TFBs could be less troublesome than for BFBs.

The reactor performance of CTFB was studied for the first time in this work. The distributions of ozone conversion were closely related to the corresponding distributions of solids holdup. In the axial direction, the ozone conversion increased with elevation. A large portion of reaction took place in the bottom region, due to the vigorous gas-solids contacting and high ozone concentration in the region. In the radial direction, the ozone conversion continuously increased from the centre to the wall, resulting from the non-uniform radial distribution of solids holdup. Moreover, the ozone conversion increased with the solids circulation rate, presumably caused by the enlarging gas-solids (reactant-catalysts) contacting area with the increasing solids holdup. The conversion decreased with increasing superficial gas velocity, mainly due to the reducing reactant-gas residence time and solids holdup.

The reactor performances of various types of fluidized beds, including BFB, TFB, CTFB, CFB riser and downer, were evaluated and compared based on the same reactor size, the same reaction and the same catalyst particles. Clear correlations between the overall ozone conversions and the mean solids holdups were established in all fluidization regimes. The overall conversions increased with the mean solids holdups, albeit following different manners, indicating the flow structures, including the behaviour and distributions of gas/solids, essentially determined the reactor performances.

The CTFB and the downer had comparable ozone conversions that were very close to that of a plug-flow reactor, resulting from their homogeneous flow structures with little back-mixing. While the TFB showed fairly favourable reactor performance due to the relatively vigorous gas-solids interaction, the CTFB is still superior in reactor efficiency. The reactor performances of

the BFB and CFB riser further deviated from that of a plug-flow reactor due to the bypassing and back-mixing of reactant-gas.

The reactor performances of the fluidized beds were quantitatively assessed by the gas-solids contact efficiency. The CTFB generally showed the highest contact efficiency because of the dense solids concentration, uniform axial distribution of solids holdup, and homogeneous gas/solids mixing, etc. The contact efficiency of the downer reactor was equivalent or slightly lower than that of the CTFB. Although the TFB also demonstrated fairly high contact efficiency, it was still lower than the CTFB and downer. As a result of the gas/solids segregation, though in different forms, in the BFB and the CFB riser, their contact efficiencies were significantly reduced.

Appendices

A. Reproducibility and confidence intervals of ozone concentration results

The reaction rate of catalytic ozone decomposition is affected by humidity, temperature and pressure. A humidity meter and a thermometer were used to monitor the relative humidity and temperature of the air supply respectively. The relative humidity was maintained at 19%, and temperature remained at 20℃ without significant fluctuation. A regulator was used to set the pressure of the air supply at 172.3kPa.

During the ozone concentration measurements, 4 g of catalyst particles were taken out of the reactor for checking the activity in the small fixed bed reactor, before and after each experimental run. The reaction rate constant showed no significant variance, so that the ozone concentration results were considered to be obtained at the same catalytic activity.

A single concentration test of the ozone analyser lasted 1 min and generated 15 data points. In each sampling position, five tests were conducted at different times. As examples, Table A.1, Table A.2 and Table A.3 present the ozone concentrations and standard deviations in the BFB, TFB and CTFB under certain operation conditions. The standard deviation in each position was calculated based on the average values of five groups of data. The standard deviation results indicate good reproducibility of the ozone concentration measurement.

Table A.1 Ozone concentrations and standard deviations in the BFB at U_g=0.3 m/s, D_T=152mm and H_0=1.0m (*mean*=mean value, *s*=standard deviation)

BFB, U_g=0.3 m/s				
		H=0.22m	*H*=0.79m	*H*=1.80m
r/R=0	*mean*	0.4687	0.2463	0.1876
	s	0.0100	0.0056	0.0158
0.316	*mean*	0.4693	0.2636	0.1743
	s	0.0140	0.0092	0.0129
0.548	*mean*	0.4537	0.2413	0.1861
	s	0.0175	0.0145	0.0112
0.707	*mean*	0.3823	0.2554	0.1861
	s	0.0164	0.0035	0.0148
0.837	*mean*	0.4069	0.1725	0.1861
	s	0.0100	0.0146	0.0064
0.950	*mean*	0.3672	0.1541	0.1925
	s	0.0024	0.0069	0.0043

Table A.2 Ozone concentrations and standard deviations in the TFB at U_g=0.8 m/s D_T=152mm and H_0=1.0m (*mean*=mean value, *s*=standard deviation)

TFB, U_g=0.8 m/s				
		H=0.22m	*H*=0.79m	*H*=1.80m
r/R=0	*mean*	0.5653	0.4194	0.2677
	s	0.0155	0.0137	0.0087
0.316	*mean*	0.5690	0.3799	0.2672
	s	0.0114	0.0055	0.0083
0.548	*mean*	0.5358	0.3993	0.2238
	s	0.0101	0.0112	0.0051
0.707	*mean*	0.4996	0.3568	0.2552
	s	0.0122	0.0063	0.0071
0.837	*mean*	0.4915	0.3520	0.2592
	s	0.0083	0.0084	0.0089
0.950	*mean*	0.5101	0.3504	0.2025
	s	0.0092	0.0075	0.0022

Table A.3 Ozone concentrations and standard deviations in the CTFB at U_g=3.0 m/s, G_s=200 kg/m^{2}s, D_T=76mm (*mean*=mean value, *s*=standard deviation)

CTFB, U_g=3.0 m/s, G_s=200 kg/m^{2}s				
		H=0.56m	*H*=1.47m	*H*=2.39m
r/R=0	*mean*	0.7659	0.6708	0.5334
	s	0.0126	0.0028	0.0111
0.316	*mean*	0.7182	0.6134	0.4747
	s	0.0072	0.0185	0.0007
0.548	*mean*	0.7046	0.5569	0.4630
	s	0.0078	0.0096	0.0038
0.707	*mean*	0.6462	0.5047	0.4494
	s	0.0189	0.0120	0.0108
0.837	*mean*	0.6039	0.4829	0.3968
	s	0.0172	0.0091	0.0069
0.950	*mean*	0.5559	0.4317	0.3583
	s	0.0194	0.0174	0.0099

For applied science, a 95% confidence interval is usually applied. If the sample size is small (<30), a 95% confidence interval can be calculated by:

$$\bar{x} \pm t(\frac{\alpha}{2}; n-1) \cdot \frac{s}{\sqrt{n}} \qquad \text{Eq. A1}$$

where x is the sample mean, 1-α is the confidence coefficient (α=0.05), n is the amount of samples (n=5), s is the standard deviation, and t is the "student-t" in statistics (t=2.776 found in the student-t distribution table).

The data in Table A.1, Table A.2 and Table A.3 were analysed as examples to evaluate the confidence interval. The confidence interval results for the mean ozone concentrations are shown in Figure A.1, Figure A.2 and Figure A.3. The interval breadth is of the same order as the height of the symbols in the figures. By checking all the ozone concentration results, the confidence intervals are within ± 0.025.

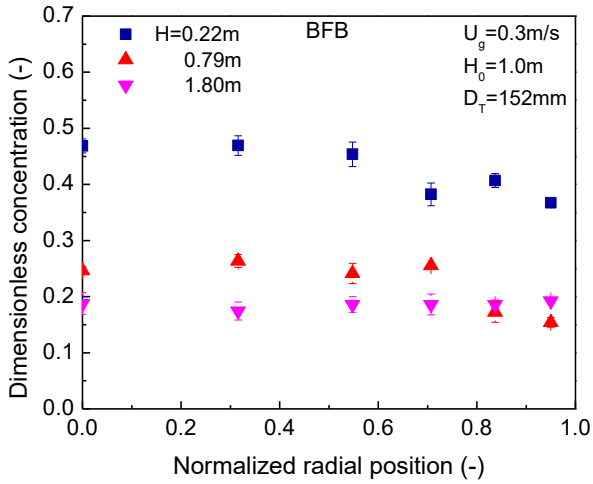

Figure A.1 Ozone concentration results with confidence intervals in the BFB at U_g=0.3 m/s

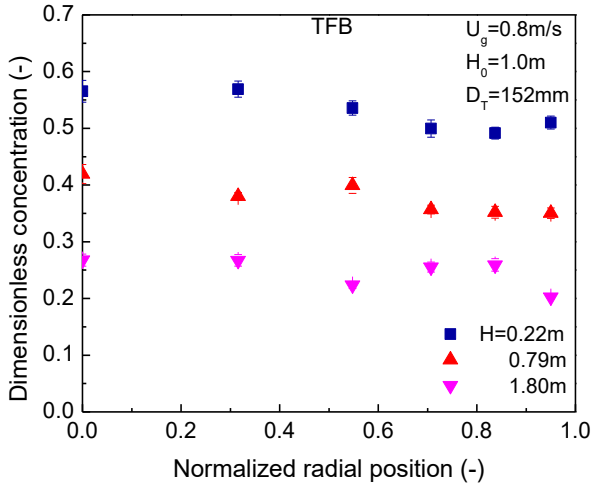

Figure A.1 Ozone concentration results with confidence intervals in the TFB at U_g=0.8 m/s

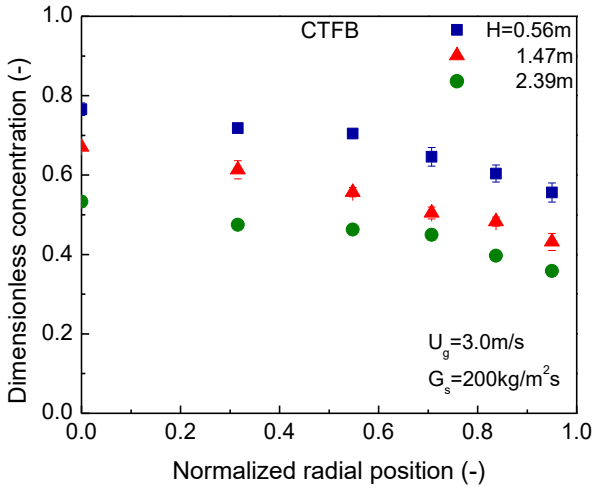

Figure A.1 Ozone concentration results with confidence intervals in the CTFB at U_g=3.0 m/s, G_s=200 kg/m^{2}s

B. Raw data of solids holdup and ozone concentration in the BFB, TFB and CTFB

The data of solids holdup, standard deviation and ozone concentration are shown in the tables.

List of symbols

ε_s	Solids holdup	σ_s	Standard deviation of solids holdup
C/C_0	Ozone concentration	U_g	Superficial gas velocity [m/s]
G_s	Solids circulation rate [kg/m^{2}s]	H_0	Static bed height [m]
D_T	Bed diameter [mm]	H	Measuring height [m]
r/R	Normalized radial position		

B.1 ε_s and σ_s in the column of D_T=76mm and H_0=1.0m

U_g=0.3 m/s							
ε_s	r/R=0	0.316	0.548	0.707	0.837	0.95	Average
H=0.25	0.2696	0.3098	0.3504	0.3688	0.3952	0.3374	0.3520
0.56	0.2772	0.2773	0.2928	0.3026	0.3276	0.3468	0.3098
1.02	0.2776	0.2694	0.2883	0.2935	0.2834	0.3459	0.2966
1.47	0.2102	0.2526	0.2325	0.2301	0.2549	0.3521	0.2634
1.93	0.0163	0.0197	0.0174	0.0161	0.0165	0.0162	0.0171
2.39	0.0156	0.0155	0.0154	0.0155	0.0154	0.0154	0.0155
σ_s	r/R=0	0.316	0.548	0.707	0.837	0.95	
H=0.25	0.1756	0.1565	0.1439	0.1143	0.0588	0.0013	
0.56	0.1740	0.1849	0.1745	0.1658	0.1539	0.1347	
1.02	0.1969	0.2003	0.1838	0.1881	0.1824	0.1452	
1.47	0.2031	0.2052	0.2023	0.2030	0.1980	0.1697	
1.93	0.0015	0.0217	0.0110	0.0009	0.0024	0.0006	
2.39	0.0001	0.0001	0.0001	0.0001	0.0001	0.0001	

U_g=0.5 m/s							
ε_s	r/R=0	0.316	0.548	0.707	0.837	0.95	Average
H=0.25	0.2522	0.2713	0.3265	0.3687	0.4011	0.3797	0.3501
0.56	0.2194	0.2276	0.2523	0.2182	0.2885	0.3652	0.2707
1.02	0.1986	0.2445	0.2387	0.2502	0.2302	0.3310	0.2579
1.47	0.2249	0.2145	0.2270	0.2387	0.2570	0.3393	0.2560
1.93	0.0975	0.1167	0.1392	0.1109	0.1030	0.1490	0.1234
2.39	0.0178	0.0175	0.0249	0.0181	0.0314	0.0200	0.0225
σ_s	r/R=0	0.316	0.548	0.707	0.837	0.95	
H=0.25	0.1756	0.1726	0.1680	0.1302	0.0791	0.0016	

0.56	0.1954	0.1931	0.1898	0.1786	0.1700	0.1316	
1.02	0.1951	0.1889	0.1840	0.1892	0.1854	0.1560	
1.47	0.1904	0.1887	0.1751	0.1893	0.1665	0.1513	
1.93	0.1492	0.1667	0.1767	0.1401	0.1419	0.1639	
2.39	0.0021	0.0020	0.0491	0.0028	0.0581	0.0027	

U_g=0.8 m/s							
ε_s	***r/R*=0**	**0.316**	**0.548**	**0.707**	**0.837**	**0.95**	**Average**
***H*=0.25**	0.2197	0.2425	0.2717	0.3700	0.4093	0.4738	0.3542
0.56	0.2061	0.2078	0.2408	0.2322	0.2733	0.3641	0.2643
1.02	0.1745	0.1610	0.1627	0.2339	0.2574	0.3056	0.2251
1.47	0.1843	0.1650	0.1949	0.1796	0.2233	0.3270	0.2191
1.93	0.1264	0.1778	0.1471	0.1681	0.2082	0.2874	0.1964
2.39	0.0937	0.0610	0.1171	0.0914	0.0755	0.1109	0.0926
σ_s	***r/R*=0**	**0.316**	**0.548**	**0.707**	**0.837**	**0.95**	
***H*=0.25**	0.1721	0.1720	0.1701	0.1346	0.0827	0.0022	
0.56	0.1780	0.1802	0.1826	0.1694	0.1612	0.1293	
1.02	0.1793	0.1663	0.1598	0.1868	0.1625	0.1472	
1.47	0.1699	0.1710	0.1754	0.1624	0.1690	0.1460	
1.93	0.1538	0.1672	0.1555	0.1537	0.1444	0.1220	
2.39	0.1411	0.0981	0.1541	0.1409	0.0864	0.1216	

U_g=1.0 m/s							
ε_s	***r/R*=0**	**0.316**	**0.548**	**0.707**	**0.837**	**0.95**	**Average**
***H*=0.25**	0.2288	0.2124	0.3087	0.3600	0.3938	0.4328	0.3438
0.56	0.1833	0.2100	0.2421	0.2318	0.3014	0.3176	0.2606
1.02	0.1736	0.1806	0.1744	0.2195	0.2580	0.2997	0.2267
1.47	0.1756	0.1668	0.2102	0.1853	0.2389	0.2579	0.2127
1.93	0.1244	0.1618	0.1479	0.1604	0.1809	0.2619	0.1818
2.39	0.1092	0.1107	0.1143	0.1042	0.0968	0.1363	0.1124
σ_s	***r/R*=0**	**0.316**	**0.548**	**0.707**	**0.837**	**0.95**	
***H*=0.25**	0.1741	0.1638	0.1737	0.1302	0.1035	0.0025	
0.56	0.1756	0.1765	0.1738	0.1725	0.1592	0.1360	
1.02	0.1728	0.1754	0.1654	0.1683	0.1673	0.1515	
1.47	0.1668	0.1643	0.1747	0.1665	0.1716	0.1585	
1.93	0.1341	0.1578	0.1526	0.1462	0.1480	0.1421	
2.39	0.1389	0.1443	0.1419	0.1211	0.0967	0.1165	

U_g=1.2 m/s							
ε_s	***r/R*=0**	**0.316**	**0.548**	**0.707**	**0.837**	**0.95**	**Average**
***H*=0.25**	0.2293	0.2093	0.3325	0.3273	0.4070	0.3632	0.3302
0.56	0.1959	0.1876	0.2249	0.2432	0.3095	0.3179	0.2577
1.02	0.1706	0.1546	0.1503	0.2317	0.2576	0.2692	0.2137
1.47	0.1594	0.1565	0.1788	0.2010	0.2227	0.2765	0.2078

1.93	0.1295	0.1356	0.1493	0.1399	0.1741	0.2788	0.1758
2.39	0.0942	0.0991	0.0748	0.0956	0.1241	0.1666	0.1119
σ_s	***r/R*=0**	**0.316**	**0.548**	**0.707**	**0.837**	**0.95**	
***H*=0.25**	0.1698	0.1701	0.1514	0.1456	0.0515	0.0014	
0.56	0.1709	0.1720	0.1702	0.1706	0.1560	0.1306	
1.02	0.1689	0.1602	0.1522	0.1712	0.1737	0.1522	
1.47	0.1717	0.1703	0.1557	0.1571	0.1563	0.1562	
1.93	0.1445	0.1409	0.1422	0.1269	0.1356	0.1263	
2.39	0.1184	0.1173	0.0954	0.1011	0.1257	0.1340	

B.2 ε_s and σ_s in the column of D_T=76mm and H_0=1.9m

				U_g=0.3 m/s			
ε_s	***r/R*=0**	**0.316**	**0.548**	**0.707**	**0.837**	**0.95**	**Average**
***H*=0.25**	0.3353	0.3623	0.3983	0.4189	0.4210	0.4155	0.4031
0.56	0.2705	0.2989	0.3706	0.3568	0.3948	0.4206	0.3687
1.02	0.3414	0.3268	0.3061	0.3661	0.3566	0.3844	0.3485
1.47	0.3313	0.3234	0.3533	0.3452	0.3953	0.3634	0.3568
1.93	0.2851	0.2881	0.3327	0.3565	0.3458	0.3548	0.3362
2.39	0.1181	0.1001	0.0658	0.0693	0.0620	0.1238	0.0843
σ_s	***r/R*=0**	**0.316**	**0.548**	**0.707**	**0.837**	**0.95**	
***H*=0.25**	0.2038	0.1962	0.1701	0.0235	0.0017	0.0017	
0.56	0.2362	0.2346	0.2236	0.2144	0.2013	0.1709	
1.02	0.2414	0.2400	0.2470	0.2287	0.2125	0.1864	
1.47	0.2350	0.2452	0.2289	0.2252	0.1911	0.2009	
1.93	0.2410	0.2345	0.2282	0.2182	0.2153	0.2041	
2.39	0.2012	0.1837	0.1498	0.1449	0.1277	0.1842	

				U_g=0.5 m/s			
ε_s	***r/R*=0**	**0.316**	**0.548**	**0.707**	**0.837**	**0.95**	**Average**
***H*=0.25**	0.2322	0.2719	0.3407	0.3971	0.3815	0.4667	0.3719
0.56	0.2212	0.2533	0.2666	0.2462	0.2781	0.3453	0.2774
1.02	0.2240	0.1984	0.2455	0.2440	0.2848	0.2737	0.2507
1.47	0.2285	0.2179	0.2469	0.2646	0.2706	0.3238	0.2656
1.93	0.2211	0.2356	0.2508	0.2607	0.2746	0.3140	0.2672
2.39	0.2354	0.2004	0.2068	0.2006	0.2083	0.2580	0.2159
σ_s	***r/R*=0**	**0.316**	**0.548**	**0.707**	**0.837**	**0.95**	
***H*=0.25**	0.1679	0.1727	0.1503	0.1066	0.0350	0.0032	
0.56	0.1898	0.1875	0.1849	0.1765	0.1606	0.1406	
1.02	0.1901	0.1849	0.1867	0.1839	0.1717	0.1644	
1.47	0.2026	0.1963	0.1992	0.1891	0.1822	0.1638	
1.93	0.1928	0.1899	0.1880	0.1777	0.1784	0.1539	
2.39	0.2117	0.1993	0.1952	0.1862	0.1821	0.1759	

U_g=0.8 m/s							
ε_s	*r/R*=0	0.316	0.548	0.707	0.837	0.95	Average
H=0.25	0.2358	0.2945	0.3442	0.4112	0.4220	0.3713	0.3682
0.56	0.2156	0.1865	0.2609	0.2485	0.3233	0.3501	0.2758
1.02	0.1952	0.2092	0.1977	0.1961	0.2842	0.3039	0.2381
1.47	0.1901	0.2027	0.1939	0.1758	0.2388	0.2586	0.2137
1.93	0.1724	0.2120	0.2379	0.2391	0.2319	0.2864	0.2409
2.39	0.1672	0.1725	0.1800	0.1881	0.2126	0.2874	0.2084
σ_s	*r/R*=0	0.316	0.548	0.707	0.837	0.95	
H=0.25	0.1914	0.1823	0.1671	0.1078	0.0957	0.0015	
0.56	0.1901	0.1761	0.1869	0.1873	0.1663	0.1517	
1.02	0.1975	0.1974	0.1889	0.1796	0.1785	0.1606	
1.47	0.1938	0.1949	0.1900	0.1748	0.1882	0.1766	
1.93	0.1995	0.2028	0.1889	0.1874	0.1940	0.1696	
2.39	0.1959	0.1787	0.1946	0.1737	0.1722	0.1609	

U_g=1.0 m/s							
ε_s	*r/R*=0	0.316	0.548	0.707	0.837	0.95	Average
H=0.25	0.1796	0.2514	0.2684	0.2631	0.4393	0.4323	0.3300
0.56	0.1653	0.2055	0.2251	0.2510	0.3165	0.3550	0.2704
1.02	0.1550	0.1758	0.1616	0.2030	0.2229	0.3144	0.2153
1.47	0.1670	0.1852	0.1831	0.2175	0.2215	0.2886	0.2190
1.93	0.1416	0.1467	0.1629	0.2153	0.2113	0.3089	0.2096
2.39	0.1473	0.1298	0.1414	0.1800	0.1883	0.2464	0.1781
σ_s	*r/R*=0	0.316	0.548	0.707	0.837	0.95	
H=0.25	0.1553	0.1719	0.1699	0.1544	0.0623	0.0072	
0.56	0.1956	0.1912	0.1813	0.1876	0.1505	0.1424	
1.02	0.1656	0.1786	0.1667	0.1713	0.1654	0.1529	
1.47	0.1714	0.1960	0.1638	0.1774	0.1737	0.1559	
1.93	0.1746	0.1618	0.1552	0.1735	0.1579	0.1407	
2.39	0.1655	0.1576	0.1526	0.1675	0.1551	0.1434	

U_g=1.2 m/s							
ε_s	*r/R*=0	0.316	0.548	0.707	0.837	0.95	Average
H=0.25	0.1840	0.1885	0.3225	0.3997	0.4294	0.4707	0.3645
0.56	0.2094	0.1711	0.2548	0.2150	0.3154	0.3924	0.2721
1.02	0.1496	0.1558	0.1933	0.2138	0.2472	0.3234	0.2274
1.47	0.1740	0.1671	0.1678	0.1781	0.2294	0.2679	0.2026
1.93	0.1119	0.1419	0.1386	0.1616	0.1693	0.3002	0.1819
2.39	0.0971	0.0993	0.1551	0.1465	0.1387	0.2095	0.1505
σ_s	*r/R*=0	0.316	0.548	0.707	0.837	0.95	
H=0.25	0.1697	0.1662	0.1735	0.1135	0.0785	0.0030	
0.56	0.1908	0.1711	0.1841	0.1803	0.1658	0.1216	
1.02	0.1669	0.1676	0.1743	0.1679	0.1761	0.1528	

1.47	0.1768	0.1736	0.1667	0.1651	0.1710	0.1599	
1.93	0.1347	0.1515	0.1431	0.1421	0.1391	0.1410	
2.39	0.1161	0.1204	0.1565	0.1353	0.1347	0.1321	

B.3 ε_s and σ_s in the column of D_T=152mm and H_0=0.8m

U_g=0.1 m/s							
ε_s	***r/R*=0**	**0.316**	**0.548**	**0.707**	**0.837**	**0.95**	**Average**
***H*=0.22**	0.3493	0.4007	0.4281	0.4450	0.4690	0.4585	0.4395
0.53	0.3743	0.3961	0.3817	0.4511	0.4726	0.4722	0.4345
0.79	0.3686	0.3667	0.3647	0.4298	0.4515	0.4301	0.4090
1.04	0.0160	0.0159	0.0159	0.0158	0.0177	0.0162	0.0163
σ_s	***r/R*=0**	**0.316**	**0.548**	**0.707**	**0.837**	**0.95**	
***H*=0.22**	0.1042	0.1001	0.0822	0.0598	0.0362	0.0466	
0.53	0.1228	0.1190	0.1275	0.0862	0.0666	0.0413	
0.79	0.1197	0.1153	0.0995	0.0938	0.0704	0.0462	
1.04	0.0014	0.0017	0.0019	0.0008	0.0142	0.0021	

U_g=0.3 m/s							
ε_s	***r/R*=0**	**0.316**	**0.548**	**0.707**	**0.837**	**0.95**	**Average**
***H*=0.22**	0.3064	0.3253	0.3395	0.3834	0.4088	0.4298	0.3775
0.53	0.2805	0.3029	0.2869	0.3571	0.3462	0.4401	0.3464
0.79	0.2933	0.3068	0.3354	0.3473	0.3728	0.4422	0.3612
1.04	0.1878	0.1592	0.1714	0.2594	0.2243	0.2819	0.2206
1.30	0.0229	0.0179	0.0185	0.0188	0.0276	0.0228	0.0213
σ_s	***r/R*=0**	**0.316**	**0.548**	**0.707**	**0.837**	**0.95**	
***H*=0.22**	0.1177	0.1121	0.0875	0.0832	0.0873	0.0283	
0.53	0.1357	0.1328	0.1341	0.1193	0.1150	0.0606	
0.79	0.1480	0.1506	0.1453	0.1439	0.0828	0.0929	
1.04	0.1613	0.1095	0.1131	0.1675	0.1622	0.1578	
1.30	0.0346	0.0015	0.0024	0.0028	0.0446	0.0093	

U_g=0.5 m/s							
ε_s	***r/R*=0**	**0.316**	**0.548**	**0.707**	**0.837**	**0.95**	**Average**
***H*=0.22**	0.3217	0.3539	0.3630	0.3789	0.3966	0.4143	0.3809
0.53	0.2831	0.2979	0.2813	0.3539	0.3509	0.3883	0.3344
0.79	0.2536	0.2801	0.2965	0.3466	0.3561	0.3884	0.3335
1.04	0.1800	0.1800	0.2526	0.2418	0.2489	0.3113	0.2480
1.30	0.0724	0.0788	0.0745	0.0703	0.0830	0.0949	0.0801
1.55	0.0252	0.0299	0.0216	0.0220	0.0404	0.0386	0.0303
1.80	0.0223	0.0214	0.0186	0.0186	0.0210	0.0212	0.0202
σ_s	***r/R*=0**	**0.316**	**0.548**	**0.707**	**0.837**	**0.95**	
***H*=0.22**	0.1094	0.1148	0.0784	0.0653	0.0761	0.0361	
0.53	0.1623	0.1594	0.1585	0.1427	0.1496	0.1308	

0.79	0.1558	0.1543	0.1523	0.1401	0.1350	0.1211
1.04	0.1344	0.1370	0.1586	0.1585	0.1509	0.1409
1.30	0.1019	0.1101	0.1124	0.0978	0.1197	0.1276
1.55	0.0201	0.0456	0.0081	0.0084	0.0876	0.0661
1.80	0.0068	0.0195	0.0028	0.0028	0.0040	0.0042

U_g=0.8 m/s							
ε_s	***r/R*=0**	**0.316**	**0.548**	**0.707**	**0.837**	**0.95**	**Average**
***H*=0.22**	0.2740	0.3019	0.3477	0.3831	0.4117	0.4328	0.3757
0.53	0.2473	0.2511	0.2826	0.3289	0.3324	0.3751	0.3147
0.79	0.2377	0.2743	0.2491	0.2506	0.3380	0.3994	0.3015
1.04	0.1361	0.1603	0.2172	0.1912	0.2363	0.2365	0.2085
1.30	0.0828	0.0837	0.1385	0.0980	0.1273	0.1776	0.1257
1.55	0.0412	0.0390	0.0585	0.0536	0.0632	0.0460	0.0524
1.80	0.0266	0.0267	0.0396	0.0311	0.0326	0.0675	0.0397
2.34	0.0231	0.0221	0.0208	0.0215	0.0215	0.0265	0.0225
σ_s	***r/R*=0**	**0.316**	**0.548**	**0.707**	**0.837**	**0.95**	
***H*=0.22**	0.1108	0.1039	0.0892	0.0845	0.0691	0.0616	
0.53	0.1555	0.1544	0.1500	0.1440	0.1288	0.1301	
0.79	0.1512	0.1500	0.1412	0.1393	0.1167	0.1001	
1.04	0.1289	0.1431	0.1556	0.1528	0.1523	0.1441	
1.30	0.0964	0.0995	0.1423	0.1104	0.1324	0.1468	
1.55	0.0519	0.0315	0.0915	0.0867	0.0882	0.0361	
1.80	0.0102	0.0116	0.0754	0.0284	0.0182	0.1107	
2.34	0.0068	0.0072	0.0039	0.0056	0.0052	0.0092	

U_g=1.0 m/s							
ε_s	***r/R*=0**	**0.316**	**0.548**	**0.707**	**0.837**	**0.95**	**Average**
***H*=0.22**	0.3036	0.3006	0.3515	0.3710	0.4131	0.4245	0.3732
0.53	0.2316	0.2484	0.2581	0.2987	0.2941	0.3800	0.2959
0.79	0.2116	0.2191	0.2019	0.2333	0.2484	0.2740	0.2352
1.04	0.1062	0.1188	0.1401	0.1192	0.1541	0.1966	0.1458
1.30	0.0599	0.0751	0.0767	0.0781	0.0998	0.1256	0.0908
1.55	0.0388	0.0361	0.0432	0.0480	0.0389	0.0584	0.0451
1.80	0.0323	0.0346	0.0325	0.0368	0.0383	0.0435	0.0371
2.34	0.0239	0.0233	0.0260	0.0271	0.0266	0.0321	0.0271
σ_s	***r/R*=0**	**0.316**	**0.548**	**0.707**	**0.837**	**0.95**	
***H*=0.22**	0.1111	0.1155	0.0884	0.0764	0.0495	0.0407	
0.53	0.1550	0.1472	0.1497	0.1481	0.1410	0.0788	
0.79	0.1424	0.1445	0.1332	0.1355	0.1357	0.1216	
1.04	0.1023	0.1139	0.1326	0.1075	0.1258	0.1256	
1.30	0.0684	0.0894	0.0929	0.0852	0.1158	0.1264	
1.55	0.0364	0.0207	0.0520	0.0375	0.0228	0.0441	
1.80	0.0149	0.0185	0.0199	0.0334	0.0222	0.0267	
2.34	0.0079	0.0071	0.0091	0.0105	0.0079	0.0137	

B.4 ε_s and σ_s in the column of D_T=152mm and H_0=1.0m

U_g=0.1 m/s							
ε_s	*r/R*=0	0.316	0.548	0.707	0.837	0.95	Average
H=0.22	0.4466	0.4677	0.4131	0.4192	0.4106	0.4605	0.4330
0.53	0.3952	0.3958	0.3927	0.4303	0.4480	0.4541	0.4244
0.79	0.3740	0.3835	0.3948	0.4527	0.4537	0.4516	0.4275
1.04	0.3798	0.3764	0.3855	0.4275	0.4446	0.4512	0.4176
1.30	0.0593	0.0500	0.0434	0.0512	0.0561	0.0615	0.0527
σ_s	*r/R*=0	0.316	0.548	0.707	0.837	0.95	
H=0.22	0.0816	0.0749	0.1164	0.1174	0.1160	0.0826	
0.53	0.1162	0.1241	0.1241	0.1152	0.1033	0.0514	
0.79	0.1215	0.1220	0.1058	0.0954	0.0533	0.0511	
1.04	0.1336	0.1246	0.1212	0.0981	0.0858	0.0552	
1.30	0.0834	0.0760	0.0684	0.0754	0.0831	0.0901	

U_g=0.3 m/s							
ε_s	*r/R*=0	0.316	0.548	0.707	0.837	0.95	Average
H=0.22	0.3947	0.3728	0.3959	0.4300	0.4667	0.4565	0.4256
0.53	0.3468	0.3508	0.3668	0.3782	0.4387	0.4603	0.3994
0.79	0.3298	0.3291	0.3494	0.4060	0.4393	0.4595	0.3975
1.04	0.3244	0.3555	0.3619	0.3909	0.4325	0.4410	0.3960
1.30	0.3084	0.2896	0.2943	0.3722	0.3660	0.4226	0.3500
1.55	0.1013	0.1000	0.0735	0.1087	0.1049	0.1480	0.1070
1.80	0.0184	0.0218	0.0319	0.0227	0.0270	0.0192	0.0245
σ_s	*r/R*=0	0.316	0.548	0.707	0.837	0.95	
H=0.22	0.1118	0.1225	0.1138	0.1050	0.0567	0.0577	
0.53	0.1310	0.1277	0.1281	0.1202	0.0772	0.0516	
0.79	0.1451	0.1471	0.1500	0.1310	0.1065	0.0751	
1.04	0.1643	0.1605	0.1624	0.1573	0.1155	0.0825	
1.30	0.1725	0.1748	0.1702	0.1623	0.1195	0.0898	
1.55	0.1452	0.1483	0.1160	0.1538	0.1141	0.0778	
1.80	0.0020	0.0168	0.0572	0.0350	0.0507	0.0051	

U_g=0.5 m/s							
ε_s	*r/R*=0	0.316	0.548	0.707	0.837	0.95	Average
H=0.22	0.2739	0.3155	0.4213	0.4389	0.4500	0.4556	0.4168
0.53	0.3135	0.3120	0.3546	0.3732	0.4208	0.4113	0.3753
0.79	0.2981	0.3006	0.3286	0.3502	0.3890	0.4284	0.3600
1.04	0.2919	0.3160	0.2821	0.3362	0.3452	0.4275	0.3409
1.30	0.2822	0.2495	0.2968	0.3409	0.3134	0.3880	0.3195
1.55	0.1767	0.2011	0.2247	0.2017	0.2827	0.3147	0.2449
1.80	0.0437	0.0589	0.0821	0.1032	0.0578	0.0719	0.0747
2.34	0.0203	0.0201	0.0198	0.0204	0.0196	0.0225	0.0205

σ_s	*r/R*=0	0.316	0.548	0.707	0.837	0.95
***H*=0.22**	0.1439	0.1306	0.0946	0.1030	0.1132	0.0568
0.53	0.1769	0.1754	0.1691	0.1665	0.1478	0.0924
0.79	0.1792	0.1781	0.1764	0.1700	0.1424	0.1030
1.04	0.1841	0.1797	0.1755	0.1718	0.1443	0.1102
1.30	0.1840	0.1799	0.1815	0.1761	0.1571	0.1307
1.55	0.1695	0.1922	0.1782	0.1758	0.1814	0.1566
1.80	0.0604	0.1023	0.1437	0.1688	0.0862	0.1047
2.34	0.0057	0.0035	0.0033	0.0037	0.0027	0.0045

U_g=0.8 m/s							
ε_s	*r/R*=0	0.316	0.548	0.707	0.837	0.95	Average
***H*=0.22**	0.3033	0.3106	0.3880	0.4417	0.4240	0.4592	0.4059
0.53	0.2779	0.3064	0.3271	0.3598	0.3905	0.4152	0.3597
0.79	0.2552	0.2980	0.2920	0.3254	0.3454	0.4071	0.3328
1.04	0.2257	0.2336	0.2616	0.2865	0.2954	0.3806	0.2920
1.30	0.1999	0.2056	0.2639	0.2187	0.2513	0.3397	0.2565
1.55	0.1450	0.1409	0.1451	0.1795	0.2578	0.2203	0.1893
1.80	0.0663	0.0911	0.0642	0.1188	0.1400	0.1297	0.1082
2.34	0.0336	0.0320	0.0352	0.0332	0.0353	0.0343	0.0341
σ_s	*r/R*=0	0.316	0.548	0.707	0.837	0.95	
***H*=0.22**	0.1251	0.1247	0.0707	0.0935	0.0889	0.0646	
0.53	0.1558	0.1569	0.1513	0.1537	0.1280	0.1149	
0.79	0.1593	0.1566	0.1579	0.1492	0.1232	0.1080	
1.04	0.1517	0.1528	0.1563	0.1540	0.1301	0.1164	
1.30	0.1436	0.1427	0.1440	0.1428	0.1331	0.1262	
1.55	0.1478	0.1496	0.1482	0.1589	0.1794	0.1487	
1.80	0.0771	0.1183	0.0702	0.1301	0.1502	0.1357	
2.34	0.0228	0.0148	0.0410	0.0380	0.0216	0.0139	

U_g=1.0 m/s							
ε_s	*r/R*=0	0.316	0.548	0.707	0.837	0.95	Average
***H*=0.22**	0.3397	0.3308	0.3574	0.4039	0.4448	0.4369	0.3958
0.53	0.2556	0.2856	0.3377	0.3388	0.3510	0.4033	0.3434
0.79	0.2379	0.2587	0.2830	0.3045	0.3313	0.4074	0.3172
1.04	0.2111	0.2651	0.2233	0.2819	0.2960	0.3820	0.2883
1.30	0.1571	0.1907	0.2067	0.2235	0.2935	0.3138	0.2454
1.55	0.1353	0.0849	0.1461	0.1512	0.1886	0.2131	0.1591
1.80	0.0680	0.0718	0.0791	0.0762	0.0910	0.1045	0.0846
2.34	0.0309	0.0321	0.0354	0.0412	0.0477	0.0469	0.0407
σ_s	*r/R*=0	0.316	0.548	0.707	0.837	0.95	
***H*=0.22**	0.0575	0.1356	0.0535	0.0648	0.0570	0.0505	
0.53	0.1465	0.1471	0.1462	0.1451	0.1029	0.0870	
0.79	0.1540	0.1541	0.1487	0.1410	0.1195	0.0980	

1.04	0.1569	0.1538	0.1460	0.1471	0.1261	0.1040
1.30	0.1263	0.1355	0.1364	0.1373	0.1346	0.1236
1.55	0.1192	0.0882	0.1233	0.1152	0.1276	0.1152
1.80	0.0801	0.0769	0.0995	0.0927	0.0989	0.1014
2.34	0.0135	0.0130	0.0183	0.0437	0.0626	0.0366

B.5 ε_s and σ_s in the CTFB

U_g=1.0 m/s, G_s=100 kg/m^{2}s							
ε_s	***r/R*=0**	**0.316**	**0.548**	**0.707**	**0.837**	**0.95**	**Average**
***H*=0.25**	0.2030	0.2571	0.3399	0.4017	0.4446	0.4901	0.3871
0.56	0.1636	0.1875	0.2549	0.2814	0.3954	0.4484	0.3145
1.02	0.1434	0.1909	0.2361	0.2738	0.3507	0.4528	0.3010
1.47	0.1818	0.1677	0.2310	0.2870	0.3443	0.4557	0.2991
1.93	0.1394	0.1577	0.2144	0.2679	0.3187	0.4055	0.2738
2.39	0.1751	0.1500	0.1979	0.2563	0.2965	0.4113	0.2644
σ_s	***r/R*=0**	**0.316**	**0.548**	**0.707**	**0.837**	**0.95**	
***H*=0.56**	0.1627	0.1785	0.1774	0.1756	0.1109	0.1348	
1.02	0.1577	0.1849	0.2018	0.2002	0.1757	0.1280	
1.47	0.1757	0.1748	0.1916	0.1923	0.1596	0.0936	
1.93	0.1680	0.1721	0.1974	0.2009	0.1634	0.1103	
2.39	0.1803	0.1686	0.1818	0.1887	0.1826	0.0910	

U_g=1.0 m/s, G_s=200 kg/m^{2}s							
ε_s	***r/R*=0**	**0.316**	**0.548**	**0.707**	**0.837**	**0.95**	**Average**
***H*=0.25**	0.2505	0.2579	0.3395	0.3838	0.4180	0.5342	0.3882
0.56	0.2034	0.2196	0.2813	0.3605	0.3749	0.4958	0.3476
1.02	0.2094	0.2342	0.2559	0.3377	0.3595	0.4752	0.3330
1.47	0.1880	0.2045	0.2634	0.3171	0.3623	0.4657	0.3237
1.93	0.1901	0.2270	0.2438	0.3066	0.3452	0.4615	0.3169
2.39	0.1739	0.2065	0.2425	0.2952	0.3470	0.4494	0.3085
σ_s	***r/R*=0**	**0.316**	**0.548**	**0.707**	**0.837**	**0.95**	
***H*=0.56**	0.1934	0.1790	0.1822	0.1534	0.1369	0.0728	
1.02	0.1756	0.1865	0.1957	0.1752	0.1791	0.1209	
1.47	0.1841	0.1940	0.1702	0.1827	0.1641	0.1268	
1.93	0.1797	0.1760	0.1879	0.1899	0.1722	0.1175	
2.39	0.1728	0.1853	0.1914	0.1944	0.1716	0.1323	

U_g=1.0 m/s, G_s=300 kg/m^{2}s							
ε_s	***r/R*=0**	**0.316**	**0.548**	**0.707**	**0.837**	**0.95**	**Average**
***H*=0.56**	0.2435	0.2556	0.3000	0.3768	0.4173	0.5004	0.3711
1.02	0.2025	0.2333	0.2613	0.3423	0.4114	0.4979	0.3498
1.47	0.2381	0.2280	0.2771	0.3456	0.4026	0.4892	0.3502
1.93	0.2039	0.2063	0.2615	0.3545	0.3984	0.4823	0.3422
2.39	0.2136	0.2047	0.2365	0.3583	0.3853	0.4611	0.3308

σ_s	*r/R*=0	0.316	0.548	0.707	0.837	0.95
***H*=0.56**	0.1676	0.1472	0.1508	0.1047	0.0606	0.0044
1.02	0.1584	0.1613	0.1681	0.1673	0.1366	0.0878
1.47	0.1762	0.1727	0.1860	0.1519	0.1469	0.0044
1.93	0.1620	0.1738	0.1774	0.1840	0.1522	0.0708
2.39	0.1918	0.1767	0.1717	0.1855	0.1255	0.0658

U_g=2.0 m/s, G_s=100 kg/m^{2}s							
ε_s	*r/R*=0	0.316	0.548	0.707	0.837	0.95	Average
***H*=0.25**	0.2290	0.2115	0.2963	0.3561	0.4151	0.5117	0.3605
0.56	0.0999	0.1548	0.2070	0.2872	0.3436	0.4834	0.2955
1.02	0.1016	0.1410	0.2070	0.2664	0.3651	0.4361	0.2839
1.47	0.1008	0.1368	0.2027	0.2604	0.3521	0.4130	0.2738
1.93	0.1055	0.1253	0.2229	0.2413	0.3446	0.4221	0.2727
2.39	0.1213	0.1457	0.2050	0.2257	0.3075	0.4069	0.2590
σ_s	*r/R*=0	0.316	0.548	0.707	0.837	0.95	
***H*=0.56**	0.0911	0.1475	0.1484	0.1634	0.1323	0.0968	
1.02	0.0939	0.1252	0.1577	0.1543	0.1598	0.1288	
1.47	0.0909	0.1236	0.1451	0.1192	0.1183	0.1041	
1.93	0.0981	0.1163	0.1722	0.1288	0.0952	0.0714	
2.39	0.1249	0.1410	0.1609	0.1635	0.0808	0.0860	

U_g=2.0 m/s, G_s=200 kg/m^{2}s							
ε_s	*r/R*=0	0.316	0.548	0.707	0.837	0.95	Average
***H*=0.25**	0.2436	0.2721	0.2975	0.3261	0.4019	0.4599	0.3517
0.56	0.1375	0.1894	0.2418	0.3379	0.4051	0.4327	0.3217
1.02	0.1367	0.1637	0.2477	0.322	0.3595	0.4699	0.3138
1.47	0.1309	0.1533	0.2286	0.2988	0.3646	0.4353	0.2974
1.93	0.1267	0.1402	0.2331	0.2818	0.3571	0.4746	0.2991
2.39	0.1494	0.1507	0.2133	0.2996	0.3979	0.4423	0.3026
σ_s	*r/R*=0	0.316	0.548	0.707	0.837	0.95	
***H*=0.56**	0.1292	0.1699	0.1731	0.1352	0.0541	0.0352	
1.02	0.1200	0.1296	0.1552	0.1446	0.1034	0.0621	
1.47	0.1123	0.1303	0.1496	0.1134	0.1157	0.0938	
1.93	0.1000	0.1300	0.1620	0.1244	0.1088	0.0955	
2.39	0.1311	0.1325	0.1547	0.1282	0.0977	0.0850	

U_g=2.0 m/s, G_s=300 kg/m^{2}s							
ε_s	*r/R*=0	0.316	0.548	0.707	0.837	0.95	Average
***H*=0.25**	0.2580	0.3046	0.3156	0.3562	0.4060	0.4363	0.3632
0.56	0.2105	0.2331	0.2500	0.3303	0.4205	0.5081	0.3491
1.02	0.1557	0.1780	0.2422	0.3211	0.4025	0.4983	0.3297
1.47	0.1394	0.2004	0.2592	0.3365	0.4387	0.5059	0.3484
1.93	0.1262	0.1624	0.2525	0.3563	0.4142	0.4814	0.3347
2.39	0.1570	0.1943	0.2376	0.3216	0.4076	0.4916	0.3312

σ_s	*r/R*=0	0.316	0.548	0.707	0.837	0.95
***H*=0.56**	0.1848	0.2032	0.1614	0.1369	0.0758	0.0567
1.02	0.1255	0.1424	0.1430	0.1607	0.1043	0.0805
1.47	0.1110	0.1550	0.1290	0.1256	0.1017	0.0854
1.93	0.0988	0.1522	0.1613	0.1286	0.1067	0.0777
2.39	0.1457	0.1529	0.1440	0.1243	0.1066	0.0725

U_g=3.0 m/s, G_s=100 kg/m^{2}s							
ε_s	*r/R*=0	0.316	0.548	0.707	0.837	0.95	Average
***H*=0.25**	0.1998	0.1918	0.2209	0.3261	0.4091	0.4566	0.3226
0.56	0.0662	0.0698	0.1535	0.2025	0.3429	0.4614	0.2481
1.02	0.0680	0.0746	0.1506	0.2189	0.3372	0.4549	0.2492
1.47	0.0657	0.0776	0.1613	0.1977	0.2999	0.4638	0.2418
1.93	0.0504	0.0675	0.1400	0.2041	0.3151	0.4554	0.2380
2.39	0.0511	0.0650	0.1351	0.2080	0.3046	0.4278	0.2297
σ_s	*r/R*=0	0.316	0.548	0.707	0.837	0.95	
***H*=0.56**	0.0864	0.0955	0.1846	0.1833	0.0928	0.1119	
1.02	0.0735	0.0922	0.1665	0.2112	0.2009	0.0935	
1.47	0.0622	0.0819	0.1640	0.1918	0.2406	0.0966	
1.93	0.0636	0.0669	0.1495	0.1930	0.1067	0.0840	
2.39	0.0743	0.0772	0.1404	0.2071	0.0910	0.0957	

U_g=3.0 m/s, G_s=200 kg/m^{2}s							
ε_s	*r/R*=0	0.316	0.548	0.707	0.837	0.95	Average
***H*=0.25**	0.1537	0.2034	0.2721	0.3621	0.4468	0.4907	0.3557
0.56	0.0795	0.0860	0.1947	0.2815	0.4314	0.4821	0.2977
1.02	0.0806	0.0894	0.1716	0.2595	0.4054	0.4880	0.2849
1.47	0.0753	0.0869	0.1952	0.2632	0.4146	0.4811	0.2905
1.93	0.0740	0.0854	0.1645	0.2623	0.3957	0.4940	0.2825
2.39	0.0657	0.0714	0.1585	0.2569	0.4008	0.4751	0.2749
σ_s	*r/R*=0	0.316	0.548	0.707	0.837	0.95	
***H*=0.56**	0.0894	0.1059	0.1379	0.1441	0.1676	0.0545	
1.02	0.0833	0.0922	0.1585	0.1839	0.1558	0.0670	
1.47	0.0671	0.0770	0.1441	0.1714	0.1349	0.0743	
1.93	0.0635	0.0762	0.1455	0.1598	0.1158	0.0868	
2.39	0.0832	0.1003	0.1457	0.1709	0.0676	0.0847	

U_g=3.0 m/s, G_s=300 kg/m^{2}s							
ε_s	*r/R*=0	0.316	0.548	0.707	0.837	0.95	Average
***H*=0.25**	0.1938	0.2612	0.3058	0.3803	0.5007	0.5027	0.3900
0.56	0.0917	0.1224	0.2194	0.3230	0.4547	0.5271	0.3311
1.02	0.0813	0.1048	0.1983	0.2926	0.4273	0.5011	0.3067
1.47	0.0739	0.0938	0.2053	0.3043	0.4711	0.5091	0.3191
1.93	0.0860	0.1037	0.2177	0.2967	0.4219	0.5023	0.3107
2.39	0.0868	0.0980	0.1976	0.2922	0.4094	0.5055	0.3028

σ_s	*r/R*=0	0.316	0.548	0.707	0.837	0.95
***H*=0.56**	0.1156	0.1479	0.1793	0.1991	0.1013	0.0706
1.02	0.0773	0.0897	0.1500	0.1865	0.1566	0.1108
1.47	0.0643	0.0810	0.1325	0.1354	0.1328	0.0849
1.93	0.0776	0.0893	0.1484	0.1604	0.1291	0.0960
2.39	0.0968	0.1126	0.1467	0.1603	0.1455	0.0870

B.6 C/C_0 in the column of D_T=76mm and H_0=1.0m

U_g=0.3 m/s							
C/C_0	*r/R*=0	0.316	0.548	0.707	0.837	0.95	Average
***H*=0.25**	0.4258	0.3992	0.3844	0.3623	0.3327	0.3586	0.3677
0.56	0.2730	0.2429	0.2109	0.2204	0.1993	0.2620	0.2275
1.02	0.1876	0.1737	0.1559	0.1569	0.1407	0.1509	0.1557
1.47	0.1122	0.1044	0.1022	0.0979	0.1063	0.0783	0.0980
1.93	0.1244	0.1258	0.1324	0.1373	0.1324	0.1150	0.1286
2.39	0.1605	0.1368	0.1222	0.1325	0.1308	0.1182	0.1285

U_g=0.5 m/s							
C/C_0	*r/R*=0	0.316	0.548	0.707	0.837	0.95	Average
***H*=0.25**	0.4959	0.4691	0.4427	0.4768	0.3985	0.3747	0.4325
0.56	0.3962	0.3704	0.3307	0.3060	0.3022	0.2411	0.3099
1.02	0.2550	0.2387	0.2034	0.1997	0.2086	0.1787	0.2057
1.47	0.1881	0.1712	0.1360	0.1477	0.1346	0.1523	0.1484
1.93	0.2056	0.1822	0.1769	0.1756	0.1635	0.1676	0.1736
2.39	0.2034	0.1689	0.1791	0.1641	0.1670	0.1406	0.1648

U_g=0.8 m/s							
C/C_0	*r/R*=0	0.316	0.548	0.707	0.837	0.95	Average
***H*=0.25**	0.5496	0.5224	0.4914	0.4694	0.4548	0.4200	0.4716
0.56	0.4397	0.4170	0.4246	0.3579	0.3356	0.3009	0.3673
1.02	0.3687	0.3341	0.3453	0.3101	0.2879	0.2361	0.3033
1.47	0.2892	0.2774	0.2682	0.2412	0.2584	0.2341	0.2559
1.93	0.2684	0.2460	0.2358	0.2222	0.2146	0.2073	0.2255
2.39	0.2519	0.2352	0.2249	0.2272	0.2017	0.1954	0.2170

U_g=1.0 m/s							
C/C_0	*r/R*=0	0.316	0.548	0.707	0.837	0.95	Average
***H*=0.25**	0.6265	0.5843	0.5504	0.5541	0.5259	0.4985	0.5431
0.56	0.5009	0.4540	0.4511	0.4263	0.4223	0.3825	0.4281
1.02	0.4080	0.3967	0.3357	0.3230	0.3119	0.3187	0.3365
1.47	0.3056	0.2904	0.2787	0.2541	0.2671	0.2734	0.2729
1.93	0.3003	0.2997	0.2748	0.2591	0.2340	0.2466	0.2623
2.39	0.2628	0.2379	0.2517	0.2501	0.2382	0.2272	0.2417

U_g=1.2 m/s							
C/C_0	r/R=0	0.316	0.548	0.707	0.837	0.95	Average
H=0.25	0.6405	0.6217	0.5957	0.5707	0.5542	0.5465	0.5776
0.56	0.5013	0.5020	0.4721	0.4760	0.4348	0.4115	0.4587
1.02	0.4191	0.4100	0.3888	0.3657	0.3359	0.3517	0.3701
1.47	0.3791	0.3649	0.3400	0.3246	0.2867	0.2950	0.3220
1.93	0.3767	0.3602	0.3341	0.2950	0.2867	0.2535	0.3056
2.39	0.3323	0.3274	0.3397	0.2844	0.2322	0.2543	0.2873

B.7 C/C_0 in the column of D_T=76mm and H_0=1.9m

U_g=0.3 m/s							
C/C_0	r/R=0	0.316	0.548	0.707	0.837	0.95	Average
H=0.25	0.3973	0.3751	0.3497	0.3391	0.3089	0.3613	0.3469
0.56	0.2539	0.2297	0.2258	0.2235	0.1822	0.2014	0.2129
1.02	0.1830	0.1618	0.1706	0.1429	0.1143	0.1370	0.1457
1.47	0.1316	0.1340	0.0874	0.1012	0.0889	0.1046	0.1026
1.93	0.1165	0.0918	0.0774	0.0628	0.0788	0.0658	0.0757
2.39	0.1808	0.1046	0.0855	0.0730	0.0951	0.0754	0.0883

U_g=0.5 m/s							
C/C_0	r/R=0	0.316	0.548	0.707	0.837	0.95	Average
H=0.25	0.4608	0.4286	0.4665	0.4109	0.3987	0.3988	0.4216
0.56	0.3407	0.3064	0.3206	0.2924	0.2670	0.2841	0.2949
1.02	0.2328	0.2135	0.2417	0.2213	0.2030	0.1909	0.2147
1.47	0.1850	0.1581	0.1733	0.1644	0.1455	0.1566	0.1603
1.93	0.1554	0.1484	0.1527	0.1321	0.1225	0.1284	0.1369
2.39	0.1495	0.1248	0.1388	0.1306	0.1133	0.1234	0.1269

U_g=0.8 m/s							
C/C_0	r/R=0	0.316	0.548	0.707	0.837	0.95	Average
H=0.25	0.5163	0.5027	0.4808	0.4582	0.4313	0.4084	0.4561
0.56	0.4072	0.4105	0.3645	0.3449	0.3256	0.3454	0.3573
1.02	0.3112	0.3101	0.2781	0.2901	0.2765	0.2918	0.2890
1.47	0.2332	0.2604	0.2408	0.2141	0.2052	0.2160	0.2262
1.93	0.1721	0.1965	0.1837	0.1988	0.1668	0.1760	0.1835
2.39	0.1956	0.1761	0.1919	0.1954	0.1515	0.1503	0.1736

U_g=1.0 m/s							
C/C_0	r/R=0	0.316	0.548	0.707	0.837	0.95	Average
H=0.25	0.6154	0.5916	0.5467	0.5123	0.4751	0.5076	0.5263
0.56	0.4758	0.4692	0.4338	0.3900	0.3654	0.4022	0.4115
1.02	0.3725	0.3786	0.3352	0.3026	0.2725	0.3247	0.3217
1.47	0.2867	0.2799	0.2688	0.2427	0.2241	0.2576	0.2545

1.93	0.2910	0.2930	0.2764	0.2461	0.2279	0.1972	0.2475
2.39	0.2848	0.2524	0.2672	0.2384	0.1811	0.1540	0.2192

U_g=1.2 m/s							
C/C_0	**r/R=0**	**0.316**	**0.548**	**0.707**	**0.837**	**0.95**	**Average**
***H*=0.25**	0.6075	0.5915	0.5679	0.5351	0.5357	0.5195	0.5498
0.56	0.4903	0.4591	0.4463	0.4293	0.4388	0.4141	0.4380
1.02	0.4360	0.4109	0.3853	0.3788	0.3614	0.2916	0.3656
1.47	0.3578	0.3627	0.3396	0.3383	0.2662	0.2809	0.3168
1.93	0.3262	0.3430	0.3074	0.3316	0.2091	0.2404	0.2851
2.39	0.2993	0.2908	0.3242	0.2603	0.1857	0.2480	0.2618

B.8 C/C_0 in the column of D_T=152mm and H_0=0.8m

U_g=0.1 m/s							
C/C_0	**r/R=0**	**0.316**	**0.548**	**0.707**	**0.837**	**0.95**	**Average**
***H*=0.22**	0.3544	0.3738	0.3323	0.2960	0.3219	0.2450	0.3125
0.53	0.2872	0.2476	0.2420	0.1867	0.1776	0.1726	0.2058
0.79	0.1280	0.1296	0.1186	0.1138	0.1063	0.1142	0.1163
1.04	0.1657	0.1645	0.1594	0.1487	0.1577	0.1359	0.1531
1.30	0.1653	0.1692	0.1578	0.1681	0.1382	0.1267	0.1517
1.80	0.1588	0.1651	0.1765	0.1506	0.1473	0.1327	0.1542

U_g=0.3 m/s							
C/C_0	**r/R=0**	**0.316**	**0.548**	**0.707**	**0.837**	**0.95**	**Average**
***H*=0.22**	0.4818	0.4486	0.4683	0.4047	0.4125	0.3613	0.4197
0.53	0.3738	0.3457	0.3299	0.2804	0.2874	0.2550	0.2998
0.79	0.1980	0.1967	0.1876	0.1813	0.1587	0.1612	0.1769
1.04	0.2310	0.2228	0.2209	0.2187	0.2185	0.2289	0.2222
1.30	0.2293	0.2293	0.2186	0.2149	0.2148	0.2197	0.2193
1.80	0.2211	0.2114	0.2092	0.2204	0.2261	0.2280	0.2193
2.34	0.2298	0.2252	0.2148	0.2197	0.2226	0.2176	0.2200

U_g=0.5 m/s							
C/C_0	**r/R=0**	**0.316**	**0.548**	**0.707**	**0.837**	**0.95**	**Average**
***H*=0.22**	0.4886	0.5063	0.5375	0.4533	0.4248	0.4192	0.4675
0.53	0.3832	0.3981	0.4223	0.3359	0.3143	0.3006	0.3536
0.79	0.3271	0.3170	0.3375	0.3302	0.2503	0.2680	0.3008
1.04	0.3073	0.3162	0.2753	0.2657	0.2336	0.2499	0.2672
1.30	0.2708	0.2769	0.2571	0.2666	0.2915	0.2175	0.2615
1.80	0.2552	0.2540	0.2649	0.2554	0.2576	0.2590	0.2583
2.34	0.2604	0.2582	0.2573	0.2564	0.2597	0.2583	0.2580

U_g=0.8 m/s							
C/C_0	r/R=0	0.316	0.548	0.707	0.837	0.95	Average
H=0.22	0.5823	0.5775	0.5507	0.5322	0.4960	0.4794	0.5266
0.53	0.4381	0.4364	0.4397	0.4688	0.4532	0.3547	0.4306
0.79	0.3902	0.3930	0.3603	0.3407	0.4012	0.3232	0.3632
1.04	0.3856	0.4008	0.3361	0.3410	0.2954	0.2491	0.3230
1.30	0.3426	0.3372	0.3405	0.3032	0.2898	0.2643	0.3069
1.80	0.2867	0.2934	0.2947	0.2885	0.2981	0.2825	0.2912
2.34	0.3039	0.3024	0.2916	0.2967	0.2917	0.2791	0.2922

U_g=1.0 m/s							
C/C_0	r/R=0	0.316	0.548	0.707	0.837	0.95	Average
H=0.22	0.7142	0.6153	0.6372	0.5875	0.5660	0.5731	0.5982
0.53	0.5436	0.4930	0.5534	0.5209	0.5349	0.4041	0.5030
0.79	0.4219	0.4381	0.4272	0.3863	0.4511	0.3993	0.4197
1.04	0.3974	0.4065	0.3999	0.3571	0.3793	0.3578	0.3796
1.30	0.3754	0.3806	0.3702	0.3183	0.3230	0.3286	0.3436
1.55	0.3547	0.3329	0.3477	0.3234	0.3171	0.3335	0.3315
2.34	0.3411	0.3212	0.3313	0.3279	0.3237	0.3313	0.3277

B.9 C/C_0 in the column of D_T=152mm and H_0=1.0m

U_g=0.1 m/s							
C/C_0	r/R=0	0.316	0.548	0.707	0.837	0.95	Average
H=0.22	0.4153	0.3855	0.3322	0.3155	0.3253	0.2337	0.3183
0.53	0.4285	0.3632	0.1730	0.1762	0.2120	0.1309	0.2102
0.79	0.1655	0.1611	0.1381	0.1273	0.1084	0.1128	0.1292
1.04	0.1193	0.0950	0.0857	0.0916	0.1001	0.0992	0.0949
1.30	0.1674	0.1438	0.1357	0.1262	0.1379	0.1104	0.1312
1.55	0.1489	0.1438	0.1344	0.1198	0.1323	0.1072	0.1274
1.80	0.1168	0.1222	0.1254	0.1338	0.1485	0.1048	0.1269

U_g=0.3 m/s							
C/C_0	r/R=0	0.316	0.548	0.707	0.837	0.95	Average
H=0.22	0.4687	0.4693	0.4537	0.3823	0.4069	0.3672	0.4152
0.53	0.2831	0.3233	0.3237	0.3301	0.2680	0.2142	0.2906
0.79	0.2463	0.2636	0.2413	0.2554	0.1725	0.1540	0.2164
1.04	0.2323	0.2348	0.1779	0.1374	0.1182	0.1204	0.1566
1.30	0.1802	0.1630	0.1315	0.1667	0.1387	0.1348	0.1470
1.55	0.1995	0.1766	0.2098	0.1898	0.2024	0.1713	0.1909
1.80	0.1876	0.1743	0.1861	0.1861	0.1861	0.1924	0.1855
2.34	0.1809	0.1809	0.1621	0.1809	0.1809	0.2041	0.1817

U_g=0.5 m/s							
C/C_0	r/R=0	0.316	0.548	0.707	0.837	0.95	Average
H=0.22	0.5132	0.5098	0.5028	0.4657	0.4249	0.3831	0.4568
0.53	0.3967	0.3873	0.3384	0.3494	0.3258	0.3349	0.3467
0.79	0.3268	0.3088	0.2835	0.3218	0.1675	0.2868	0.2736
1.04	0.2844	0.2680	0.2566	0.2288	0.2182	0.1960	0.2335
1.30	0.2064	0.2155	0.2326	0.2524	0.1581	0.1732	0.2061
1.55	0.1705	0.1885	0.1885	0.1885	0.1874	0.1885	0.1878
1.80	0.2100	0.2117	0.2117	0.2117	0.2370	0.2117	0.2168
2.34	0.1967	0.2093	0.2093	0.2093	0.2177	0.2093	0.2107

U_g=0.8 m/s							
C/C_0	r/R=0	0.316	0.548	0.707	0.837	0.95	Average
H=0.22	0.5653	0.5690	0.5358	0.4996	0.4915	0.5101	0.5204
0.53	0.5105	0.4624	0.4843	0.4019	0.4434	0.3770	0.4348
0.79	0.4194	0.3799	0.3993	0.3568	0.3520	0.3504	0.3686
1.04	0.3698	0.3471	0.3595	0.2752	0.2390	0.3371	0.3118
1.30	0.2851	0.2879	0.3025	0.2836	0.3181	0.2891	0.2963
1.55	0.3196	0.2874	0.2596	0.2743	0.2874	0.2417	0.2706
1.80	0.2677	0.2672	0.2238	0.2552	0.2592	0.2026	0.2411
2.34	0.2270	0.2270	0.2540	0.2270	0.2519	0.2270	0.2376

U_g=1.0 m/s							
C/C_0	r/R=0	0.316	0.548	0.707	0.837	0.95	Average
H=0.22	0.6320	0.5979	0.6144	0.5324	0.5558	0.5419	0.5691
0.53	0.5538	0.5291	0.5195	0.4958	0.3723	0.4197	0.4672
0.79	0.4765	0.4651	0.4013	0.3773	0.3578	0.4022	0.4000
1.04	0.3456	0.3005	0.3720	0.3991	0.3930	0.3112	0.3573
1.30	0.3672	0.3693	0.3551	0.3245	0.2769	0.2584	0.3162
1.55	0.3249	0.2972	0.3015	0.2922	0.2873	0.2148	0.2791
1.80	0.2861	0.2876	0.3138	0.3055	0.2614	0.1656	0.2667
2.34	0.2850	0.2850	0.2686	0.2716	0.2416	0.2311	0.2592

B.10 C/C_0 in the CTFB

U_g=1.0 m/s, G_s=100 kg/m^{2}s							
C/C_0	r/R=0	0.316	0.548	0.707	0.837	0.95	Average
0.56	0.3222	0.3216	0.2900	0.2529	0.2301	0.1730	0.2527
1.02	0.2881	0.2982	0.2388	0.1922	0.1887	0.1460	0.2114
1.47	0.2421	0.2308	0.2122	0.1904	0.1604	0.1403	0.1865
1.93	0.1976	0.2039	0.2153	0.1593	0.1443	0.1365	0.1714
2.39	0.1836	0.1656	0.1712	0.1258	0.1353	0.1405	0.1480

U_g=1.0 m/s, G_s=200 kg/m^{2}s							
C/C_0	**r/R=0**	**0.316**	**0.548**	**0.707**	**0.837**	**0.95**	**Average**
0.56	0.3196	0.2861	0.2840	0.2489	0.1959	0.1601	0.2353
1.02	0.2819	0.2635	0.2405	0.1846	0.1353	0.1116	0.1867
1.47	0.2374	0.2023	0.1893	0.1510	0.1163	0.0858	0.1492
1.93	0.1969	0.1810	0.1601	0.1231	0.1044	0.0767	0.1288
2.39	0.1734	0.1541	0.1286	0.1152	0.0871	0.0551	0.1079

U_g=1.0 m/s, G_s=300 kg/m^{2}s							
C/C_0	**r/R=0**	**0.316**	**0.548**	**0.707**	**0.837**	**0.95**	**Average**
0.56	0.3005	0.2799	0.2394	0.2077	0.1703	0.1296	0.2049
1.02	0.2527	0.2456	0.1636	0.1592	0.1090	0.0915	0.1526
1.47	0.1755	0.1707	0.1045	0.1077	0.0755	0.0547	0.1017
1.93	0.1338	0.1248	0.0880	0.0731	0.0721	0.0464	0.0805
2.39	0.0987	0.1022	0.0875	0.0725	0.0450	0.0212	0.0652

U_g=2.0 m/s, G_s=30 kg/m^{2}s							
C/C_0	**r/R=0**	**0.316**	**0.548**	**0.707**	**0.837**	**0.95**	**Average**
0.25	0.9390	0.9239	0.8945	0.8778	0.8203	0.6854	0.8398
0.56	0.8544	0.8742	0.8664	0.7793	0.7267	0.5929	0.7663
1.47	0.7817	0.7714	0.7827	0.7435	0.6584	0.5307	0.6969
2.39	0.7328	0.7239	0.7224	0.6814	0.5728	0.4738	0.6342

U_g=2.0 m/s, G_s=60 kg/m^{2}s							
C/C_0	**r/R=0**	**0.316**	**0.548**	**0.707**	**0.837**	**0.95**	**Average**
0.25	0.9098	0.8550	0.8044	0.7840	0.7041	0.6441	0.7585
0.56	0.7405	0.6991	0.6894	0.6391	0.5863	0.4964	0.6223
1.47	0.5851	0.5733	0.6061	0.5471	0.5152	0.3902	0.5264
2.39	0.5309	0.5291	0.5291	0.5085	0.4701	0.3209	0.4711

U_g=2.0 m/s, G_s=100 kg/m^{2}s							
C/C_0	**r/R=0**	**0.316**	**0.548**	**0.707**	**0.837**	**0.95**	**Average**
0.25	0.6951	0.6823	0.6263	0.5787	0.5539	0.4945	0.5862
0.56	0.6523	0.6218	0.5605	0.5084	0.4586	0.4183	0.5129
1.02	0.5911	0.5417	0.4923	0.4710	0.4040	0.3641	0.4547
1.47	0.5269	0.4934	0.4350	0.4170	0.3980	0.3292	0.4143
1.93	0.4881	0.4443	0.4012	0.3842	0.3594	0.3030	0.3787
2.39	0.4656	0.4290	0.3942	0.3750	0.3481	0.2852	0.3664

U_g=2.0 m/s, G_s=200 kg/m^{2}s							
C/C_0	**r/R=0**	**0.316**	**0.548**	**0.707**	**0.837**	**0.95**	**Average**
0.25	0.6630	0.6639	0.6466	0.5629	0.5026	0.4836	0.5709
0.56	0.5980	0.5731	0.4997	0.4483	0.3914	0.3771	0.4570
1.02	0.5420	0.5124	0.4470	0.3811	0.3311	0.3225	0.3981

1.47	0.4863	0.4589	0.3921	0.3195	0.3003	0.2919	0.3518
1.93	0.4287	0.3934	0.3575	0.2969	0.2556	0.2555	0.3116
2.39	0.4041	0.3818	0.3355	0.2822	0.2531	0.2426	0.2958

U_g=2.0 m/s, G_s=300 kg/m^{2}s							
C/C$_0$	***r/R*=0**	**0.316**	**0.548**	**0.707**	**0.837**	**0.95**	**Average**
0.25	0.5943	0.5761	0.6061	0.5496	0.4615	0.4718	0.5332
0.56	0.5064	0.4401	0.4223	0.3723	0.3355	0.3251	0.3800
1.02	0.4711	0.4024	0.4124	0.3502	0.2738	0.2570	0.3403
1.47	0.4199	0.3631	0.3381	0.2807	0.2335	0.2198	0.2875
1.93	0.3788	0.3438	0.3198	0.2484	0.2059	0.1902	0.2615
2.39	0.3550	0.3297	0.3106	0.2282	0.2085	0.1798	0.2511
U_g=3.0 m/s, G_s=100 kg/m^{2}s							
C/C$_0$	***r/R*=0**	**0.316**	**0.548**	**0.707**	**0.837**	**0.95**	**Average**
0.56	0.8867	0.8118	0.7523	0.7089	0.6621	0.6033	0.7082
1.02	0.7834	0.7387	0.6688	0.6330	0.5867	0.5135	0.6278
1.47	0.6817	0.6412	0.5674	0.5912	0.5471	0.4925	0.5678
1.93	0.6586	0.5861	0.5843	0.5298	0.4964	0.4548	0.5315
2.39	0.5930	0.5599	0.5393	0.5178	0.4963	0.4111	0.5051

U_g=3.0 m/s, G_s=200 kg/m^{2}s							
C/C$_0$	***r/R*=0**	**0.316**	**0.548**	**0.707**	**0.837**	**0.95**	**Average**
0.56	0.7659	0.7182	0.7046	0.6462	0.6039	0.5559	0.6462
1.02	0.6738	0.6141	0.5979	0.5613	0.5341	0.4878	0.5599
1.47	0.7007	0.6134	0.5569	0.5047	0.4829	0.4317	0.5188
1.93	0.6173	0.5505	0.5294	0.4833	0.4280	0.3832	0.4757
2.39	0.5866	0.5279	0.5010	0.4570	0.4120	0.3659	0.4294

U_g=3.0 m/s, G_s=300 kg/m^{2}s							
C/C$_0$	***r/R*=0**	**0.316**	**0.548**	**0.707**	**0.837**	**0.95**	**Average**
0.56	0.7457	0.6942	0.6485	0.6014	0.5748	0.5417	0.6123
1.02	0.6607	0.5936	0.5697	0.5216	0.4898	0.4485	0.5255
1.47	0.6166	0.6105	0.4880	0.4558	0.4104	0.3845	0.4679
1.93	0.5714	0.5171	0.4474	0.3905	0.3426	0.3266	0.4047
2.39	0.5202	0.4759	0.4052	0.3796	0.3628	0.3073	0.3860

Curriculum Vitae

Name: Jiangshan Liu

Post-secondary Education and Degrees:

Ph.D.
The University of Western Ontario
London, Ontario, Canada, 2013-2016

M.E.Sc.
The University of Western Ontario
London, Ontario, Canada, 2012-2013

B.Eng.
Beijing University of Chemical Technology
Beijing, China, 2008-2012

Honours and Awards:

Honour of Outstanding Graduate
2012

BASF Chemical Company Sponsored Scholarship
2011

Renmin Scholarship
2008, 2009 2010

Related Work Experience

Teaching Assistant
The University of Western Ontario
2013-2016

Internship
Institute of Process Engineering, Chinese Academy of Sciences
2011-2012

Publications:

H.G. Gomaa, **J. Liu**, R.Sabouni, J. Zhu, "Operational characteristics of oscillatory micro-screen emulsifier: coupling effects and energy dissipation", Chemical Engineering Science, 2014, 117:161-172

H.G. Gomaa, **J. Liu**, R.Sabouni, J. Zhu, "Experimental and theoretical analysis of emulsification characteristics using a high porosity microscreen under oscillatory shear conditions", Colloids and Surfaces A: Physicochemical and Engineering Aspects, 2014, 456:160-168

J. Liu, "Oil-in-water emulsification using oscillatory micro-screen", Dissertation, University of Western Ontario, London, 2013

W. Zeng, H.G. Gomaa, **J. Liu**, J. Zhu, "Intensification of production of O/W emulsions using oscillatory woven metal micro-screen (WMMS)", Chemical Engineering and Processing: Process Intensification, 2013, 73:111-118

F. Ye, W. Hu, H. Liu, **J. Liu**, J. Li, X. Wang, J. Yang, "Pt-IrO2 nanorod array electrode for oxygen evolution in PEM water electrolysis cell", Asia-Pacific Journal of Chemical Engineering, 2012, 8(2):271–277